John M. Wills
Mebarek Alouani
Per Andersson
Anna Delin
Olle Eriksson
Oleksiy Grechnyev

Full-Potential Electronic Structure Method

Energy and Force Calculations with Density Functional and Dynamical Mean Field Theory

⨎ Springer

Springer Series in

SOLID-STATE SCIENCES

The Springer Series in Solid-State Sciences consists of fundamental scientific books prepared by leading researchers in the field. They strive to communicate, in a systematic and comprehensive way, the basic principles as well as new developments in theoretical and experimental solid-state physics.

John M. Wills · Mebarek Alouani
Per Andersson · Anna Delin
Olle Eriksson · Oleksiy Grechnyev

Full-Potential Electronic Structure Method

Energy and Force Calculations
with Density Functional
and Dynamical Mean Field Theory

With 59 Figures

 Springer

John M. Wills
Los Alamos National Laboratory
Theoretical Division
PO Box 1663, Los Alamos, NM 87545, USA
E-mail: jxw@lanl.gov

Dr. Per Andersson
FOI, Swedish Defence Research Agency
Stockholm, Sweden
E-mail: per.andersson@foi.se

Professor Olle Eriksson
Uppsala University
Department of Physics and Astronomy
PO Box 516, 75120 Uppsala, Sweden
E-mail: olle.eriksson@fysik.uu.se

Professor Mebarek Alouani
Université Strasbourg
CNRS-UMR 7504
Institut Physique et Chimie
des Matériaux de Strasbourg (IPCMS)
rue du Loess 22, 67034 Strasbourg CX2, France
E-mail: mea@ipcms.u-strasbg.fr

Anna Delin
Royal Institute of Technology (KTH)
Deptartment of Materials Science
and Engineering
Brinellvägen 23, 100 44 Stockholm, Sweden
E-mail: annadel@kth.se

Dr. Oleksiy Grechnyev
National Academy of Sciences of Ukraine
B. Verkin Institute for Low Temperature
Physics and Engineering
Lenin Ave. 47, 61103 Kharkov, Ukraine
E-mail: shrike4625@yahoo.com

Series Editors:

Professor Dr., Dres. h. c. Manuel Cardona
Professor Dr., Dres. h. c. Peter Fulde*
Professor Dr., Dres. h. c. Klaus von Klitzing
Professor Dr., Dres. h. c. Hans-Joachim Queisser

Max-Planck-Institut für Festkörperforschung, Heisenbergstrasse 1, 70569 Stuttgart, Germany

* Max-Planck-Institut für Physik komplexer Systeme, Nöthnitzer Strasse 38
  01187 Dresden, Germany

Professor Dr. Roberto Merlin
Department of Physics, University of Michigan
450 Church Street, Ann Arbor, MI 48109-1040, USA

Professor Dr. Horst Störmer
Dept. Phys. and Dept. Appl. Physics, Columbia University, New York, NY 10027 and
Bell Labs., Lucent Technologies, Murray Hill, NJ 07974, USA

Cover design: Integra Software Services Pvt. Ltd., Pondicherry

Printed on acid-free paper

We dedicate this book to
Barry, Börje, Hans, Mike, and Ole

Preface

This is a book describing electronic structure theory and application within the framework of a methodology implemented in the computer code RSPt. In 1986, when the code that was to become RSPt was developed enough to be useful, it was one of the first full-potential, all-electron, relativistic implementations of DFT (density functional theory). While RSPt was documented parasitically in many publications describing the results of its application, it was many years before a publication explicitly describing aspects of the method appeared. In the meantime, several excellent all-electron, full-potential methods had been developed, published, and become available. So why a book about RSPt now?

The code that became RSPt was initially developed as a personal research tool, rather than a collaborative effort or as a product. As such it required some knowledge of its inner workings to use, and as it was meant to be maximally flexible, the code required experience to be used effectively. These attributes inhibited, but did not prevent, the spread of RSPt as a research tool. While applicable across the periodic table, the method is particularly useful in describing a wide range of materials, including heavier elements and compounds, and its flexibility provides targeted accuracy and a convenient and accurate framework for implementing and assessing the effect of new models. A fair number of informal developers arose in the course of doctoral, postdoctoral, and professional research, principally at Uppsala University and at many other institutions as well. As a consequence, a number of innovative extensions to the code were developed, many of which were never integrated in the "official" version of RSPt and were consequently lost or shelved, often to be re-invented at a later date.

This situation started to change in 2006 when a group of researchers with a stake in the methodology met to establish a protocol for continuous development of a single RSPt thread. We established a code repository with developing branches merged periodically and a web site to facilitate communication, disseminate stable versions of the code, and provide a forum for user support and discussion. This group meets yearly to evolve the organization and suggest

ongoing and future efforts. The results of this organization have been grat-
ifying. Computationally, data structures and memory allocation have been
substantially reworked, eliminating non-standard and annoying remnants of
Fortran 77 and enhancing modularity. RSPt is now k-point-, band-, and FFT-
parallel. In methodology, physics modules such as DMFT and SIC are now
present in the stable version, and forces are finally available without restric-
tion.

No one is explicitly paid to do this development. At best, code and method
development support particular research directions. The development contin-
ues, however, largely because the developers believe that expanding the capa-
bility and efficiency of RSPt will benefit their research, and that making RSPt
more accessible will enhance the research of others. This book, encompassing
electronic structure theory, technical detail, and representative application, is
another step in this process.

Los Alamos   *John Wills*
Uppsala   *Olle Eriksson*
August 2010

Contents

Part I

Formalisms

1

Introductory Information

Abstract In this introductory chapter a short historical note on the history of linear muffin-tin orbital methods is given, together with general background information and units used throughout the book. The main objectives with the book are presented as well as information about web-based information, which easier enables using the full-potential linear muffin-tin orbitals method.

1.1 Objectives and What You Will Learn from Reading This Book

The purpose of this book is to give a full account of an implementation of a method for calculating the electronic structure of materials, using linear muffin-tin orbitals as basis functions. The method is referred to as RSPt (relativistic spin-polarized test), where after some 20 years of use and development the letter "t" is a mystery. The invention of linear muffin-tin orbitals is due to Andersen [11] and the first step toward what now is RSPt was taken by Wills and Cooper [258]. From reading this book you will be familiar with electronic structure theory in general, including density functional theory [116, 140], a theory for which Walter Kohn shared the Nobel Prize in chemistry 1998. You will also be familiar with the use of linear muffin-tin orbitals as basis functions for calculations of electronic structures of solids. This book contains in addition to a technical description of linear muffin-tin orbitals and their implementation in RSPt, several examples of the use of RSPt in the field of phase stability, magnetism, optics, and excited state properties. Simple instructions on how to download the source code from the RSPt web site (http://www.rspt.net/), how to compile it and perform test runs of the code, and a manual for input and output are also provided here, with the hope that from reading this book you will be comfortable in setting up the code, run it on a single- or multi-processor computer architecture, assess the quality of the calculations, and to analyze the calculated results. By

the time you have read this book, you will find that a database with calculated electronic structures using the RSPt method is available at the web site http://gurka.fysik.uu.se/esp/, where tens of thousands of results from already made electronic structure calculations can be found and extracted.

In order to successfully absorb the information provided in this book, it is recommended that you have studied elementary textbooks in solid state physics, e.g., the book of Kittel [134], Marder [163], or by Ashcroft and Mermin [22]. It is also recommended to study a book on molecular orbital theory, e.g., the book by Atkins [24].

1.2 On Units

Throughout this book we make use of atomic Rydberg units, in which $\hbar = 1$, $e^2 = 2$, and the electron mass $m = 1/2$. The unit of length is the Bohr radius $a_0 = \hbar^2/me^2 = 0.529178\,\text{Å}$, the unit of energy is the Rydberg, $\text{Ry} = e^2/2a_0 = 13.6058\,\text{eV}$, and the rest energy of the electron $mc^2 = e^2/a_0\alpha^2$ where $\alpha \sim 1/137$ is the fine-structure constant.

1.3 Obtaining RSPt and the RSPt Web Site

The source code, RSPt, can be downloaded from http://www.rspt.net/. Here one finds also a manual for the input and the output of the code, information on how to install the source code, as well as a user's forum, where one can obtain answers for most technical questions concerning installing and running RSPt. A full account of the installation and running of RSPt is given in Chap. 9. The RSPt source code is freely available.

1.4 A Short Comment on the History of Linear Muffin-Tin Orbitals and RSPt

The RSPt method is an all-electron, full-potential (FP) implementation of density functional theory using linear muffin-tin orbitals (LMTOs) as basis functions, and the technique is in general often referred to as an FP-LMTO method. By "all-electron" it is meant that all electrons in the solid are considered in the calculation of electron density and total energy (as opposed, for instance, to a pseudo-potential method, where only the valence electrons are considered). The term "full potential" implies that no approximation is made to the shape of the electron density or the electronic potential (as opposed to the popular atomic sphere approximation, ASA [11], where the crystal is considered to be composed of space-filling atomic spheres, with a spherically symmetric potential inside each sphere).

The development of linear muffin-tin orbitals is due to Andersen, as is the use of linear augmented plane waves [11]. The LMTO basis set can be obtained from the older Korringa–Kohn–Rostocker (KKR) method [139, 142], where the main difference is the linearization of the energy-dependent basis functions. We will describe this technical difference between the two methods in Chaps. 5 and 6. The use of linear muffin-tin orbitals is by now well documented, and since the original suggestion of their usefulness some 4,000 applications have to this date been published (according to ISI web of knowledge). By now, several implementations of electronic structure methods which are based on LMTOs can be found, with varying degrees of sophistication. The most efficient and computationally least demanding variant of the method relies on the aforementioned atomic sphere approximation (ASA). An early account of this method, which often is described as LMTO-ASA, is the original reference of Andersen, but also in the book of Skriver [209] and in the works of [38]. Extensions of the original ideas of LMTOs can be found in the tight-binding version of the method [12], as well as the full-charge density implementation of it [248]. The LMTO-ASA method has also been adopted in a Green's function formalism with the capability of treating disordered alloys in the coherent-potential approximation (CPA) [1, 210, 254]. In addition to the RSPt implementation of a full-potential LMTO method, there exists other independent, separate full-potential implementations using linear muffin-tin orbitals [199]. It should also be mentioned here that a derivative of the LMTO method exists in the form of the exact muffin-tin orbitals method (EMTO) [13, 247].

The main advantage with a full-potential implementation using linear muffin-tin orbitals, as described here, is that the electronic structure problem is solved with very high accuracy, so that total energies and Hellman–Feynman forces can be calculated with high precision, while maintaining a limited basis set, which makes the analysis of the calculated results straightforward. As will be shown in Chap. 11, an accuracy of the total energy (or rather difference in total energy for two different crystallographic geometries) of order μRy is needed to calculate, e.g., the elastic constants of materials. In Chap. 12 it is argued that an accuracy better than $0.1\,\mu$Ry is needed to calculate the difference in total energy for two different magnetic orientations of regular magnetic transition metals like bcc Fe or hcp Co, and that the RSPt method can reach such high accuracy.

This implementation in RSPt is the result of both planning and evolution. One motivation for developing the method that eventually became RSPt was to be able to investigate the properties of f-electron elements and compounds, testing the applicability of density functional theory (DFT), in the local or nearly local approximation in describing the often unusual properties of these materials. Thus RSPt was born as a "full-potential" electronic structure method, expressing the shape of the electron density and potential in full generality. There were (and are) several other approximations to overcome, such as the "frozen core" approximation, in which the core electron density

is an external, constant input, and the lack of relativistic effects, particularly the spin–orbit interaction. RSPt treats all electrons on the same footing ("all-electron") and includes relativistic effects such as the spin–orbit interaction in the one-electron Hamiltonian as well as spin polarization.

Another motivation for developing a new method was to provide a basis, based on first principles, for going beyond DFT, to include many-electron effects (strong correlation). The first use of the method, in fact, was to parametrize a Schrieffer–Wolff Hamiltonian to treat hybridization-mediated magnetic interactions in cerium monopnictides [258]. The Schreiffer–Wolff Hamiltonian, like most phenomenological Hamiltonians treating strong correlation in solids, treats on-site correlation explicitly. As this was a motivating factor for the development of a new method, therefore, the natural choice was to use a site-centered basis. Thus RSPt uses linear muffin-tin orbitals (LMTOs), described in this book, as the basis for one-electron wave functions. Chapter 7 illustrates the usefulness of this choice. By choosing LMTO bases, RSPt, like other FP-LMTO methods, builds on a minimal basis set, emphasizing the applicability of the basis functions rather than basis set size, simplicity, or completeness.

The FP-LMTO method, as expressed in RSPt, solves the DFT electronic structure problem using a standard variational procedure based on the Kohn–Sham procedure [140] with a local (e.g., LDA [140]) or nearly local (e.g., GGA [179, 180]) approximation for the exchange and correlation functional as appropriate for that procedure. An input potential, an estimate of the exact potential (RSPt uses the one-electron potential as the variational parameter), is used to construct a one-electron Hamiltonian, and the eigenvalues and eigenvectors of this Hamiltonian are found within the span of a particular basis (the FP-LMTO method uses non-orthogonal linear muffin-tin orbitals). The Fermi energy is found by occupying the eigenstates in order, constrained by the required number of electrons, and the electron density is constructed by summing the occupied one-electron densities and used to construct a new one-electron potential. This potential is combined with the input potential to produce a new estimate of the exact potential, and the process continued until the input and output potentials are identical within a specified tolerance. When this self-consistency is achieved, the total energy calculated from self-consistent potential is the accurate ground state energy for the exchange-correlation functional used.

There have been several "FP-LMTO" implementations [168, 198, 199, 225, 255, 258]. In what follows, we try to distinguish features common to many implementations (labeled as "FPLMTO") from our particular methodology (labeled "RSPt").

Density Functional Theory
and the Kohn–Sham Equation

Abstract The basic formulas of density functional theory (DFT) are derived, together with a discussion about the form and accuracy of different approximations to the energy functional used in DFT. Central concepts in DFT, like exchange and correlation hole, exchange and correlation energy, and the Kohn–Sham equation are presented. A short description about the historical development of density functional theory as also given.

Calculations of material properties using density functional theory (DFT) have become a very active field of research in recent years. The basic idea of DFT is to use the electron charge density $n(\mathbf{r})$ as the basic variable instead of the many-electron wave function used in Hartree–Fock theory. This seemingly small – but in reality very nontrivial – step has provided the framework for fast and efficient calculations on highly complex materials, so it is easy to understand that DFT is popular. Figure 2.1 illustrates how the field
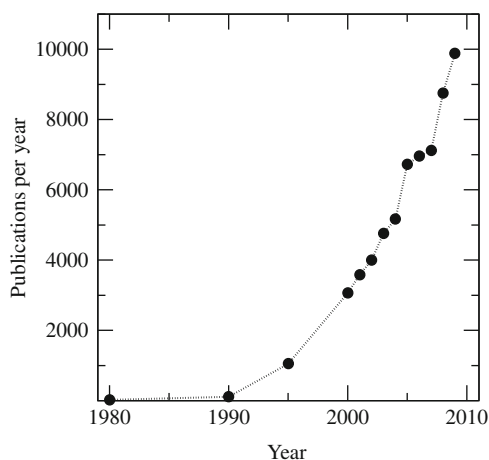
Fig. 2.1. Number of publications per year with topic "density functional" according to Web of Science (www.isiknowledge.com)

has grown in recent years. The number of publications per year in the field appears to have increased nearly exponentially during the last two decades. Nowadays, DFT-based computational methods are must-have tools in materials research and quantum chemistry. In recognition of the enormous success of DFT and computational schemes based on DFT, Walter Kohn and John A. Pople received the 1998 Nobel Prize in chemistry.

Over the years, the original formulation of DFT and the Kohn–Sham approach has been extended to cover a large number of situations, as, for instance, degenerate ground states [138], spin-polarized systems [188, 250], relativistic systems [162, 189], diamagnetic effects [246], finite temperature [166], excited states [102, 182, 234], fractional occupation numbers [158, 183], or multicomponent systems like electron–hole liquids [130, 196] and systems where the Born–Oppenheimer approximation is not valid [44]. In this chapter, we give a brief overview of the basic DFT machinery. More complete treatments can be found, e.g., in [75, 164].

2.1 The Many-Particle Problem

The basic problem in condensed matter theory which DFT attempts to solve is how to deal mathematically with the interactions of a large number of particles. If the system we are interested in is an atom or a small molecule, the number of particles is still rather small, but if we are dealing with larger systems, describing the wave function of the system explicitly becomes infeasible.

Despite these seemingly insurmountable difficulties, let us anyway start by writing the full Hamiltonian, in the non-relativistic case, of the many-body problem for a metal or other material in terms of the individual coordinates of each particle. The solid is a strongly coupled system consisting of two species – electrons and nuclei – with Coulomb interaction both between themselves and each other. The Hamiltonian (in SI units) will therefore consist of the following terms:

$$\mathcal{H} = -\frac{\hbar^2}{2} \sum_I \frac{\nabla_I^2}{M_I} + \frac{1}{2} \sum_{I \neq J} \frac{Z_I Z_J e^2}{4\pi\epsilon_0 |\mathbf{R}_I - \mathbf{R}_J|} - \frac{\hbar^2}{2m} \sum_i \nabla_i^2$$
$$+ \frac{1}{2} \sum_{i \neq j} \frac{e^2}{4\pi\epsilon_0 |\mathbf{r}_i - \mathbf{r}_j|} - \sum_{i,I} \frac{Z_I e^2}{4\pi\epsilon_0 |\mathbf{r}_i - \mathbf{R}_I|} , \tag{2.1}$$

where the indices i, j are used for electrons and I, J are for atomic nuclei, M_I denotes nuclear masses, m is the electron mass, $\mathbf{R}_I$ and $\mathbf{r}_i$ stand for nuclear and electron coordinates, respectively, and Z_I denotes atomic number. All attempts to find the eigenvectors and eigenvalues to this Hamiltonian involve approximations. To begin with, the nuclei are far more massive than the electrons and their velocities are therefore relatively low in comparison. Therefore, one may assume that the time scale for electron relaxation is much

shorter than the time scale of atom movement, so that the electron cloud can be assumed to be completely relaxed at any moment even if the atoms are, e.g., vibrating. This is called the Born–Oppenheimer (BO) approximation, which permits us to separate the time scales of electron and atom motion and thus to treat the terms in (2.1) dealing with the electron states separately from the ones dealing with the atomic nuclei. Further, the BO approximation allows us to recast the term describing the Coulomb interaction between the atomic nuclei and the electron cloud – the last term in (2.1) – as an external potential acting on the electrons. Although the Born–Oppenheimer approximation is very accurate in most cases, it does not always apply. One example is graphene [128].

Thus, our many-particle problem has been reduced to a strongly interacting "gas"[1] or liquid of electrons moving in an external potential, and the Hamiltonian acting on the electrons can now be written as

$$\mathcal{H} = -\frac{1}{2}\sum_i \nabla_i^2 + \frac{1}{2}\sum_{i\neq j}\frac{e^2}{|\mathbf{r}_i - \mathbf{r}_j|} - \sum_{i,I}\frac{Z_I e^2}{|\mathbf{r}_i - \mathbf{R}_I|} = T + W + V_{\text{ext}}\,. \quad (2.2)$$

The first term, T, is the kinetic energy operator of the electrons. The second, W, is the Coulomb potential from electron–electron interaction, and the third term, V_{ext}, is the external potential, i.e., the Coulomb potential from the interactions between the electrons and the nuclei. The corresponding total energy E is the expectation value of $\mathcal{H}$ in (2.2), i.e.,

$$E = \langle \Psi\,|\mathcal{H}|\,\Psi\rangle = T + W + \int \mathrm{d}^3r\, V_{\text{ext}}(\mathbf{r})n(\mathbf{r})\,, \quad (2.3)$$

with T and W now denoting the expectation values of the kinetic energy and electron–electron interaction operators, respectively. From classical physics we know that the Coulomb energy of a charge density interacting with itself is

$$E_{\text{Hartree}} = \frac{1}{2}\int \mathrm{d}^3r\,\mathrm{d}^3r'\frac{n(\mathbf{r})n(\mathbf{r}')}{|\mathbf{r} - \mathbf{r}'|}\,. \quad (2.4)$$

This term is called the Hartree energy and is an important part of the middle term W in (2.3), but obviously not the full story. To begin with, the Hartree energy contains a spurious self-interaction. Further, since electrons are particles, their motions will be correlated causing a depletion in the charge density around each electron. In addition, the quantum-mechanical nature of electrons causes a special type of correlation – exchange – due to the exclusion principle. These extra terms are usually grouped together in the so-called exchange-correlation energy E_{xc}.

---

[1] The original meaning of the word gas, *chaos*, may provide a better association.

2.2 Early Attempts to Solve the Many-Particle Problem

Before describing the DFT approach to solving the many-electron problem, it is instructive to briefly summarize some of its forerunners. We start with the free electron model (FEM), which actually works very well for many simple metals such as aluminum. We then proceed with the Hartree and Hartree–Fock approaches and finally the Thomas–Fermi model, which might be thought of as a very early form of DFT since it uses the electron charge density as the basic variable instead of the wave function.

2.2.1 Free Electron Model

A very early attempt to solve the above electron problem for metals was the free electron model (FEM) [221–223]. In this very simple model, the conduction electrons in metals are assumed to constitute an ideal gas of fermions, i.e., by construction, the electrons are assumed to interact with each other in the same way as do neutral gas molecules in an ideal gas, with the added feature that the electrons obey fermion statistics. The ion cores and nuclei are taken as stationary.

FEM, originally due to Sommerfeld, succeeds in describing metals like silver or aluminum surprisingly well. However, this does not mean that the conduction electrons in a metal are free. If they were, these metals would soon disintegrate and not be the rather tough and tenacious substances we know. As already mentioned, the electrons interact very strongly with each other and with the nuclei through the Coulomb interaction. The reason why FEM works so well has been formulated in the Landau hypothesis [150], which states that a system composed of a large number of interacting particles has low-lying excited states that can be viewed as particles themselves, called quasiparticles, and that in many cases the energy spectrum of the quasiparticle system is very similar to the spectrum of the interacting system. Physically, a quasiparticle in the electron system may be viewed as a single electron surrounded by an equilibrium distribution of other electrons. The idea is similar to the charge renormalization of the naked Dirac electron due to vacuum polarization.

Another idea in the same direction is to map the many-electron problem onto an independent electron moving in an effective potential. This is the conceptual core of the Kohn–Sham formulation of DFT, as will be explained in more detail later in this chapter. This is of fundamental importance, since although the theorems of DFT are very general and powerful they do not, as we will see, provide us with a practical scheme for actually performing calculations. For that, we need the Kohn–Sham approach.

2.2.2 The Hartree and Hartree–Fock Approaches

The Hartree approach [113] assumes that the electrons are non-interacting, so that each electron i obeys a Schrödinger-like equation

$$\mathcal{H}_{\text{eff}}\psi_i(\mathbf{r}) = \left(-\frac{1}{2}\nabla^2 + V_{\text{eff}}(\mathbf{r})\right)\psi_i(\mathbf{r}) = \epsilon_i\psi_i(\mathbf{r})\,, \tag{2.5}$$

where the electrons move in an effective potential $V_{\text{eff}}(\mathbf{r})$. The ground state is determined by occupying the lowest lying eigenstates, while obeying the Pauli principle. The difficulty and great limitation of this approach is to decide the form of $V_{\text{eff}}(\mathbf{r})$.

In contrast, in the Hartree–Fock method, one uses a total wave function for the system instead of separate single-particle wave functions $\psi_i(\mathbf{r})$. The total Hartree–Fock wave function is symmetrized so that it changes sign when two electron quantum numbers are switched, i.e., the effect of "exchange" is built into the wave function by construction. However, because of the use of a single Slater determinant other electron–electron correlations are neglected. Actually, one might consider this the definition of "exchange." The Hamiltonian (2.2) acts on the Hartree–Fock wave function and the solution is found by variational calculus, i.e., minimization of the total energy with respect to the coefficients in the expansion of the wave function. In the absence of spin–orbit coupling, the Hartree–Fock wave function can be written as a Slater determinant [211]. The Hartree–Fock approach has had large success and was, until the development of hybrid functionals such as P3LYP [227], the method of choice in quantum chemistry.

2.2.3 Thomas–Fermi Theory

The idea of replacing the wave function with the charge density was proposed in 1927 [236], resulting in the so-called Thomas–Fermi approach to electronic structure. Dirac improved on the theory by including a term describing the exchange energy [74]. The total energy of the system is written as

$$E_{\text{TF}} = C_1 \int \mathrm{d}^3r\, n(\mathbf{r})^{5/3} + \int \mathrm{d}^3r\, V_{\text{ext}}(\mathbf{r})n(\mathbf{r})$$
$$+ C_2 \int \mathrm{d}^3r\, n(\mathbf{r})^{4/3} + \frac{1}{2}\int \mathrm{d}^3r\, \mathrm{d}^3r' \frac{n(\mathbf{r})n(\mathbf{r}')}{|\mathbf{r}-\mathbf{r}'|}\,, \tag{2.6}$$

with $C_1 = (3/10)(3\pi^2)^{2/3}$ and $C_2 = -(3/4)(3/\pi)^{1/3}$. The first term describes the kinetic energy, then follows the electron–nuclei interaction, the exchange and finally the Hartree term. In the expression above, the kinetic energy and correlation terms of the many-electron system are calculated assuming a homogeneous electron gas (HEG). The HEG is of fundamental importance in DFT, and thus we repeat the definition of it here and also the definition of the often used parameter r_{s}. The density n of the homogeneous electron gas is

$$n = \frac{N}{\Omega}\,, \tag{2.7}$$

where N is the total number of electrons in the volume Ω. The electron density is often expressed using the parameter r_{s}, defined as

$$r_{\mathrm{s}} = \left(\frac{3}{4\pi n}\right)^{1/3}. \tag{2.8}$$

Here, r_{s} is the radius of a sphere containing exactly one electron. The larger the r_{s} is, the lower is the electron density. In atoms and materials, the electron density is far from being homogeneous, and not so surprisingly, the HEG approximation turns out to be too coarse. The Thomas–Fermi theory failed to produce any quantitatively impressive results, but the basic idea – using the electron charge density as the basic variable instead of the wave function – turned out to be most fruitful. Finally, we note that in (2.6), all terms are integrals of the charge density, i.e., they are functionals[2] of the charge density.

2.3 Density Functional Theory

Physical systems with the same number of electrons but different external potentials have different charge densities $n(\mathbf{r})$ in their ground states. This is obvious in the case of, for example, C_2H_2 and N_2, two molecules which both contain 14 electrons but have very different external potentials. Interestingly, it is also a completely general and exact statement and constitutes as such an important part of density functional theory (DFT). The example above illustrates the underlying idea in DFT, which is to use the charge density n as the basic variable.

In the following, the basic theorems of DFT will be presented [116]. The Kohn–Sham ansatz [140], which is of central importance in the practical use of DFT, is also described. The aim is to present ideas and assumptions rather than mathematical detail, and therefore only the simplest version of the theory, i.e., the non-degenerate, non-relativistic, non-spin-polarized case will be discussed explicitly.

2.3.1 Hohenberg–Kohn Theory

The theorems initially formulated by Hohenberg and Kohn [116] constitute the theoretical basis of DFT. The formulation here follows the one in [75]. Consider a system of charged spinless fermions (in practice, a paramagnetic system of electrons) with a non-degenerate ground state described by the non-relativistic time-independent Hamiltonian (2.2). The theory, originally developed by Hohenberg and Kohn, can be summarized in three statements.

Statement 1 (Uniqueness): The ground state expectation value of any observable is a unique functional of the exact ground state density $n(\mathbf{r})$.

Thus, for example, the ground state total energy E of a system can always and unambiguously be written as $E[n]$.

---

[2] A *functional* is a mapping from a function to a number. Functionals are usually denoted with square brackets [ ].

Statement 2 (Variational Principle) : The exact ground state density minimizes the total energy functional $E[n]$.

This statement provides us, at least in principle, with a scheme how to find the ground state charge density. Simply try all possible densities and choose the one that gives the lowest energy.

For the third statement, we need to rewrite our total energy expression (2.3) slightly. The part of the energy functional associated with the external potential can be singled out the remaining terms are summarized in a new functional $F[n]$ containing the kinetic energy and the electron–electron interaction energy. The total energy functional can then be written as

$$E[n] = F[n] + \int \mathrm{d}^3r \, V_{\mathrm{ext}}(\mathbf{r})n(\mathbf{r}) \,. \tag{2.9}$$

Statement 3 (Universality) : The functional $F[n]$ is universal in the sense that it does not depend on $V_{\mathrm{ext}}(\mathbf{r})$.

Thus, the mathematical form of $F[n]$ will be the same irrespective of system. It will be the same for plutonium metal, a hydrogen molecule, and a superconducting ceramic.

To proceed further, we follow the path by Kohn and Sham [140] and rewrite the universal functional $F[n] = T[n] + W[n]$ as

$$F[n] = T_{\mathrm{S}}[n] + \frac{1}{2} \int \mathrm{d}^3r \, \mathrm{d}^3r' \, \frac{n(\mathbf{r})n(\mathbf{r}')}{|\mathbf{r} - \mathbf{r}'|} + E_{\mathrm{xc}}[n] \,. \tag{2.10}$$

The first term, $T_{\mathrm{S}}[n]$, is the kinetic energy of a hypothetical non-interacting electron gas with the same density, and the second term is easily recognized as the classical Coulomb interaction. The functional $E_{\mathrm{xc}}[n]$ is called the exchange and correlation energy. All many-particle effects are contained in $E_{\mathrm{xc}}[n]$; among others, the many-particle contribution to the kinetic energy and the effects due to the Pauli exclusion principle. In order for the term $T_{\mathrm{S}}[n]$ to be meaningful at all, the density $n(\mathbf{r})$ has to be a ground state density of a non-interacting particle system, i.e., it has to be non-interacting V-representable.[3]

In principle, it is possible to calculate the ground state charge density and total energy from (2.9) using the variational principle (statement 2 in the Hohenberg–Kohn theory). In order to do this, we need to know the functionals $E_{\mathrm{xc}}[n]$ and $T_{\mathrm{S}}[n]$, the two remaining unknown terms in the total energy functional.

As regards $E_{\mathrm{xc}}[n]$, many approximative functionals have been developed, although we can probably never hope to find the exact functional since this functional retains in its heart all the difficulties of the many-particle problem. More surprisingly, the single-particle kinetic energy $T_{\mathrm{S}}[n]$ has yet escaped

---

[3] A density is V-representable if it is the density of a ground state of the Hamiltonian for some (local) external potential V_{ext}. In order to make use of the variational principle, one has to ascertain that each trial density is V-representable.

all attempts to be exactly written as a functional of the density. This latter difficulty is in fact the reason for not using the total energy expression directly in the variational procedure. Instead, one works around the problem with the help of the Kohn–Sham scheme.

2.3.2 The Kohn–Sham Equation

The basic idea of the Kohn–Sham scheme is to map the many-particle problem onto a system of non-interacting particles with the same ground state density $n(\mathbf{r})$ as the original many-particle system. To this end, we perform the variation of the energy functional (2.9) of the many-particle system, with $F[n]$ defined by (2.10):

$$\delta E[n] = 0 \qquad (2.11)$$

gives[4]

$$\mu = \frac{\delta E[n]}{\delta n(\mathbf{r})} = V_{\text{ext}} + \int \mathrm{d}^3 r' \frac{n(\mathbf{r}')}{|\mathbf{r} - \mathbf{r}'|} + \frac{\delta T_{\text{S}}[n]}{\delta n(\mathbf{r})} + \frac{\delta E_{\text{xc}}[n]}{\delta n(\mathbf{r})} , \qquad (2.12)$$

where μ is the Lagrange multiplier corresponding to the requirement of integer particle number. μ is also the chemical potential. Now, perform the same exercise on the energy functional of a system of non-interacting particles moving in some external potential, say V_{eff}. This energy functional is

$$E[n] = T_{\text{S}}[n] + \int \mathrm{d}^3 r \, V_{\text{eff}}(\mathbf{r}) n(\mathbf{r}) \qquad (2.13)$$

and variation gives, expressed in the standard way of writing functional derivatives,

$$\mu = \frac{\delta E[n]}{\delta n(\mathbf{r})} = \frac{\delta T_{\text{S}}[n]}{\delta n(\mathbf{r})} + V_{\text{eff}} . \qquad (2.14)$$

We see that (2.12) can be written in the form of (2.14) provided

$$V_{\text{eff}} = V_{\text{ext}} + \int \mathrm{d}^3 r' \frac{n(\mathbf{r})}{|\mathbf{r} - \mathbf{r}'|} + \frac{\delta E_{\text{xc}}[n]}{\delta n(\mathbf{r})} . \qquad (2.15)$$

---

[4] $\delta E[n]/\delta n(\mathbf{r})$ is the functional derivative of $\delta E[n]$ with respect to $n(\mathbf{r})$. When the functional has the simple form

$$F[\phi] = \int \mathrm{d}^3 r f(\mathbf{r}, \phi(\mathbf{r})) ,$$

i.e., F is an integral depending on $\phi(\mathbf{r})$ (but not on the gradient of $\phi(\mathbf{r})$ or any higher order derivatives such as the Laplacian), then the functional derivative is

$$\frac{\delta F[\phi]}{\delta \phi} = \frac{\partial f}{\partial \phi} .$$

The reason for the name V_{eff} is now clear. It can be looked upon as an effective external potential in which the non-interacting electrons are moving. The last term in (2.15) is called the exchange-correlation potential, i.e.,

$$V_{\text{xc}} = \frac{\delta E_{\text{xc}}[n]}{\delta n(\mathbf{r})} \,. \tag{2.16}$$

The effective potential V_{eff} transforms the many-particle problem to a single-particle formulation, and the Hamiltonian $\mathcal{H}_{\text{eff}}$ corresponding to (2.13) is

$$\mathcal{H}_{\text{eff}} = -\frac{1}{2}\nabla^2 + V_{\text{eff}}(\mathbf{r}) \,, \tag{2.17}$$

which gives a set of coupled Schrödinger-like equations, also called the Kohn–Sham (KS) equations

$$\mathcal{H}_{\text{eff}}(\mathbf{r})\psi_i(\mathbf{r}) = \left[-\frac{1}{2}\nabla^2 + V_{\text{eff}}(\mathbf{r})\right]\psi_i(\mathbf{r}) = \epsilon_i\psi_i(\mathbf{r}) \,. \tag{2.18}$$

The solutions $\{\epsilon_i, \psi_i(\mathbf{r})|\epsilon_1 \leq \epsilon_2 \leq \epsilon_3 \leq \cdots\}$ to (2.18) are called Kohn–Sham eigenvalues and eigenfunctions (or orbitals). The ground state density is given by

$$n(\mathbf{r}) = \sum_{i=1}^{N} |\psi_i(\mathbf{r})|^2 \,, \tag{2.19}$$

where the sum is over the N lowest eigenstates of $\mathcal{H}_{\text{eff}}$, and since $\mathcal{H}_{\text{eff}}$ directly depends on $n(\mathbf{r})$, (2.19) constitutes the coupling between the N one-electron equations in (2.18). With knowledge of the solution to (2.18), the kinetic energy term T_{S} can be exactly calculated by multiplying the Kohn–Sham equation (2.18) with ψ_i^* from the left, sum over i and integrate over all space, i.e.,

$$T_{\text{S}} = \sum_{i=1}^{N}\langle\psi_i| - \frac{1}{2}\nabla^2|\psi_i\rangle = \sum_{i=1}^{N}\epsilon_i - \int \mathrm{d}^3r V_{\text{eff}}(\mathbf{r})n(\mathbf{r}) \,, \tag{2.20}$$

and thus the problem of calculating the value of the functional $T_{\text{S}}[n]$ is solved. Only with the Kohn–Sham approach outlined above has one been able to calculate ground state properties of many-electron systems with an accuracy that compares favorably both with the results of much more involved configuration interaction calculations as well as experimental data.

The somewhat hand waving line of reasoning above does of course not constitute a proof of the validity of the KS approach. In fact, the underlying assertion that all interacting V-representable densities are assumed to be also non-interacting V-representable is not at all obvious. However, it can be shown that this assertion is equivalent to the question of whether an extension of $T_{\text{S}}[n]$ can be constructed whose functional derivative is well defined at interacting V-representable densities. Such an extension has been shown to exist [84], and thus the KS approach is established rigorously.

Total Energy

Finally, by combining (2.13), (2.15), (2.16), and (2.20), we obtain the following expression for the total energy:

$$E = \sum_{i=1}^{N} \epsilon_i - \frac{1}{2} \int \mathrm{d}^3 r \, \mathrm{d}^3 r' \, \frac{n(\mathbf{r})n(\mathbf{r}')}{|\mathbf{r} - \mathbf{r}'|} - \int \mathrm{d}^3 r \, V_{\mathrm{xc}}[n]n(\mathbf{r}) + E_{\mathrm{xc}}[n] \,. \quad (2.21)$$

It is worth noting that apparently the total energy is not equivalent to the sum of Kohn–Sham eigenvalues, contrarily to what one might naively expect. Mathematically, the Kohn–Sham eigenvalues are nothing more than Lagrange multipilers introduced to handle the constraint that the number of electrons must be conserved.

2.3.3 Approximations to $E_{\mathrm{xc}}[n]$

The one term in the total energy functional yet to be discussed is the exchange-correlation energy, E_{xc}. By construction, this term has to be approximated in some way, and with an approximative expression for E_{xc}, there is of course no longer a true variational principle. This implies that there is no guarantee that the energy obtained by minimizing the approximate energy functional will be higher than the exact ground state energy. Furthermore, the true ground state charge density will not in general minimize the approximate energy functional. However, the variation principle will still be employed, and the resulting density will be taken as the ground state density.

The Exchange-Correlation Hole

The exchange-correlation hole $n_{\mathrm{xc}}(\mathbf{r}, \mathbf{r}')$ is a useful concept when discussing approximations to $E_{\mathrm{xc}}[n]$. It is also sometimes called the Fermi-Coulomb hole, and its definition involves the pair-correlation function, which is the probability of finding a particle at $\mathbf{r}$ if we know there is one at $\mathbf{r}'$. The physical origin of the exchange-correlation hole is that electrons will correlate their motion so as to screen out the electric field. The electron is left surrounded by a hole in the electron density which contains an equal and opposite charge. The exchange-correlation energy as it appears in the Kohn–Sham equation may then be interpreted physically as the energy due to interaction of the electrons with the exchange-correlation hole. In this way, the exchange-correlation energy can be written as

$$E_{\mathrm{xc}}[n] = \int \mathrm{d}^3 r \, \mathrm{d}^3 r' \, n(\mathbf{r}) W(\mathbf{r}, \mathbf{r}') n_{\mathrm{xc}}(\mathbf{r}, \mathbf{r}') \,, \quad (2.22)$$

where $W(\mathbf{r}, \mathbf{r}')$ is the interaction potential. Charge neutrality of the electron–hole systems leads directly to the charge conservation sum rule

$$\int \mathrm{d}^3 r' \, n_{\mathrm{xc}}(\mathbf{r}, \mathbf{r}') = -1 \quad \forall \mathbf{r} \,. \tag{2.23}$$

This sum rule should always be fulfilled since the total charge of the electron and its exchange-correlation hole add up to zero. An interesting result is that if the interaction potential $W(\mathbf{r}, \mathbf{r}')$ depends only on the distance between the particles, i.e., $W = W(|\mathbf{r} - \mathbf{r}'|)$, then only the spherical average of the exchange-correlation hole contributes to E_{xc} [107].

Local Density Approximation (LDA)

The local density approximation (LDA) consists of the replacement of the exact $E_{\mathrm{xc}}[n]$ by the LDA functional

$$E_{\mathrm{xc}}^{\mathrm{LDA}}[n] = \int \mathrm{d}^3 r \, n(\mathbf{r}) \epsilon_{\mathrm{xc}}(n) \,, \tag{2.24}$$

where $\epsilon_{\mathrm{xc}}(n)$ is the exchange and correlation energy per particle of a homogeneous electron gas with density $n(\mathbf{r})$. The exchange-correlation potential, defined by (2.16) as the variation of the exchange-correlation energy, assumes a simple form in LDA; variation of (2.24) gives

$$V_{\mathrm{xc}}^{\mathrm{LDA}} = \frac{\partial(n\epsilon_{\mathrm{xc}})}{\partial n} \,. \tag{2.25}$$

Several expressions for the function $\epsilon_{\mathrm{xc}}(n)$ have been developed [48, 114, 183, 250]. It can be shown [108] that the LDA exchange-correlation hole is spherical and satisfies the charge conservation sum rule, (2.23), as well as other relations based on various physical criteria [133]. We note also that all functionals in wide use are actually spin density functionals in order to be able to address the spin degree of freedom. In spin density functionals, one defines two charge densities – one for spin up and one for spin down. For simplicity, we do not mention the spin degree of freedom explicitly in the discussion below.

Since LDA is derived from the homogeneous electron gas, one expects that it should work well only for systems with slowly varying densities. However, the applicability of LDA goes way beyond this and has proven to produce good results even for systems regarded as very inhomogeneous. One reason for this success may be found in the fact that if the interaction potential depends only on the distance between the particles, the approximate hole does not have to be very similar to the true hole. It is quite sufficient that the *spherical average* is well approximated, since that is the only part which will affect E_{xc}. It has been verified explicitly that LDA meets this criterion. The exact hole is poorly reproduced, but the spherical average is very well reproduced [107]. Another reason is that since LDA satisfies the charge conservation sum rule, a systematic cancellation of errors must be present.

More Elaborate Functionals

Although LDA works much better than one would expect, it does produce some systematic errors which of course are relevant to try to remove or at least diminish. For instance, LDA overestimates the bonding, leading to too small lattice parameters and too large bulk moduli. Since the birth of DFT, extensions of LDA to higher order in density gradients have been investigated, but it was not until the 1990s that a useful expression was finally developed.

Generalized Gradient Approximation

A general approach – in which E_{xc} is assumed to depend in some general way on the charge density and its gradients – gives rise to a family of approximations called the generalized gradient approximations (GGA). If we let the magnitude of the first-order gradient of the density enter the expression, the exchange correlation energy can be written as

$$E_{xc}^{GGA}[n] = \int d^3 r \, n(\mathbf{r}) f(n, |\nabla n|) \, , \tag{2.26}$$

where $f(n, |\nabla n|)$ is some function which is to be modeled so that the resulting functional behaves well according to various criteria. Perdew and coworkers [177–179] have constructed functionals in this way. The exchange-correlation potential in the GGA becomes an intricate expression involving terms of type n, $|\nabla n|$, $\nabla^2 n$, and $\nabla n \cdot \nabla |\nabla n|$.[5] Attempts such as this one to set up alternatives to or go beyond the LDA by modeling the exchange-correlation hole are usually classified as non-local or semi-local density schemes. The schemes developed by Perdew and coworkers give functionals which retain the attractive features of LDA, while at the same time improving the description of the average hole through the use of the gradient. In many cases these functionals are superior to LDA and have therefore become the most commonly used ones in modern DFT calculations.

Orbital-Dependent Functionals

Although GGA in many ways is a great step forward compared to LDA, it still does not solve the long-standing problems connected with the so-called strongly correlated systems. Examples of such systems are transition

---

[5] When the functional has the form

$$F[\phi] = \int d^3 r \, f(\mathbf{r}, \phi(\mathbf{r}), \nabla \phi(\mathbf{r})) \, ,$$

the functional derivative is

$$\frac{\delta F[\phi]}{\delta \phi} = \frac{\partial f}{\partial \phi} - \nabla \cdot \frac{\partial f}{\partial \nabla \phi} \, .$$

metal oxides, lanthanides, actinides, and heavy fermion systems. Apparently, there is room for improvement in the description of correlations. In the self-interaction correction (SIC), one attempts to remove the spurious self-interaction present in the usual treatment of the electron–electron interaction. The self-interactions are canceled exactly in the Hartree–Fock approach and also in exact exchange (EXX) schemes, but these schemes have other drawbacks. Another popular scheme is LDA+U [14], in which an orbital-dependent interaction is introduced via the parameter U. Historically, the first attempts to incorporate the effect of a Hubbard U in an electronic structure calculation was made by Lopez-Aguilar and Costa-Quintana [159] but even before that there were recipes discussed as to how to do this in the Hartree–Fock approximation [233]. Almost a decade later came the implementation of Anisimov et al. [14] with the application to NiO and an independent work of Boring et al. [36] with an application to Ce metal.

Hybrid Functionals

The LDA and GGA functionals work well for the solid state but less well for atoms and molecules. In quantum chemistry, therefore, hybrid functionals like B3LYP [227] have become very popular. Hybrid functionals are constructed by combining an orbital-dependent Hartree–Fock part and an explicit density functional. The coefficients in the parameterizations are determined by fitting to atomic and molecular data.

Functionals Based on the Airy Gas

Another way of treating strongly inhomogeneous regions of the charge density is to abandon the homogeneous electron gas and replace it with the Airy gas. The Airy gas is a model of an edge electron gas moving in the effective Airy potential

$$V_{\mathrm{eff}}(z) = \begin{cases} \infty & \text{for } z \leq -L \\ Fz & \text{for } -L < z < \infty \end{cases}, \tag{2.27}$$

which is linear in z, independent of x and y, and has a hard wall at $-L$ far from the electronic edge at $z = 0$. This is the route followed in the development of the LAG [148] and AM05 [20] functionals. Test calculations show that this indeed seems to be a very promising route. Results comparable to the best GGA are obtained for atoms and molecules as well as solids.

3

Consequences of Infinite Crystals and Symmetries

Abstract In this short chapter the consequences of periodicity and general symmetry of a crystal is presented. The seven crystal lattices are introduced and as an example the point group operations of a cubic material are illustrated.

Normally calculation of the electronic structure of materials is an application of density functional theory (i.e., one tries to find a solution to the Kohn–Sham equation, discussed in Sect. 2.3.2), to a crystalline environment, which means that an infinite, periodic object is considered. Although crystals can grow very large, an example is shown in Fig. 3.1, they are not infinite. The effect of the finiteness of the crystal, the surface, sometimes influences the physical and chemical properties investigated in an experiment, and it is not seldom that one tries to isolate these very properties, in the fields of surface physics. Here, we shall be concerned by bulk properties, essentially ignore the surfaces, and mostly consider the mathematical advantages of considering an infinite crystal.

A crystal has a periodicity which is defined by the Bravais lattice vectors. The lattice points R for which the environment is identical are hence defined by $\mathbf{R} = n_1\mathbf{R}_1 + n_2\mathbf{R}_2 + n_3\mathbf{R}_3$, where n_1, n_2, and n_3 are integers and $\mathbf{R}_j (j = 1 - 3)$ are the Bravais lattice vectors. A crystal is made up of one or several atoms per unit cell. The symmetry properties of a crystal lattice are of great importance, since the computational cost may be reduced significantly when utilizing these symmetries. For a three-dimensional material there are in general 7 lattice systems (shown in Table 3.1) and 14 Bravais lattices. As an example we mention that the group of cubic lattice systems contains three Bravais lattices: the body-centered cubic (bcc) lattice, the face-centered cubic (fcc) lattice, and the simple cubic lattice (sc). As a side mark, we note that Po is the only element of the periodic table which crystallizes as sc at ambient conditions. As an example the sc lattice is shown in Fig. 3.2. The symmetry properties of a crystal are described by the space group, which in three dimensions is made from combinations of 32 crystallographic point groups combined with translations. The combination of all symmetry operations of a

Fig. 3.1. Gypsum crystal illustrating that crystals may grow big [94], although not infinitely large

three-dimensional lattice results in a total of 230 space groups describing all possible crystal symmetries.

Let us as an example consider the different point group operations of a cubic structure. We illustrate this structure as a cubic building block in Fig. 3.3. The simplest symmetry operation which leaves the cube invariant is the identity operation. In the figure the three (red) arrows indicate the relevant axis for which we can perform rotations which leave this cubic building block invariant. It is around the axis aligned along the 100-direction possible to perform three 90° rotations (i.e., rotations with angles 90, 180 and 270°, the fourth rotation, 360°, is identical to the identity). There are three axes of such rotations (100, 010, and 001) and hence there are nine rotations of this kind. Around the 111-axis it is possible to make two 120° rotations (the third such

Table 3.1. Table showing the seven crystal lattices

Crystal lattice	Symmetry requirements
Cubic	4 threefold axes
Hexagonal	1 sixfold axis of rotation
Rhombohedral and Trigonal	1 threefold axis of rotation
Tetragonal	1 fourfold axis of rotation
Orthorhombic	Either 3 twofold axes of rotation or 1 twofold axis of rotation and two mirror planes
Monoclinic	Either 1 twofold axis of rotation or 1 mirror plane
Triclinic	All cases not satisfying the requirements of any other system

Fig. 3.2. Unit cell of the simple cubic structure. Picture kindly provided by Albin Nilsson
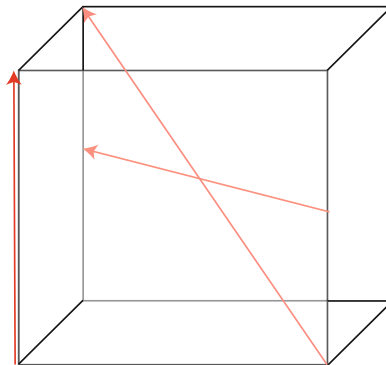
Fig. 3.3. Schematic picture of a cubic building block (*crystal*) and its symmetry axis (*red arrows*)

rotation is identical to the identity). There are four such axis, which amounts
to eight rotations of this kind. Finally, the arrow along the 110-direction al-
lows for one 180° rotation (a second such rotation is identical to the identity).
There are six such axis, and hence six rotations of this kind. Summing up the
identity and all possible rotations hence amounts to 24 symmetry operations.
All these 24 operations can for the sc, fcc, or bcc crystal structure be com-
bined with a subsequent inversion of the lattice, which results in an additional
24 allowed symmetry operations. Some of these latter symmetry operations
are equivalent to a reflection of the lattice through a plane, but some of them
cannot be described as such and are referred to as roto-inversions. Taken to-
gether there are hence 48 point group operations for a cubic material such
as the sc, fcc, or bcc crystal structure. However, a Bravais lattice of sc, fcc,
or bcc type with more than one atom in the primitive cell (more than one
atom in the crystallographic basis) may have a lower number of point group
operations. An example of this is the zinc blende (diamond) structure, with
two atoms per unit cell, one at (0,0,0) and one at (1/4,1/4,1/4). GaAs crys-
tallizes in this structure with the Ga atom at position (0,0,0) and the As atom
at (1/4,1/4,1/4). This material has no inversion, which means that there are
only 24 allowed point group operations.

4

Introduction to Electronic Structure Theory

Abstract An introduction to electronic structure theory of solids is presented, including the general form of the one-electron wave function. The evaluation of the electron density, density of states as well as the calculation of energy bands is described. Different types of integration of reciprocal space are presented, and numerical examples given for their accuracy. The calculation of a self-consistent field is also described, as is the Rayleigh-Ritz variational method.

4.1 Born–Oppenheimer Approximation and One-Electron Theory

All theories for calculating the material properties and the total energy of solids, surfaces, and interfaces start out by, as noted in Chap. 2, adopting the Born–Oppenheimer approximation. This approximation simply neglects the movement of the atomic nuclei and the electrons are considered to be moving around in a material where all nuclei are at fixed positions. The motivation for this is that the electrons are much lighter than the nuclei and thus move much faster. For most materials this approximation is a very good one. One can now focus solely on the electrons, which in itself is a formidable problem. The electrons interact with the positive atomic nuclei and with each other, via Coulombic forces. Although the former interaction is by no means simple, it can be treated, whereas the latter interaction is in general impossible to calculate and one must resort to approximations, like DFT, discussed in Chap. 2. This results in that an effective one-electron Schrödinger-like equation needs to be solved.

4.2 Born–von Karman Boundary Condition and Bloch Waves

Due to the periodic symmetry of bulk materials, discussed in Chap. 3, a number of additional simplifications evolve. A discussion of this can also be found in, for instance, the textbook by Ashcroft and Mermin [22]. First of all one

observes that the one-electron potential is periodic with respect to translations involving a Bravais lattice vector. In the Kohn–Sham equation this means that $V_{\text{eff}}(\mathbf{r}) = V_{\text{eff}}(\mathbf{r} + \mathbf{R})$, where $\mathbf{R}$ is a Bravais lattice vector of the materials. By introducing the Born–von Karman boundary condition for the wave function of the electron states,

$$\psi_{i,\mathbf{k}}(\mathbf{r} + N\mathbf{R}) = \psi_{i,\mathbf{k}}(\mathbf{r})\,, \tag{4.1}$$

where N is a (large) integer, one can show that electrons moving through a infinite, periodic crystal must obey Bloch's theorem [22]. This theorem states that the one-electron wave function (e.g., the solution to the Kohn–Sham equation) must obey the following condition:

$$\psi_{i,\mathbf{k}}(\mathbf{r} + \mathbf{R}) = e^{i\mathbf{k}\cdot\mathbf{R}}\psi_{i,\mathbf{k}}(\mathbf{r})\,. \tag{4.2}$$

Note that a vector $\mathbf{k}$ has been introduced. This is a vector of reciprocal space[1] and one has only to consider $\mathbf{k}$-vectors which lie inside the first Brillouin zone (BZ). An example of a BZ is shown in Fig. 4.1 for an fcc Bravais lattice. In addition one needs to solve the Kohn–Sham equation for a solid for each $\mathbf{k}$-vector being separate and independent of the others. Note that in (4.2) an index "i" appears, since for each $\mathbf{k}$-point there are in general several eigenstates to the Kohn–Sham equation. The one-electron density, the so very crucial ingredient in density functional theory, is then calculated as a sum over all possible $\mathbf{k}$-vectors and occupied eigenstates,

$$n(\mathbf{r}) = \sum_{i}^{\text{occupied}} \sum_{\mathbf{k}} |\psi_{i,\mathbf{k}}(\mathbf{r})|^2\,. \tag{4.3}$$

4.3 Energy Bands and the Fermi Level

A popular way to display the result of an electronic structure calculation, i.e., the self-consistent solution to the Kohn–Sham equation, is to plot the eigenvalues of the Kohn–Sham equation as a function of $\mathbf{k}$-point, preferably along the high symmetry lines and high symmetry points of the BZ (e.g., the ones shown in Fig. 4.1 for the fcc lattice). An example of such a plot of the electronic structure, the "band plot", is shown on the left-hand side of Fig. 4.2, for CeN. This compound crystallizes in the rock-salt structure which is an fcc Bravais lattice with two atoms per unit cell. For this reason the high symmetry lines and high symmetry points of the "band plot" in Fig. 4.2 are the same as the ones shown in Fig. 4.1. Note from Fig. 4.2 that the highest occupied energy, the Fermi level, is marked as a horizontal dashed line. Electron states below this energy are hence occupied and the states above are unoccupied.

---

[1] Reciprocal space is spanned by the vectors $\mathbf{G}_i$, defined as $\mathbf{G}_i \cdot \mathbf{R}_j = 2\pi\delta_{ij}$.
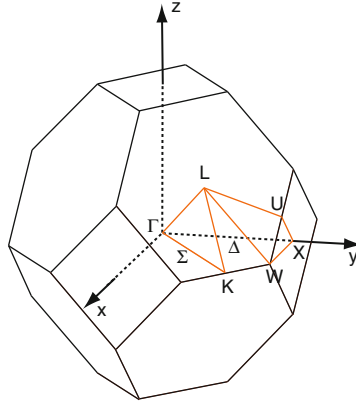
Fig. 4.1. Example of a Brillouin zone (BZ). The BZ is shown for an fcc lattice. In the figure high symmetry points and lines are marked and labeled (Γ, Σ, Δ, etc.)
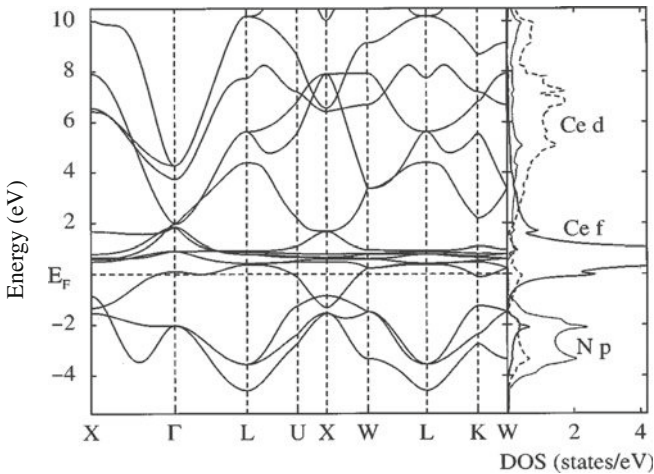
Fig. 4.2. Energy band structure of CeN (*left part of the figure*). The *horizontal dashed line* is the Fermi level. *Symmetry lines* of the plot refer to the **k**-points shown in Fig. 4.1. The corresponding DOS function is shown in the *right part of the figure*. Here are also shown partial DOS, projected onto the 4f and 5d orbitals of the Ce atom as well as the 2p orbitals of the N atom. Figure redrawn after [68]

4.4 Different Types of k-Space Integration

One more of the popular outputs of an electronic structure calculation is, apart from the total energy and the energy bands discussed above, the density of states (DOS). This is a property of the electronic structure which is very useful for analyzing and understanding a calculation. We will discuss this point further in the section on applications. The DOS may also be used to calculate

the charge density from a calculation, as well as the sum of eigenvalues of all occupied states. Both these entities enter the expression for the total energy of the material. A derivation of the DOS may be found in most textbooks on solid state physics and it is not repeated here. Instead we quote the result that the DOS, for spin-degenerate states, can be calculated from,

$$D(E) = \sum_i \frac{1}{4\pi^3} \int_{\mathrm{BZ}} \delta(E - E_{i\mathbf{k}}) \mathrm{d}\mathbf{k} \,. \tag{4.4}$$

The Fermi level can now be calculated from the DOS via the expression

$$N_{\mathrm{val}} = \int_{-\infty}^{E_{\mathrm{F}}} D(E) \mathrm{d}E \,, \tag{4.5}$$

where N_{val} is the number of valence electrons considered in the calculation.

RSPt calculates the DOS function using either the so-called linear tetrahedron method [126, 153] or the so-called Gaussian broadening method (GBM) [169]. The general principles of the so-called linear tetrahedron method, LTM, can best be illustrated using a two-dimensional Brillouin zone as an example. The basic philosophy of the LTM is the same for two- and three-dimensional systems, and since two-dimensional objects are easier to visualize we continue describing the essentials of the LTM using a two-dimensional Brillouin zone as an example. We will for simplicity also consider only one spin-degenerate energy band. In Fig. 4.3 we show the reciprocal lattice vectors as well as the Brillouin zone (BZ) for the considered hypothetical two-dimensional crystal. In this figure we show in color the part of the BZ where the eigenvalues of the Kohn–Sham equation are lower than a certain energy, E. This energy could be the Fermi level or any other chosen energy. The number of electrons which are found up to this energy, the number of states at energy E, is proportional to the colored area in Fig. 4.3. If the colored area is the same as the area of the full Brillouin zone, the number of state equals 2 (since this corresponds to a completely filled, spin-degenerate energy band). Hence the number of states occupying the band at energy E is proportional to two times the area of the colored region divided by the area of the BZ, i.e., the number of states can be calculated as

$$N(E) = 2 \cdot \frac{a_{\mathrm{occupied}}(E)}{A_{\mathrm{BZ}}} \,. \tag{4.6}$$

The DOS can then be calculated as $D(E) = \frac{\mathrm{d}N(E)}{\mathrm{d}E}$. The question then is how to calculate $a_{\mathrm{occupied}}(E)$ and its energy derivative. In the LTM this is done by first setting up a uniform mesh of $\mathbf{k}$-points forming a triangular pattern in the BZ, as shown in Fig. 4.3 (for a three-dimensional BZ the triangles are replaced by corner sharing tetrahedra). The Kohn–Sham equation is solved for $\mathbf{k}$-points at the corners of each triangle. Hence every triangle is associated with three $\mathbf{k}$-points defining the corners, $\mathbf{k}_1$, $\mathbf{k}_2$, and $\mathbf{k}_3$, with corresponding eigenvalues,
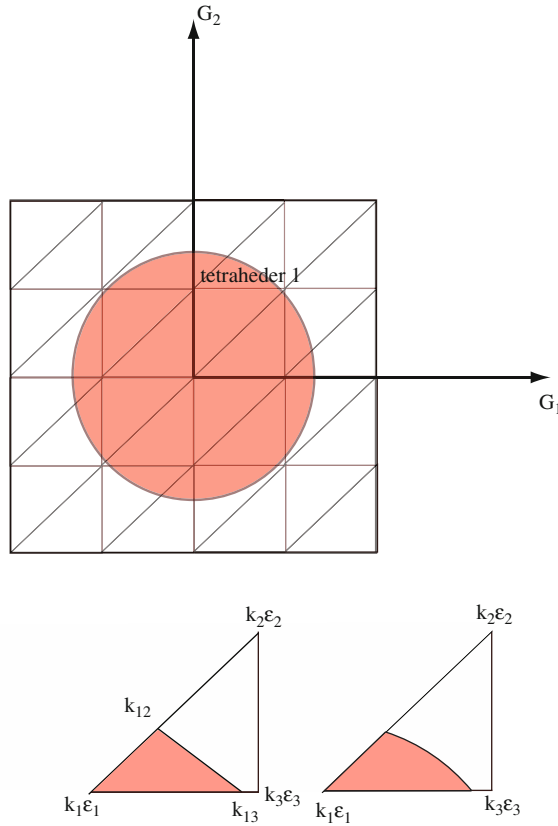
Fig. 4.3. Illustration of the LTM in two dimensions. The BZ is divided into *triangles*, and the **k**-states which is occupied up to an energy E are shown as the *colored region* (*top*). The tetraheder labeled "tetraheder 1" is shown in the *lower right part of the figure*. In the *lower, left part of the figure* an approximate linear interpolation of the occupied area is shown. For details see text

ϵ_1, ϵ_2, and ϵ_3. The area $a_{\mathrm{occupied}}(E)$ can now be calculated as a sum of the colored part of the areas of each triangle in Fig. 4.3. If the considered energy, E, is larger than ϵ_1, ϵ_2, and ϵ_3 of a certain triangle, the area of this triangle contributes fully to the sum, and if E is smaller than ϵ_1, ϵ_2, and ϵ_3, the chosen triangle does not contribute at all. This represents the simple triangles, since the area of a triangle which contributes fully can be calculated easily. The case when E is larger than ϵ_1 but smaller than ϵ_2 and ϵ_3 provides somewhat of a challenge. Such a triangle is illustrated in the lower right-hand part of Fig. 4.3. A good approximation of the occupied area of this triangle is shown in the lower left part of Fig. 4.3. Here the area is defined by the **k**-points $\mathbf{k}_1$, $\mathbf{k}_{12}$, and $\mathbf{k}_{13}$. The point $\mathbf{k}_1$ is known, since it was generated in the uniform mesh. The point $\mathbf{k}_{12}$ is calculated by linear interpolation between points $\mathbf{k}_1$ and $\mathbf{k}_2$ in the following way, $\mathbf{k}_{12} = \mathbf{k}_1 + (\mathbf{k}_2 - \mathbf{k}_1) \cdot (E - \epsilon_1)/(\epsilon_2 - \epsilon_1)$. In a similar way

the point $\mathbf{k}_{13}$ is calculated to be equal to $\mathbf{k}_1 + (\mathbf{k}_3 - \mathbf{k}_1) \cdot (E - \epsilon_1)/(\epsilon_3 - \epsilon_1)$. Once these $\mathbf{k}$-points have been identified via linear interpolation it is easy to calculate the colored area of the triangle in the lower left part of Fig. 4.3. A similar procedure can be applied to calculate the area of the triangle where ϵ_1 and ϵ_2 are lower in energy than E, but where ϵ_3 is higher. One then makes a sum of the occupied areas of all triangles. The approximation of replacing the area of the triangle in the lower right-hand part of Fig. 4.3 with the one in the lower left part of this figure becomes better for smaller triangles, since then the linear interpolation is more accurate. Hence all reliable implementations of the LTM require a rather large number of triangles (or tetrahedra). The LTM provides an analytical expression of $a_{\text{occupied}}(E)$ which involves a large sum of the contribution of all triangles. Since there is an explicit energy expression from the contribution from every triangle (tetrahedron), it is an easy task to calculate $\frac{\mathrm{d}N(E)}{\mathrm{d}E}$, i.e., the density of states function.

It is worthwhile to note that a modification of the linear tetrahedron method, called modified tetrahedron method (MTM), was suggested by Blöchl et al. [33]. The MTM corrects for the curvature of the energy band to some extent, and as we show in a numerical example below this does result in an improved convergence of the total energy as a function of number of $\mathbf{k}$-points.

In addition to the use of the tetrahedron method, RSPt also makes use of a direct summation of electron states, in order to evaluate the Fermi level, charge density, and eigenvalue sum. This is done using the expression,

$$N = \sum_i \int_{-\infty}^{\infty} f(E) \frac{1}{4\pi^3} \int_{\text{BZ}} \delta(E - E_{i\mathbf{k}}) \mathrm{d}\mathbf{k}\mathrm{d}E \,, \tag{4.7}$$

where $f(E)$ is Fermi distribution function, which attains the value 1 below the Fermi energy and 0 above. This method also makes use of a uniform mesh of $\mathbf{k}$-points, distributed as to fulfill the symmetry of the space group of the lattice. The sum in (4.7) can be written as weighted sums over the bands, i, and the discrete set of sampled $\mathbf{k}$-points, $\mathbf{k}_j$, with weight functions, w_{ji}. The sum over $\mathbf{k}$-points is now carried out first by considering a convolution of each discrete eigenvalue with a Gaussian function of width, ω. This method, referred to as Gaussian broadening method (GBM), leads to a fast and stable convergence of the charge and spin densities, as well as the total energy. The GBM can be seen as a truncation of a complete series expansion of a δ-function in terms of Hermite polynomials, H_n, with a Gaussian weight function [169]. Then the step function, $f(E)$, can be written as

$$f(E) = f_0(E,\omega) + \sum_{n=1}^{\infty} A_n H_{2n-1}\left(\frac{E - E_{\text{F}}}{\omega}\right) \mathrm{e}^{\left(-\left(\frac{E - E_{\text{F}}}{\omega}\right)^2\right)} \,, \tag{4.8}$$

where $f_0(E,\omega) = \frac{1}{2}(1 - \mathrm{erf}(\frac{E-E_{\text{F}}}{\omega}))$ (erf stands for error function) and A_n are coefficients which may be calculated analytically. In practical calculations one has to truncate the sum in the equation above and the resulting "step"
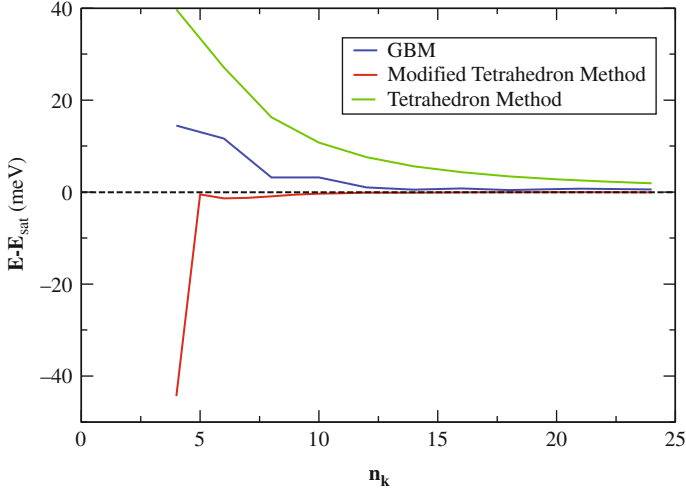
Fig. 4.4. Calculated total energy of fcc Cu using three different **k**-space integrations. The x-axis shows the number of divisions of the BZ in one direction, n_k. The total number of **k**-points in the full Brillouin zone is hence $(n_k)^3$. Picture kindly provided by Mr. Sumanta Bhandary

function is called $f_N(E; \omega)$, if N terms are kept in the sum in (4.8). If the function which is "smeared" by $f_N(E; \omega)$ can be represented by a polynomial of $2N$ there is no error involved in the truncation [169]. In RSPt a choice is possible for how many terms one would like to consider in (4.8), i.e., N, as well as the value of ω. The default values are $N = 0$ and $\omega = 20 \, \text{mRy}$.

In Fig. 4.4 we compare three different **k**-space integration methods and how fast the total energy converges for fcc Cu, with respect to the number of **k**-points in the BZ. Note that the linear tetrahedron method is by far the most slowly converging method, which is a general feature in first principles electronic structure calculations. Among the other two methods, the GBM and the modified tetrahedron method, one can observe that the latter converges faster, and that the two methods approach the same total energy. As a matter of fact, Fig. 4.4 suggests that also the linear tetrahedron method approaches the same total energy as that from the modified tetrahedron method, and from theoretical grounds one can show that this must be the case when the number of **k**-points approaches infinity. As a rule of thumb the modified tetrahedron method is preferred, and this is also the standard setting of RSPt.

4.5 Self-Consistent Fields

The Kohn–Sham equation (2.18) is an example of what is referred to as a self-consistent field calculation. The effective potential in the Kohn–Sham equation depends, among other things, on the electron charge and magnetization

density. The density is hence an input to this equation. However, via (4.3) the electron density is also an output to the equation, and it is necessary that the input density and output density are the same, i.e., that a self-consistent field is obtained in the calculation. This is done by guessing a trial density (in RSPt this is done from charge densities obtained from an atomic calculation, which are placed on the atomic positions of the unit cell in the calculations), solving the Kohn–Sham equation with this trial density, and via (4.3) calculate a new density, which may be used as an input to a second iteration. The process is iterated until self-consistency is achieved, i.e., until the input and output densities differ only by a small amount. In practical calculations this is a very important convergence to check for, with respect to the number of iterations, and together with the convergence of the total energy it represents the most important parameter to monitor during the self-consistent cycle. In practice it is impossible to use the entire output density of one iteration as an input density of a consecutive iteration. Hence, it is necessary to mix some of the input density and some of the output density of a given iteration, to form a new trial input density for the next iteration. The simplest way to do this is to use a linear mixing procedure, according to the equation

$$n_{i+1}^{\text{input}}(\mathbf{r}) = (1 - \alpha)n_i^{\text{input}}(\mathbf{r}) + \alpha n_i^{\text{output}}(\mathbf{r}). \qquad (4.9)$$

In this equation i and $i + 1$ denote two consecutive iterations in the self-consistent cycle, and α is the mixing parameter. Although it might be desired to chose as large value of α as possible, since this in principle could reduce the number of iterations in a calculation, one has in practice to find a suitable choice of the mixing parameter. If too much of the output density of one iteration is used as input to the next, there is a risk that uncontrolled oscillations in the charge density and total energy will occur, and self-consistency is never obtained. A smaller amount of mixing of the output density of one iteration used as input to the next avoids this problem and the convergence of the density and total energy occurs without oscillations. However, a too small choice of α may produce a very slow convergence, and it is desirable to find an "optimal" mixing parameter. The value of the optimal mixing parameter varies from material to material.

RSPt uses as its standard setting a mixing scheme which more efficiently reaches self-consistency, compared to (4.9), and the improved method is referred to as the Broyden mixing scheme [41]. In this method the form of the equation describing the mixing is similar to the form in (4.9), with the difference being that the scalar entities α and $1 - \alpha$ are replaced by matrices $\tilde{\alpha}$ and $\tilde{\beta}$, to yield

$$n_{i+1}^{\text{input}}(\mathbf{r}) = \tilde{\beta} n_i^{\text{input}}(\mathbf{r}) + \tilde{\alpha} n_i^{\text{output}}(\mathbf{r}). \qquad (4.10)$$

The matrices $\tilde{\alpha}$ and $\tilde{\beta}$ are updated during the self-consistent iterations in order to quicker reach self-consistency, according to the analysis of [40]. In the first iteration RSPt uses for $\tilde{\alpha}$ and $\tilde{\beta}$ diagonal matrices, where the diagonal matrix

elements are the scalar value α and $1 - \alpha$, respectively. α is hence an input parameter to RSPt. Typical values of this parameter range from ~ 0.2, for systems which are well behaved and easy to converge (fcc Cu is an example), to 0.005 for very difficult systems (a surface of Ce would be an example of this). For a simple system, convergence may be obtained after 5–10 iterations, whereas for difficult materials hundreds of iterations may be needed to achieve self-consistency.

In practice the densities used by RSPt, and in reality in all electronic structure codes, are stored on a grid. RSPt uses a real space representation inside the muffin-tin spheres and a Fourier representation for the interstitial density. This can symbolically be expressed as the density being stored on discrete points as $n(\mathbf{r_j})$, where the "points," r_j, are either points of real space or the components of the Fourier expansion. A good test for convergence which is used by RSPt is

$$\frac{1}{N} \sum_{j}^{N} \sqrt{(n^{\text{output}}(\mathbf{r}_j) - n^{\text{input}}(\mathbf{r}_j))^2} \,. \tag{4.11}$$

This mean square difference, which in the RSPt community is referred to as "fsq" (this parameter will appear several times, later on in this book), should for most materials reach values of the order of $10^{-7} - 10^{-10}$, if the total energy should be converged to within a fraction of a mRy.

4.6 Rayleigh–Ritz Variational Procedure

We have outlined above a number of concepts which appear due to the translational symmetry of a solid, i.e., the Kohn–Sham equation must be solved for a number of $\mathbf{k}$-vectors which, for a given cycle in the self-consistent loop, may be treated as independent of each other. In addition one has to find ways to approximate the $\mathbf{k}$-space summation of the electron states and we have given examples of how one may do this. We are now ready to tackle the toughest part of the problem, namely to find a solution to the Kohn–Sham equation itself. One approach is to expand the (unknown) Kohn–Sham wave function in a set of (known) basis functions as

$$\psi_{\mathbf{k}}(\mathbf{r}) = \sum_{l}^{l_{\max}} c_{l\mathbf{k}} \chi_{l\mathbf{k}}(\mathbf{r}) \,. \tag{4.12}$$

There are several choices of basis functions, which have given rise to different electronic structure methods with different names, such as LCAO (linear combination of atomic orbitals), LAPW (linear augmented plane waves), PPW (pseudo-potential plane waves), and LMTO (linear muffin-tin orbitals). The

sum in the equation above is truncated after sufficiently many basis functions have been included and the coefficients $c_{li\mathbf{k}}$ are, via the Rayleigh–Ritz principle [24], determined from the following secular equation:

$$\sum_{l}^{l_{\max}}[H_{ll'} - E_{i\mathbf{k}}O_{ll'}]c_{li\mathbf{k}} = 0\,, \tag{4.13}$$

where

$$H_{ll'} = \int_{U_c} \chi^*_{l\mathbf{k}}(\mathbf{r}) \left(\frac{-\nabla^2}{2} + V_{\text{eff}}\right) \chi_{l'\mathbf{k}}(\mathbf{r})\mathrm{d}^3r \equiv \int_{U_c} \chi^*_{l\mathbf{k}}(\mathbf{r}) h_{\text{eff}} \chi_{l'\mathbf{k}}(\mathbf{r})\mathrm{d}^3r \tag{4.14}$$

and

$$O_{ll'} = \int_{U_c} \chi^*_{l\mathbf{k}}(\mathbf{r})\chi_{l'\mathbf{k}}(\mathbf{r})\mathrm{d}^3r\,, \tag{4.15}$$

where the integral is over the unit cell (U_c). Once $H_{ll'}$ and $O_{ll'}$ have been evaluated the eigenvalues, $E_{i\mathbf{k}}$ ($i = 1 - l_{\max}$), are determined by [24]

$$\det|H_{ll'} - E_{i\mathbf{k}}O_{ll'}| = 0\,, \tag{4.16}$$

a standard numerical problem, which may be solved by existing software such as LAPACK or BLAS.

5

Linear Muffin-Tin Orbital Method in the Atomic Sphere Approximation

Abstract In this chapter the linear muffin-tin orbitals (LMTO) are defined, which includes linearization of the radial part of the wave function, the 'head' and 'tails' of the basis functions, and the so called structure constant. The atomic sphere approximation (ASA) is introduced and a comparison between the Korringa–Kohn–Rostoker (KKR) method and the linear muffin-tin orbital method is made. The advantages and disadvantages of the LMTO-ASA method are discussed.

5.1 Muffin-Tin Methods

It is crucial to use a good basis set for the study of the electronic structure of materials. The full-potential augmented plane wave [160, 212] (APW) and the Korringa–Kohn–Rostoker [139, 142] (KKR) methods can be used, in principle, to solve exactly the Kohn–Sham equation. However, these methods are numerically involved and their linearization, introduced by Andersen [11], is most efficient. Andersen's linearization has not only made the techniques for solving the electronic structure problem transparent by reducing it merely to a diagonalization of a matrix, containing as elements the one-electron Hamiltonian. Linearization also cuts the cost of calculation by at least an order of magnitude. The linearized versions of these two powerful methods were named the linear augmented plane wave (LAPW) and linear muffin-tin orbital (LMTO) methods, respectively [11].

In this chapter we present the LMTO basis set used to calculate the electronic structure of solids. In the next chapter we discuss the most general basis used for an all-electron calculation where the potential is not supposed to be spherical nor of muffin-tin type. This most general description allows the study of open structures without having to use the so-called empty spheres. In this chapter, we start by introducing the LMTO-ASA method and its derivation and show its connection to the KKR method.

To define the basis set, space is divided into non-overlapping spheres called "muffin-tin" spheres and the region between these spheres is called the interstitial region (see Fig. 5.1). Inside each muffin-tin sphere in the unit cell the Schrödinger equation is solved at a fixed energy e_ν for each angular
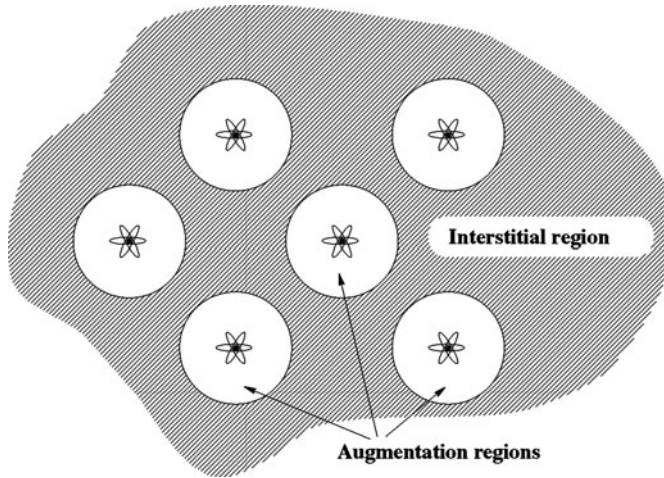
Fig. 5.1. Illustration of how space in a crystal is divided into muffin-tin and interstitial regions

momentum ℓ, and in the interstitial region the Helmholtz equation is solved for each variational parameter κ (which will be defined later). The linearization amounts to the use of a linear combination of the solution $\phi_\ell(e, r)$ of the Schrödinger equation (or Kohn–Sham equation) for a fixed energy and its energy derivative $\dot{\phi}_\ell(e, r)$ inside each muffin-tin sphere. These linear combinations are matched to an envelop function (Hankel function) in the interstitial region. In this chapter we discuss mainly the LMTO basis set in the so-called atomic sphere approximation (ASA). We will start from the KKR method and derive the LMTO method from it.

The LMTO method uses partial waves to solve the Schrödinger equation in the solid. Thus it combines the best features of both the KKR method and the linear combination of atomic orbitals (LCAO) method without the drawback of those methods. In the ASA, the atomic unit cell, which is in a form of a polyhedron, is approximated by a sum of atomic spheres of the same volume [11]. In making this approximation one deals with a system of slightly overlapping spheres, but as long as this overlap is not too large, the calculated energy bands and total energies are accurately described. In general, closely packed solids are well described with this approximation. However, for open or loosely packed systems one needs to use the so-called *empty spheres*, which are placed in natural voids of the crystal in such a way that the overlap between all spheres in the unit cell is minimal. With the empty spheres, all regions of space are described by local spherical potentials [209].

5.1.1 The Korringa, Kohn, and Rostoker (KKR) Method

The KKR method is an exact solution for a muffin-tin potential. Each atom is surrounded by a muffin-tin sphere of radius S. The region between atoms
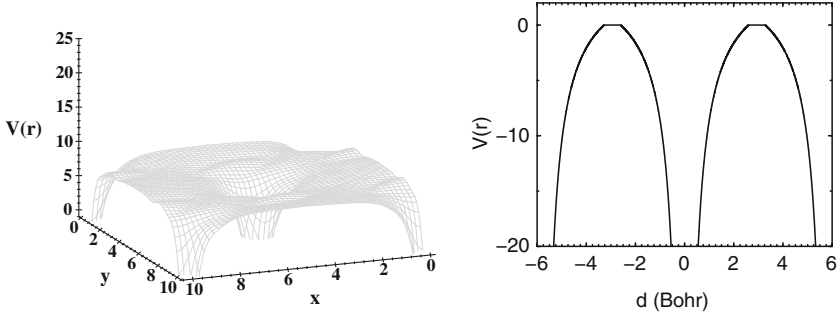
Fig. 5.2. Full-potential (*left*) and muffin-tin approximation to this potential (*right*). In the interstitial region the potential is constant. In the muffin-tin region the potential has a spherical symmetry. In most compact materials, where the interstitial region is small the muffin-tin potential is very close to the all-electron full potential

is called the interstitial region. This is shown in Fig. 5.1, where the potential is flat in between the muffin-tin spheres. In Fig. 5.2 we show the full effective potential that electrons feel when moving through a solid, as given by the DFT and the Kohn–Sham equation. The potential has no geometrical constraints to it and is therefore called the full potential. In Fig. 5.2 we also show an approximation to this full potential, where a spherical average has been made within the muffin-tin spheres and in between the muffin-tin spheres (interstitial region) a constant average is used. This is the so-called muffin-tin potential and is given by

$$V(\mathbf{r}) = \sum_{R} v(|\mathbf{r} - \mathbf{R}|)\theta(\mathbf{S} - |\mathbf{r} - \mathbf{R}|), \tag{5.1}$$

around each atomic nucleus, with a constant value in between. The constant potential in between muffin-tin spheres is often denoted the muffin-tin zero and labeled V_{mtz}.

The KKR wave function is given by

$$\Phi_L(e, \mathbf{r}) \equiv \mathcal{Y}_{\mathbf{L}}(\hat{\mathbf{r}}) \begin{Bmatrix} \phi_\ell(e, r), & r \leq S \\ a_\ell \mathcal{K}_\ell(\sqrt{e}, r) + b_\ell \mathcal{J}_\ell(\sqrt{e}, r), & r \geq S \end{Bmatrix}, \tag{5.2}$$

where $\mathcal{Y}_{\ell m}(\hat{\mathbf{r}}) \equiv i^\ell Y_{\ell m}(\hat{\mathbf{r}})$ and $L \leftrightarrow \ell m$. The function ϕ is a numerical solution to the Schrödinger equation (or Kohn–Sham) at energy e for the potential V.

$$\left(-\nabla^2 + V(r)\theta(S - r)\right)\phi_\ell(e, r) = e\phi_\ell(e, r). \tag{5.3}$$

In (5.2) the function inside S is called the "head" of the basis function, and the function outside is referred to as the "tail". The linear combination of $\mathcal{K}$ and $\mathcal{J}$ (the Hankel and Bessel functions, respectively) is a solution to the Helmholtz equation:

$$\left(\nabla^2 + \kappa^2\theta(r - S)\right)\left(a\mathcal{K}_\ell(\kappa, r) + b\mathcal{J}_\ell(\kappa, r)\right) = 0 \quad (\kappa^2 = e - V_{\text{mtz}}) \quad (5.4)$$

$$\mathcal{J}_\ell(\kappa, r) \equiv \kappa^{-\ell} j_\ell(\kappa r)$$

$$\mathcal{K}_\ell(\kappa, r) \equiv -\kappa^{\ell+1}\left\{\begin{array}{ll} n_\ell(\kappa r), & \kappa^2 > 0 \\ n_\ell(\kappa r) - i j_\ell(\kappa r) & \kappa^2 < 0, \ (\kappa = i|\kappa|) \end{array}\right\},$$

where n_ℓ and j_ℓ are, respectively, the spherical Neumann and Bessel functions. The function Φ in (5.2) is not normalizable at negative energies because of the Bessel function $\mathcal{J}$. A solution at (almost) all energies is obtained by making a Bloch wave from the function

$$\chi_L(e, \mathbf{r}) = \Phi_L(e, \mathbf{r}) - b_\ell \mathcal{J}_L(\sqrt{e}, r)\mathcal{Y}_L(\hat{\mathbf{r}}). \quad (5.5)$$

The wave function

$$\psi(e, \mathbf{k}, \mathbf{r}) \equiv \sum_L A_L \sum_R e^{i\mathbf{k}\cdot\mathbf{R}}\chi_L(e, \mathbf{r} - \mathbf{R}) \quad (5.6)$$

is a solution for the Kohn–Sham equation, if the tails of all orbitals cancel the Bessel function $\mathcal{J}$ in all muffin-tin spheres.

The tail expansion of the wave function can be written as [11]

$$\sum_R e^{i\mathbf{k}\cdot\mathbf{R}}\left(1 - \delta(R, 0)\right)\mathcal{K}_\ell(\kappa, |\mathbf{r} - \mathbf{R}|)\mathcal{Y}_\mathbf{L}(\mathbf{r} - \mathbf{R})\Big|_{\mathbf{r} < \mathbf{s}}$$

$$= \sum_{L'} \mathcal{J}_{\ell'}(\kappa, r)\mathcal{Y}_{L'}(\hat{\mathbf{r}}), B_{L', L}(\kappa, \mathbf{k}), \quad (5.7)$$

where the coefficients B are the so-called *structure constants*. It can be shown [173] that

$$\mathcal{K}_L(\kappa, \mathbf{r} - \mathbf{R}) = \sum_{L'} B_{L', L}(\kappa, \mathbf{R} - \mathbf{R}')\mathcal{J}_{\mathbf{L}'}(\kappa, \mathbf{r} - \mathbf{R}'), \qquad |\mathbf{r} - \mathbf{R}'| < |\mathbf{R} - \mathbf{R}'|$$

which means that a tail function centered on one lattice site can be expanded around some other lattice site with Bessel functions centered on this other site, a fact which can be used to derive the KKR equation.

The KKR Equation

We are now ready to apprehend the KKR equation for obtaining a solution to the Kohn–Sham equation of a muffin-tin potential. In order to do this we consider a sphere at $R = 0$, where the wave function can be written as

$$\psi(e, \mathbf{k}, \mathbf{r})\Big|_{\mathbf{R}=0} = \sum_L A_L\Big(\phi_L(e, r) - b_\ell \mathcal{J}_\ell(\kappa, r)\mathcal{Y}_L(\hat{\mathbf{r}}) \quad (5.8)$$

$$+ a_\ell \sum_{L'} \mathcal{J}_{\ell'}(\kappa, r)\mathcal{Y}_{L'}(\hat{\mathbf{r}})B_{L', L}(e, \mathbf{k})\Big). \quad (5.9)$$

In this equation, the last term represents the sum of tail functions centered at lattice sites not equal to $\mathbf{R} = 0$, expanded in Bessel functions centered at $\mathbf{R} = 0$. For these tails to cancel the term $b_\ell \mathcal{J}_\ell(\kappa, r)\mathcal{Y}_L(\hat{\mathbf{r}})$ in the equation above, we obtain the tail cancellation equation

$$\sum_L \left(B_{L',L}(e, \mathbf{k}) - \delta_{LL'} \frac{b_\ell}{a_\ell} \right) A_L = 0 \,. \tag{5.10}$$

The coefficients a_ℓ and b_ℓ are calculated so that a tail is attached continuously and differentiably to ϕ:

$$\left(\phi(S) \ S\phi'(S) \right) = \left(a \ b \right) \begin{pmatrix} \mathcal{K}(S) \ S\mathcal{K}'(S) \\ \mathcal{J}(S) \ S\mathcal{J}'(S) \end{pmatrix}.$$

Given that $S^2(\mathcal{K}\mathcal{J}' - \mathcal{K}'\mathcal{J}) = 1$, where $\mathcal{K}'(S)$ and $\mathcal{J}'(S)$ are the radial derivatives of $\mathcal{K}$ and $\mathcal{J}$ at S, the KKR equation becomes

$$\sum_L \left(B_{L',L}(e, \mathbf{k}) + \delta_{LL'} \frac{\mathcal{K}_\ell(\kappa, S)}{\mathcal{J}_\ell(\kappa, S)} \frac{\mathcal{D}_\mathcal{K} - \mathcal{D}_\phi}{\mathcal{D}_\mathcal{J} - \mathcal{D}_\phi} \right) A_L = 0 \,, \tag{5.11}$$

where $\mathcal{D}_\phi \equiv S\phi'(S)/\phi(S)$.

5.1.2 The KKR-ASA Method

To obtain the KKR-ASA method we extend the muffin-tin radius to the Wigner–Seitz radius such that the volume of the spheres is equal to the volume of the unit cell. In this approximation the overlap between the spheres and the void which occurs between the spheres are ignored. Without the interstitial region the functions $\mathcal{K}$ and $\mathcal{J}$ can have any energy with the only condition that the tail cancellation holds.

In the KKR-ASA method the limit $\kappa \to 0$ is taken [11], in which the Hankel and Bessel functions are given by

$$\mathcal{K}_\ell(S) \to (2\ell - 1)!!/S^{\ell+1}, \quad \mathcal{J}_\ell(S) \to S^\ell/(2\ell + 1)!!, \quad \mathcal{D}_\mathcal{K} \to -\ell - 1, \quad \mathcal{D}_\mathcal{J} \to \ell$$

In the limit where $\kappa \to 0$ the KKR equation gives the KKR-ASA equation

$$\sum_L \left(S_{L',L}(\mathbf{k}) + \delta_{LL'}(2\ell + 1)\frac{\mathcal{D}_\phi(e) + \ell + 1}{\mathcal{D}_\phi(e) - \ell} \right) A_L = 0 \,, \tag{5.12}$$

where the KKR-ASA (and also the LMTO-ASA) structure function is defined as

$$S_{L',L}(\mathbf{k}) \equiv \frac{S^{\ell'+1} B_{L',L}(0, \mathbf{k}) s^\ell}{(2\ell' - 1)!!(2\ell - 1)!!} \,. \tag{5.13}$$

The structure function (or structure constant) $S_{L',L}$ expands $(S/r)^{\ell+1}\mathcal{Y}_L$ centered at a sphere $\mathbf{R} \neq 0$, in functions $(r/S)^\ell$ centered at $\mathbf{R} = 0$. All the energy dependence is in the *potential parameters*

$$P_\ell(e) = (2\ell + 1)\frac{\mathcal{D}_\phi(e) + \ell + 1}{\mathcal{D}_\phi(e) - \ell}. \tag{5.14}$$

The KKR-ASA equations are more stable than the KKR ones and have an easier interpretation.

5.1.3 The LMTO-ASA Method

One of the main advantages with the LMTO-ASA method is computational efficiency which is obtained by suppressing the energy dependence of the KKR wave function

$$\chi_L(e, \mathbf{r}) = \Phi_L(e, \mathbf{r}) - b_\ell \mathcal{J}_L(\sqrt{e}, r)\mathcal{Y}_L(\hat{\mathbf{r}}). \tag{5.15}$$

To obtain a variational energy-independent basis set, and therefore to a computationally efficient eigenvalue problem, we need the following:

(1) Fix the tail function energies: $\sqrt{e} \to \kappa$, so that it is now a parameter.
(2) Taylor expands the radial function for each angular momentum around some fixed energy e_ν

$$\phi(e, r) \approx \phi(e_\nu, r) + \dot{\phi}(e_\nu, r)(e - e_\nu) \quad (\dot{\phi} \equiv \partial\phi/\partial e), \tag{5.16}$$

where ϕ and $\dot{\phi}$ are orthogonal to the core states, i.e., any solution of the same Hamiltonian contained entirely within the muffin-tin or atomic sphere. The tail functions are not orthogonal to the core states, and without strict tail cancellation one may find core eigenvalues.
(3) Replace all Bessel functions inside the spheres by a linear combinations of ϕ and $\dot{\phi}$, in a continuous and differentiable way. This is the so-called *augmentation* part of the LMTO (or LAPW) basis functions.

The LMTO basis functions are independent of energy, i.e., the energy derivative χ_L

$$\dot{\chi}_L(e, \mathbf{r}) = \dot{\Phi}_L(e, \mathbf{r}) - \dot{b}_\ell \tilde{\mathcal{J}}_L(\kappa, r)\mathcal{Y}_L(\hat{\mathbf{r}}) \tag{5.17}$$

is zero at $e = e_\nu$. We define therefore the augmented Bessel functions:

$$\tilde{\mathcal{J}}_L(\kappa r) = \begin{cases} \frac{\dot{\Phi}_\ell(e_\nu, r)}{b_\ell}, \ r \le R_{\mathrm{MT}} \\ j_\ell(\kappa r), \quad r > R_{\mathrm{MT}}. \end{cases}$$

Given the normalized wave function $\phi_\ell(e, r) = \langle \Phi_\ell^2(e, r)\rangle^{-\frac{1}{2}}\Phi_\ell(e, r)$, in the muffin-tin sphere. In this case

$$\begin{aligned}\dot{\Phi}_\ell(e_\nu, r) &= \langle \dot{\Phi}_\ell^2(e_\nu, r)\rangle^{\frac{1}{2}}\phi_\ell(e_\nu, r) + \langle < \Phi_\ell^2(e_\nu, r)\rangle^{\frac{1}{2}}\dot{\phi}_\ell(e_\nu, r) \\ &= \langle \dot{\Phi}_\ell^2(e_\nu, r)\rangle^{\frac{1}{2}}\Phi_\ell(\mathcal{D}_{\dot{\Phi}}, r) = \langle \dot{\Phi}_\ell^2(e_\nu, r)\rangle^{\frac{1}{2}}\Phi_\ell(\mathcal{D}_{j_\ell}, r), \tag{5.18}\end{aligned}$$

because $\mathcal{D}_{\dot{\Phi}} = \mathcal{D}_{j_\ell}$.

To insure the differentiability of the function at the muffin-tin radius, the function Φ should be given by

$$\Phi_\ell(\mathcal{D}, r) \equiv \left(\phi_\ell(r) + \omega(\mathcal{D})\dot{\phi}_\ell(r)\right) \quad \text{with} \quad \omega(\mathcal{D}) = -\frac{\phi(S)}{\dot{\phi}(S)}\frac{\mathcal{D} - \mathcal{D}_\phi}{\mathcal{D} - \mathcal{D}_{\dot{\phi}}}. \quad (5.19)$$

In this equation $\phi(S) = \phi(e_\nu, r = S)$ and $\dot{\phi}(S) = \dot{\phi}(e_\nu, r = S)$. At the boundary of the muffin-tin sphere at $R = 0$

$$\mathcal{K}_L(\kappa, \mathbf{r}) = \Phi_L(e, \mathbf{r}) + b_\ell \mathcal{J}_L(\kappa, \mathbf{r}). \quad (5.20)$$

The tail $\tilde{\mathcal{K}}_L$ muffin-tin orbital, arising from site $\mathbf{R}$, can be expanded using $\tilde{\mathcal{J}}_L$ functions centered around another site $\mathbf{R}'$:

$$\tilde{\mathcal{K}}_L(\kappa, \mathbf{r} - \mathbf{R}) = \begin{cases} \sum_{L'} \tilde{\mathcal{J}}_{L'}(\kappa, \mathbf{r} - \mathbf{R})B_{L',L}(\kappa, \mathbf{R}' - \mathbf{R}), & |\mathbf{r} - \mathbf{R}'| \leq \mathbf{R_{MT}}, \\ \mathcal{K}_L(\kappa, \mathbf{r} - \mathbf{R}), & |\mathbf{r} - \mathbf{R}'| \geq \mathbf{R_{MT}}, \end{cases}$$

where the functions $\tilde{\mathcal{J}}_L$ are defined by

$$\tilde{\mathcal{J}}_L(\kappa, \mathbf{r}) = \begin{cases} \frac{\mathcal{J}_\ell(\kappa, S)}{\Phi_\ell(\mathcal{D}_\mathcal{J}, S)}\Phi_L(\mathcal{D}_\mathcal{J}, \mathbf{r}), & r \leq S, \\ \mathcal{J}_L(\kappa, \mathbf{r}), & r \geq S. \end{cases}$$

The linear muffin-tin orbital is now given by

$$\tilde{\chi}_L(\kappa, \mathbf{r}) = \begin{cases} \frac{\mathcal{K}_\ell(\kappa, S)}{\Phi_\ell(\mathcal{D}_\mathcal{K}, S)}\Phi_L(\mathcal{D}_\mathcal{K}, \mathbf{r}), & r \leq S, \\ \tilde{\mathcal{K}}_L(\kappa, \mathbf{r}), & r \geq S. \end{cases}$$

$$\chi_L^{\mathbf{k}}(\kappa, \mathbf{r})\Big|_{r<S} \equiv \sum_{\mathbf{R}} e^{i\mathbf{k}\cdot\mathbf{R}}\tilde{\chi}_\mathbf{L}(\mathbf{r} - \mathbf{R})\Big|_{r<S} = \sum_{L'} \mathcal{Y}_\mathbf{L}(\hat{\mathbf{r}}) \quad (5.21)$$

$$\times \left(\frac{\mathcal{K}_\ell(\kappa, S)}{\Phi_\ell(\mathcal{D}_\mathcal{K}, S)}\Phi_\ell(\mathcal{D}_\mathcal{K}, r)\delta(L, L') + \frac{\mathcal{J}_\ell(\kappa, S)}{\Phi_\ell(\mathcal{D}_\mathcal{J}, S)}\Phi_{\ell'}(\mathcal{D}_\mathcal{J}, r)B_{L',L}(\kappa, \mathbf{k}) \right).$$

One Site Expansion

The crystal wave function for a muffin-tin potential is now given by a linear combination of the function defined in (5.21), i.e.,

$$\Psi_{n\mathbf{k}}(\kappa, \mathbf{r}) = \sum_{\mathbf{L}} \alpha_\mathbf{L}^{n\mathbf{k}}\chi_\mathbf{L}^{\mathbf{k}}(\kappa, \mathbf{r}). \quad (5.22)$$

Here $\chi_L^{\mathbf{k}}(\kappa, \mathbf{r})$ is a Bloch wave function (5.21) which can be written as

$$\chi_L^{\mathbf{k}}(\kappa, \mathbf{r}) = \sum_{\mathbf{R}} e^{i\mathbf{k}\mathbf{R}}\tilde{\chi}_L(\kappa, \mathbf{r} - \mathbf{R})$$

$$= \tilde{\chi}_L(\kappa, \mathbf{r}) + \sum_{L'}\left(\sum_{\mathbf{R}\neq 0} e^{i\mathbf{k}\mathbf{R}}B_{L',L}(\kappa, \mathbf{0} - \mathbf{R})\right)\tilde{\mathcal{J}}_{L'}(\kappa, \mathbf{r} - 0)$$

$$= \tilde{\chi}_L(\kappa, \mathbf{r}) + \sum_{L'}\tilde{\mathcal{J}}_{L'}(\kappa, \mathbf{r} - 0)B_{L',L}(\kappa, \mathbf{k}). \quad (5.23)$$

The limits $S \to S_{WS}$ and $\kappa \to 0$ produce the LMTO-ASA method [11, 209], and when $\kappa \neq 0$ we obtain the so-called augmented spherical wave (ASW) method [90, 257].

5.1.4 Matrix Elements of the Hamiltonian

To calculate the matrix elements of the Hamiltonian and the wave function overlap, Andersen showed [11] that one needs only the so-called potential parameters obtained at the muffin-tin radii and the structure constants which carry information of the geometry of the lattice. We will limit ourselves here to the case where $\kappa = 0$ and start this section by defining the four potential parameters. Let us exploit the fact that for any angular momentum, ℓ, the functions ϕ and $\dot{\phi}$ are orthogonal if ϕ is square summable[1]:

$$\frac{\partial}{\partial e} \int_0^s \mathrm{d}r r^2 \phi(r)^2 = 2 \int_0^s \mathrm{d}r r^2 \phi(r) \dot{\phi}(r) = 0 \,. \tag{5.24}$$

This leads to

$$H\phi = e_\nu \phi, \qquad H\dot{\phi} = \phi + e_\nu \dot{\phi} \,, \tag{5.25}$$

where e_ν is a fixed energy for which the wave function ϕ is computed for every angular momentum, ℓ, and atomic species, t, in the unit cell. Note also that ϕ and $\dot{\phi}$ are orthogonal to the core states. The trial wave function for a given radial logarithmic derivative $\mathcal{D}$ is given by (5.19). As discussed, the parameter $\omega(\mathcal{D})$ is obtained in terms of the logarithmic derivatives at the boundary of the muffin-tin spheres, $\mathcal{D}_\phi$ and $\mathcal{D}_{\dot{\phi}}$ of $\phi(S)$ and $\dot{\phi}(S)$, respectively:

$$\omega(\mathcal{D}) = -\frac{\phi(S)}{\dot{\phi}(S)} \frac{\mathcal{D} - \mathcal{D}_\phi}{\mathcal{D} - \mathcal{D}_{\dot{\phi}}} \,. \tag{5.26}$$

We have therefore the flexibility to choose any logarithmic derivative for the trail wave function at the muffin-tin sphere boundaries. This flexibility will allow us to match the trial functions at the boundary of the sphere to any tail function. The matrix elements of the Hamiltonian in any muffin-tin sphere are given by matrix elements involving the structure constants and the function defined in (5.19). The matrix elements of the latter can be evaluated from the expression

$$\langle \Phi_{t'\ell'm'} | H - e_{\nu t\ell m} | \Phi_{t\ell m} \rangle = \delta_{t't} \delta_{\ell'\ell} \delta_{m'm} \omega_{t\ell}(\mathcal{D}) \,. \tag{5.27}$$

We will also omit the atomic species index, t, for simplicity, since it is clear that all wave functions and energy derivatives inside the muffin-tin spheres depend on the index t. The corresponding contribution to the overlap is given by

---

[1] Note that we will omit the subscript ℓ of the wave function ϕ when no confusion is possible.

$$\langle \Phi_{\ell' m'} | \Phi_{\ell m} \rangle = \delta_{\ell' \ell} \delta_{m' m} (1 + \langle \dot{\phi}^2 \rangle \omega_{t\ell}^2(\mathcal{D})) \,. \tag{5.28}$$

Note that we are assuming only one trial wave function per angular momentum, ℓ, and atomic species, t. A generalization to many wave functions per angular momentum is readily incorporated and will be discussed in Chap. 6. It is then clear that all matrix elements can be written in terms of the structure constants and five "potential parameters": $\phi(S)$, $\dot{\phi}(S)$, $\langle \dot{\phi}^2 \rangle$, $\mathcal{D}_\phi$, and $\mathcal{D}_{\dot{\phi}}$. However, it can be shown using Green's second identity that one of the potential parameters is dependent on the other parameters. Indeed let us choose two wave functions ϕ_1 and ϕ_2 computed at the energies e_1 and e_2, respectively. We then get the relationship

$$\int_0^S dr \, \left((r\phi_1(r)) \frac{\partial^2}{\partial r^2} (r\phi_2(r)) - (r\phi_2(r)) \frac{\partial^2}{\partial r^2} (r\phi_1(r)) \right)$$

$$= -(e_2 - e_1) \int_0^S dr \, r^2 \phi_1(r) \phi_2(r)$$

$$= S^2 \big(\phi_1(r) \phi_2'(r) - \phi_1'(r) \phi_2(r) \big) \Big|_{r=S} .$$

In the last step of this equation we have used Green's second identity. We now divide the left-hand side by $e_2 - e_1$ and obtain

$$\int_0^S dr \, r^2 \phi_1(r) \phi_2(r) = S^2 \left(\phi_1'(r) \frac{(\phi_2(r) - \phi_1(r))}{(e_2 - e_1)} - \phi_1(r) \frac{(\phi_2'(r) - \phi_1'(r))}{(e_2 - e_1)} \right) \Big|_S .$$

Then we let $e_2 - e_1$ go to zero and ϕ_2 approach ϕ_1 (we thus drop the "1" and use ϕ) and so obtain the energy derivatives of ϕ and ϕ', denoted, respectively, by $\dot{\phi}$ and $\dot{\phi}'$:

$$\int_0^S dr \, r^2 \phi^2(r) = S^2 \big(\phi'(r) \dot{\phi}(r) - \phi(r) \dot{\phi}'(r) \big) \Big|_S$$

$$= S(\mathcal{D}_\phi - \mathcal{D}_{\dot{\phi}}) \phi(S), \dot{\phi}(S) \,. \tag{5.29}$$

Since the left-hand side is normalized and equals 1, the derived relation lets us express, for example, $\mathcal{D}_{\dot{\phi}}$ in terms of $\phi(S)$, $\dot{\phi}(S)$, and $\mathcal{D}_\phi$. These potential parameters depend strongly on the choice of the fixed energy e_ν. Instead of these parameters Andersen [11] used the equivalent potential parameters $\omega_\ell(-\ell - 1)$, $S\Phi_\ell^2(-\ell - 1, S)$, $\Phi_\ell(-\ell - 1, S)/\Phi_\ell(\ell, S)$, and $\langle \dot{\phi}_\ell^2 \rangle^{-1/2}$. To simplify the notation, we note that one often uses the short hand notation: $\Phi_\ell(-\ell - 1, S) \equiv \Phi_\ell(-)$, $\omega_\ell(-\ell - 1) \equiv \omega_\ell(-)$, $\Phi_\ell(\ell, S) \equiv \Phi_\ell(+)$.

In the ASA the Bloch wave function, given by (5.21), can be rewritten in the limit where $\kappa = 0$ as

$$\chi_L^{\mathbf{k}}(\mathbf{r}) = \Phi_L(-, \mathbf{r}) - \sum_{L'} \frac{\Phi_{L'}(\ell', \mathbf{r})}{2(2\ell' + 1)} \frac{\Phi_\ell(-)}{\Phi_{\ell'}(\ell')} S_{L', L}(\mathbf{k}) \,. \tag{5.30}$$

Using the above potential parameters and the Bloch wave function given by (5.30), the matrix elements of the Hamiltonian and the overlap can be written as

$$
\langle \chi_{L'}^{\mathbf{k}} | H - e_\nu | \chi_L^{\mathbf{k}} \rangle
$$
$$
= \omega_\ell(-)\delta_{L,L'} - \left(1 + \frac{\omega_{\ell'}(\ell')}{\omega_{\ell'}(-\ell'-1) - \omega_{\ell'}(\ell')} + \frac{\omega_\ell(\ell)}{\omega_\ell(-) - \omega_\ell(\ell)} \right) T_{L',L}(\mathbf{k})
$$
$$
+ \sum_{L''} T_{L',L''}(\mathbf{k}) \frac{\omega_{\ell''}(\ell'')}{[\omega_{\ell''}(-\ell''-1) - \omega_{\ell''}(\ell'')]^2} T_{L'',L}(\mathbf{k}) \,.
$$

$$
\langle \chi_{L'}^{\mathbf{k}} | \chi_L^{\mathbf{k}} \rangle = \left(1 + \langle \dot{\phi}_\ell^2 \rangle \omega_\ell^2(-) \right) \delta_{L,L'} - \left(\frac{1 + \langle \dot{\phi}_{\ell'}^2 \rangle \omega_{\ell'}(-\ell'-1)\omega_{\ell'}(\ell')}{\omega_{\ell'}(-\ell'-1) - \omega_{\ell'}(\ell')} \right.
$$
$$
\left. + \frac{1 + \langle \dot{\phi}_\ell^2 \rangle \omega_\ell(-)\omega_\ell(\ell)}{\omega_\ell(-) - \omega_\ell(\ell)} \right) T_{L',L}(\mathbf{k})
$$
$$
+ \sum_{L''} T_{L',L''}(\mathbf{k}) \frac{\omega_{\ell''}(\ell'')}{[\omega_{\ell''}(-\ell''-1) - \omega_{\ell''}(\ell'')]^2} T_{L'',L}(\mathbf{k}) \,, \qquad (5.31)
$$

where the normalized structure constants $T_{L',L}(\mathbf{k})$ are defined in terms of $S_{L',L}(\mathbf{k})$ as

$$
T_{L',L}(\mathbf{k}) = S\Phi_{\ell'}(-\ell'-1)S_{L',L}(\mathbf{k})\Phi_\ell(-) \,. \qquad (5.32)
$$

The matrix elements given by (5.31) and (5.31) are thus readily computed once the four potential parameters are known and it is these parameters which are recalculated each time in the self-consistent cycle of the LMTO-ASA method. The structure constants $S_{L',L}(\mathbf{k})$ are only computed once and may be stored to be used over and over, in the self-consistent calculation. This makes the LMTO-ASA one of the fastest ab initio band structure method. This method can be improved by correcting the above matrix elements by means of the so-called combined correction terms which will take into account approximately the interstitial region wave function. We will not discuss those corrections in this chapter and direct the reader to the original paper of Andersen [11] for further details. However, in the next chapter we will describe the full-potential version of the LMTO method, which goes beyond the combined correction to the ASA. We will in this chapter show how one can overcome the ASA and treat correctly the interstitial region, the charge density, and the potential. Before we do this we make a comment on the choice of linearization energy as well as the main advantages and drawbacks of the LMTO-ASA method.

5.1.5 Logarithmic Derivatives and Choice of the Linearization Energies

The bandwidth may be estimated similar to the Wigner–Seitz rule, from the logarithmic derivative, which is defined to lie between zero and minus infinity
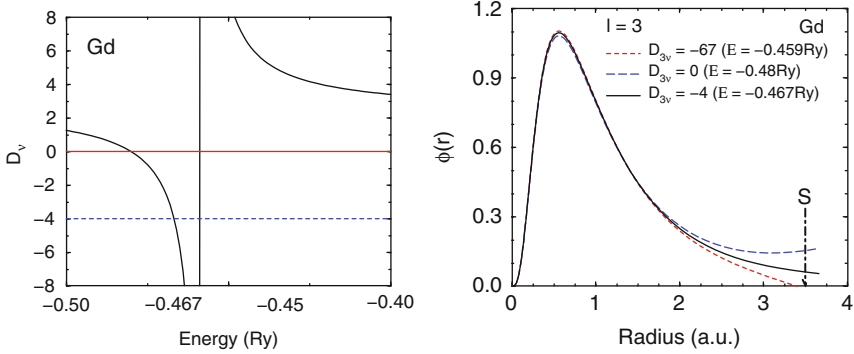
Fig. 5.3. The logarithmic derivative as a function of energy (*left*) and the atomic wave function (*right*) of the Gd 4f wave function

(an example is shown in Fig. 5.3 for Gd). Here, $\mathcal{D}_\phi = 0$ corresponds to the bottom of the canonical band, $\mathcal{D}_\phi = -\ell - 1$ to the center of the canonical band, and $\mathcal{D}_\phi = -\infty$ to the top of the canonical band. To avoid the so-called "ghost bands" (for a more detailed analysis of the "ghost bands", see [209]) one must be careful in choosing the linearization energies. A good check is always to restrict the linearization energy to the center of the band. As it can be seen from the ϕ wave function of Gd (Fig. 5.3 right) when $\mathcal{D}_\phi$ approaches large negative energies the wave function has a node at the muffin-tin radius, which corresponds to an antibonding state at the top of the band. The bonding state is obtained when $\mathcal{D}_\phi$ is close to zero, since the radial derivative of the wave function is zero at the muffin-tin radius, which corresponds to the Wigner–Seitz rule for the bonding state. Skriver has used extensively the Wigner–Seitz rule to describe the canonical band structures many materials, including Pt_3Sn, β'-MgHg, and β'-MgTl [207, 208].

5.1.6 Advantages of LMTO-ASA Method

The LMTO-ASA method has the following advantages: (1) ease of interpretation, (2) speed, and (3) simplicity. The advantage follows from the fact that this method is very close to the LCAO formalism, i.e., instead of the atomic potential, the muffin-tin potential defines the basis set to construct the Bloch wave function of the material. The atomic wave function is constructed using only s, p, d basis function for transition metals. For rare-earths and actinides one have to also include the f orbitals in the expansion of the crystal wave function. This use of a minimal basis set makes the method extremely fast, because one has to diagonalize only a small-sized Hamiltonian. For example, to obtain the band structure of silicon (with two atoms per unit cell) one need only diagonalize an eight by eight Hamiltonian.

Disadvantages of the method are as follows: (1) The limited accuracy in particular that Hellman–Feynman forces have been difficult to evaluate

accurately with this method; (2) the method is limited to close-packed systems, which means, e.g., that oxides might be difficult to handle accurately; (3) for open structures, as stated in the beginning one has to use the so-called *empty spheres* to make the system close packed, and although this works it is an inconvenience especially when structure optimizations are needed. In the next chapter we will see that a full-potential treatment overcomes this problem, allowing for highly accurate calculations while maintaining an acceptable speed. When this text is written it is readily possible to carry out a full-potential calculation with linear muffin-tin orbitals, on a single processor of a standard computer, for a crystal which contains 50–100 atoms of an f-electron system and 200–300 atoms for a transition metal system. The LMTO-ASA calculations can easily handle 5–10 times as many atoms in the unit cell.

6

The Full-Potential Electronic Structure Problem and RSPt

Abstract The full-potential methodology is presented in this chapter, with details of how the non-spherical electron density and potential are expanded in the muffin-tin regions, as well as the interstitial region. Details in the implementation of the full-potential linear muffin-tin orbitals (FP-LMTO) method are presented, with a general definition of the mathematical functions used and the symmetry aspects of these functions. The difference between a minimal, double and triple basis set is described, and numerical tests of the convergence of these basis functions are presented.

6.1 General Aspects

In this chapter we describe in detail how RSPt solves the full-potential problem of a solid, using linear muffin-tin orbitals as basis functions. The chapter highlights the difference to the LMTO-ASA method and includes a description of base geometry of the full-potential calculations, the choice of basis functions, how to calculate matrix elements of the Hamiltonian and overlap, as well as how to construct a potential from a calculated charge density. In order to successfully use RSPt one does not need to follow in detail all the aspects of this implementation, although it is of course desired.

6.1.1 Notation

Descriptions of electronic structure methods unavoidably carry a high overhead in functional symbols and indices, and what follows is no exception. For reference we define here special symbols and functions used extensively; other symbols will be defined as they are used. The particular forms of the functions and parameters (although not necessarily the symbols we use) are in common use in LMTO literature (see, for example, [209]).

Spherical Harmonics

$$\mathcal{Y}_L(\hat{\boldsymbol{r}}) \equiv i^\ell Y_L(\hat{\boldsymbol{r}}), \tag{6.1}$$

$$C_L(\hat{\boldsymbol{r}}) \equiv \sqrt{\frac{4\pi}{2\ell+1}}\, Y_L(\hat{\boldsymbol{r}}), \tag{6.2}$$

$$\mathcal{C}_L(\hat{\boldsymbol{r}}) \equiv i^\ell C_L(\hat{\boldsymbol{r}}), \tag{6.3}$$

$$L \equiv \{\ell, m\}, \tag{6.4}$$

where Y is a spherical harmonic [124]. The real space functions $\mathcal{Y}_{\ell m}$ and $\mathcal{C}_{\ell m}$ have convenient properties under rotations and are used for wave functions ($\mathcal{Y}$) and electron densities and potentials ($\mathcal{C}$) around atomic sites. The function $C_{\ell m}$ is used for functions in reciprocal space. Note that the harmonics defined above are complex. Basis functions in RSPt are complex for all symmetries.

Bessel Functions

The envelope functions of LMTO bases are spherical waves, the radial components of which are solutions to the Helmholtz equation with both positive and negative energies. In what follows, the argument κ, the square root of a kinetic energy, falls in the interval $\pi/2 > \arg(\kappa) > 0$ and is continued to the real or imaginary axis. The following definitions create solutions to the Helmholtz equations with distinct energy scaling:

$$\mathcal{K}_\ell(\kappa, r) \equiv -\kappa^{\ell+1} \begin{cases} n_\ell(\kappa r) - ij_\ell(\kappa r), & \kappa^2 < 0 \\ n_\ell(\kappa r), & \kappa^2 > 0 \end{cases}, \tag{6.5}$$

$$\mathcal{K}_L(\kappa, \boldsymbol{r}) \equiv \mathcal{K}_\ell(\kappa, r)\mathcal{Y}_L(\hat{\boldsymbol{r}}), \tag{6.6}$$

$$\mathcal{J}_\ell(\kappa, r) \equiv j_\ell(\kappa r)/\kappa^\ell, \tag{6.7}$$

$$\mathcal{J}_L(\kappa, \boldsymbol{r}) \equiv \mathcal{J}_\ell(\kappa, r)\mathcal{Y}_L(\hat{\boldsymbol{r}}), \tag{6.8}$$

where L denotes ℓm and n_ℓ and j_ℓ are spherical Neumann and Bessel functions, respectively [124]. For simplicity, we refer to $\mathcal{K}$ as a *generalized* Hankel function.

The Lattice, Unit Cell, and Atom Positions

In the language of RSPt, a material is described as a three-dimensional, infinite, periodic system, i.e., a crystal lattice. The lattice is described by a set of vectors $\boldsymbol{R} = R\boldsymbol{n}$, where the 3×3 matrix R is a lattice basis and the vectors $\boldsymbol{n}$ are integer vectors. The reciprocal to this lattice is the set of vectors

$\boldsymbol{G} = \boldsymbol{Gm}$ where G is the inverse transpose of R. The lattice defines a unit cell at each lattice site with atom sites at positions $\boldsymbol{\tau}$, relative to each lattice point $\boldsymbol{R}$. Thus the position of a particular atom in space is the site $\boldsymbol{R} + \boldsymbol{\tau}$. The set of sites $\boldsymbol{\tau}$ related to each other, up to a lattice vector, by a symmetry operation of the point group of the lattice we call a *type*, designated by t and defined by $t(\tau) = \{\tau' : P\boldsymbol{\tau}' = \boldsymbol{\tau} + \boldsymbol{R}\}$. Every type corresponds to a space group coordinate position set label. The unit cell of the reciprocal lattice is equivalent to the Brillouin zone of the lattice, and points in this cell are labeled by $\boldsymbol{k}$, so that a Fourier representation $\tilde{f}$ of a function f is $f(\boldsymbol{r}) = \sum_{\boldsymbol{G}} \int_G \exp(\mathrm{i}(\boldsymbol{k} + \boldsymbol{G}) \cdot \boldsymbol{r}) \tilde{f}(\boldsymbol{k} + \boldsymbol{G}) \mathrm{d}^3 k$.

6.1.2 Dividing Space: The Muffin-Tin Geometry

The electron density in a material varies continuously between two extremes. Near atomic sites, the potential is dominated by the spherically symmetric Coulomb potential of the atomic nucleus. In the region between atoms, the nuclear Coulomb potential is screened by electron density near the nucleus, and the electron density in this region is better described by deviations from uniformity. In a full-potential electronic structure method, we seek to describe the electron density and potential as accurately as necessary and as efficiently as possible. To accomplish this in FPLMTO methods a spherical region is defined around each atomic site in which a spherical wave expansion is most efficient, and in the region between the spheres, a plane-wave expansion is used to most efficiently describe nearly uniform behavior. An appropriate slice through a crystal thus looks like a muffin-tin. The spheres surrounding atomic sites are thus called *muffin-tin spheres*, and the region between the spheres is called the *interstitial*, denoted by $\mathcal{I}$. The muffin-tin radius of a sphere at site τ is denoted by S_t where t is the type of τ. To give a frivolous illustration, a point in the material can be described by

$$\boldsymbol{r} = \sum_{\boldsymbol{R}} \sum_{\tau} (\boldsymbol{r}' + \boldsymbol{\tau} + \boldsymbol{R})\theta(S_t - r') + \boldsymbol{r}\theta(\boldsymbol{r} \in \mathcal{I}),$$

where $\boldsymbol{r}' = \boldsymbol{r} - \boldsymbol{\tau} - \boldsymbol{R}$. The muffin-tin radius is chosen to make the overall convergence of functional expansions efficient, subject to the constraint that spheres do not overlap. Factors to be considered in choosing a muffin-tin radius are discussed below.

6.1.3 A Note on the Language of FPLMTO Methods

The previous chapter described muffin-tin orbitals, linearization, and the LMTO-ASA, a method which has contributed greatly to our understanding of the behavior of materials [209]. The LMTO-ASA describes the electronic structure and bonding of a material in terms of a minimal basis and a few, physically transparent, parameters which facilitate a physically intuitive

description of material properties. FPLMTO, which might be said to have LMTO-ASA as a parent, uses much of the same language with that method. In departing from LMTO-ASA to achieve its goals, however, this language becomes less precise. A simple example of this is the association of particular bands with a particular atomic site and angular momentum character (e.g., a Ce $4f$ band). Because an accurate calculation of necessity represents regions that belong to no atomic site, this characterization becomes less precise even when electron bands are derived from site-centered spherical waves. Another example is linearization. The LMTO-ASA basis, consisting of a radial function and its energy derivative, has a precise relationship to a linear expansion of an "exact" calculation. The full-potential LMTO basis uses this same radial basis, but with no corresponding derivative expansion in the region between spheres. Thus linearization in the full-potential LMTO becomes a choice of basis, rather than a derivative expansion. Although the language is still useful, it should be remembered that the language of accurate electronic structure method becomes less precise as the predictions of the method become more accurate.

6.2 Symmetric Functions in RSPt

RSPt makes explicit use of symmetry in its expressions. For example, the density and potential of body-centered tetragonal (*bct*) elemental crystal will be expressed in functional expansions explicitly containing that symmetry. Motivations for this are efficiency in calculation and expression as well as the damping of numerical noise. RSPt calculates the crystal symmetry from the input lattice basis R, the positions $\{\tau\}$ of atoms in the unit cell, and parameters of the calculation such as spin polarization and relativity. In a calculation sampling many possible symmetries, such as a structural relaxation, the lowest possible symmetry should be used for all calculations, and all higher symmetries sampled will be implicit, rather than explicit. If desired, of course, the minimal symmetry, i.e., the point group with one element, can be used routinely, although the calculation will be somewhat harder to converge and not filtered for numerical noise. The form of symmetric functions in RSPt determines the form and interpretation of input and output quantities.

Another example of RSPt's manic use of symmetry is found in the use of a local coordinate system attached to each atomic site. In a material in which any type contains more than one site (any space group position set of multiplicity greater than 1), the local symmetry of each site of that type is lower than the point group symmetry, the elements factored out being used to rotate between all the sites of a type. In order to use the same linear combinations of spherical harmonics to describe the crystal harmonics of the local point group on each site, the coordinate systems of each atomic site in a type must rotate into each other, i.e., they must be symmetrically related. Rotating coordinate systems is more efficient than rotating coefficients since

the rotation in this case never has to be explicitly be done. It does add, however, to an already over-burdened collection of symbols and indices by defining the rotation $\mathcal{D}_\tau$ from global to local coordinates. Another instance in which local coordinate systems are useful, regardless of type multiplicity, is found in spin-polarized electronic structure coupled to the lattice through the spin–orbit interaction. With a fixed spin direction, orienting local coordinates along the spin axis simplifies the expression of crystal harmonics.

As examples of symmetric functions in RSPt, we describe the one-electron potential $V(r)$ and the density $n(r)$ of a crystal. Recalling the division of the crystal into muffin-tin spheres and an interstitial, two forms of symmetric expansions (*crystal harmonic* and *reciprocal lattice star*) are used. Within the muffin-tin region, the potential and density are expressed as an expansion in crystal harmonics D, linear combinations of spherical harmonics $\mathcal{C}$ invariant under the local group of the atomic site. The potential and density expanded around site τ at cell $R = 0$ are

$$V(\boldsymbol{r})\Big|_{r_\tau < S_{t(\tau)}} = \frac{1}{r_\tau}\left(-Z_t e^2 + \sum_h v_{ht}(r_\tau)D_{ht}(\mathcal{D}_\tau \hat{\boldsymbol{r}}_\tau)\right), \qquad (6.9)$$

$$n(\boldsymbol{r})\Big|_{r_\tau < S_{t(\tau)}} = \frac{1}{4\pi r_\tau^2}\sum_h (2\ell_h + 1)n_{ht}(r_\tau)D_{ht}(\mathcal{D}_\tau \hat{\boldsymbol{r}}_\tau), \qquad (6.10)$$

$$D_{ht}(\hat{\boldsymbol{r}}) = \sum_m \alpha_{ht}(m)\mathcal{C}_{\ell_h m}(\hat{\boldsymbol{r}}), \qquad (6.11)$$

where $\boldsymbol{r}_\tau = \boldsymbol{r} - \boldsymbol{\tau} - \boldsymbol{R}$, $t = t(\tau)$, h indexes the set of crystal harmonics appropriate to this type, and $\mathcal{D}_\tau$ is a transformation to local coordinates. Note that the crystal harmonic D depends only on type.

In a calculation, the sum over crystal harmonics in (6.9) and (6.10) is carried out to convergence, convergence being judged by the stability of the total energy. The maximum harmonic could be different for potential and density, and indeed for every atom type. In practice, one parameter, which will be called out in this chapter to illustrate the practical use of RSPt, controls all symmetric expansions; it is ℓ_h, the maximum ℓ value of any crystal harmonic in the expansion of a symmetric function.

In the interstitial region, the potential and density are expressed in Fourier series:

$$V(\boldsymbol{r})\Big|_{r\in\mathcal{I}} = \sum_{\mathcal{S}} \tilde{V}(\mathcal{S})D_{\mathcal{S}}(\boldsymbol{r}), \qquad (6.12)$$

$$n(\boldsymbol{r})\Big|_{r\in\mathcal{I}} = \sum_{\mathcal{S}} \tilde{n}(\mathcal{S})D_{\mathcal{S}}(\boldsymbol{r}), \qquad (6.13)$$

$$D_{\mathcal{S}}(\boldsymbol{r}) = \sum_{\boldsymbol{G}\in\mathcal{S}} e^{i\boldsymbol{G}\cdot\boldsymbol{r}}. \qquad (6.14)$$

Here, $\mathcal{S}$ labels a *star* of the reciprocal lattice, the set of reciprocal lattice vectors related by point group elements P: $\mathcal{S}(\boldsymbol{G}) = \{\boldsymbol{G}' : P\boldsymbol{G} = \boldsymbol{G}'\}$. The potential defined by truncating the expansions in (6.9) and (6.12) at zeroth order is called the *muffin-tin* potential, used in the KKR method and to define FP-LMTO bases as described in Sect. 6.3.

6.2.1 The Fourier Grid for Symmetric Functions in RSPt

The star expansions, (6.12) and (6.13), like the muffin-tin crystal harmonic expansions, are truncated at a value designed to achieve convergence, as measured by the stability of the total energy. The star expansions, although representing the true density and potential only in the interstitial region, define functions, called *pseudo-functions*, continuous throughout the unit cell. The truncation of expansions in reciprocal lattice vectors is determined by the resolution imposed on these pseudo-functions in real space. A grid with points

$$\boldsymbol{r}(i,j,k) = R \begin{pmatrix} i/N_1 \\ j/N_2 \\ k/N_3 \end{pmatrix},$$

where R is the lattice basis, is laid on the unit cell of the crystal lattice for the purpose of resolving pseudo-functions, and the size and relative dimensions of this grid map directly onto the size and relative dimensions of the reciprocal lattice, which determines the extent of the expansions in (6.12) and (6.13). The gridding N_i is chosen so that the subcells have sides of approximately equal dimensions, i.e., $|r(1,00)| \sim |\boldsymbol{r}(010)| \sim |\boldsymbol{r}(001)|$. Although RSPt provides a default, the grid size, like everything else, is under user control.

6.3 Basis Functions

The basis functions of FP-LMTO methods are, just as in LMTO-ASA, linearized muffin-tin orbitals (LMTOs) – augmented spherical waves, solutions to the Helmholtz (or free-Dirac) equation in the interstitial, and atomic-like functions calculated from the spherical (zeroth order) component of the one-electron potential centered on that site.

6.3.1 Muffin-Tin Orbitals

In the (non-linear) KKR method presented in Chap. 5, energies and wave functions are "exact" solutions to an approximate potential – the "muffin-tin potential." This potential is just the RSPt potential [(6.9) and (6.12)] with expansions truncated at zeroth order: atomic-like and spherically symmetric in non-overlapping spheres surrounding atomic sites, and constant in the

interstitial region between the spheres, capturing an essential aspect of the potential in a crystal.

The KKR trial wave functions

$$\psi(\boldsymbol{k},\boldsymbol{r}) = \sum_L A_L(\boldsymbol{k}) \sum_{\boldsymbol{R}} \mathrm{e}^{\mathrm{i}\boldsymbol{k}\cdot\boldsymbol{R}} \chi_L(E,\boldsymbol{r}-\boldsymbol{R}) \tag{6.15}$$

are linear combinations of the muffin-tin orbitals χ defined by (5.2) and (5.5). The eigenfunctions of FP-LMTO methods will have the same form as KKR trial wave functions with the MTOs appropriately linearized. In seeking solutions to the wave equation for the full crystal potential, the procedure leading to (5.10) can be generalized to achieve a non-linear full-potential solution [76]. Alternatively, one could imagine using the solutions to muffin-tin potential KKR at representative energies as basis functions for a linear solution to the full-potential problem. FP-LMTO methods follow a similar but simpler route, in which the muffin-tin orbitals (MTOs) of (5.5) are transitioned to linear muffin-tin orbitals (LMTOs) and adopted as basis functions with which to construct variational eigenvalues and eigenvectors for the full-potential problem. FP-LMTO bases are described in detail below. The process of linearization in transitioning from the KKR-ASA to the LMTO-ASA is described in Chap. 5.

6.3.2 FP-LMTO Basis Functions

We now use MTOs as motivation for introducing LMTOs, the basis functions of FP-LMTO methods. The description that follows is for non- or scalar-relativistic LMTOs; the same description easily transitions to the case of Dirac spinors. Basis functions in an FP-LMTO method are generalized Hankel functions in the interstitial and numerical, atomic-like functions in the muffin-tin spheres, joined at the sphere boundaries by a condition insuring continuity and differentiability.

In the Interstitial

In the interstitial region, $\mathcal{I}$, between the muffin-tin spheres, bases are Bloch sums of spherical Hankel or Neumann functions, identical to an MTO at a fixed energy κ^2:

$$\chi_i(\boldsymbol{k},\boldsymbol{r})\Big|_{\boldsymbol{r}\in\mathcal{I}} = \sum_R \mathrm{e}^{\mathrm{i}\boldsymbol{k}\cdot\boldsymbol{R}} \mathcal{K}_{L_i}\left(\kappa_i, \boldsymbol{r}_{\tau_i+R}\right)\ .$$
$$\boldsymbol{r}_\tau = \mathcal{D}_\tau\left(\boldsymbol{r}-\boldsymbol{\tau}\right) \tag{6.16}$$

The rotation $\mathcal{D}_\tau$ in (6.16) takes the argument into a coordinate system local to each site τ, as discussed in Sect. 6.2. The function on the right-hand side of (6.16) is sometimes called the envelope function. The parameters specifying a basis function, inherent in this definition, are

τ the site in the unit cell on which the spherical wave is based,

L the angular momentum parameters ℓ and m of the spherical wave with respect to its parent site at $\tau + \boldsymbol{R}$, and

κ^2 the kinetic energy of the basis in the interstitial region, which may be positive or negative.

The angular momentum parameters specifying the basis set are chosen to represent the atomic states from which crystal eigenstates are derived. In the LMTO-ASA, it is usual to include ℓ bases one higher than the highest relevant band. In the method described here, it is more common to get this variational freedom from the multiplicity of bases. Basis sets typically include multiple bases with the same angular momentum parameters, centered on the same sites, but using different interstitial energies κ_i^2. There is no simple algorithm for choosing a consistently good set of interstitial kinetic energy parameters. Possible schemes are discussed in Sect. 6.3.4.

In the Muffin Tins

Muffin-tin orbitals, when tail cancellation occurs, are atomic-like functions in the muffin-tin spheres. Linear muffin-tin orbitals follow suit, *augmenting* the spherical wave, (6.16), by replacing $\mathcal{K}$ and its tail $\mathcal{J}$ by atomic-like basis functions. Because the Helmholtz equation is translationally invariant and singular at a single point, the envelope function ($\mathcal{K}$) can be expanded in a series of regular solutions ($\mathcal{J}$) away from its center. As a Bloch wave,

$$\sum_{\boldsymbol{R}} \mathrm{e}^{\mathrm{i}\boldsymbol{k}\cdot\boldsymbol{R}} \mathcal{K}_L(\kappa, \boldsymbol{r}-\boldsymbol{R}) = \mathcal{K}_L(\kappa, \boldsymbol{r}) + \sum_{L'} \mathcal{J}_{L'}(\boldsymbol{r}) B_{L';L}(\kappa, \boldsymbol{k}), \qquad (6.17)$$

where B is the KKR *structure constant* presented in Chap. 5. Expressing this expansion in a somewhat more compact form, the envelope function centered on site τ is expanded in the sphere at site τ' in the unit cell at $R = 0$ as

$$\sum_{\boldsymbol{R}} \mathrm{e}^{\mathrm{i}\boldsymbol{k}\cdot\boldsymbol{R}} \mathcal{K}_L(\kappa, \boldsymbol{r}_{\tau+R}) = \sum_{L'} K_{L'}^{\mathrm{T}}(\kappa, \boldsymbol{r}_{\tau'}) \mathbf{S}_{\tau'L',\tau L}(\kappa, \boldsymbol{k}), \qquad (6.18)$$

$$\boldsymbol{r}_\tau = \mathcal{D}_\tau (\boldsymbol{r} - \boldsymbol{\tau}),$$

$$K_L(\kappa, \boldsymbol{r}) = \begin{pmatrix} \mathcal{K}_L(\kappa, \boldsymbol{r}) \\ \mathcal{J}_L(\kappa, \boldsymbol{r}) \end{pmatrix}, \qquad (6.19)$$

$$\mathbf{S}_{\tau'L',\tau L}(\kappa, \boldsymbol{k}) = \begin{pmatrix} \delta(L', L)\delta(\tau', \tau) \\ B_{L'L}(\kappa, \boldsymbol{\tau}' - \boldsymbol{\tau}, \boldsymbol{k}) \end{pmatrix}. \qquad (6.20)$$

The structure constant vector $\boldsymbol{S}$ is rotated so that the initial and final states are in local site coordinates. On the surface of the muffin-tin sphere, the FP-LMTO basis is thus

$$\chi_i(\boldsymbol{k}, \boldsymbol{r})\Big|_{r_\tau = \boldsymbol{S}_t} = \sum_L K_L^{\mathrm{T}}(\kappa, S_t) \mathbf{S}_{\tau L, \tau_i L_i}(\kappa, \boldsymbol{k}) \,. \tag{6.21}$$

Inside the muffin-tin spheres, each ℓ component of the envelope function K in (6.21) is replaced by an atomic function

$$U_L(\boldsymbol{r}) = U_\ell(r)\mathcal{Y}_L(\hat{\boldsymbol{r}})$$

$$U_\ell(r) = \begin{pmatrix} u_\ell(\mathcal{K}, r) \\ u_\ell(\mathcal{J}, r) \end{pmatrix} \tag{6.22}$$

such that, at the muffin-tin radius S,

$$\big(U_\ell(S) \; U_\ell'(S)\big) = \big(K_\ell(\kappa, S) \; K_\ell'(\kappa, S)\big) \tag{6.23}$$

and the functions u are calculated from a radial wave equation $H_r(V_0)$ for the spherically averaged potential $V_0(r)$ in the muffin tins. The augmentation functions u can be obtained in a number of ways, provided only that their behavior is representative of a solution to H. For example, $u(\mathcal{K})$ and $u(\mathcal{J})$ could be constructed from two numerical solutions calculated at different energies (e.g., the bottom and center of a band, which is actually the basis of the ASW method).

A *linearized* MTO, the basis of FP-LMTO methods, represents the behavior of a solution in a range of energies around a representative energy by using a Taylor series to first order in the energy (hence *linearized*). A function ϕ and its energy derivative $\dot{\phi}$ are calculated by integrating the radial wave equation so that

$$H_r(V_0)\phi(e, r) = e\phi(e, r), \tag{6.24}$$

$$H_r(V_0)\dot{\phi}(e, r) = \phi(e, r) + e\dot{\phi}(e, r) \,. \tag{6.25}$$

If ϕ is normalized, ϕ and $\dot{\phi}$ are linearly independent. Linear combinations of ϕ and $\dot{\phi}$ are used that match both $\mathcal{K}$ and $\mathcal{J}$:

$$\Phi_L(e, \boldsymbol{r}) = \Phi_\ell(e, r)\mathcal{Y}_L(\hat{\boldsymbol{r}}) = \begin{pmatrix} \phi_\ell(e, r) \\ \dot{\phi}_\ell(e, r) \end{pmatrix} \mathcal{Y}_L(\hat{\boldsymbol{r}}), \tag{6.26}$$

$$U_L(\boldsymbol{r}) = \Omega_\ell^{\mathrm{T}}\Phi_L(e, \boldsymbol{r}),$$
$$\Omega^{\mathrm{T}} = \big(K_\ell \; K_\ell'\big)\big(\Phi_\ell \; \Phi_\ell'\big)^{-1} \,. \tag{6.27}$$

Finally, we can write an FP-LMTO basis function in any sphere as

$$\chi_i(\boldsymbol{k}, \boldsymbol{r})\Big|_{r_\tau < S_t} = \sum_L \Phi_{Lt}^{\mathrm{T}}(e_{\ell t}(i), \boldsymbol{r}_\tau)\Omega_{\ell t}(e_{\ell t}(i), \kappa_i)\mathbf{S}_{\tau L, \tau_i L_i}(\kappa_i, \boldsymbol{k}) \,. \tag{6.28}$$

The basis set, expanded in a muffin tin, acquires an additional parameter to add to the set of parameters specifying a basis function. The parameter e_i

in (6.28) is a set of energies $e_{\ell t}(i)$ used by basis set χ_i for its representation in the muffin tins. Thus e_i is the set of energies used to expand an RSPt basis in a muffin-tin sphere and it is analogous to a principal quantum number and is another parameter specifying a basis function. It often happens in heavy elements that energy levels derived from atomic states having different principle quantum numbers but the same angular momentum quantum number are part of the same, fully hybridizing basis. For example, describing the properties of elemental actinides at any pressure requires a basis with both $6p$ and $7p$ characters, since both electron states form energy bands with dispersion. Similarly, an adequate calculation of the structural properties of transition metal oxides requires both semi-core and valence s and p states on the transition metal ions. In the RSPt basis, the "energy set" parameter e_i distinguishes bases with the same angular momentum behavior. The description of the evolution of core states from localized to itinerant under pressure also requires multiple principle quantum numbers per ℓ value. In the RSPt basis, the "energy set" parameter e_i distinguishes bases with the same angular momentum behavior.

In principle, and as implemented, each $(\tau \ell \kappa)$ basis can use its own unique energy set. It is more usual to use a common energy set for a set of basis states giving rise to bands of similar energies within the scope of a particular calculation. The configuration of the basis shown in Table 6.1, for example, uses a set of energies for "semi-core" $6s$ and $6p$ bases, and another set of energies to represent "valence" bases. The choice of energies in an energy parameter set is discussed below.

The sum over L in (6.28) introduces another parameter in RSPt. As the upper component of S in (6.20) is only non-zero for χs parent L, this sum is essentially a sum over the tails of χ in a muffin tin. The extent of this summation

Table 6.1. Parameters for the default basis set for an elemental actinide: parent angular momentum parameter (ℓ), energy set for radial expansions (e-set), and the index of the kinetic energy in the interstitial region (κ-index). The default set of κ^2 values, corresponding to the kinetic energy indices, is given at the bottom of the table (see discussion in the text)

n	ℓ	e-Set	κ-Index	n	ℓ	e-Set	κ-Index	n	ℓ	e-Set	κ-Index
6	s	1	1	7	s	2	1	6	d	2	1
6	s	1	2	7	s	2	2	6	d	2	2
6	p	1	1	7	s	2	3	5	s	2	1
6	p	1	2	7	p	2	1	5	s	2	2
				7	p	2	2				
				7	p	2	3				

κ^2:	1:	0.3
	2:	-2.3
	3:	-0.6

introduces another parameter; ℓ_m, the maximum ℓ in the expansion of the tails of the basis functions in any muffin-tin sphere. The parameter ℓ_m is chosen to converge the total energy and generally takes on values $6 \leq \ell_m \leq 12$. Because the tail expansion is carried out to a higher ℓ than is usual for any basis parent, the structure constant (S or B) is rectangular.

Radial Basis Functions in RSPt

The description of the radial functions ϕ and $\dot{\phi}$ used to represent basis functions in muffin-tin spheres presented above [(6.24), (6.25), and (6.26)] is appropriate for the Schrödinger equation for $V_0(r)$ in a muffin tin. The radial bases in RSPt are actually four-component spinors obtained from the Harmon–Koelling (H–K) equation [137], a modification of the Dirac equation for the spherical potential V_0. In a slightly varied form, the Harmon–Koelling equation designed to obtain all relativistic effects except the spin–orbit interaction produces functions G and F such that

$$(H_\mathrm{D} - mc^2)\psi_{\kappa m}(e, \boldsymbol{r}) = e\psi_{\kappa m}(e, \boldsymbol{r}) + \hat{V}_{so}(\boldsymbol{r}) \begin{pmatrix} G_\ell(e, r)/r \\ 0 \end{pmatrix} \langle \boldsymbol{r}|\kappa m\rangle, \quad (6.29)$$

$$\hat{V}_{so}(\boldsymbol{r}) = \frac{1}{2r}\left(\frac{\partial}{\partial r}\frac{1}{M(e,r)}\right)\boldsymbol{\sigma}\cdot\boldsymbol{\mathcal{L}}, \quad (6.30)$$

$$\psi_{\kappa m}(e, \boldsymbol{r}) = \frac{1}{r}\begin{pmatrix} G_\ell(e, r) \\ -\mathrm{i}\sigma_r\left(F_\ell(e, r) - \frac{\boldsymbol{\sigma}\cdot\boldsymbol{\mathcal{L}}}{2Mcr}G_\ell(e, r)\right) \end{pmatrix}\langle \boldsymbol{r}|\kappa m\rangle, \quad (6.31)$$

where H_D is the Dirac Hamiltonian, $\sigma_r = \hat{\boldsymbol{r}}\cdot\boldsymbol{\sigma}$, $M(e,r) = m + (e - V(r))/2c^2)$, and

$$\langle \boldsymbol{r}|\kappa m\rangle = \sum_{m_\ell m_s} Y_{\ell m}(\hat{\boldsymbol{r}})|m_s\rangle \left(\ell\ m_\ell\ s\ m_s|\ell\ s\ j\ m\right),$$

$$\kappa = \begin{cases} j - \frac{1}{2}, & j = \ell - \frac{1}{2}, \\ -(j + \frac{1}{2}), & j = \ell + \frac{1}{2}, \end{cases}$$

κ is not to be confused with the basis kinetic energy parameter.

G and F in (6.29) and (6.31) depend only on ℓ. The RSPt radial basis function ϕ is obtained from (6.29) by transforming from $|\ell s j m\rangle$ to $|\ell m_\ell s m_s\rangle$ to obtain

$$\phi_L(e, \boldsymbol{r})|m_s\rangle = \frac{1}{r}\begin{pmatrix} G_\ell \\ -\mathrm{i}\sigma_r\left(F_\ell - \frac{\boldsymbol{\sigma}\cdot\boldsymbol{\mathcal{L}}}{2Mcr}G_\ell\right) \end{pmatrix}\mathcal{Y}_L(\hat{\boldsymbol{r}})|m_s\rangle. \quad (6.32)$$

Thus, formally, the Dirac Hamiltonian, acting on a muffin-tin basis, returns the energy times the muffin-tin basis and a spin–orbit term. The muffin-tin

basis function ϕ also has a spin–orbit term in its lower component; that term is carried through all calculations with every term coupling spins in the result ignored. This definition of ϕ includes all relativistic effects to all orders, with the exception the spin–orbit interaction, while maintaining a basis with spin and orbit (almost) decoupled, and facilitating the incorporation of the spin–orbit interaction; a fully relativistic calculation amounts to not neglecting the second term in (6.29).

The second radial basis function, $\dot{\phi}$, is obtained from (6.25) using an analytic derivative of the radial wave equation, including energy dependence of $M(e, r)$.

6.3.3 Choosing a Basis Set

The range of energies captured in a normal calculation extends from the $1s_{1/2}$ deep core state to well above the Fermi energy E_F. Most of these states are localized in core region and are calculated separately. The variational basis will contain basis functions designed to represent the highest energy atomic configuration, and possible the next highest energy configuration as well. Also included in the basis will be accommodation for the highest significant angular momentum component. For example, the atomic configuration of Al is $3s^{(2)}3p^{(1)}$; the corresponding valence basis would contain $3s$, $3p$, and $3d$ LMTOs; as discussed below, a good choice would have three s and p orbitals with different interstitial kinetic energies and two d orbitals with different kinetic energies. We write this as

- $3 \times (3s, 3p), 2 \times 3d$ (Al)

As a rule of thumb, valence s and p states use three tails, higher angular momentum and semi-core states would use two tails. For a $4d$ and $5d$ transition metals, it may be advantageous to include semi-core states. Examples are

- $2 \times (4s, 4p), 3 \times (5s, 5p), 2 \times (4d)$ (Mo)
- $2 \times (5s, 5p, 4f), 3 \times (6s, 6p), 2 \times (5d)$ (W)

For f-electron materials, semi-core states are important, even at zero pressure. Table 6.1 gives the default basis configuration for an actinide element.

6.3.4 Choosing Basis Parameters

Interstitial Kinetic Energies

There is no simple algorithm for choosing a consistently good set of interstitial kinetic energy parameters κ^2 (also called *tails*), the parameters that generate the representation of the bases in the interstitial region. Proposed schemes include bracketing the relevant energy spectrum [198] and finding and fixing a representative set to use for all calculations, eliminating variation between

calculations [168]. Another scheme is to use a single tail per energy set $e(i)$ but to minimize the energy with respect to the value of that tail at each volume and configuration [187]. Minimizing the total energy with respect to the values (and number) of tails is a natural choice, but it is time consuming and reduces the value of using a compact basis set. Instead, it is desirable to find a scheme to generate good choices for general use, possibly based on energies generated in the course of a calculation. For example, it can be shown that, for a single tail, the value that minimizes the total energy is close to the average interstitial kinetic energy, $\langle \hat{T} \rangle_{\mathcal{I}}$.

RSPts default configuration for most materials gives a basis with three tails in the highest energy set (a "triple κ basis"), representing the nominal valence bands, and two tails in the next lower energy set, representing the uppermost core levels. The values of κ^2 are drawn from the same set of three values: $\kappa^2 \in \{0.3, -2.3, -0.6\}$. These values were obtained from minimizing the total energy for a particular actinide in its ground state and have been found to give reasonable results in general. The highest value is close to the $\langle \hat{T} \rangle_{\mathcal{I}}$ in a metal, and in fact the highest value is generally replaced iteratively by the calculated $\langle \hat{T} \rangle_{\mathcal{I}}$ from a previous iteration. Choosing the same values for both valence and "semi-core" states lends stability but diminishes the physical significance of the κs in distinguishing between states of very different character. This tail configuration is accompanied by a particular choice for muffin-tin energy parameters for radial bases differing only in principle quantum number. In the default configuration, both semi-core and valence s and p states are present in the basis (for example, semi-core $6s$ and $6p$ and valence $7s$ and $7p$ for an actinide). In this configuration, energies for the valence s and p are chosen so that the valence radial bases are strictly orthogonal to the corresponding semi-core bases (see "Muffin-tin energy parameters" below). This results in high values for the $e_{\ell t}$(valence) but maximizes the completeness of the combined basis.

Another successful configuration is that used by researchers at Uppsala University. This scheme assigns two low-energy tails for semi-core states and two different and higher energy tails for the valence bands. All κ^2 are negative. The algorithm for choosing the values, as given by Björkman [32], is to set the highest of the four κ^2 to -0.1, the lowest to the minimum of the lowest semi-core band, and to space the other two tails evenly between these values. By using different energies for semi-core and valence bands, these tails have more physical significance than the RSPt default setup. The Uppsala configuration has been used successfully to describe many different properties of materials. In this configuration, the $e_{\ell t}$ are set to resonance energies for semi-core states and to ℓ-projected energies for valence states (see "Muffin-tin energy parameters" below).

Björkman [32] analyzed these two configurations by considering the stability of a calculation against changes in the underlying muffin-tin geometry. FP-LMTO bases change character at the muffin-tin radius, but if functional expansions of the eigenstates in the interstitial as well as the muffin-tins are sufficiently complete, the total energy will be insensitive to the precise value
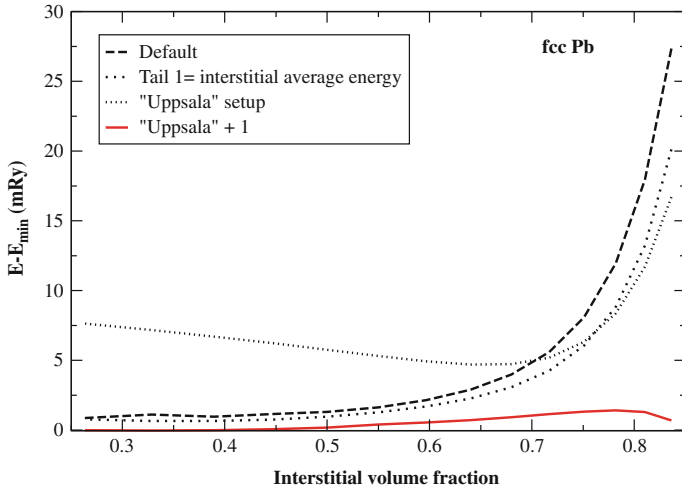
Fig. 6.1. Energy as a function of sphere size for different choices of energy parameters

of the boundary. Björkman applied this criterion to evaluate different configurations. Figure 6.1, drawn from [32], shows the total energy of fcc Pb as a function of the interstitial volume fraction, for four different tail configurations. The minimum volume fraction (the spheres cannot overlap) is 0.26. The first configuration, labeled "Default" is the default RSPt configuration; the second is the default configuration with the highest κ^2 replaced by the $\langle \hat{T} \rangle_{\mathcal{I}}$. Both of these configurations are relatively stable and give a low energy until a volume fraction ~ 0.5, where the energy starts to rise steeply. The use of the interstitial average does not change this behavior significantly, possibly because this energy is close to 0.3 for a close-packed metal. The Uppsala configuration, in contrast, has a higher energy and more variation at low volume fractions, and also rises steeply at high fractions. It should be noted, however, that the comparison is between a "triple-κ" and a "double-κ" basis set, the former presumably having more variational freedom. This presumption is born out by examining the results for the last configuration, labeled "Uppsala+1." This configuration is obtained from the Uppsala configuration by the addition of a third tail in the valence energy set, with a value set to the $\langle \hat{T} \rangle_{\mathcal{I}}$, and by using the default RSPt $e_{\ell t}$ configuration for semi-core and valence energy sets. Not only is the energy lowest of all the configurations, but variation is less than $\sim 2\,\mathrm{mRy}$ over the range of interstitial volume fractions from 0.26 to 0.8. This result would seem to show the value of (1) a triple-κ basis for valence states, (2) tying the κ^2 to physically meaningful energies, and (3) maintaining orthogonality between muffin-tin energy sets. It appears that Björkman's "Uppsala+1" configuration (red curve) would make a good starting point for developing and testing parameter sets for other and more complex materials.

Muffin-Tin Energy Parameters: "e_ν"s

In electronic structure methods using muffin-tin orbitals, the muffin-tin energy parameters $\{e_\ell\}$ are usually taken from "ℓ-projected average energies." With multiple energy sets, energy predictions for each set are necessary, so the projected energies become "ℓ and energy set projected average energies," defined for each type by

$$\left(\bar{E}_{\ell t}(e_i, e_j), \bar{Q}_{\ell t}(e_i, e_j)\right) = \sum_n \frac{V_c}{(2\pi)^3} \int \mathrm{d}^3 k\, \Theta(E_F - e_{nk})\, (e_{nk}, 1) \qquad (6.33)$$

$$\times \sum_m \sum_{\tau \in t} \int_\tau r^2 \mathrm{d}r \langle \psi_{nk} | \ell m e_i \rangle \langle \ell m e_j | \psi_{nk}(r) \rangle,$$

where the e_{nk} are the eigenvalues and ψ_{nk} the eigenvectors. For a single energy set, a well-defined prediction for $e_{\ell t}(i)$ is $\bar{E}_{\ell t}(i)/\bar{Q}_{\ell t}(i)$. With multiple energy sets, this is a reasonable estimate provided that the basis set using separate sets gives rise to bands well separated in energy. Because this is not always the case, the ℓ-projected charge is a sum over cross-terms between energy sets

$$\bar{Q}_{\ell t} = \sum_{ij} \bar{Q}_\ell(e_i, e_j).$$

These energy and charge matrices must be made diagonal to obtain reasonable predictions of the $e_{\ell t}(i)$. RSPt does this with a simple Mulliken population analysis [170].

Another scheme, particularly useful for states using different energy sets or not having significant occupation, is to set the $e_{\ell t}(i)$ to particular energy criteria. RSPt optionally sets the $e_{\ell t}(i)$ using criterion for minimum and maximum band energies and resonance energies, with principal quantum numbers identified by counting nodes in the muffin-tin spheres. Yet another, complementary, method is to maximize the completeness of the radial basis in the muffin-tin sphere. To accomplish this, assuming the energy parameter for a low energy state $e_\ell(1)$ is determined, the energy parameters for the same ℓ in higher energy sets may be chosen so that the radial function has one more node and the same logarithmic derivative at the muffin-tin radius, hence

$$\int_0^S r^2 \mathrm{d}r\, \phi_\ell(e_1, r)\phi_\ell(e_i, r) = 0, \quad i > 1. \qquad (6.34)$$

Although this usually generates energy parameters out of the range of occupied states (since the logarithmic derivative of semi-core states is usually large in magnitude and negative), this choice seems to give a total energy close to the minimum with respect to this parameter.

Choosing Muffin-Tin Radii

There are many relevant considerations in choosing muffin-tin radii. Assuming all expansions are taken to convergence, the density and potential depend on the muffin-tin radii only through the dependence of basis functions on the radii. As discussed above, basis functions have a different functional form inside the muffin-tin spheres, and the choice of muffin-tin radius affects this crossover. Hence, assuming the Hamiltonian is the same inside and outside the spheres (the treatment of relativity may affect this as discussed below), the muffin-tin radii are variational parameters and the optimum choice minimizes the total energy. If the basis is large enough, however (suitably complete within and without the spheres), the energy is insensitive to the choice of radii. A reasonable choice results from choosing radii that are within both the minimum in charge density and the maximum in potential along a line between nearest neighbors. Relativistic effects are usually taken into account only in the muffin-tin spheres, in which case the Hamiltonian depends on the radii; hence, when relativistic effects are important, the radii are not variational parameters. Muffin-tin radii also affect the convergence of the pseudo-bases used to calculate the interstitial potential matrix and the interstitial density. See the discussion below.

6.4 Matrix Elements

6.4.1 Muffin-Tin Matrix Elements

The potential in a muffin tin at $\boldsymbol{\tau}$ is given in (6.9). Note that the normalization for the spherical harmonic $\mathcal{C}$ in (6.3) is such that $(-Z_t e^2 + v_{ht}(r))/r$ is the potential when $\ell_h = 0$. Note that this part of the potential is contained in the energy parameter e of the radial basis functions.

Combining (6.9) and (6.28), the matrix elements of the non-spherical potential in the muffin tins are

$$\left\langle\chi_i\middle|V_{h>0}\middle|\chi_j\right\rangle\Big|_{mt} = \sum_{\tau}\sum_{L} S^{\dagger}_{\tau L,\tau_i L_i}(\kappa_i, \boldsymbol{k}) \tag{6.35}$$

$$\times\left(\sum_h\sum_{L'}\Omega^{\mathrm{T}}_{\ell t}(e_i,\kappa_i)\left\langle\Phi_{\ell t}(e_i)\middle|v_{ht}\middle|\Phi^{\mathrm{T}}_{\ell' t}(e_j)\right\rangle\Omega_{\ell' t}(e_j,\kappa_j)\right.$$

$$\left.\times\left\langle L\middle|D_{ht}\middle|L'\right\rangle S_{\tau L',\tau_j L_j}(\kappa_j,\boldsymbol{k})\right).$$

The matrix element of the D_{ht} is a sum over Gaunt coefficients:

$$\left\langle L\middle|D_{ht}\middle|L'\right\rangle = \sum_{m_h}\alpha_{ht}(m_h)\mathcal{G}\left(\ell',\,m';\,\ell,\,m;\,\ell_h,\,m_h\right)$$

$$\mathcal{G}\left(\ell',\,m';\,\ell,\,m;\,\ell_h,\,m_h\right) = \int \mathcal{Y}_{\ell'm'}\mathcal{Y}^*_{\ell m}\mathcal{C}_{\ell_h m_h}.$$

6.4.2 Interstitial Matrix Elements

Overlap and Kinetic Energy

The interstitial overlap matrix can be easily obtained from an integral over the interstitial surface (the only non-zero contributions, in a crystal periodic in three dimensions, come from the surfaces of the muffin-tin spheres) and the kinetic energy is proportional to the overlap:

$$
\int_{\mathcal{I}} \chi_i^\dagger(\boldsymbol{r}) \chi_j(\boldsymbol{r}) = -(\kappa_j^2 - \kappa_i^2)^{-1} \int_{\mathcal{I}} \left(\chi_i^\dagger \nabla^2 \chi_j - (\nabla^2 \chi_i^\dagger) \chi_j \right)
$$

$$
= (\kappa_j^2 - \kappa_i^2)^{-1} \sum_\tau s_t^2 \int \mathrm{d}\Omega_\tau W(\chi_i^\dagger, \chi_j) \,, \qquad (6.36)
$$

where $W(f, g) = fg' - f'g$. Basis functions on muffin-tin spheres are given in (6.21), hence

$$
\left\langle \chi_i \middle| \chi_j \right\rangle \bigg|_{\mathcal{I}} = \sum_\tau s_t^2 \sum_L S_{L,L_i}^\dagger(\kappa_i, \boldsymbol{\tau} - \boldsymbol{\tau}_i, \boldsymbol{k})
$$

$$
\times \frac{W\big(K_\ell(\kappa_i, s_t), K_\ell^{\mathrm{T}}(\kappa_j, s_t)\big)}{\kappa_j^2 - \kappa_i^2} S_{L,L_j}(\kappa_j, \boldsymbol{\tau} - \boldsymbol{\tau}_j, \boldsymbol{k}) \,. \quad (6.37)
$$

In the limit $\kappa_j^2 \to \kappa_i^2$, the evaluation of (6.36) requires the derivative with respect to κ^2 of the structure constant.

Potential Matrix Elements

The greatest difference between LMTO-based full-potential methods is in the way the matrix elements of the potential are calculated over the interstitial region. The method being described here uses a Fourier representation of basis functions and the interstitial potential to calculate these matrix elements. Other approaches for computing these elements are described in the literature [168, 225].

A Fourier transform of the basis functions described in Sect. 6.3.2 would be too poorly convergent for practical use. However, the evaluation of the interstitial potential matrix requires only a correct treatment of basis functions and potential in the interstitial region. This degree of freedom can be used to design "pseudo-basis set," equal to the true basis in the interstitial region although not in the muffin-tin spheres, and has a Fourier transform which converges rapidly enough for practical use. We define this pseudo-basis set by

$$
\tilde{\chi}_i(\boldsymbol{k}, \boldsymbol{r}) \bigg|_{\boldsymbol{r} \in \mathcal{I}} = \sum_R \mathrm{e}^{\mathrm{i}\boldsymbol{k}\cdot\boldsymbol{R}} \tilde{\mathcal{K}}_{\ell_i}(\kappa_i, |\boldsymbol{r} - \boldsymbol{\tau}_i - \boldsymbol{R}|) \mathcal{Y}_{L_i}(\boldsymbol{r} - \boldsymbol{\tau}_i - \boldsymbol{R}) \quad (6.38)
$$

$$
\tilde{\mathcal{K}}_\ell(\kappa, r) \equiv \mathcal{K}_\ell(\kappa, r) \,, \quad r > S \,, \quad S \le S_\tau \,. \qquad (6.39)
$$

Since rapid Fourier convergence is the criterion for constructing the pseudo-basis, it is useful to consider the Fourier integral of a Bloch function with wave number $\boldsymbol{k}$:

$$\tilde{\chi}(\boldsymbol{G}) = -\frac{1}{V_c(|\boldsymbol{k} + \boldsymbol{G}|^2 - \kappa^2)} \int_{V_c} \mathrm{d}^3 r \, \mathrm{e}^{-\mathrm{i}(\boldsymbol{k}+\boldsymbol{G})\cdot\boldsymbol{r}} \left(\nabla^2 + \kappa^2\right) \tilde{\chi}(\boldsymbol{r}), \quad (6.40)$$

where V_c is the unit cell volume. Equation (6.40) is obtained by casting $\nabla^2 + \kappa^2$ on the plane wave then doing two partial integrations; surface terms vanish due to periodicity. From (6.40) it is evident that the Fourier integral of a pseudo-basis satisfying the first criterion (equal to the true basis in the interstitial region) may be obtained from integral over muffin-tin spheres. If in addition, the pseudo-basis is different from a Hankel function only in its parent sphere, the Fourier integral is a finite integral over a single muffin-tin sphere. The problem then is to find a function $\tilde{\chi}$ such that $(\nabla^2 + \kappa^2)\tilde{\chi}$ has a rapidly convergent Fourier integral, vanishes outside a radius less than or equal to the parent muffin-tin radius for the basis, and has a value and slope equal to $\mathcal{K}$ at this radius.

A good choice for such a function is obtained by solving

$$\left(\nabla^2 + \kappa^2\right) \tilde{\mathcal{K}}_\ell(\kappa, r)\mathcal{Y}_L(\hat{\boldsymbol{r}}) = -c_\ell \left(\frac{r}{S}\right)^\ell \left[1 - \left(\frac{r}{S}\right)^2\right]^n \mathcal{Y}_L(\hat{\boldsymbol{r}})\Theta(S - r), \quad (6.41)$$

for a radius $S < S_{t_i}$ and with c_ℓ chosen to match onto $\mathcal{K}$ at S. This is easily done analytically. The resulting Fourier transform is

$$\tilde{\chi}_i(\boldsymbol{k} + \boldsymbol{G}) = \frac{4\pi}{V_c} \frac{Y_{L_i}(\boldsymbol{k} + \boldsymbol{G})\mathrm{e}^{-\mathrm{i}(\boldsymbol{k}+\boldsymbol{G})\cdot\boldsymbol{\tau}_i}}{(|\boldsymbol{k} + \boldsymbol{G}|^2 - \kappa_i^2)} |\boldsymbol{k} + \boldsymbol{G}|^{\ell_i} \frac{\mathcal{J}_N(|\boldsymbol{k} + \boldsymbol{G}|, S)}{\mathcal{J}_N(\kappa_i, S)}, \quad (6.42)$$

where $N = \ell_i + n_i + 1$. The subscript i has been purposely left off N and s (see below).

These coefficients converge like $1/G^{n+4}$, provided $\mathcal{J}_N(|\boldsymbol{k} + \boldsymbol{G}|, s)$ achieves its large argument behavior, and n can be chosen to optimize convergence. Weinert [253] used an analogous construction as a tool to solve Poisson's equation. He proposed a criterion for the convergence of the Fourier series (6.42) which amounts to choosing the exponent n in (6.42) so that $|\boldsymbol{k}+\boldsymbol{G}_{\max}|s$ would be greater than the position of the first node of $\mathcal{J}_{\ell+n+1}$. We find this criterion to be useful provided anisotropy in reciprocal space is accounted for. This is accomplished by using the minimum reciprocal lattice vector on the surface of maximal reciprocal lattice vectors, rather than simply using $G_{\max}$.

Notice that this criterion is a criterion for $N = \ell + n + 1$. The basis Fourier components are simplified, and the amount of information stored reduced, by simply using a single argument for all bases, i.e., all bases use the same value of N. It is also possible to use a single radius s, less than or equal to the smallest muffin-tin radius, since the only requirement is on the pseudo-bases in the interstitial region. In practice, a few radii are desirable if large and small

atoms are present in the same calculation, since small radii give less convergent Fourier coefficients. In any event, no more than a few radii are necessary to handle systems with many atoms. Notice also that local coordinates have been left out of (6.42). The resulting potential matrix may be easily rotated to local coordinates at the end of the calculation.

As expressed in (6.42), the Fourier components are products of phases $\mathrm{e}^{-\mathrm{i}(\boldsymbol{k}+\boldsymbol{G})\cdot\boldsymbol{\tau}}$, which scale like the number of atoms squared (the size of the reciprocal lattice grid grows linearly with the number of atoms), and a function of lattice vectors and a few parameters, which scales linearly with the number of atoms. The phase factors are simple to calculate by accumulation and need not be stored.

The potential in the interstitial region is similarly obtained from a "pseudo-potential" $\tilde{V}$ that equals the true potential in the interstitial region and has rapidly converging Fourier coefficients:

$$V(\boldsymbol{r})\Big|_{\mathcal{I}} = \tilde{V}(\boldsymbol{r})\Big|_{\mathcal{I}}, \tag{6.43}$$

$$\tilde{V}(\boldsymbol{r}) = \sum_{\mathcal{S}} \tilde{V}(\mathcal{S})D_{\mathcal{S}}(\boldsymbol{r}), \tag{6.44}$$

$$D_{\mathcal{S}} = \sum_{\boldsymbol{G}\in\mathcal{S}} \mathrm{e}^{\mathrm{i}\boldsymbol{G}\cdot\boldsymbol{r}}. \tag{6.45}$$

The sum in (6.44) is over stars $\mathcal{S}$ of the reciprocal lattice.

Integrals over the interstitial region are performed by convoluting the potential with an interstitial region step function and integrating over the unit cell:

$$\langle \chi_i | V | \chi_j \rangle_{\mathcal{I}} = \langle \tilde{\chi}_i | \tilde{V} | \tilde{\chi}_j \rangle_{\mathcal{I}} = \langle \tilde{\chi}_i | \theta_{\mathcal{I}} \tilde{V} | \tilde{\chi}_j \rangle_c .$$

The potential matrix element is calculated by convoluting the convoluted potential with a basis and performing a direct product between convoluted and unconvoluted bases. If basis functions are calculated n^3 reciprocal lattice vectors, the interstitial potential will be calculated on $(2n)^3$ vectors. The convolution is exact if it is carried out on a lattice containing $(4n)^3$ vectors. The size of the set of reciprocal lattice vectors necessary to converge the total energy using this treatment of the interstitial region varies from between ≈ 150 and 300 basis plane waves per atom, depending on the smoothness of the potential and the convergence required.

Another way of integrating over the interstitial region, more usual in site-centered methods, is to integrate Fourier series over the unit cell and subtract the muffin-tin contributions with pseudo-bases and pseudo-potential expressed as an expansion in spherical waves. The convolution has an advantage in acting with a single representation, and, given a finite representation for bases and potential, the convolution may be done exactly.

The Fourier Grid for Pseudo-basis Functions in RSPt

The normal Fourier grid is constructed to resolve the pseudo-density and potential, which give the true density and potential in the interstitial, in the unit cell. The density is constructed from products of wave functions, and potential matrix elements are taken with products of pseudo-bases, thus the Fourier grid for a pseudo-basis function is half the size, in each dimension, of the normal Fourier grid. Remembering that the pseudo-basis converges only if $\mathcal{J}_N(|\boldsymbol{k} + \boldsymbol{G}_{\max}|, S_\tau)$ reaches its asymptotic behavior, the muffin-tin radius must be large enough for this to occur given that $G_{\max}S$ on the pseudo-basis Fourier grid is $\approx 1/8$ its value on the normal grid. Convergence error and warning messages can sometimes be trace to small radii.

6.5 Charge Density

When a solution to the wave equation at every physical energy is available, the charge density may be obtained from a set of energy-dependent coefficients. The spherically symmetric charge density in a muffin-tin sphere, coupled with an ℓ-projected density of states, is an example. In a variational calculation, as is being described here, all that is available is a (variational) solution to the wave equation at a set of discrete energies, and the charge density must be obtained simply from the square of the eigenvectors, or equivalently from expectation values of occupation numbers.

Having calculated a set of eigenvalues and eigenvectors $\mathcal{A}$ of the generalized eigenvalue problem, the charge density in the interstitial region is

$$\tilde{n}(\boldsymbol{r})\Big|_{\mathcal{I}} = \sum_{\mathcal{S}} \tilde{n}(\mathcal{S})D_{\mathcal{S}}(\boldsymbol{r}) \tag{6.46}$$

$$\tilde{n}(\mathcal{S}) = \frac{1}{N_{\mathcal{S}}} \sum_{\boldsymbol{G} \in \mathcal{S}} \sum_{nk} w_{nk} \frac{1}{V_{\mathrm{c}}} \int_{V_{\mathrm{c}}} \mathrm{d}^3 r\, \mathrm{e}^{-\mathrm{i}\boldsymbol{G}\cdot\boldsymbol{r}} \Big| \sum_i \tilde{\psi}_i(k, \boldsymbol{r})\mathcal{A}_i(nk) \Big|^2, \tag{6.47}$$

where $N_{\mathcal{S}}$ is the number of vectors in the reciprocal lattice star $\mathcal{S}$, and $\sum_{nk} w_{nk}$ is used to sum over occupied states. The square of the wave function is obtained by convoluting the Fourier components of ψ with $\mathcal{A}$, Fourier transforming, and taking the modulus.

In the muffin-tin spheres the charge density is

$$n(\boldsymbol{r})\Big|_{r_\tau < s_t} = \sum_h n_{ht}(r_\tau)D_{ht}(\hat{\boldsymbol{r}}_\tau), \tag{6.48}$$

$$n_{ht}(r) = \sum_{e\ell} \sum_{e'\ell'} \Phi_{t\ell'}^{\mathrm{T}}(e_{i'}, r)M_{ht}(e\ell, e'\ell')\Phi_{t\ell}(e_i, r), \tag{6.49}$$

$$M_{ht}(e\ell, e'\ell') = \frac{2\ell_h + 1}{4\pi} \sum_{m_h m m'} \alpha_{ht}^*(m_h) \mathcal{G}\left(\ell, m; \ell', m'; \ell_h, m_h\right) \quad (6.50)$$

$$\times \sum_{nk} w_{nk} \mathcal{V}_{\tau\ell m}(e) \mathcal{V}_{\tau\ell'm'}^\dagger(e'),$$

$$\mathcal{V}_{\tau L}(e) = \sum_i \delta(e, e_i) \Omega_{t\ell}(e, \kappa_i) \mathcal{S}_{\tau L, \tau_i L_i}(\kappa_i, \boldsymbol{k}) \mathcal{A}_i(n\boldsymbol{k}). \quad (6.51)$$

The process of calculation is evident in the sequence of equations.

6.6 Core States

In principle, though rarely in practice, the variational basis can be used to find *all* of the electron eigenvalues and vectors, starting from the deep core $1s_{1/2}$ state. In practice, electron states that are localized (i.e., have minimal extent outside a muffin-tin sphere) are placed in a *core*. The radial functions of these core states are solved for as in an atomic calculation, which also determines their energy. The wave equation used for core states can optionally be different from that of the valence states or the core states can be calculated just as the valence is; i.e., spin polarized if the valence is polarized, fully relativistic if the valence is fully relativistic.

Core states, even spherically symmetric complete shells, contribute non-muffin-tin components to the interstitial region and to muffin-tin spheres surrounding other sites. Whether it is essential to include this contribution depends on the size of the contribution, and any sizable contribution implies that there are states being treated as localized which are not localized within the scope of the calculation. Nevertheless, confining states to the core is often useful, and including the core contribution to the full potential is not difficult. One possibility, the one used in this method, is to fit the part of the core electron density to a linear combination of Hankel functions and expand this density in the interstitial region as a Fourier series and in the muffin-tin spheres in a harmonic series, in the same way the basis functions are treated.

6.7 Potential

6.7.1 Coulomb Potential

The Coulomb potential is obtained by first calculating the Coulomb potential in the interstitial region, then, using the value of the interstitial potential on the muffin-tin sphere, calculating the potential in the spheres by a numerical Coulomb integral of the muffin-tin electron density for each harmonic.

The interstitial Coulomb potential is calculated in a way similar to that suggested by Weinert [253]. Express the electron density as

$$n(\boldsymbol{r}) = \tilde{n}(\boldsymbol{r}) + \sum_{R\tau}\left(n(\boldsymbol{r}) - \tilde{n}(\boldsymbol{r})\right)\Theta(s_t - r_\tau), \quad (6.52)$$

where $\tilde{n}$ is the squared modulus of the pseudo-eigenvectors, which is equal to the true electron density in the interstitial region. The first term on the right-hand side of (6.52) has, by construction, a convergent Fourier series. The second term is confined to muffin-tin spheres. To calculate the Coulomb potential in the interstitial region, this term may be replaced by any density also confined to the muffin-tin spheres and having the same multipole moments. If a charge density satisfies these requirements and also has a convergent Fourier series, the Coulomb potential in the interstitial region may be easily calculated from the combined Fourier series. Such a charge density can be constructed in a similar way to that detailed for the pseudo-bases. Construct a pseudo-charge density satisfying

$$\tilde{n}^{(p)}(\boldsymbol{r}) = \sum_{R\tau} \sum_h \tilde{n}^{(p)}(ht, r_{R\tau}) D_{ht}(\mathcal{D}_\tau \boldsymbol{r}\hat{}_{R\tau}), \tag{6.53}$$

$$\tilde{n}_{ht}^{(p)}(r) = c_{ht}\left(\frac{r}{s_t}\right)^{\ell_h}\left(1 - \left(\frac{r}{s_t}\right)^2\right)^n \Theta(s_t - r), \tag{6.54}$$

$$0 = \int_\tau \mathrm{d}^3 r\, r_\tau^\ell D_{ht}^*(\mathcal{D}_\tau \hat{\boldsymbol{r}}_\tau)\big(\tilde{n}^{(p)}(\boldsymbol{r}) - n(\boldsymbol{r}) + \tilde{n}(\boldsymbol{r})\big). \tag{6.55}$$

This charge density has Fourier components

$$\tilde{n}^{(p)}(\boldsymbol{r}) = \sum_\tau \sum_h \mathrm{e}^{-\mathrm{i}\boldsymbol{G}\cdot\boldsymbol{\tau}}(-\mathrm{i})^{\ell_h} D_{ht}(\mathcal{D}_\tau \boldsymbol{G}) \frac{4\pi}{V_\mathrm{c}} \frac{(Q_{ht}\{n\} - Q_{ht}\{\tilde{n}\})}{s^{\ell_h + n + 1}}$$

$$\times \frac{\big(2(\ell_h + n + 1) + 1\big)!!}{(2\ell_h + 1)!!} G^{\ell_h} \mathcal{J}_{\ell_h + n + 1}(G, s_t), \tag{6.56}$$

where the multipole moments Q are defined by

$$Q_{ht}\{n\} = \frac{2\ell_h + 1}{4\pi} \int_{s_t > r_\tau} r_\tau^{\ell_h} D_{ht}(\hat{\boldsymbol{r}}_\tau) n(\boldsymbol{r}) \, \mathrm{d}^3 r_\tau. \tag{6.57}$$

The Fourier components $\tilde{n}^{(p)}(\boldsymbol{r})$ converge like $1/G^{n+2}$ provided $j_{\ell+n+1}$ attains its asymptotic form. The exponent n is chosen using the same considerations as for the pseudo-basis set.

The Coulomb potential in the interstitial region is then given by

$$V_\mathrm{c}(\boldsymbol{r})\Big|_\mathcal{I} = \tilde{V}_\mathrm{c}(\boldsymbol{r})\Big|_\mathcal{I} = \sum_{G \neq 0} \frac{4\pi e^2 \big(\tilde{n}(G) + n^{(p)}(G)\big)}{G^2} \mathrm{e}^{\mathrm{i}\boldsymbol{G}\cdot\boldsymbol{r}}. \tag{6.58}$$

From the Coulomb potential in the interstitial region follows the Coulomb potential on the surface of the muffin-tin spheres. The Coulomb potential inside the muffin-tin spheres is

$$V^{(c)}(\boldsymbol{r})\Big|_{r_\tau < s_t} = \sum_h D_{ht}(\mathcal{D}_\tau \hat{\boldsymbol{r}}_\tau)\Bigg[e^2 \int_0^{s_t} \frac{r_<^{\ell_h}}{r_>^{\ell_h + 1}} \frac{4\pi r'^2 n_h(r)}{2\ell_h + 1} \mathrm{d}r' \tag{6.59}$$

$$+ \left(V_h^{(c)}(s) - \frac{e^2}{s^{\ell_h + 1}} \int_0^s \frac{4\pi r'^{\ell_h + 2} n_h(r')}{2\ell_h + 1} \mathrm{d}r'\right)\left(\frac{r}{s}\right)^{\ell_h}\Bigg],$$

where

$$V_{ht}^{(c)}(s_t) \equiv \frac{2\ell_h + 1}{4\pi} \int_{r_\tau = s_t} d\hat{\boldsymbol{r}} D_{ht}^*(\mathcal{D}_\tau \hat{\boldsymbol{r}}) V^{(c)}(\boldsymbol{r}) \qquad (6.60)$$

is the harmonic component of the potential on a sphere boundary.

6.7.2 Density Gradients

Gradients of the electron density are needed for the evaluation of gradient-corrected density functionals. These functionals depend on invariants (with respect to the point group) constructed from density gradients (e.g., $|\boldsymbol{\nabla} n|^2$). This reduces computation significantly in the muffin-tin spheres, for if f and g are invariant functions (i.e., $f(\boldsymbol{r}) = \sum_h f_h(r) D_h(\hat{\boldsymbol{r}})$), and $d = \boldsymbol{\nabla} f \cdot \boldsymbol{\nabla} g$, then $d(\boldsymbol{r}) = \sum_h d_h(r) D_h(\hat{\boldsymbol{r}})$ with

$$\frac{4\pi r^2}{2\ell_h + 1} d_h(r) = \sum_{h,h'} \sum_{k,k'=\pm 1} f_h^{(k)}(r) g_{h'}^{(k')}(r) I(kk'; hh') , \qquad (6.61)$$

where the set of parameters I is easily calculable from $3j$ and $6j$ coefficients and integrals over the harmonic functions D_h, and

$$f_h^{(k)} = \frac{4\pi}{2\ell + 1} \begin{cases} rf' - \ell_h, & k = 1, \\ rf' + \ell_h + 1, & k = -1, \end{cases} \qquad (6.62)$$

and similarly for g.

Gradients of the interstitial charge density, represented as a Fourier series, are poorly represented by differentiating the series term by term. A stable representation of the density gradient that converges well is obtained by defining the derivative as the difference between adjacent grid points, divided by twice the grid spacing as suggested by Lanczos [149]. This is equivalent to differentiating, term by term, the Lanczos-damped series for the charge density.

6.8 All-Electron Force Calculations

6.8.1 Symmetry

The set of internal forces acting on the atomic sites of a crystal is a symmetric, discrete function of atomic coordinates and has a spherical expansion on the crystal sites with the same coefficients as the continuous symmetric functions (6.9) and (6.10). Since forces are vectors, their representation has $\ell = 1$, and if a site has no invariant harmonics with $\ell = 1$, there is no force on that site. So the force on an atomic site may be expressed as

$$\boldsymbol{f}(\tau) = \sum_{h:\ell_h=1} f_{ht} \sum_m \alpha_m \hat{\mathbf{e}}_m \, \mathcal{U}_\tau , \qquad (6.63)$$

where the coefficients α are as in (6.11), the $\hat{\mathbf{e}}_m$ are spherical unit vectors [82], and $\mathcal{U}_\tau$ is the transformation to local coordinates for spherical vectors. A force calculation is, as much as possible, a calculation of the set $\{f_{ht}\}$. The size of this set is often much smaller than three times the number of atoms. The displacements of atoms allowed by symmetry also have the form of (6.63):

$$\delta\boldsymbol{\tau} = \sum_{h:\ell_h=1} \delta\tau_{ht} \sum_m \alpha_m \hat{\mathbf{e}}_m \, \mathcal{U}_\tau \,. \tag{6.64}$$

Minimizing the energy with respect to the atomic positions is a process of finding the set $\{\delta\tau_{ht}\}$ that gives $f_{ht} = 0$.

6.8.2 Helmann–Feynman and Incomplete Basis Set Contributions

The calculation of forces in an all-electron method has been nicely described by Yu et al. [267] for the LAPW method. In addition to the terms discussed in that paper, a force calculation using a site-centered basis has the additional, and significant, complication that the bases depend on atomic position not only through augmentation but also through parentage.

The contributions to the total force on a site in an all-electron calculation follow directly from a derivative of the LDA total energy with respect to atomic positions. The terms listed by Yu et al. are (1) a "Helmann–Feynman" term, $\partial E/\partial\boldsymbol{\tau}$, which accounts for the explicit dependence of the energy functional on atomic positions; (2) an "incomplete basis set" (IBS) term, which arises when derivatives of basis functions are not contained in the space covered by the basis set; (3) a core-correction term, arising because core states are calculated using only the spherical average of the potential; and (4) a muffin-tin term, a surface term arising from the change in integration boundaries when atoms are moved and the discontinuity of the second derivative of basis functions across muffin-tin boundaries. There are two other terms to consider. The first arises when a calculation is not fully self-consistent and has the form $-\int_{V_c}(V_{\text{out}} - V_{\text{in}})\mathrm{d}n(\boldsymbol{r})/\mathrm{d}\boldsymbol{\tau}$, where V_{out} and V_{in} are output and input potentials. The second term arises from the way in which Brillouin zone integrals are done. Whether by quadrature or linear interpolation, the result is a set of weights (occupations) multiplying quantities evaluated at discrete Brillouin zone points. The terms listed above do not take into account the change of weights with atomic positions.

The evaluation of the IBS term in a method using site-centered bases is significantly more involved than in the LAPW method. This term has the form

$$\boldsymbol{F}_{\text{IBS}} = -\sum_{n\boldsymbol{k}} w_{n\boldsymbol{k}} \sum_{ij} \mathcal{A}_{i,n\boldsymbol{k}}^* \Big(\big\langle \psi_i \big| H - e_{n\boldsymbol{k}} \big| \mathrm{d}\psi_j/\mathrm{d}\boldsymbol{\tau} \big\rangle$$
$$+ \big\langle \mathrm{d}\psi_i/\mathrm{d}\boldsymbol{\tau} \big| H - e_{n\boldsymbol{k}} \big| \psi_j \big\rangle \Big) \mathcal{A}_{j,n\boldsymbol{k}} \,, \tag{6.65}$$

where the $\mathcal{A}$ are eigenvectors. Both LAPW and LMTO methods have a dependence on atomic positions through augmentation (the expansion of the basis

set in atomic-like spherical waves) in the muffin-tin spheres, and both methods have an implicit dependence of basis functions on atomic positions through self-consistency, a term largely ignored and usually negligible. A site-centered basis, however, depends on atomic positions also through its parent site (the site it is centered on). The contribution from augmentation is fairly easily accounted for at the density stage of a calculation, after integrals over the Brillouin zone have been done. The parent contribution, however, requires evaluation at the part of the calculation where eigenvalues and vectors are obtained, which makes its calculation time consuming.

There are four types of contributions to $\mathrm{d}\psi/\mathrm{d}\boldsymbol{\tau}$:

$$-\frac{\mathrm{d}}{\mathrm{d}\boldsymbol{\tau}}\psi_i(\boldsymbol{k},\boldsymbol{r}) = \mathrm{i}\Big(\boldsymbol{\delta}_\tau^{(1)} + \boldsymbol{\delta}_\tau^{(2)} + \boldsymbol{\delta}_\tau^{(3)} + \boldsymbol{\delta}_\tau^{(4)}\Big)\psi_i(\boldsymbol{k},\boldsymbol{r}), \tag{6.66}$$

$$\boldsymbol{\delta}_\tau^{(1)}\psi_i(\boldsymbol{k},\boldsymbol{r}) \equiv \Theta(\boldsymbol{r}\in\mathcal{I})\delta(\tau_i,\tau)\hat{\boldsymbol{p}}\psi_i(\boldsymbol{k},\boldsymbol{r}), \tag{6.67}$$

$$\boldsymbol{\delta}_\tau^{(2)}\psi_i(\boldsymbol{k},\boldsymbol{r}) \equiv \delta(\tau_i,\tau)\sum_{\tau'L}\Theta(s_{t'}-r_{\tau'})\Phi_{t'L}^{\mathrm{T}}(e_i,\boldsymbol{r}_{\tau'})\Omega_{t'\ell}(e_i,\kappa_i)$$
$$\times \begin{pmatrix} 0 \\ -\mathrm{i}\boldsymbol{\nabla}_\tau B_{L,L_i}(\kappa_i,\boldsymbol{\tau}'-\boldsymbol{\tau}_i,\boldsymbol{k}) \end{pmatrix}, \tag{6.68}$$

$$\boldsymbol{\delta}_\tau^{(3)}\psi_i(\boldsymbol{k},\boldsymbol{r}) \equiv \Theta(s_t-r_\tau)\sum_L \hat{\boldsymbol{p}}\Phi_{tL}^{\mathrm{T}}(e_i,\boldsymbol{r}_\tau)\Omega_{t\ell}(e_i,\kappa_i)S_{L,L_i}(\kappa_i,\boldsymbol{\tau}-\boldsymbol{\tau}_i,\boldsymbol{k}), \tag{6.69}$$

$$\boldsymbol{\delta}_\tau^{(4)}\psi_i(\boldsymbol{k},\boldsymbol{r}) \equiv -\Theta(s_t-r_\tau)\sum_L \Phi_{tL}^{\mathrm{T}}(e_i,\boldsymbol{r}_\tau)\Omega_{t\ell}(e_i,\kappa_i)$$
$$\times \begin{pmatrix} 0 \\ -\mathrm{i}\boldsymbol{\nabla}_\tau B_{L,L_i}(\kappa_i,\boldsymbol{\tau}-\boldsymbol{\tau}_i,\boldsymbol{k}) \end{pmatrix}, \tag{6.70}$$

where $\hat{\boldsymbol{p}}$ is the momentum operator $-\mathrm{i}\boldsymbol{\nabla}$. The first two terms, (6.67) and (6.68), are parent terms, change in a basis due to a change in the site the basis is centered on. The first term, (6.67), is the derivative of the wave function in the interstitial region (6.16) with respect to its parent site. Since the gradient of a solution to the Helmholtz equation is a solution to the Helmholtz equation, matrix elements $\langle\psi_i\hat{\boldsymbol{p}}\psi_j\rangle_\mathcal{I}$ and $\langle\psi_i|-\nabla^2|\hat{\boldsymbol{p}}\psi_j\rangle_\mathcal{I}$ are calculated as integrals over the surface of the muffin-tin spheres. As in (6.37), when interstitial region tail parameters are the same, the evaluation requires κ^2 derivatives of structure functions. Working out this contribution proceeds as in (6.37), although arriving at a finite form requires identities such as

$$\sum_\mu \hat{\boldsymbol{e}}_\mu \mathcal{U}_{\tau_b}\Big(B_{\ell_a m_a,\ell_b-1 m_b-\mu}(\kappa_b,\boldsymbol{\tau}_a-\boldsymbol{\tau}_b,\boldsymbol{k})\mathcal{G}\big(\ell_b-1,m_b-\mu;\ell_b,m_b;1,\mu\big)\kappa_b^2$$
$$-B_{\ell_a m_a,\ell_b+1\,m_b-\mu}(\kappa_b,\boldsymbol{\tau}_a-\boldsymbol{\tau}_b,\boldsymbol{k})\mathcal{G}\big(\ell_b+1,m_b-\mu;\ell_b,m_b;1,\mu\big)\Big)$$
$$= \sum_\mu \hat{\boldsymbol{e}}_\mu \mathcal{U}_{\tau_a}\Big(B_{\ell_a+1 m_a+\mu,\ell_b m_b}(\kappa_b,\boldsymbol{\tau}_a-\boldsymbol{\tau}_b,\boldsymbol{k})\mathcal{G}\big(\ell_a,m_a;\ell_a+1,m_a+\mu;1,\mu\big)$$
$$-B_{\ell_a-1 m_a+\mu,\ell_b m_b}(\kappa_b,\boldsymbol{\tau}_a-\boldsymbol{\tau}_b,\boldsymbol{k})\mathcal{G}\big(\ell_a,m_a;\ell_a-1,m_a+\mu;1,\mu\big)\kappa_b^2\Big). \tag{6.71}$$

Potential matrix elements $\langle\psi_i|V|\psi_j\rangle$ are calculated using Fourier series as in Sect. 6.4.2 with gradients taken as discussed after (6.62).

The second term, (6.66), is the analog of the first term in the muffin-tin spheres, i.e., this term is the derivative of a basis with respect to its parent site evaluated in the muffin-tin spheres. This term requires the gradient with respect to atomic positions of the structure function B. This gradient is easily obtained from the structure function itself:

$$
\begin{aligned}
\boldsymbol{B}'_{\ell m,\ell'm'}(\kappa,\boldsymbol{\tau}-\boldsymbol{\tau}',\boldsymbol{k}) &\equiv \frac{\partial}{\partial\boldsymbol{u}}B_{\ell m,\ell'm'}(\kappa,\boldsymbol{u},\boldsymbol{k})\Big|_{\boldsymbol{u}=\boldsymbol{\tau}-\boldsymbol{\tau}'} \\
&\equiv \sum_\mu \mathrm{i}\hat{e}_\mu \mathcal{U}_\tau \mathcal{B}'^{(\mu)}_{\ell m,\ell'm'}(\kappa,\boldsymbol{\tau}-\boldsymbol{\tau}',\boldsymbol{k}),
\end{aligned}
$$

$$
\begin{aligned}
\mathcal{B}'^{(\mu)}_{\ell m,\ell'm'}(\kappa,\boldsymbol{\tau}-\boldsymbol{\tau}',\boldsymbol{k}) = \Big(&\mathcal{G}\big(\ell,m;\ell+1,m+\mu;1,\mu\big) \\
&\times B_{\ell+1m+\mu,\ell'm'}(\kappa,\boldsymbol{\tau}-\boldsymbol{\tau}',\boldsymbol{k}) \\
&-\kappa^2\mathcal{G}\big(\ell,m;\ell-1,m+\mu;1,\mu\big) \\
&\times B_{\ell-1m+\mu,\ell'm'}(\kappa,\boldsymbol{\tau}-\boldsymbol{\tau}',\boldsymbol{k})\Big)
\end{aligned}
$$

$$
\boldsymbol{\tau}-\boldsymbol{\tau}' \neq 0. \tag{6.72}
$$

If convergence with respect to ℓ on the left-hand side of the structure function is sufficient for the energy, terms in $\ell_{\max}+1$ in (6.72) may be neglected in evaluating forces. As stated above, the evaluation of these terms is somewhat time consuming.
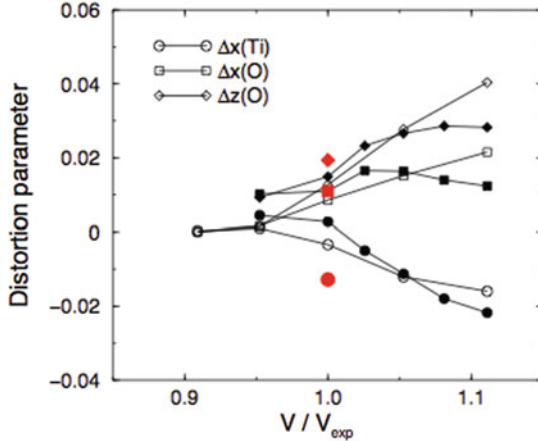
Fig. 6.2. The deviation of the internal coordinates of rhombohedral BaTiO$_3$ from ideal, calculated using all-electron force calculations as a function of volume with both LDA (*open symbols*) and GGA (*filled symbols*) exchange-correlation functions. The *red filled symbols* are experimental points [147]. The LDA equilibrium volume is $0.958\,V_{\exp}$; the GGA volume is $1.037\,V_{\exp}$. The energy was also minimized with respect to the rhombohedral angle at each volume

Examples of the use of forces for structural relaxation are given in Figs. 6.2 and 6.3. Figure 6.2 shows deviations from ideal lattice positions calculated for rhombohedral $BaTiO_3$ as a function of volume compared to experiment [147]. The rhombohedral angle was also relaxed at each volume in this calculation. The Ti coordinate is a displacement along [109]. The oxygen displacements Δx are along face diagonals while Δz is toward the cell center. These calculations included Ti $3s$ and $3p$ and Ba $5s$ and $5p$ along with the usual valence bases in a single, fully hybridizing basis. At convergence, forces on internal coordinates were less than $1\,mRy/Bohr$. Figure 6.3 is a calculation of structural relaxation of As-vacancy-interstitial complex in Si. To a 64-atom Si supercell was added an As impurity at a tetrahedral interstitial position and a Si interstitial at an exchange position both surrounding a vacancy. The crystal, far from equilibrium, was then allowed to relax. Two internal coordinates (of a total of 106) were fixed to fix the center of mass of the crystal. The energy was minimized with respect to the other 104 internal coordinates by zeroing the forces (to within $1\,mRy/Bohr$). The forces were zeroed using a simple Broyden's method.
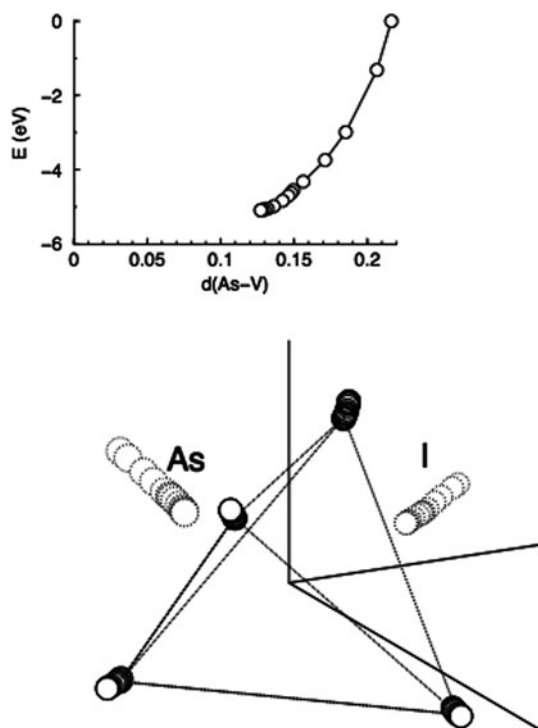
Fig. 6.3. Relaxation of a silicon 65 atom supercell containing a vacancy, a Si interstitial, and an As interstitial. Of the 106 internal coordinates in this cell, 104 were allowed to relax (two coordinates were fixed to fix the center of mass of the crystal). The calculation used a simple Broyden's method to zero atomic forces

7

Dynamical Mean Field Theory

Abstract The basic reasons for why the common approximation to the exchange and correlation energy of density functional theory is inaccurate for certain materials are outlined. A possible fix to this problem, in terms of dynamical mean field theory (DMFT) is described, and details of how it is implemented in the FP-LMTO method are presented. The different choices of correlated orbitals which are to be considered in DMFT are also given. Examples of DMFT calculations are presented using different approximations to the 'impurity part' of the DMFT calculations.

7.1 Strong Correlations

Density functional theory within the LDA and GGA approximation is nowadays a standard tool for electronic structure calculations. It gives quantitative description of the electronic structure and ground state properties of most solids, and we will discuss several aspects of this in Chaps. 10, 11, and 12. However, LDA and GGA are derived in the limit of a nearly uniform electron density, and they fail in the opposite limit of localized electron states with strong Coulomb correlations.

Consider an example. Sodium (Na) crystallizes in the body-centered cubic structure with lattice constant approximately 4.29 Å. It is a good metal with nearly free $3s$ electrons. Now let us increase the lattice constant to 1 m, creating a system of virtually isolated Na atoms. LDA still gives a metallic solution, albeit with a very narrowband (with bandwidth W). In reality, such system would be insulating, of course. If two conduction electrons happen to be on the same Na site, there is a loss of energy equal to U (on-site Coulomb interaction). If $U \gg W$, a current cannot flow and the system is an insulator (more specifically, a *Mott insulator*). In other words, the motion of electrons becomes *correlated*. Such on-site (Hubbard-like) correlation effects are not properly treated by LDA/GGA, although these functionals can describe well other correlation effects (such as screening). Several review articles have covered this issue [220].

The strength of the on-site correlations is determined by the parameter U/W, where U is the screened on-site Coulomb interaction and W is the bandwidth. If $U/W \ll 1$ then the system is weakly correlated and well described by LDA/GGA. The strongly correlated regime $U/W \gg 1$ gives us atomic-like behavior (Hubbard bands, Mott insulators). For the most interesting case $U/W \sim 1$ we have a mixture of band-like and atomic-like behavior, as well as Kondo behavior, intermediate valence, or heavy fermion materials. Since W depends strongly on unit cell volume, all solids are Mott insulators at very large volumes (like in the example above of Na) and good metals at very small volumes (metallization under pressure). Under ambient conditions, many d and f metals and their compounds display strong correlation effects and should not be treated within LDA/GGA.

Dynamical mean field theory (DMFT) [96] is an approximate method for solving the Hubbard model. It covers the whole range of the parameter U/W from uncorrelated metal to Mott insulator. The formal small parameter of DMFT is $1/d$, where d is the number of spatial dimensions. DMFT is exact in the limit of infinite dimensions, while for $d = 3$ DMFT is a reasonable approximation. Recently DMFT has been combined with LDA-based first-principles calculation to create the LDA/GGA+DMFT method [15, 95, 115, 143, 157]. This method is able to calculate the electronic structure of strongly correlated solids ab initio. LDA/GGA+DMFT has been recently implemented in the FP-LMTO code RSPt [72, 73, 106, 237], which is sometimes loosely referred to as "Brianna." We will in the remainder of this text refer to this technique as RSPt+DMFT. In the following sections we briefly outline the LDA/GGA+DMFT formalism, followed by details of our implementation, and, finally, a few examples. The presentation is based on [73, 106, 237] and can also be found in the thesis of [72].

7.2 LDA/GGA+DMFT Method

The LDA/GGA+DMFT formalism in its most typical form [95, 115, 143] is based on several key assumptions:

- All physics of sp electrons is described well enough by the LDA/GGA.
- The solid is represented by an effective multiband Hubbard Hamiltonian, called $H_{\mathrm{LDA/GGA+U}}$.
- The hopping part of $H_{\mathrm{LDA/GGA+U}}$ is the LDA/GGA Hamiltonian, H_{eff}.
- The Hubbard-U term is added "by hand" for the correlated electrons (d or f states) only.
- The resulting Hamiltonian is treated within the DMFT scheme [96].
- A double-counting correction is applied to avoid including certain effects twice.

All of these assumptions are approximations; they are not rigorously true [115]. In the end, just like with LDA and GGA, we have to rely on our physical

experience to judge whether the LDA/GGA+DMFT method is good for a given physical problem or not.

7.2.1 LDA/GGA+U Hamiltonian

In LDA/GGA, a solid is described by the Kohn–Sham (KS) equation, (2.18), which we here cast in a slightly different form

$$[H_{\text{eff}} - \epsilon] \, |\psi\rangle = 0 \,, \tag{7.1}$$

where the one-particle LDA/GGA Hamiltonian H_{eff} acts in the Hilbert space of one-electron states $|\psi\rangle$. Solution of the KS equation gives the KS eigenvalues and eigenvectors. While, in principle, the KS eigenspectrum is an auxiliary quantity without direct physical meaning, in practice it is often regarded as the ab initio band structure. In contrast to the true electron and hole excitations, however, the "KS quasiparticles" have infinite lifetime, hence each calculated spectral property has zero lifetime broadening.

A typical correlated solid includes delocalized sp states and more localized d or f states. The LDA/GGA+DMFT method assumes that the correlation effects of the sp states are treated well within LDA/GGA, while DMFT is necessary only for the more localized states. This method defines a subspace of "correlated states" $|\mathbf{R}, \xi\rangle$, where $\mathbf{R}$ is a Bravais lattice vector, and the index ξ numbers all correlated states within a unit cell. The correlated states are normally required to be orthogonal and normalized $\langle \mathbf{R}_1, \xi_1 | \mathbf{R}_2, \xi_2 \rangle = \delta_{\mathbf{R}_1, \mathbf{R}_2} \delta_{\xi_1, \xi_2}$. Usually the correlated states are defined as atomic-like d or f orbitals (represented as orthogonalized muffin-tin orbitals or Wannier-like functions). In that case, the quantum number ξ stands for the atomic quantum numbers m, σ and the correlated site τ within the unit cells (if there are more than one such site).

The LDA/GGA+U Hamiltonian is

$$H_{\text{LDA/GGA+U}} = H_{\text{eff}} + \frac{1}{2} \sum_{\mathbf{R}} \sum_{\xi_1, \xi_2, \xi_3, \xi_4} U_{\xi_1, \xi_2, \xi_3, \xi_4} c^{\dagger}_{\mathbf{R}, \xi_1} c^{\dagger}_{\mathbf{R}, \xi_2} c_{\mathbf{R}, \xi_4} c_{\mathbf{R}, \xi_3} \,, \tag{7.2}$$

where the Coulomb parameters ("4-index U")

$$U_{\xi_1, \xi_2, \xi_3, \xi_4} = \int \int \mathrm{d}\mathbf{r} \mathrm{d}\mathbf{r}' \Psi^{*}_{\mathbf{R}, \xi_1}(\mathbf{r}) \Psi^{*}_{\mathbf{R}, \xi_2}(\mathbf{r}') V_{\text{ee}}(\mathbf{r} - \mathbf{r}') \Psi_{\mathbf{R}, \xi_3}(\mathbf{r}) \Psi_{\mathbf{R}, \xi_4}(\mathbf{r}') \tag{7.3}$$

are the matrix elements of the screened Coulomb interaction $V_{\text{ee}}(\mathbf{r} - \mathbf{r}')$ between four correlated orbitals $\{|\mathbf{R}, \xi\rangle\}$ located *at the same site*; and

$$H_{\text{eff}} = \sum_i H_{\text{eff}}(\mathbf{r}_i) \,, \tag{7.4}$$

where $\mathbf{r}_i$ are the coordinates of all electrons. For the atomic-like correlated orbitals, the Coulomb parameters can be expressed in terms of Slater parameters F^n:

$$U_{\xi_1,\xi_2,\xi_3,\xi_4} = \sum_{n=0}^{2l} a_n(\xi_1,\xi_3,\xi_2,\xi_4)F^n\,, \tag{7.5}$$

where

$$a_n(\xi_1,\xi_3,\xi_2,\xi_4) = \frac{4\pi}{2n+1}\sum_{q=-n}^{+n}\langle\xi_1|Y_{nq}|\xi_3\rangle\,\langle\xi_2|Y_{nq}^*|\xi_4\rangle\,. \tag{7.6}$$

The values of the Slater parameters, F^n, are calculated in RSPt from radial integrals of wave functions [128]. The first Slater integral, F^0, has to be scaled down significantly, since it always turns out too big in a direct calculation, a well-known effect which is ascribed to screening effects.

For d electrons, one often uses just two parameters U and J

$$U = F^0\,, \quad J = \frac{F^2 + F^4}{14}\,, \tag{7.7}$$

assuming $F^4/F^2 = 0.625$.

7.2.2 LDA/GGA+DMFT Equations

The LDA/GGA+U Hamiltonian has the form of a multiband Hubbard Hamiltonian. H_{eff} plays the role of "hopping." However, H_{eff} already includes Hartree and exchange terms, as well as some correlation effects (e.g., screening). The Hubbard-U term is added to take care of the correlation effects not accounted for by LDA/GGA. The DMFT scheme [96] is then applied to this Hamiltonian. The basic quantity of DMFT is the local Green's function $G_{\mathbf{R}}(z)$. It is defined as the one-electron Green's function (GF) projected to the correlated states at site $\mathbf{R}$

$$G_{\mathbf{R}}(z) = P_{\mathbf{R}}G(z)P_{\mathbf{R}}\,, \quad P_{\mathbf{R}} = \sum_{\xi}|\mathbf{R},\xi\rangle\langle\mathbf{R},\xi|\,, \tag{7.8}$$

where

$$G(z) = [z + \mu - H_{\text{eff}} - \Sigma(z)]^{-1} \tag{7.9}$$

is the one-electron GF, $\Sigma(z)$ is the self-energy, and z in our calculations takes values of the Matsubara frequencies

$$z = i\omega_n = i\pi T(2n+1)\,, \quad n = 0, \pm 1, \pm 2, \ldots\,, \tag{7.10}$$

where T is the temperature of the system. Explicitly, the matrix elements of $G_{\mathbf{R}}(z)$ are

$$(G_{\mathbf{R}}(z))_{\xi_1,\xi_2} \equiv \langle \mathbf{R}, \xi_1 | G_{\mathbf{R}}(z) | \mathbf{R}, \xi_2 \rangle = \langle \mathbf{R}, \xi_1 | G(z) | \mathbf{R}, \xi_2 \rangle . \qquad (7.11)$$

The approximation of DMFT is the *locality* of the one-electron self-energy, namely it states that $\Sigma(z)$ can be written as the sum of local self-energies for all Bravais lattice sites

$$\Sigma(z) = \sum_{\mathbf{R}} \Sigma_{\mathbf{R}}(z). \qquad (7.12)$$

This expression is local in the sense that it has zero matrix elements between different sites

$$\langle \mathbf{R}_1, \xi_1 | \Sigma | \mathbf{R}_2, \xi_2 \rangle = \delta_{\mathbf{R}_1,\mathbf{R}_2} \left(\Sigma_{\mathbf{R}_1} \right)_{\xi_1,\xi_2} . \qquad (7.13)$$

Moreover, if there are several correlated sites within the unit cell, and the Hubbard-U term does not have matrix elements between different sites, $(\Sigma_{\mathbf{R}})_{\xi_1,\xi_2}$ takes a block diagonal form with a block for each site.

The DMFT equations can be derived (together with the locality of Σ) in the infinite-dimension limit of the Hubbard model [96, 115]; or, alternatively, they can be obtained as the best local solution of the *spectral density functional theory* [95, 143]. In DMFT, the lattice problem is substituted by the *impurity problem (effective Anderson model)*, i.e., the problem of a single correlated site in the self-consistent bath described by the *bath GF (or dynamical mean field)* $\mathcal{G}_0(\mathbf{R}, z)$ defined by

$$\mathcal{G}_0^{-1}(\mathbf{R}, z) = G_{\mathbf{R}}^{-1}(z) + \Sigma_{\mathbf{R}}(z). \qquad (7.14)$$

There exist a number of algorithms (called *solvers*) for solving the impurity problem numerically. A typical solver gets $\mathcal{G}_0^{-1}(\mathbf{R}, z)$ and $U_{\xi_1,\xi_2,\xi_3,\xi_4}$ as input data and provides the new $\Sigma_{\mathbf{R}}(z)$ on output. The DMFT version of RSPt currently includes three solvers, but several additional ones are being developed. The SPTF solver is best suited for weak correlations, but it is fast, works in spin-polarized case (while treating crystal field and spin–orbit effects correctly), and gives accurate DOS and spectral densities. The quantum Monte Carlo (QMC) solver is numerically exact (works for any U/W), but it cannot be used directly in the spin-polarized case, and it gives poor-quality DOS curves. RSPt also includes the Hubbard-I solver, which is basically the limiting case of DMFT for $U \gg W$. A double-counting correction must be applied to all DMFT calculations. The simplest double-counting correction for metals is

$$\Sigma(\mathrm{i}\omega_n) \to \Sigma(\mathrm{i}\omega_n) - \Sigma(+\mathrm{i}0),$$

which only marginally changes the Fermi surface. A somewhat better choice is obtained by averaging $\Sigma(+\mathrm{i}0)$ over orbital indices.

The new corrected Σ is then plugged back to (7.9), closing the DMFT cycle, which should be repeated self-consistently until convergence is reached.

Just like in LDA/GGA, the chemical potential μ (Fermi energy) must be updated on every iteration to produce the correct number of electrons

$$N = \lim_{\delta \to +0} T \sum_{i\omega_n} e^{i\omega_n \delta} \mathrm{Tr}\, G(i\omega_n) = T \sum_{i\omega_n} \mathrm{Tr}\, \left[G(i\omega_n) + \frac{1}{2} \right] . \qquad (7.15)$$

Once the convergence is reached, various physical quantities can be calculated, such as the density of states (DOS)

$$D(\epsilon) = -\frac{1}{\pi} \mathrm{Tr}\, \left[\mathrm{Im}\, \hat{G}(\epsilon + i0) \right] , \qquad (7.16)$$

and the spectral density (**k**-resolved DOS)

$$A(\mathbf{k}, \epsilon) = -\frac{1}{\pi} \sum_{\chi} \langle \mathbf{k}, \tilde{\chi} | \mathrm{Im}\, G(\epsilon + i0) | \mathbf{k}, \chi \rangle , \qquad (7.17)$$

which is the correlated quasiparticle band structure ($\{ |\mathbf{k}, \chi\rangle \}$ is the **k**-space LDA/GGA basis set, see below). In the absence of self-energy it reduces to the usual Kohn–Sham band structure

$$A_{\mathrm{KS}}(\mathbf{k}, \epsilon) = \sum_n \delta \left(\epsilon - \epsilon_n(\mathbf{k}) \right) .$$

The real part of Σ simply shifts the bands, while the imaginary part of Σ introduces smearing due to the finite lifetime of quasiparticles. Apart from coherent (quasiparticles) features, a spectral density might also have noncoherent (virtually **k**-independent) ones, such as Hubbard bands and satellites.

The LDA/GGA+DMFT total energy is given by [73]

$$E = E_{\mathrm{LDA/GGA}} - \sum_{\mathbf{k}\nu} \epsilon_{\mathbf{k}\nu} \Theta(\mu - \epsilon_{\mathbf{k}\nu}) + \sum_{i\omega_n} \mathrm{Tr}\, (H_{\mathrm{eff}} G) + \frac{1}{2} \sum_{i\omega_n} \mathrm{Tr}\, (\Sigma G) ,$$

where the first term is the LDA/GGA total energy, the second one is the eigenvalues sum of occupied Kohn–Sham states (with minus sign). The third term is $\langle H_{\mathrm{eff}} \rangle$, the expectation value of the first term in (7.2). Together with the second term, it gives the DMFT correction to the LDA/GGA eigenvalues sum. Finally, the fourth term is $\langle H_{\mathrm{U}} \rangle$, the expectation value of the second term in (7.2).

7.3 Implementation

As mentioned, the LDA/GGA+DMFT scheme has been implemented in RSPt [72, 73, 106, 237]. The DMFT implementation in RSPt is one of a few current all-electron full-potential LDA/GGA+DMFT implementations (previously, most LDA/GGA+DMFT implementations were based on LMTO-ASA or KKR-ASA). Below we summarize the main features of the implementation.

7.3.1 Using the LMTO Basis Set

In the implementation, the set of correlated orbitals $\{|\mathbf{R}, \xi\rangle\}$ is defined independently of the $\mathbf{k}$-space FP-LMTO basis set $\{|\mathbf{k}, \chi\rangle\}$. It is not possible to use the set $\{|\mathbf{R}, \xi\rangle\}$ as the basis set for the entire LDA/GGA+DMFT calculation, as it is far from being complete. As H_{eff} in (7.9) is defined for the FP-LMTO basis set, it is necessary to use both sets of functions in an LDA/GGA+DMFT calculation. As the basis set $\{|\mathbf{k}, \chi\rangle\}$ is neither orthogonal, nor normalized, one should be very careful, as the rules of the linear algebra are quite different from the case of an orthonormal basis set. With the overlap matrix $S_{\chi_1, \chi_2} = \langle \chi_1 | \chi_2 \rangle$, the conjugate basis set $\{|\tilde{\chi}\rangle\}$ is defined by the relations

$$\langle \tilde{\chi}_1 | \chi_2 \rangle = \langle \chi_1 | \tilde{\chi}_2 \rangle = \delta_{\chi_1, \chi_2}, \quad \sum_{\chi} |\tilde{\chi}\rangle\langle \chi| = \hat{1}, \tag{7.18}$$

or, explicitly,

$$\left|\tilde{\chi}_1\right\rangle = \left(S^{-1}\right)_{\chi_2, \chi_1} \left|\tilde{\chi}_2\right\rangle, \quad \left\langle\tilde{\chi}_1\right| = \left(S^{-1}\right)_{\chi_1, \chi_2} \left\langle\tilde{\chi}_2\right|. \tag{7.19}$$

With the definition of the matrix elements of an operator

$$A_{\chi_1, \chi_2} = \langle \chi_1 | \hat{A} | \chi_2 \rangle, \quad \hat{A} = \sum_{\chi_1, \chi_2} |\tilde{\chi}_1\rangle A_{\chi_1, \chi_2} \langle \tilde{\chi}_2|, \tag{7.20}$$

we obtain the following rules of linear algebra (operator to matrix correspondence):

$$\hat{A} \rightarrow A \qquad \text{operator,} \tag{7.21}$$
$$\hat{1} \rightarrow S \qquad \text{unity operator,} \tag{7.22}$$
$$\hat{A}\hat{B} \rightarrow AS^{-1}B \qquad \text{product of two operators,} \tag{7.23}$$
$$\hat{A}^{-1} \rightarrow SA^{-1}S \qquad \text{inverse of an operator.} \tag{7.24}$$

Here we have put a hat above operators to distinguish them from matrices.

To transform physical quantities back and forth between sets $\{|\mathbf{k}, \chi\rangle\}$ and $\{|\mathbf{R}, \xi\rangle\}$, we assume the completeness of the basis set $\{|\mathbf{k}, \chi\rangle\}$ in the subspace spanned by $\{|\mathbf{R}, \xi\rangle\}$. The local GF (7.8) becomes

$$G_{\xi_1, \xi_2}(z) = \sum_{\mathbf{k}, \chi_1, \chi_2} \langle \xi_1 | \chi_1 \rangle \left[S(\mathbf{k})(z + \mu) - H_{\text{eff}}(\mathbf{k}) - \Sigma(\mathbf{k}, z) \right]^{-1}_{\chi_1, \chi_2} \langle \chi_2 | \xi_2 \rangle, \tag{7.25}$$

where

$$\Sigma_{\chi_1, \chi_2}(\mathbf{k}, z) = \sum_{\xi_1, \xi_2} \langle \mathbf{k}, \chi_1 | \xi_1 \rangle \Sigma_{\xi_1, \xi_2}(z) \langle \xi_2 | \mathbf{k}, \chi_2 \rangle \tag{7.26}$$

is the self-energy in the FP-LMTO basis set.

7.3.2 Correlated Orbitals

At present, the RSPt+DMFT implementation has two choices for correlated orbitals. The first, more traditional, one uses orthogonalized d or f type RSPt basis functions transformed to the real space. We call it orthogonalized LMTO (ORT) correlated subspace. It is poorly localized, and the orbitals $|\mathbf{R}, \xi\rangle$ do not have pure lm character due to both tail cancellation and orthogonalization. This approach requires using only one kinetic energy tail (minimal basis set) for correlated electrons in the LDA/GGA part of the calculation, although sp electrons can still use two or more tails.

The second choice is somewhat opposite, since it involves well-localized correlated orbitals. We call it muffin-tin-only (MT) correlated subspace. $|\mathbf{R}, \xi\rangle$ is chosen as

$$
\Psi_{\mathbf{R},\xi}(\mathbf{r}) = \begin{cases} \Phi_l(|\mathbf{r} - \mathbf{R}_\xi|)Y_{\mathrm{lm}}(\widehat{\mathbf{r} - \mathbf{R}_\xi}), & |\mathbf{r} - \mathbf{R}_\xi| < R_{\mathrm{MT},\xi} \\ 0, & |\mathbf{r} - \mathbf{R}_\xi| > R_{\mathrm{MT},\xi} \end{cases} , \qquad (7.27)
$$

$\mathbf{R}_\xi \equiv \mathbf{R} + \tau_\xi$ is the site where the orbital $|\mathbf{R}, \xi\rangle$ is located and $R_{\mathrm{MT},\xi}$ is the muffin-tin radius for this site. The LMTO radial function $\Phi_l(r)$ is the solution of the radial Schrödinger equation in the spherically averaged Kohn–Sham potential, for a certain energy E_ν (before the linearization). This function is zero outside a given muffin tin, thus it is well localized, and the orbitals from different sites do not overlap. The orbitals now have pure lm character, and it is possible to use two or more tails for correlated electrons. Other choices of the correlated orbitals are possible, e.g., hybrid orbitals or a linear combinations of Wannier functions.

7.3.3 Other Technical Details

When implementing the DMFT formalism in a computer code, one uses many technical tricks to make the code robust and efficient [72, 73, 106, 237]. Here is the list of some:

- Only the Matsubara frequencies above the real axis are used, because $G(-i\omega_n)$ is just the complex conjugate of $G(i\omega_n)$.
- Since the calculation of the local GF (7.25) involves inverting a matrix in the RSPt basis set for each Matsubara frequency and each $\mathbf{k}$-point (a rather time-consuming procedure), a smaller linear-logarithmic Matsubara mesh is used. However, solvers use the normal (linear) Matsubara mesh, so G and Σ are transformed back and forth between the two meshes using cubic splines.
- The sum in (7.15) converges very slowly; therefore, a rather elaborate scheme for calculating the number of electrons is used in practice [73].
- When calculating the DOS and the spectral density, the GF is calculated at the $z = \epsilon + i\lambda$ contour, where λ is a small constant value ($\approx 10^{-3}$ Ry). $\Sigma(z)$ is evaluated at this contour using Pade analytical continuation algorithm.

This does not work with the QMC solver, where a different approach (MAXENT) is used for calculating the DOS.

- The **k**-sum in (7.25) involves integration over the entire Brillouin zone. In practice, this involves the weighted sum over **k**-points in the irreducible wedge of the Brillouin zone plus the sum over all symmetry group operations, which are applied to each of the $(2l + 1) \times (2l + 1)$ blocks of $\langle \xi_1 | G | \xi_2 \rangle$.

7.4 Examples

7.4.1 Body-Centered Cubic Iron

The LDA/GGA+DMFT self-energy and spectral function of bcc iron are presented in Figs. 7.1 and 7.2. For this calculation the SPTF solver was used,
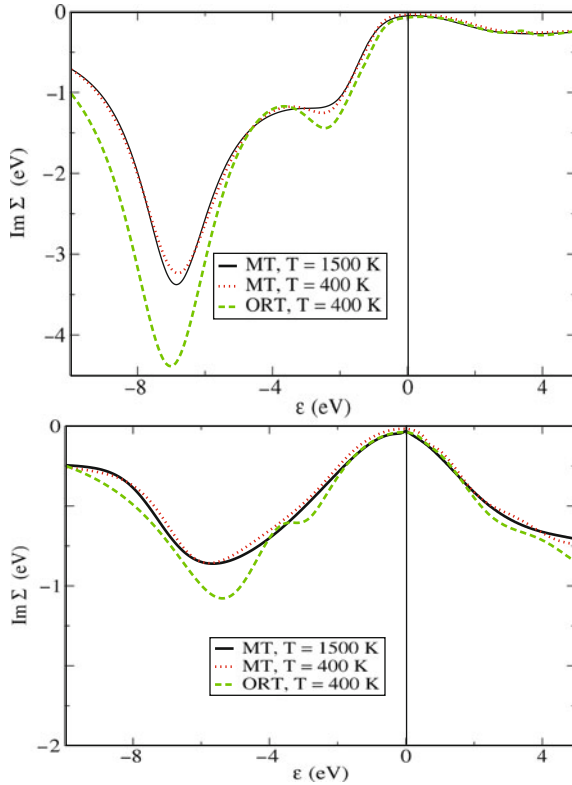
Fig. 7.1. Imaginary part of the self-energy Im $\Sigma(\epsilon + i0)$ for bcc iron, majority spin (*top*), and minority spin (*bottom*) for orthogonalized LMTO (ORT) and muffin-tin-only (MT) correlated subspaces (from [106])
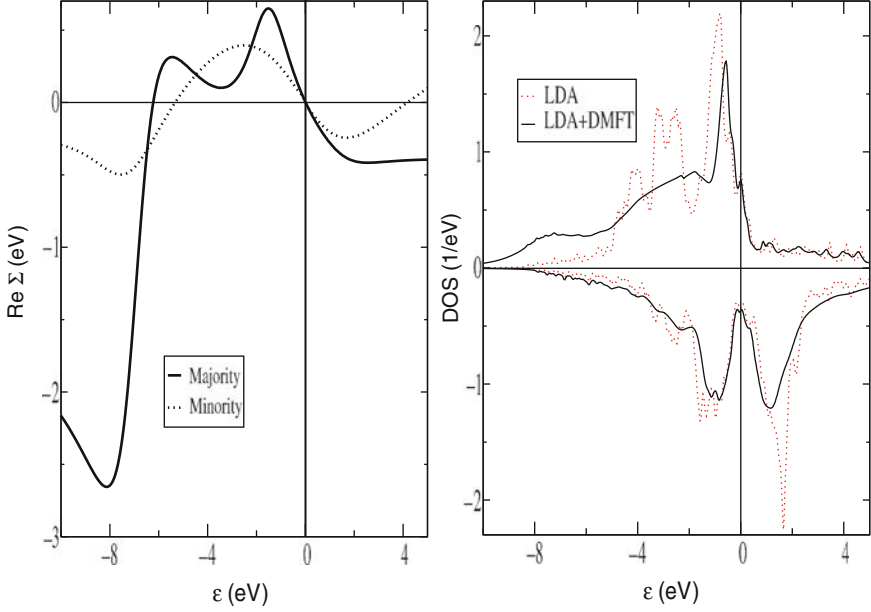
Fig. 7.2. Real part of the self-energy Re $\Sigma(\epsilon + i0)$ (*left*) and density of states (*right*) for bcc iron (from [106]). Data from LDA are given as *red dotted lines* and DMFT data are given as *solid lines*

with $U = 2.3\,\text{eV}$ and $J = 0.9\,\text{eV}$. In Fig. 7.1 we show the imaginary part of the self-energy Im $\Sigma(\epsilon + i0)$ for majority and minority spins. The three curves in Fig. 7.1 are calculations with different selections of correlated orbitals and different temperatures. It may be noted that they are qualitatively similar, proving that both MT- and ORT-correlated orbitals can be used to describe iron within LDA/GGA+DMFT, although we consider the MT set the better of the two. The exact amplitude of the peaks in Σ depends on the choice of the correlated orbitals, which illustrates the importance of selecting correlated orbitals wisely. A slight change in the values of U and J can often compensate for a specific choice of correlated orbitals. Notice also that Σ is basically temperature independent in a wide range of temperatures. In Fig. 7.2 (left panel) we show the real part of Σ (only for the MT orbitals). Figure 7.2 (right panel) shows the total density of states of bcc Fe (LDA/GGA+DMFT vs LDA/GGA), while the spectral density is presented in Fig. 7.3 for high-symmetry directions.

The majority spin Im $\Sigma(\epsilon + i0)$ in Fig. 7.1 has the major peak at $\epsilon \simeq -7\,\text{eV}$, of amplitude $-3.4\,\text{eV}$. This gives rather strong damping of quasiparticles and a broadening of the spectral features, as we can observe in Fig. 7.3. However, Im $\Sigma(\epsilon + i0) = 0$ at $\epsilon = \mu$; therefore, the quasiparticles are well defined close to the Fermi level. There is also a shoulder-like feature at $\epsilon \simeq -2\,\text{eV}$. The correlation effects are more pronounced for the majority spin electrons, which
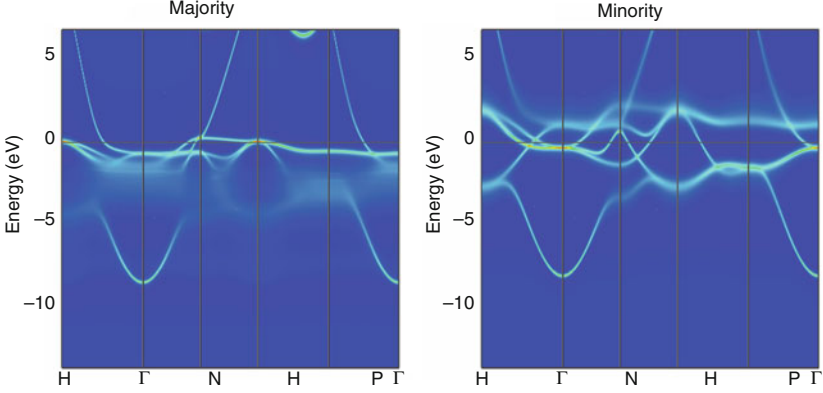
Fig. 7.3. Spectral density for bcc iron (from [106])

is a well-known fact for Fe and Co (as the minority spin d band has more empty states than the majority spin band).

The LDA/GGA+DMFT density of states (Fig. 7.2, right panel) shows the narrowing of the majority- spin d-band compared to the LDA DOS and also a satellite at $\epsilon \simeq -7$ eV. This is the effect of $\mathrm{Re}\,\Sigma(\epsilon + \mathrm{i}0)$. The positive region of $\mathrm{Re}\,\Sigma$ for the majority spin electrons between -6 eV and the Fermi level in Fig. 7.2 (left panel) leads to the narrowing of the band, while the sharp negative peak at -8 eV "draws" the electrons down in energy, creating the DOS satellite. The photoemission satellite (at -6 eV in the experiment) is an experimentally observed noncoherent spectral feature in Fe (also in Co and particularly fcc Ni), which is a correlation effect not reproduced by LDA/GGA. The smearing of the quasiparticle bands, given by $\mathrm{Im}\,\Sigma$, is a common many-body effect for d and f metals, which is absent in standard LDA/GGA calculations of the DOS.

7.4.2 Systems Close to Localization, the Hubbard-I Approximation

For materials where the Coulomb interaction within a given electronic shell dominates all other interactions, it has been shown that the Hubbard-I approximation is very efficient and appropriate [152, 157, 232, 237]. Examples of such materials are the rare-earth elements and compounds with rare-earths. In this approximation one starts with an atomic model, which describes correlated (e.g., f) states of a single ion at a given site R:

$$H_R^{\mathrm{at}} = \frac{1}{2} \sum_{m_j} U_{m_1 m_2 m_3 m_4}^R c_{R,m_1}^\dagger c_{R,m_2}^\dagger c_{R,m_3} c_{R,m_4} + \xi \sum_i \mathbf{l}_i \cdot \mathbf{s}_i - \mu \sum_m c_{R,m}^\dagger c_{R,m}\,. \tag{7.28}$$

The index m_j labels the correlated spin orbitals (for an f-system this means the index runs from 1 to 14), and $c_m^\dagger$ and c_m are the corresponding creation

and annihilation operators; see also (7.2). Note that in (7.28) we use for the correlated orbitals, ξ_i, spherical harmonics functions, labeled m_i. In the Hubbard-I approximation, the spin–orbit coupling is included in the second term of (7.28) where ξ is the spin–orbit constant, and $\mathbf{l}$ and $\mathbf{s}$ are the orbital and spin angular momentum operators. The last term in (7.28) contains the chemical potential, μ.

The Hamiltonian in (7.28) is diagonalized in the complete space of all Slater determinants of a given f^n configuration. In addition to the f^n configurations found in the (mixed) ground states also their neighboring $f^{n\pm1}$ configurations must be included in the calculation to account for possible excitations. From the eigenvalues, E_μ (E_ν), and eigenvectors, $|\mu\rangle$ ($|\nu\rangle$), one can then construct a local one-particle Green's function

$$G^{\mathrm{at}}_{mm'}(\omega) = \frac{1}{Z} \sum_{\mu\nu} \frac{\langle\mu|c_m|\nu\rangle\langle\nu|c^\dagger_{m'}|\mu\rangle}{\omega + E_\mu - E_\nu} \left(\mathrm{e}^{-\beta E_\mu} + \mathrm{e}^{-\beta E_\nu}\right), \qquad (7.29)$$

where $\beta = \frac{1}{K_{\mathrm{B}}T}$ and Z the partition function. An atomic self-energy can now be calculated from

$$\Sigma^{\mathrm{at}}(\omega) = (G^{\mathrm{at}}_0)^{-1}(\omega) - (G^{\mathrm{at}})^{-1}(\omega), \qquad (7.30)$$
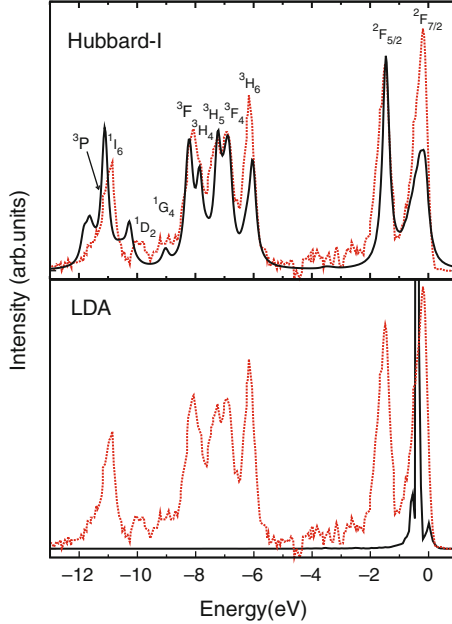
Fig. 7.4. Spectral density for YbInCu$_4$ (from [237]). In the *lower panel* the experimental spectrum (*dots*) is compared to an LDA calculation (*full line*) and in the *upper panel* to a DMFT Hubbard-I calculation (*full line*)

where $G_0^{\mathrm{at}}(\omega) = [(\omega - \mu) - H_{\mathrm{eff}}]^{-1}$. The Hubbard I approximation states that the atomic self-energy $\Sigma^{\mathrm{at}}(\omega)$ for a set of strongly correlated orbitals is approximately the local self-energy $\Sigma_{\mathrm{R}}(\omega)$ of the corresponding single impurity problem used in the DMFT scheme.

In Fig. 7.4 we show the calculated spectral properties using RSPt+DMFT in the Hubbard-I approximation, for a well-known mixed valence compound YbInCu$_4$. Note that we show in the figure experimental data from [59] and we compare these data to a regular LDA calculation (bottom panel) and a Hubbard-I calculation (top panel). As it is clear from the figure the LDA calculation fails completely in reproducing the observed spectral properties, whereas the Hubbard-I calculation essentially reproduces all observed features. Some of the peaks of the Hubbard-I calculation are positioned at binding energies slightly off-set from the observations. Also, the intensity of some peaks are not perfectly given from the theory, but the overall features of the spectral properties are reproduced. A full account of this study can be found in [237].

8

Implementation

Abstract Details of the implementation of the FP-LMTO method are presented in this chapter. This includes programming language, routines for numerical operations like diagonalization and fast Fourier transforms, and parallelization aspects.

Over the years RSPt has grown and more and more features have been added by different developers. The unspoken agreement between what used to be the small number of developers was to keep the code small and fast sometimes at the cost of ease of readability and developer friendliness. The coding style and preferences of the developers differed and a large number of different versions with different features implemented existed. All these changed with a wish to make RSPt a public Open Source project. The source code was moved into an SVN repository and most of the codes have been documented. There is work in progress to remove the pre-Fortran90 ad hoc dynamical memory allocation using Cray pointers. Any developer wishing to contribute to the project can apply for access to the software repository through the Forum at the project homepage http://www.rspt.net.

RSPt is still a comparably small code. The main trunk in the repository is less than 80,000 lines of code. This is partly due to the extensive use of built-in or library-provided functionality and reuse of code. For example, the two most time-consuming parts of the ground state calculation, the Fourier transforms used when constructing the basis set, and the diagonalization of the Hamiltonian where the program can spend up 90% of the execution time are performed using highly optimized external numerical libraries.

8.1 Fortran-C Interface

RSPt is written in both Fortran and C and this mixture places some constraints on the code. The top function, "main," is written in C, most of the different features in Fortran, and the core functions used to construct the basis

set are written in C so there are Fortran subroutines calling C functions and the other way around. The perhaps most obvious difference between the two languages is the naming conventions. Most, but not all, Fortran compilers add an underscore to the subroutine names and they are case insensitive whereas most, with very few exceptions, C compilers are case sensitive and do not add any character to the name. In RSPt an explicit underscore has been added to the names of the functions in the C part of the code that is called by Fortran subroutines and to the calls from C to Fortran. In the source code comments have been left describing how to implement two other methods that can be used to handle the different naming conventions, namely precompiler macros and dynamical naming through functions. Neither method is fully portable and is therefore not used.

The difference in call-by-name and call-by-reference between Fortran and C is handled by using pointers in C functions.[1] No strings are passed between Fortran subroutines and C functions to avoid portability problems with the termination of strings. The lack of a complex type in C is addressed in two different ways. In most places a struct made out of two floats is used as a complex type but in the C code connected to the Fourier transforms the real and imaginary components of each number are put after each other in an array of length $2N$. The memory layout of the two methods are in most cases the same but to avoid portability issues the two methods are never mixed.

Most of the older COMMON blocks have been transformed into modules but some remain, especially the block containing the MPI-related variables, see below. The different blocks are imported into the relevant C functions as external structs in the header file mpicom.h.

Finally, as the program is linked using the C compiler, unless an explicit link step is used, the necessary Fortran libraries must be added to the list of libraries to be linked in the file RSPTmake.inc. Exactly which libraries that are needed depends on the choice of compiler. Some examples can be found in the directory RSPTmakes in the source code distribution.

8.2 Diagonalization

There are four different methods available in RSPt for diagonalizing the Hamiltonian matrix. The performance of the different methods depends on the hardware, choice of performance library, and the size of the matrix. Three of the methods use LAPACK so it is very important to use an efficient implementation of the performance library to reach the highest possible performance. All four methods start by transforming the matrix into a bi- or tridiagonal form, in some cases with an initial LU transformation and depending on the

---

[1] Users of classical AT&T UNIX (e.g., older Sun OS and different flavors of BSD) might have to add the length of the arrays pointed to as additional arguments in the function definitions in the C part of the code calling or called by Fortran.

details of the setup the diagonalization can end with a back-transform to the original form.

The default method used in the automatic setup by the program symt, diag=1, is the LAPACK subroutine *zhpevx* where a selected subset of the eigenvalues and eigenvectors is calculated using a QR or QL algorithm. A parallel case is diag=3 where *zhpevr* is used instead and all eigenvalues and vectors are calculated.

An alternative is diag=2 which uses the LAPACK subroutine *zheevr*. This subroutine uses a different method, dpds, whose efficiency strongly depends on the hardware and the exact implementation of the algorithm. It is well worth to test the method for different matrix sizes.

The fourth method, diag=0, is internal and is also based on the QL and QR algorithms. This method can be used when there is no good performance library available. The diagonalizer returns the eigenvalues and vectors unsorted and for very large matrix sizes the sorting can take a substantial time.

It is hard to give a definite recommendation on which method to use. The optimal choice depends on the problem size and the efficiency of the performance library but in general diag=0 is the fastest for smaller sizes and diag=1 for larger matrix sizes. The critical size depends on the hardware and the performance library and should be tested. The performance of diag=2 can vary a lot but on some computers it can be much faster than the other methods. The different methods can give a very small difference in the eigenvalue spectrum for a single iteration but they all converge to the same result within the numerical precision of the computer.

8.3 Fast Fourier Transforms

Fourier transforms are used in several different places in the code for different purposes. In the ground state calculation all transforms are done using the FFTW-3 library (http://www.fftw.org/) through a driver function called fftc_.[2] Each transform is given a unique identifier so that the calling function can be identified by the driver function. FFTW creates a plan for each transform size and direction which is used to optimize the algorithm. Because of the unique identifier the plans for each transform can be preserved and stored saving the time needed to recalculate the plan.

Formally any mesh size can be used but empirical tests have shown that some sizes are much more efficient on some hardware, depending, e.g., on the number of registers in the CPU and cache size. Generally, the smaller factors the mesh size can be divided into, the higher the performance will be, but for non-uniform meshes the relation is complex and highly hardware dependent.

The Fourier transforms in the DMFT part of the program are performed in a different way. Taking advantage of the properties of Green's function

---

[2] The underscore is added to the C function name to match the Fortran naming convention.

the transform can be expressed in a closed form. First, the cubic spline of the function is calculated using the value of the function and its higher moments at a number of spline points. The transform integral can then be solved analytically.

8.4 Parallelization

Even though RSPt is relatively fast it is often desirable to shorten the wall clock time needed to finish a calculation. The sequential code is highly optimized, especially if high-performance versions of FFTW and LAPACK are used. The use of multiple processors will often shorten the wall clock time but always at the cost of the total CPU time. There is always a communication overhead and almost always some parts of the code that cannot be parallelized and therefore will add to the total execution time without adding anything of value when run on more than one processor. As long as there are more unrelated calculations to be done, e.g., different volumes, than there are processors available it is always best to run different sequential calculations. Parallel calculations should only be run when there are more processors available than tasks.

There are three different independent ways to run RSPt in parallel mode. They can be used independently or in any combination. The most basic mode is parallelization over **k**-points. It is done using MPI and is invoked with the precompiler option -DMPI. This mode is very efficient with a small communication overhead. The **k**-points are divided into contiguous blocks and all summations are performed in such a way that the behavior mimics that of the corresponding sequential summation.[3] To get the highest possible efficiency the number of **k**-points in each block should be the same. Some of the communication is blocking so the processes have to wait for the last process to finish its task before they can continue so if just one or a few processors have one extra **k**-point to calculate the rest of the processors will be idle while that **k**-point is calculated. No extra input is needed and this mode has been shown to scale fairly well to over 1,024 processors.

The next mode is over bands. It is also done using MPI but the communication overhead is higher than for parallelization over **k**-points. In this mode it is actually the construction of the matrix elements that is performed in parallel; the diagonalization of the Hamiltonian matrix is still performed sequentially.

The band-parallel mode is invoked with the combination of the precompiler options -DMPI and -DUSE_CARTESIAN_TOPOLOGY. The two-dimensional Cartesian grid size is read from the file CARTESIAN_TOPOLOGY containing two numbers in free format. The first number is the number of grid

---

[3] Summations are non-commuting on binary computers, i.e., the result depends on the order in which the terms are summed.

points in the **k**-point direction and the second the number of grid points in the band direction. The product of the two numbers must be equal to the number of processors used. For a pure parallelization over bands set the first number to 1.

This mode is of most use when calculating large supercells with fewer **k**-points than processors. The program scales well up to about six processors per **k**-point depending on the size of the Hamiltonian matrix. It is always best to spend the available processors on **k**-points rather than bands.

The third mode is parallel over the Fourier transform grid and is invoked by the precompiler option -DHAVE_FFTW3_THREADS and can be used with any of the two other modes or by itself. This mode uses threads and can therefore not be used between different hosts. The number of threads is set in the file FFTW_MAX_THREADS. FFTW can choose to use fewer threads depending on the size of the transform. The communication overhead is small but the different threads operate on the same array which may cause memory congestion if the memory bandwidth is too low. The scaling again depends on the size of the transform and the hardware but good scaling can be expected for up to four processors for smaller sizes and up to eight processors for larger sizes. FFTW must be compiled with – enable-threads and RSPt must be linked with the two libraries libfftw_threads.a and libfftw.a in that order for this mode to work.

9

Obtaining RSPt from the Web

Abstract In this short chapter details of how to obtain the FP-LMTO code from the web site http://www.rspt.net are given. In addition, a short instruction on how to install the FP-LMTO code is presented.

The source code and manual for RSPt and a few auxiliary programs are freely available at the project homepage http://www.rspt.net. Only registered users can upload or download code but it is free to register. The registration process is protected by a bot filter in the form of a security question that should be easily answered by regular users. When registering a username a valid e-mail address must be supplied. Note that Gmail addresses cannot be used. When an application has been approved a temporary password is sent to the registered e-mail address. The process of reviewing and approving applications is for security reasons manual so there can be a delay of a few days at the worst, especially during holidays.

At the homepage there is also a forum where registered users can post questions (and answers of course). The forum is read by most of the developers and the response time can of course vary but it is short most of the time. There is also a calendar where important events, like the annual FP-LMTO workshop, are announced and a wiki.

9.1 Installing RSPt

RSPt is fairly easy to install and the program has been ported to a lot of different platforms. Below is brief instruction on how to install RSPt. A more detailed instruction can be found in the manual that is included in source code package.

- Download the source code from http://www.rspt.net. The source code can be found in the section My Downloads which can be found in the top frame. The source code package is called rsptNNN.tar.gz where NNN is the SVN version number.

- Install FFTW3 (http://www.fftw.org) and LAPACK if not already installed on the computer. The performance of the code strongly depends on the efficiency of these to libraries so it is strongly recommended that an optimized performance library like MKL, ATLAS, ACML, or GOTOBlas is used.
- Unpack the package using *gzip* and *tar* or any other programs with the same functionality.
- In the directory rsptNNN edit the file *RSPTmake.inc* and adapt it to the local environment. RSPt uses both Fortran and C. Compilers from the GNU compiler suite from version 4.1.2 can be used although newer versions are preferred.
- Do *make* in the top directory. If there were no errors the executable *rspt* can now be found in the *bin* directory.
- The default setup is for a serial program. To compile any of the parallel versions edit *RSPTmake.inc* accordingly, rename *bin/rspt* so that it is not overwritten and change directory to *rsptDir/src*. Do *make clean; make*. More information on the different parallelization modes can be found in the manual.

9.2 Running RSPt

RSPt is very rich in features and input variables and the program can be run in many different ways. We refer to the manual where a technical summary as well as a detailed installation instruction and information regarding the different input and output files can be found.

RSPt needs a few input files but all but one can be created automatically. First, create a directory called *sym* in the directory where the input files are going to reside. In the directory *sym*, create a file called *symt.inp* where the lattice vectors, spin axis, atomic positions, and strain matrix are defined.

```
# Bravais lattice
 -0.50000000 0.50000000 0.50000000
 0.50000000 -0.50000000 0.50000000
 0.50000000 0.50000000 -0.50000000
# Spin axis
 0.00000000 0.00000000 1.00000000  a
# Number of elements
 1
# Data vectors
 0.00000000 0.00000000 0.00000000  26  l  x
# Strain matrix
 1.00000000 0.00000000 0.00000000
 0.00000000 1.00000000 0.00000000
 0.00000000 0.00000000 1.00000000
```

The file is in free format. In the case of non-orthogonal lattice vectors the vectors must be defined with high precision of the same order as the machine precision. Please note that the lattice vectors are defined in column order in this file but in row order in all other files. In the example the spin axis is given in Cartesian coordinates (a) but it can also be given in units of the Bravais lattice vectors (l). For other options, please see the manual.

The atomic positions can be given, among other options, in Cartesian coordinates or in units of the Bravais lattice vectors (a or l). The last item on the line, x in this case, is a tag that is used together with the atomic number (26 in this case) to group identical atoms together. Atoms with different atomic numbers or different tags are always considered inequivalent but atoms with the same atomic number and tag may be equivalent, depending on if the symmetry generator can find a symmetry operation linking the different atoms. This feature can be used, e.g., in anti-ferromagnetic structures to differ between spin-up and spin-down sites.

The strain matrix can be used to introduce a virtual distortion of the lattice that mimics the effect on the lattice while preserving the symmetry of the lattice. The strain matrix is very useful, e.g., when calculating elastic constants.

The rest of the input is created in the main directory by the program *symt* with the option *-all* using some educated guesses. First, the atomic density must be created by running *make* in the directory *atom*. The atomic density is used as a starting point for the main program. Next go to the directory *bz* and run *cub* to create the **k**-point mesh. Link the output file *cub.k.NN*, where NN is the number of mesh points in one direction, to the file spts in the main directory. In the same way link the file *cub.t.NN* containing the tetrahedron list to the file *tetra*.

Finally the files in the directory *dta* may have to be edited. In this directory there are different parts of what is going to be the main input file *data*. Please see the manual regarding all the different options. Especially the Fourier grid and the muffin-tin radii must be adopted to the particular systems. The latter can be found in the files *element_NN* where NN is the atomic number. When all the necessary files have been edited link the files length_scale and strain_matrix to the main directory and do *make data* in that directory.

RSPt can be run for only one iteration by running *rspt* in the main directory. RSPt can also be run to some convergence in fsq. This is done by the command *runs rspt level_of_convergence max_number_of_iterations*. Adapt the name of the binary that *runs* should use, the level of convergence, and the number of iterations *runs* should run before stopping if convergence is not reached depending on the situation.

There are more auxiliary programs that can be used for different tasks. All of them are documented in the manual with their arguments and, if necessary, input files.

Part II

Applications

10

Total Energy and Forces: Some Numerical Examples

Abstract Numerical examples of calculations of total energy, equation of state and Hellman-Feynman forces are given. The calculation of first principles phonons is also exemplified with fcc Al and bcc U. A comparison between a few selected exchange and correlation functionals is also made for the calculation of the equation of state.

In the remainder of this book we will give examples of applications of RSPt to materials science: in the field of magnetism, phase stability and elasticity, chemical bonding of solids, equation of state, lattice dynamics, structural phase transitions, bulk and surface physics, as well as electronic excitations. We begin this description with equation of state properties.

10.1 Equation of State

The behavior of materials under pressure is of both theoretical and practical interest in, e.g., geophysics where computer simulations sometimes are the only viable tool. Methods based on pseudo-potentials can have insurmountable difficulties in these kinds of calculations as the pseudo-potentials used most often lack the flexibility to give a good solution to the electronic structure calculation over a wide span of different pressures. All-electron methods do not have this limitation. If the basis set is flexible enough an accurate solution can be found for several orders of magnitude in compression.

As an example the calculated pressure as a function of compression is shown in Fig. 10.1. In this example aluminum has been compressed by more than two orders of magnitude. Here the equation of state is calculated using RSPt, and it is compared with the Thomas–Fermi equation of state. The latter is known to be exact in the limit of free electrons at high pressure where electron correlation is negligible [194]. Thomas–Fermi theory in its crudest form neglects shell effects and quantum-mechanical effects and therefore the total energy for the more exact RSPt method is lower over a wide interval of compressions but as the compression increases the RSPt equation of state
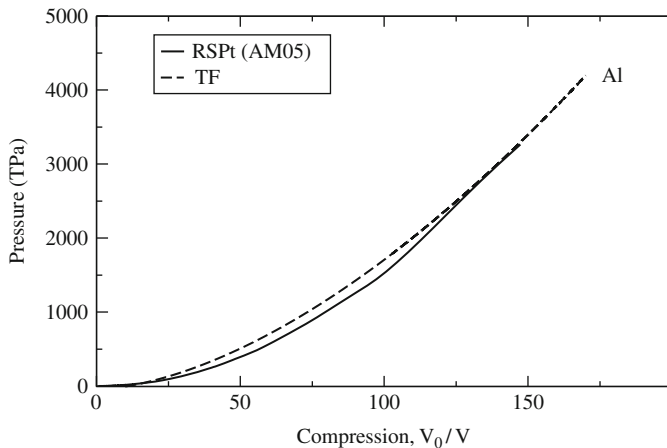
Fig. 10.1. Pressure as a function of compression in aluminum. The result from RSPt (*full line*) is in good agreement with the Thomas–Fermi result (*TF-dashed line*) at high pressure

approaches the Tomas–Fermi result as can be expected. Because RSPt is an all-electron method the effect of the deeper shells becoming band-like state can be seen in the plot as wiggles in the line.

At these extreme pressures the kinetic energy dominates the total energy, as can be seen in Table 10.1 where different contributions to the total energy are shown, and it is therefore essential to use an exchange-correlation functional with a correct asymptotic behavior at ultrahigh pressure which treats the kinetic contribution to the XC energy. This contribution is usually rather small and is often neglected. Of the different functionals implemented in RSPt, AM05 [20] is shown to give the best results at ultrahigh pressure (this functional is analyzed further in the chapter on chemical bonding). Other functionals yield an unwanted softening at high pressure. An example can be seen in Fig. 10.2.

Table 10.1. Different contributions to the energy of fcc Al at two pressures. All energies are in Ry. ΔE is the difference in energy between the highest and lowest occupied valence states. Some contributions to the total energy have been left out in the table

	Low pressure (1 bar)	High pressure (42 Gbar)
Volume	$16.95\,\text{Å}^3$	$0.099\,\text{Å}^3$
Total energy	-484.027	-298.522
Kinetic energy	168.027	550.509
XC energy	-35.582	-61.555
Eigenvalue sum	-37.193	346.116
ΔE	7.496	51.435
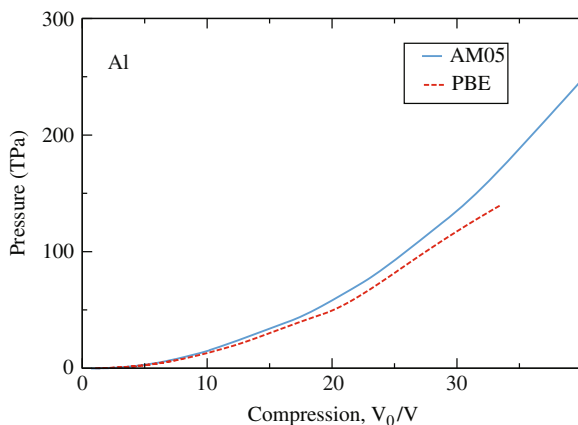
Fig. 10.2. A comparison between two different XC functionals, AM05 [20] and PBE [179], for the equation of state of Al, as implemented in RSPt. Notice the softening of the equation of state for PBE functional

To reach such ultrahigh compressions there are a few things that must be handled with care. First, the basis set must be sufficiently flexible. At low pressure the valence electrons have a finite dispersion and exhibit band-like behavior. All other electrons are atomic like without dispersion and can be handled as core states. When the pressure is increased, in Fig. 10.3 the DOS is shown as an example at the extremely high value of 42 Gbar, the valence bands will become wider, and the core states will gradually have a finite dispersion and must be treated as Bloch states which may hybridize with all other states. This usually means that a second energy set must be used, as discussed in Chap. 6, introducing the so-called pseudo-core states. In Fig. 10.3 one set of ε_ν has been used for the 2s and 2p states, and a separate set of ε_νs has been used for the 3s, 3p, and 3d valence states. At ambient pressure the 2s and 2p states have essentially no hybridization with any other state. However, as the figure shows at high pressures the 2s and 2p states are far from being core states, since they have substantial width and hybridize with each other and all other states. Hence, at these pressures the 2s and 2p states are in all respects to be viewed as valence states, since they have finite dispersion and hybridization. However, sometimes a nomenclature is used to refer to these states as pseudo-core, to indicate that they come from states which normally (at ambient conditions) are treated as core electrons.

The effect of the inclusion of a second energy set on the total energy and equilibrium volume of palladium can be seen in Fig. 10.4. The results from the calculation with a pseudo-core, i.e., two energy sets, are obtained with both the 4s and 4p states in the pseudo-core, and with the 5s, 5p, and 4d states as valence states. This configuration is compared in the figure to a calculation with only one energy set, which has the 4s and 4p states in the core and only the 5s, 5p, and 4d as valence states. As is obvious from Fig. 10.4 there
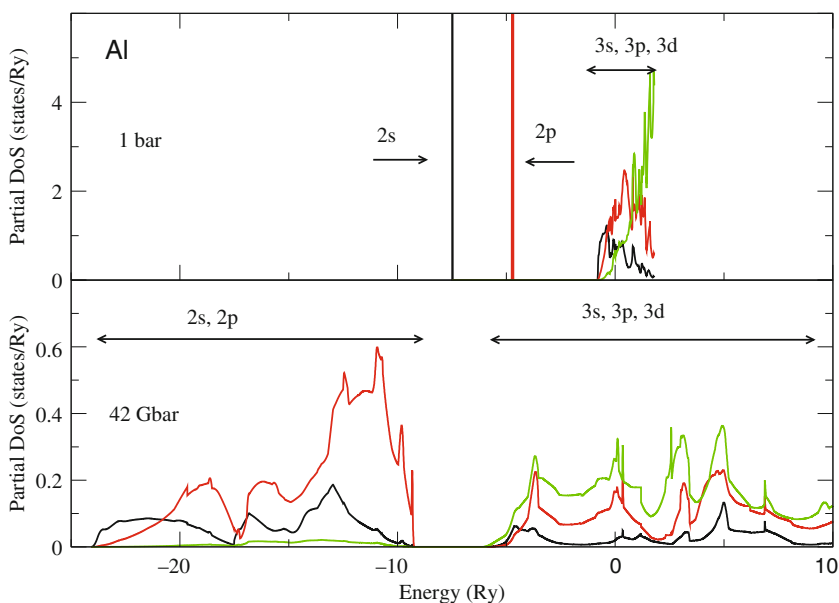
Fig. 10.3. The partial density of states of aluminum at 1 bar (*upper*) 42 Gbar (*lower*). The Fermi level is at 0 Ry. The core states 2s and 2p are indicated by *vertical lines* in the *upper graph*. Note that in the upper panel the energy range for the DOS calculation does not exceed 2 Ryd. At higher pressure the bands become wider and the 2s and 2p states now have band character with a substantial bandwidth
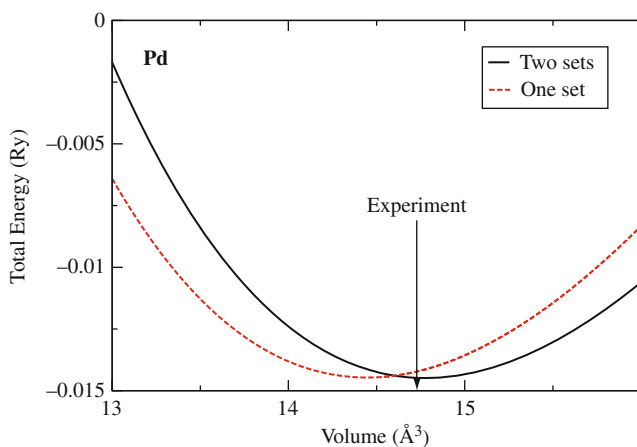
Fig. 10.4. Total energy as a function of volume for palladium for two different basis sets (*see text*). The *vertical line* is the experimental volume. The absolute energies are not directly comparable and has been shifted to coincide at the respective minima

is a marked difference between the two calculations. In addition, even though the 4s states are almost 6 Ry below the Fermi energy they contribute to the hybridization and influence the result. As a matter of fact, the omission of the 4s states from the pseudo-core makes a difference to the calculated equilibrium volume (data not shown).

To reach very small volumes in an equation of states calculation, a variable-sized muffin-tin radius that scales with the length scale should be used, as opposed to a fixed-sized radius, which is fixed for the lowest volume of the calculation. In this way, the best possible basis set for all volumes is obtained in RSPt. However, since currently spin–orbit interaction is only implemented in the muffin-tin region and not in the interstitial region, this procedure is somewhat troublesome for relativistic calculations. The strength of the spin–orbit interaction decreases rapidly away from the nucleus of the atom, meaning that the electron movement is really fast only close to the nucleus. Despite this fact, the total energy will, for relativistic calculations, depend to some degree on the choice of muffin-tin radius. The dependence of energy on muffin-tin radius was also analyzed for different basis sets, in Chap. 6, where specific choices were shown to essentially remove this energy dependence. However, for materials where the spin–orbit effect is important, typically for the actinides, the dependence of total energy with respect to muffin-tin radius cannot be avoided. Hence when comparing the energies of different crystal structures, or for the calculation of elastic constants or different magnetic configurations, it is vital that the same muffin-tin radius is used, for each considered volume of the calculation. If this is done, reliable results can be obtained.

For equation of state calculations, it has been shown [172] that the best way to handle this problem is to keep the muffin-tin radius fixed for all volumes. The muffin-tin radius must be chosen to be big enough to fit all core states (without their leaking into the interstitial) and still be small enough to fit in the smallest volume considered in the calculation.

10.1.1 Convergence

There are two different parts to the problem of convergence: to get an accurate solution and to get the correct solution. Neither of the two parts implies the other; there can be extremely accurate but wrong solutions and correct solutions of low accuracy. It is fairly easy to check the accuracy of the calculation by looking at the output parameter "fsq," which was defined in Sect. 4.6. There is no simple relation between "fsq" and the convergence in total energy but an fsq value of 10^{-10}–10^{-12} usually corresponds to a convergence in total energy of the order of parts of mRy or better, depending on the complexity of the problem.

This is usually good enough for a simple equation of state calculation or to calculate a good density of state but a stronger convergence is needed to calculate, e.g., the magnetic anisotropic energy or very accurate forces. Then

an fsq of 10^{-14}–10^{-18} can be necessary. To reach such a high convergence and get a correct solution several things must be handled correctly:

The Basis Set: With a basis set that is too small it is impossible to get an accurate and correct solution. If states that in reality have a finite dispersion are put in the core the solution will be unsatisfactory as shown in Fig. 10.4. If the dispersion of a state is high, e.g., at small volumes, a single basis function might not be flexible enough to describe the state over a wide energy range. Usually two or three basis functions with the same quantum numbers but with different tails are used.

Sampling Reciprocal Space: A simple Fermi surface can often be described with a smaller number of **k**-points, but the **k**-point density needed increases with increased complexity of the Fermi surface. The total number of **k**-points needed also depends on the size of the reciprocal space which increases with decreasing volume. It is hard to give any exact number so the convergence in **k**-points should always be tested. If a smearing-based integration method is used (Gaussian or Fermi–Dirac) the convergence in smearing width should also be tested. A small smearing demands more **k**-points but a smearing that is too large will wipe out possibly important features on the Fermi surface.

Fourier Grid: The Fourier grid is used for two things. First, it defines the cut-off for the basis set expansion in the interstitial. There is an analytical test for the convergence of the expansion and the result is presented in the output file as Fourier transform parameters. For all radii it should be 6 or higher. The Fourier grid is also used to define the shape of the muffin tin (really the transform of the muffin-tin shape) and therefore also the matching between the basis functions in the muffin tins and the interstitial. The charge density at the muffin-tin radius for the first few harmonics should match from the inside and the outside. Again the exact details depend on the type of calculation and the convergence necessary but the first few harmonics should match to within one part in 1,000 or better. The volume dependence on the number of Fourier grid points is complex and should be checked for all volumes.

10.2 Phonon Calculations

Phonons are harmonic collective distortions of the lattice which depend on the electronic structure, through the Hellman–Feynman forces in the material. A popular method used to calculate the response to a general perturbation, of which phonons are a special case, is the linear response method [27]. This method has the advantage compared to supercell-based methods that all phonon wave vectors and symmetries can be treated and compared to dielectric matrix approaches the convergence is much faster [26]. Unfortunately this method is not feasible with the current version of RSPt. The power and flexibility of the basis set come again at the price of complexity.

The linear order phonon spectrum depends on the difference between the unperturbed forces and the forces of the perturbed system, i.e., the response to a displacement of a perturbed system. The perturbation in this case is $w_\tau(\mathbf{R}) = w_\tau \exp(\mathbf{iq} \cdot \mathbf{R})$ and will affect not only the expansion coefficients but also the basis functions, as above. Instead indirect methods must be used to calculate the phonon spectrum. One such method is diagonalization of the so-called dynamical matrix.

In the harmonic approximation the potential energy is given by

$$U = \frac{1}{2} \sum_{\mathbf{R},\mathbf{R}'} \sum_{ij\alpha\beta} C_{i\alpha,j\beta}(\mathbf{R} - \mathbf{R}')w_{i\alpha}(\mathbf{R})w_{j\beta}(\mathbf{R}') \,. \tag{10.1}$$

Using this expression for the potential energy one can show that the force on atom i is given by

$$\mathbf{F}_{i\alpha}(\mathbf{R}) = \sum_{\mathbf{R}'} \sum_{j\beta} C_{i\alpha,j\beta}(\mathbf{R} - \mathbf{R}')w_{j\beta}(\mathbf{R}') \,. \tag{10.2}$$

The Fourier transform of (10.2) is

$$\mathbf{F}_{i\alpha}(\mathbf{q}) = -\sum_{j\beta} C_{i\alpha,j\beta}(\mathbf{q})w_{j\beta}(\mathbf{q}) \,, \tag{10.3}$$

where $C_{i\alpha,j\beta}(\boldsymbol{q})$ is the Fourier transform of $C_{i\alpha,j\beta}(\boldsymbol{R} - \boldsymbol{R}')$ and $w_{j\beta}(\boldsymbol{q})$ the transform of $w_{j\beta}(\boldsymbol{R}')$.

Equation (10.3) can be inverted for a given $\mathbf{q}$. The dynamical matrix is then given by

$$D_{i\alpha,j\beta}(\mathbf{q}) = \frac{C_{i\alpha,j\beta}(\mathbf{q})}{\sqrt{M_i M_j}} \,, \tag{10.4}$$

where M_i is the mass of the ith atom. The phonon frequencies and the normal modes are given by diagonalization of the dynamical matrix. This can be done using software like PHON (www.homepages.ucl.ac.uk/~ucfbdxa/phon/) or PHONON (wolf.ifj.edu.pl/phonon/).

For example, PHONON will give a list of displacements of one or more atoms in a supercell. The number of displacements grows with the complexity of the system. If the symmetry is lower than cubic a displacement in each unique direction is needed and if the unit cell contains more than one atom, each of the different atoms must be moved. When the resulting forces for each mode have been calculated the phonon spectrum is calculated through direct diagonalization of the dynamical matrix. The result is exact for high symmetry points in the phonon reciprocal space. The accuracy for low frequencies depends on the size of the supercell used. Usually a $3 \times 3 \times 3$ supercell will give acceptable results for a bcc or fcc unit cell with one or two atoms per unit cell but even such a small cell contains more than 100 atoms.

In this way the phonon structure can be calculated for any material that RSPt can handle. Figure 10.5 presents an example where the phonon structure
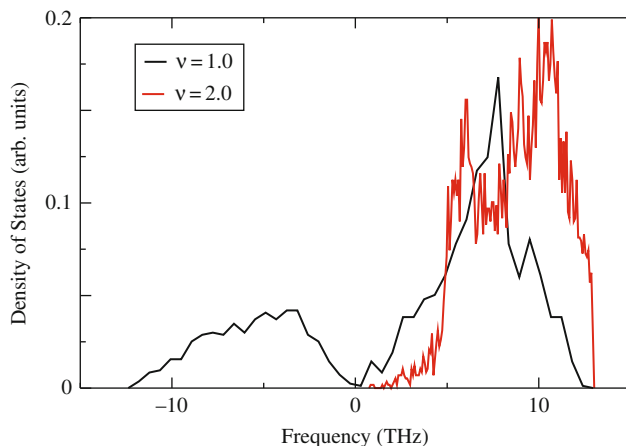
Fig. 10.5. The phonon density of states of bcc uranium at two different compressions, $\nu = 1$ corresponds to ambient pressure and $\nu = 2$ a compression where the volume is half the equilibrium volume
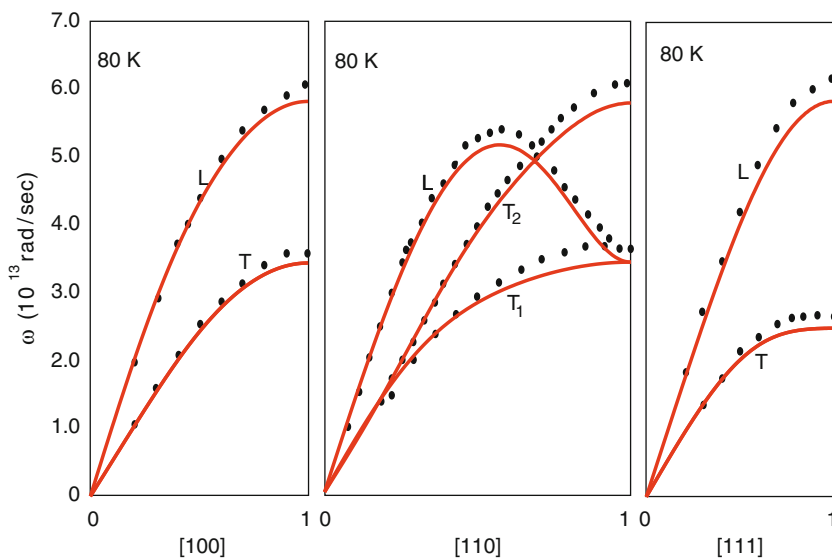
Fig. 10.6. The phonon dispersion curves of fcc aluminum along high symmetry directions. Experimental data [97] are at 80 K and shown in *black*, whereas RSPt data in *red color*. Transversal branches are marked by "T" and the longitudinal branch by "L"

of bcc uranium has been calculated. The body-centered cubic structure is not the ground state of uranium but it has been suggested that this structure will be stable at higher pressure. An unstable material will develop the so-called soft modes indicated by states with negative frequencies. The uncompressed material in the bcc structure has several soft modes but at higher compressions

the density of states is zero at negative frequencies. This implies that bcc uranium will be dynamically stable at some high pressure.

Another example of a phonon calculation is given in Fig. 10.6 where the phonon dispersion has been calculated for fcc aluminum using a $3 \times 3 \times 3$ supercell. In the figure a comparison is made with experimental data. Overall, the agreement between theory and experiment is good. The largest disagreement which can be found is that at the zone boundary the theoretical curves are somewhat too low in frequency.

11

Chemical Bonding of Solids

Abstract In this chapter an analysis of chemical binding of materials is made, introducing concepts like the crystal orbital overlap population. Numerical examples of equilibrium volume of the transition metals, lanthanides and actinides are presented. Calculated equilibrium volumes of refractory materials are compared to experimental values. The cohesive energy is defined, and calculations are compared to experiment for the lanthanides. The structural stability of sp-bonded metals, transition metals, and actinides is discussed. In addition calculations of mixed valent materials, using the Kimbal–Falicov model are described. The chapter ends with a description of calculations of elastic constants of materials. For all calculations a comment on convergence of different computational parameters is made.

First principles theory in general gives an accurate description of the chemical binding of solids. This is evidenced by the quantitative agreement between calculations and observations for several physical and chemical properties, which directly reflect the nature and strength of the chemical bonds of the solid under study. Examples of this are equilibrium volume and crystal structure, equation of state, phase stability and valency, as well as elastic constants. In general, theory reproduces these properties with an error not exceeding a few percent, which is quite remarkable. RSPt describes all these properties with high accuracy, and in general the results are similar to other full-potential, all-electron methods, such as FPLAPW.

Although theoretical calculations often reproduce observations, this alone does not guarantee that a deeper understanding of the material property under study has been gained. There are several theoretical tools available to ease interpreting a theoretical result, and one of the tools available in RSPt is the crystal orbital overlap population, COOP [117], which in RSPt is named balanced COOP, or BCOOP [105], for reasons described below. In addition, angular momentum projected occupation numbers, ionicity, and charge density are useful when analyzing a calculation. We describe below, how to use these tools in RSPt for sp-bonded materials, transition metals, f-electron systems, as well as a few intermetallic compounds.

11.1 Electron Densities

One of the more obvious ways to analyze the nature of the chemical binding of a material is to simply inspect the self-consistently calculated charge density. This is a property which on formal grounds, as described in Chapter 2, is calculated reliably. As an example of a self-consistent charge, or electron, density we show in Fig. 11.1 this property for MgB_2. This material was discovered in 2001, to be a superconductor with a rather high critical temperature, 39 K [171]. The crystal structure of this compound is hexagonal, with B planes interleaved with layers of Mg atoms. The chemical bonding in a B plane is expected to be strongly covalent and the interaction between B planes and Mg planes is primarily ionic. Hence, an inspection of the charge density in a B plane should signal covalently bonded B atoms. The density shown in Fig. 11.1, calculated with RSPt [224], shows that the electron density is located primarily in the region between B atoms, which is typical for covalent chemical bonds. In RSPt one has to specify the plane in the crystal structure where one wants to make an inspection of the charge density, as described in the manual of the program (the manual can be found at http://www.rspt.net/).
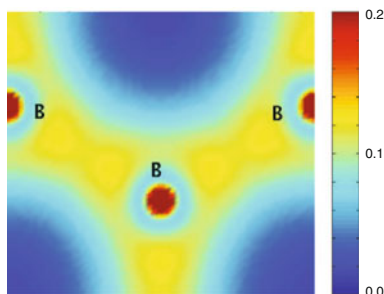
Fig. 11.1. Calculated valence charge density of MgB_2. The density is shown for a cut in a plane which contains B atoms only. The B atoms located on the *red dots*. The scale on the right-hand side gives the electron density per a.u.^{3} Picture kindly provided by P. Souvatzis

11.2 Crystal Orbital Overlap Population (COOP)

Crystal orbital overlap population (COOP) and related chemical binding indicators are used to distinguish between bonding and antibonding states in crystalline solids. The concept comes from quantum chemistry. If a molecule is described with the one-electron Kohn–Sham (or Hartree–Fock) Hamiltonian H, with the eigenspectrum $(H - \epsilon_n)|\psi_n\rangle = 0$, then the binding character of a state $|\psi_n\rangle$ is given by the orbital population (OP)

$$OP_{ij} = S_{ij}c_i^*(n)c_j(n), \tag{11.1}$$

where $S_{ij} = \langle i|j\rangle$ is the overlap matrix element between atomic orbitals $|i\rangle$ and $|j\rangle$ and $c_i(n)$ are the eigenvector's components

$$\left|\psi_n\right\rangle = \sum_i c_i(n)\left|i\right\rangle. \tag{11.2}$$

OP_{ij} tells us how does the state ψ_n contribute into the covalent bond between orbitals $\left|i\right\rangle$ and $\left|j\right\rangle$. Positive OP means ψ_n is a bonding state and negative OP means it is an antibonding state. The absolute value of the OP measures the strength of the respective contribution. The sum of all OPs (including the diagonal ones, OP_{ii}, which have no direct physical meaning) is equal to 1

$$\sum_{ij} OP_{ij} = \langle\psi_n|\psi_n\rangle = 1, \tag{11.3}$$

assuming the eigenvector is normalized. Note that, strictly speaking, the orbital population is not a physical quantity (in the sense it is not an expectation value of any hermitian operator) and it depends on the choice of the basis set $\{\left|i\right\rangle\}$. However, for reasonable choices of the basis set, the qualitative picture of the chemical binding given by OP is not much affected by this choice.

For a solid state, the crystal orbital overlap population [117] is the orbital population-weighted density of states

$$COOP_{ij}(\epsilon) = \sum_{n\mathbf{k}} \delta(\epsilon - \epsilon_{n\mathbf{k}}) c_i^*(n\mathbf{k}) c_j(n\mathbf{k}) S_{ij}(\mathbf{k}). \tag{11.4}$$

COOP is an energy-resolved quantity which is positive for bonding states (more precisely, the states that make a bonding contribution to the bond $i - j$) and negative for the antibonding ones. COOP can be defined for both real space orbitals $\left|i\mathbf{R}\right\rangle$ and the $\mathbf{k}$-space orbitals $\left|i\mathbf{k}\right\rangle = \sum_\mathbf{R} \exp(i\mathbf{k}\mathbf{R})\left|i\mathbf{R}\right\rangle$. They are connection by the expression

$$COOP_{ij}(\epsilon) = \frac{1}{N} \sum_{\mathbf{R}_1,\mathbf{R}_2} COOP_{i\mathbf{R}_1,j\mathbf{R}_2}(\epsilon) = \sum_\mathbf{R} COOP_{i\mathbf{0},j\mathbf{R}}(\epsilon), \tag{11.5}$$

where N is the number of sites in the lattice. The sum of COOP for all pairs of orbitals (including the diagonal elements) is equal to the density of states

$$\sum_{ij} COOP_{ij}(\epsilon) = DOS(\epsilon). \tag{11.6}$$

For covalent bonds (including bonds between partially filled d- and f-shells), COOP shows both bonding (positive COOP) and antibonding (negative COOP) states. For metallic bonds, COOP is positive up to the Fermi level, while for ionic bonds COOP is negative everywhere.

A related quantity is the crystal orbital Hamilton population (COHP) [77]

$$COHP_{ij}(\epsilon) = \sum_{n\mathbf{k}} \delta(\epsilon - \epsilon_{n\mathbf{k}}) c_i^*(n\mathbf{k}) c_j(n\mathbf{k}) H_{ij}(\mathbf{k}), \tag{11.7}$$

which uses the Hamiltonian matrix elements H_{ij} instead of the overlap matrix elements S_{ij}. COHP roughly has the physical meaning on the energy-resolved contribution to the binding energy of the covalent bond $i - j$

$$\int_{-\infty}^{E_{\mathrm{F}}} d\epsilon \, \mathrm{COHP}_{ij}(\epsilon) = E_{ij}^{\mathrm{bond}} \, . \tag{11.8}$$

The sign of COHP is the opposite to that of COOP (negative COHP means bonding states). The problem with COHP is that it depends on the position of the origin of the energy scale (energy zero). Namely, upon transformation $\epsilon \to \epsilon + \triangle\epsilon$, the Hamiltonian transforms as $H_{ij} \to H_{ij} + \triangle\epsilon S_{ij}$, and therefore

$$\mathrm{COHP}_{ij}(\epsilon) \to \mathrm{COHP}_{ij}(\epsilon) + \triangle\epsilon \mathrm{COOP}_{ij}(\epsilon) \, . \tag{11.9}$$

COHP is only defined unambiguously for the orthogonalized orbitals $|\tilde{\mathrm{i}}\rangle = \sum_j (S^{-1/2})_{ji} |j\rangle$. However, the process of the orthogonalization destroys the pure lm character of the atomic-like orbitals.

It is important to note that COOP is only a good quantity if the basis set is nearly orthogonal (the off-diagonal overlap matrix elements are small). In the opposite limit of the nearly linear-dependent basis set COOP diverges for the antibonding states. In RSPt, the basis set is often close to the linear dependence for certain **k**-points when more than one kinetic energy tail is used. This leads to a problem with huge antibonding peaks in the COOP. To overcome this difficulty, Grechnev et al. [105] proposed a modified version of COOP called balanced COOP (BCOOP). BCOOP is defined in the following way. Let the quantum number α include the physically significant quantum numbers (atom type t, spin projection σ, and the angular quantum number l). An eigenvector $\psi_n(\mathbf{k})$ can be written as a sum of non-orthogonal contributions $|\alpha(n, \mathbf{k})\rangle$

$$|\alpha\rangle = \sum_{i \in A(\alpha)} c_i |i\rangle \, , \quad \sum_{\alpha} |\alpha\rangle = |\psi_n(\mathbf{k})\rangle \, , \tag{11.10}$$

where $A(\alpha)$ is the set of all orbitals i with the given quantum number α, and any values of other quantum numbers, such as m, kinetic energy tail, and site within given type. The COOP in this notation is

$$\mathrm{COOP}_{\alpha_1,\alpha_2}(\epsilon) = \sum_{nk} \delta\left(\epsilon - \epsilon_n(\mathbf{k})\right) \langle \alpha_1 | \alpha_2 \rangle \tag{11.11}$$

and BCOOP is defined as

$$\mathrm{BCOOP}_{\alpha_1,\alpha_2}(\epsilon) = \sum_{nk} \delta\left(\epsilon - \epsilon_n(\mathbf{k})\right) \frac{\langle \alpha_1 | \alpha_2 \rangle}{\sum_{\alpha} \langle \alpha | \alpha \rangle} \, . \tag{11.12}$$

For "good" basis sets BCOOP practically coincides with COOP, while for "bad" basis sets (which are close to linear dependence) BCOOP is much more robust: It is much less basis set dependent and the huge antibonding peaks are avoided [105]. The calculation of BCOOP is a standard function of RSPt, and control flags for its calculation are described in the RSPt manual.

As an example of how BCOOP, implemented in RSPt, describes the chemical bonding in a transition metal, we display this function for hcp Ru in
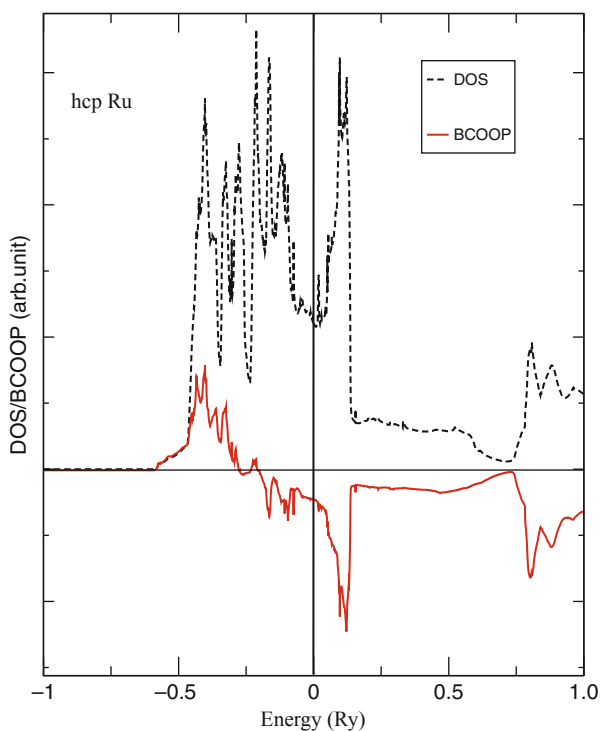
Fig. 11.2. BCOOP of hcp Ru. *Dashed curve* represents the density of states and *solid line* the BCOOP function. The Fermi level is at zero energy

Fig. 11.2. In this figure we also show the DOS. The figure shows that d-orbitals for less than a half-filled shell are bonding (positive BCOOP) and more than half-filled shell are antibonding (negative BCOOP). Hence, the chemical bonding of hcp Ru can be understood as stemming from all the bonding states have been filled and that some of the antibonding states are becoming filled, such that the Fermi level cuts through a region of antibonding states. This picture coincides perfectly with the general understanding of chemical bonding of transition metal elements, as being explained by the Friedel model [112].

11.3 Equilibrium Volumes of Materials

The equilibrium volume of a material is described extremely accurately by density functional theory in most implementations, and RSPt is no exception to this. In order to illustrate this we will use here as examples the transition metals, f-electron systems, as well as selected compounds. In RSPt the equilibrium volume is identified as the volume for which the total energy of the material has its lowest total energy. Hence, a few total energy calculations (or order 5–10) are needed to find this energy minimum. In general, the

total energy for each volume needs to be converged to a level where additional self-consistent calculations do not change the energy with more than a tenth of a mRy. The number of **k**-points needed for sampling the full Brillouin zone of simple crystal structures with one or a few atoms per unit cell is approximately 2,000–5,000. In practice, the symmetry of the crystal reduces the number of **k**-points needed, since only the irreducible wedge needs to be sampled. For instance, a crystal with cubic symmetry has 48 point group operations, and hence the irreducible wedge is 1/48 of the full Brillouin zone. Hence the number of **k**-points needed for achieving an accurate total energy, for the calculation of reliable equilibrium volumes, is only 40–100, for "easy" crystal structures with not too many atoms per cell. In general the density of **k**-points needed to achieve an accurate total energy scales inversely with the volume of the Brillouin zone. Hence, larger systems with many atoms per unit cell require in general fewer **k**-points.

11.3.1 Transition Metals

In Fig. 11.3 we show as an example of transition metals, the experimental and theoretical equilibrium volumes of the elements of the 4d transition metal series. These calculations have been performed with RSPt using the AM05 functional [20] for exchange and correlation as well as the generalized gradient correction of PBE [179]. Note that in general, theory reproduces the observed volumes with only a small error. When comparing the two functionals, it seems that overall AM05 agrees with observations somewhat better
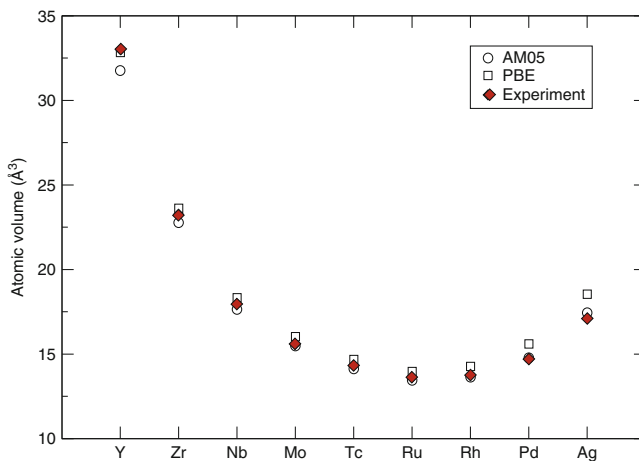
Fig. 11.3. Self-consistent calculations of equilibrium volumes of elements from the 4d transition metal series, using the AM05 functional [20] and the gradient-corrected functional for the PBE parametrization [179]. Calculations are compared to $T = 0\,\mathrm{K}$ experimental values

than PBE. The largest error made by AM05 is for Y and in general this functional seems to reproduce the later transition metals better than the earlier ones. For PBE the situation is reversed, the early elements are almost perfectly reproduced, whereas the elements later on in the series have too large volumes compared to observations. The general trend exhibited by the equilibrium volumes in Fig. 11.3 reflects the division of bonding states for the early part of the series and antibonding states for the later part, as is displayed in the BCOOP curve in Fig. 11.2. Hence, additional filling of electron states for less than a half-filled d-shell increases the strength of the chemical bond and causes therefore a contraction of the equilibrium volume. Additional filling of antibonding states will in a similar fashion cause an increase in equilibrium volume.

11.3.2 Lanthanides and Actinides

In Fig. 11.4 we show the volumes of the lanthanide series, both as given by calculations based on LDA and PBE [65, 67]. In the figure we also include experimental data. Note that the gradient-corrected functional overall performs much better in reproducing the experimental data for the lanthanides than the LDA functional. It is also clear from the figure that the volumes of the lanthanides can be divided into two groups, one with larger volumes (Ba, Eu, and Yb) and one with smaller volumes. This comes naturally from the fact that Ba, Eu, and Yb are divalent elements, with only two electrons in the valence band which can contribute to the chemical bonding. The group of rare-earth elements with lower volumes are the trivalent ones, where the extra electron in the valence band contributes to strengthen the chemical bonding, which reduces the equilibrium volume [127]. We will return to the stability of
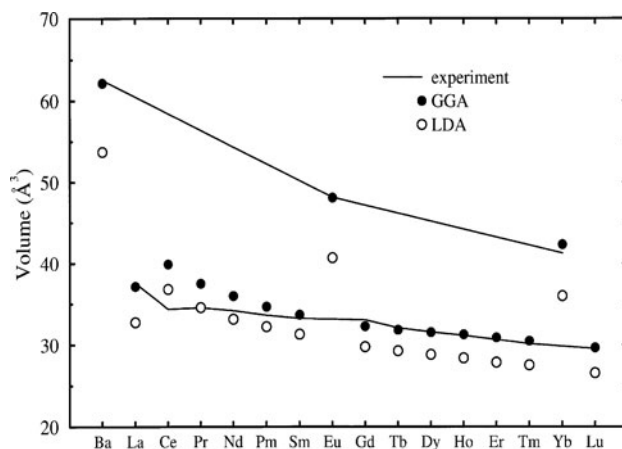
Fig. 11.4. Calculated and measured equilibrium volumes of the lanthanide series. Theoretical data made by GGA (*filled circles*) and LDA (*open circles*)

the divalent and trivalent states of the rare-earth series below. Furthermore, it should be noted that all elements of the rare-earth series, possibly with the exception of the α-phase of Ce, have a 4f shell which is atomic like and chemically inert. The other conspicuous part of the lanthanide series, which is also captured by theory, is that the volumes become contracted as one traverses the series. This behavior is referred to as the "lanthanide contraction," and reflects the incomplete screening of the nuclear charge by an additional electron of the 4f shell, when one goes from an element with nuclear charge Z to $Z + 1$.

The volumes of the light actinide series are shown in Fig. 11.5. Note that in this figure we show equilibrium volumes only of Th, Pa, U, Np, and Pu, since Ac is a normal trivalent element where the presence of the 5f electron states is hardly noticeable, at least not as concerns the equilibrium volume, and the heavy actinides (Am and onwards in the series) have a localized 5f shell, and hence a behavior of the equilibrium volumes which is similar to that of the lanthanide series [260]. For the elements Th, Pa, U, Np, and Pu the 5f-shell is in general not localized in the same way as it is in the lanthanides. Instead the 5f states are more or less itinerant, and this produces a chemical bonding which can best be described from the Friedel model, just as is the case of the d-shell of the transition metals, as discussed in Sect. 11.3.1 and around Fig. 11.2. Figure 11.5 shows an overall acceptable agreement between theory and experiment. The agreement is maybe not as good as that found for
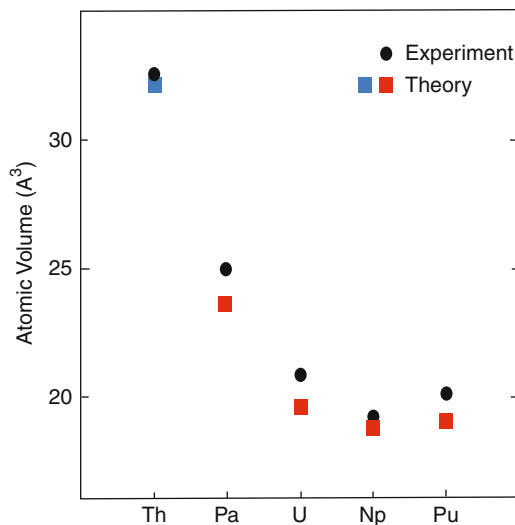
Fig. 11.5. Calculated and measured volumes of the actinide series. Experimental data given at room temperature. Theoretical data are given from GGA theory to which the experimental thermal expansion was added, to correspond to room temperature volumes. The *red squares* are from [215] and the *blue square* is from [172]

the transition metals, but nevertheless it must be viewed as satisfying. The electronic structure of the actinides is extremely complex, with an interplay between a large spin–orbit splitting in the 5f shell, which also forms a rather narrowband, so that correlation effects start to become visible. In addition, the shallow core states (the 6s and 6p states) overlap with neighboring atomic states, so that they must be treated as valence band states. Hence several electronic shells must be considered in the calculation, which poses a technical problem. This is solved in RSPt by separate energy sets, as discussed above, which forms a common fully hybridizing set of energy bands.

As an example we show the DOS of the α-phase of Pu in Fig. 11.6. In this figure we show the total DOS as well as the partial DOS of one of the
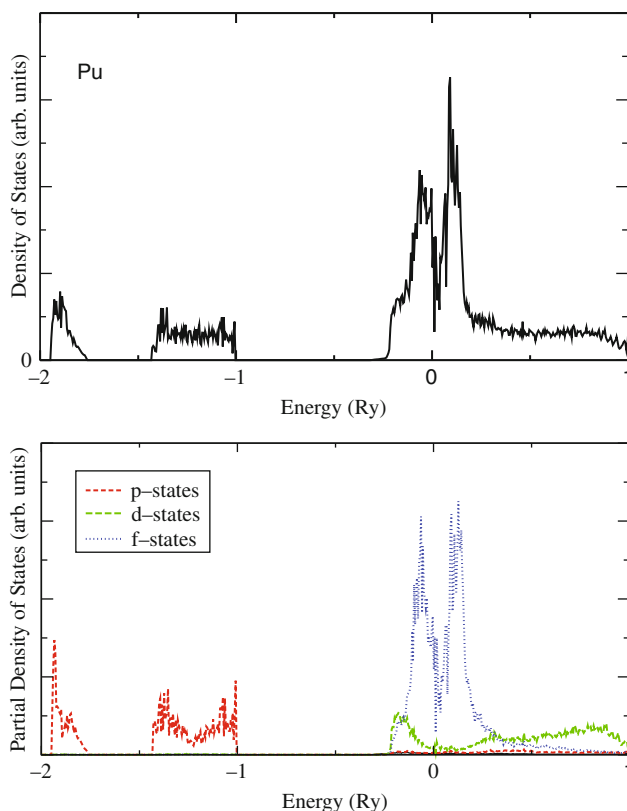
Fig. 11.6. Calculated DOS of α-Pu. In the *upper panel* the total DOS is shown, and in the *lower panel* the partial DOS of the p-states, d-states, and f-states. The partial DOS is shown only for 1 of the 16 atoms of the unit cell of the monoclinic phase of α-Pu. The $6p_{1/2}$ states are primarily located close to -2 Ry, the $6p_{3/2}$ states primarily between -1.5 and -1 Ry, the 6d states start at approximately -0.3 Ry and are extended to over 1 Ry, whereas the 5f states have a width of ≈ 0.5 Ry and are pinned by the Fermi level

atoms of the monoclinic cell of α-Pu. Note that a projection to a selection of angular momentum states is done in the figure, i.e., the p, d, and f states. This projection does not make a distinction between, e.g., 6p and 7p states, and in principle the p-partial DOS in Fig. 11.6 contains components from both 6p and 7p states. In addition, all states considered in the calculation can hybridize with each other. In a calculation of a free Pu atom the 6p states are spin–orbit split and located at $\approx -2\,\mathrm{Ry}$ for the $6\mathrm{p}_{1/2}$ states and at $\approx -1.5\,\mathrm{Ry}$ for the $6\mathrm{p}_{3/2}$ states. This atomic feature also shows up in the DOS of the electronic structure of solid Pu; the spin–orbit coupling is clearly visible, and p states are clearly seen at ≈ -2 and $\approx -1.5\,\mathrm{Ry}$, albeit broadened. If one were to plot the radial component to the eigenfunctions of the p-states at these energies, one would note that they are dominated by 6p states, not the 7p states. If on the other hand one were to investigate the radial component of p-projected states at much higher energies, e.g., above the Fermi level, one would encounter 7p states. For the 5f states the spin–orbit splitting is around $0.1\,\mathrm{Ry}$, and this has a tendency to split the 5f partial DOS into two components, which are separated by a gap. This is also visible in Fig. 11.6, but one should note that other effects, associated with the formation of electron bands, including the crystal field splitting, are active in producing a partial DOS which is separated into two regions that are separated by a gap. The width of the 5f states, as shown by Fig. 11.6, is of the order of 0.5 Ry, which is rather close to the estimates of the Hubbard-U for Pu (values between 0.2 and 0.4 seem reasonable for metallic Pu), discussed in the DMFT section. Hence there are three interactions in the 5f shell of Pu which are rather similar in strength, the spin–orbit coupling, the Coulomb repulsion among electrons, and the hopping of 5f electrons from lattice site to lattice site, producing energy bands. This feature of Pu makes it a formidable theoretical problem to investigate, and only recently has some light been cast on this outstandingly complex element [85, 198, 206].

11.3.3 Compounds

The final example of how RSPt reproduces experimental equilibrium volumes is taken for a few refractory compounds, i.e., TiC, TiN, and TiO. The calculated volumes (both from LDA and GGA) [5] are compared to observations in Fig. 11.7. Note that for TiC and TiN, the GGA results reproduce the observed volumes with only a very small error. For TiO the GGA calculation results in a slightly too large volume, which has been analyzed in part to be due to a deviation from perfect stoichiometry in the experimental sample [5]. Overall, the data in Fig. 11.7 demonstrate that also for materials with some complexity in the chemical binding, equilibrium volumes are reproduced by RSPt with good accuracy, even if the chemical binding is rather complex, and
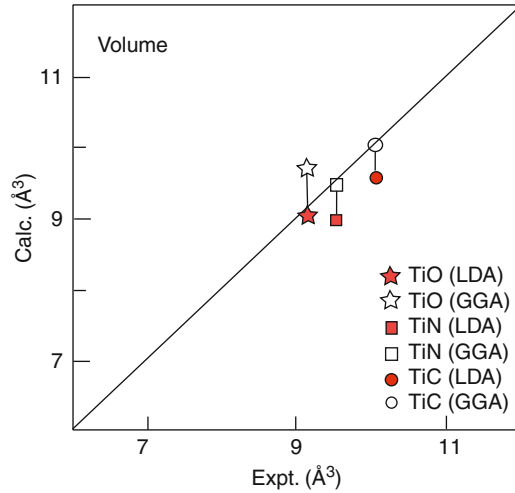
Fig. 11.7. Calculations using RSPt for the equilibrium volumes of TiC, TiN, and TiO, compared to experimental data. Data redrawn after [5]

includes a large covalent component between the d-electron element and the p-electron element.

11.4 Cohesive Energy

The cohesive energy, i.e., the energy difference of a crystalline material and the sum of the atomic energies of the elements constituting the material, is also a ground state property which in principle should be reproduced well by density functional theory. In order to illustrate how well this is captured by the RSPt implementation, we show in Fig. 11.8 the calculated cohesive energy of the lanthanide series [65, 67]. The property shown in this figure is actually the generalized cohesive energy, which according to the definition [131], has eliminated the energies of the multiplet structure of the 4f shell, as well as the promotional energy within the 4f shell. In short, the data in Fig. 11.8 display the energy gained by the non-f valence electrons when the solid is formed. Details of how this energy is defined are described in [65, 67]. Figure 11.8 shows that the trivalent materials have a larger generalized cohesive energy, compared to the divalent ones, which reflects the fact that more electron states contribute to the chemical binding here. Overall, the agreement between theory and experiment is found to be good in Fig. 11.8 and, just like for the equilibrium volumes, it is clear that the gradient-corrected functional in general reproduced observations better than LDA. The convergence needed in RSPt, in terms of the number of **k**-points sampled in the Brillouin zone, as well as the number of self-consistent iterations, is the same as for calculations of equilibrium volumes, discussed above.
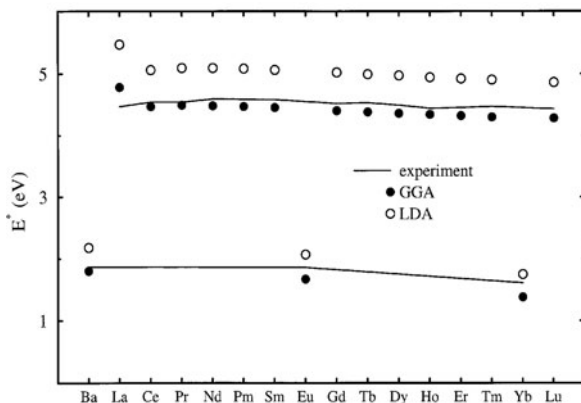
Fig. 11.8. Calculated generalized cohesive energy (*see text*) for divalent and trivalent lanthanides, compared to experimental data. Calculations have been based on LDA as well as GGA

11.5 Structural Stability and Pressure-Induced Phase Transitions

The structural stability of a material is a property which first principles calculations in general reproduce with outstanding accuracy. Several studies have confirmed this finding, where possibly the most conspicuous result was published by Skriver [209] in a paper which considered the structural stability of most elements of the periodic table. The observed structures were in this work reproduced for almost all considered elements, clearly a major achievement of a theory, and subsequent calculations have only slightly modified the structural stabilities of [209].

The calculation presented in [209] was based on the atomic sphere approximation. Subsequent calculations based on a full-potential geometry, like RSPt, give for most elements a very similar structural stability as that found by Skriver. We exemplify the accuracy of RSPt in reproducing structural stabilities by considering an sp-bonded element, Ca, a transition metal, Ti, and an actinide element, Pu. The structural stability of several other materials has been considered in the past, e.g., as reported in [87, 216, 218].

As concerns computational details, accurate calculations of structural stability require a somewhat more dense **k**-point mesh compared to a calculation of the equilibrium volume or cohesive energy, sometimes up to a factor of two to three times as dense.

11.5.1 An sp-Bonded Material, Ca

The most interesting structural properties of Ca are studied as a function of applied pressure, and we summarize shortly the relevant experimental

situation. This divalent element shows a set of phase transitions [174, 265]; starting from fcc it transforms to a bcc structure at ≈20 GPa. With further increase of the pressure, a transition to an sc phase transition was observed at ≈30 GPa. In this set of transitions, the appearance of the sc structure is unexpected, since it seldom appears for elements of the periodic table (Po is as mentioned the only known example at ambient pressure). In contrast, pressure-induced phase transitions from fcc → bcc or from bcc → fcc are very common.

In Fig. 11.9 we show calculations using RSPt [4] of the structural properties of Ca. Note that the energies of the fcc, bcc, sc, and hcp structures are compared in this figure. The experimental trend of phase stability, fcc → bcc → sc, as a function of increasing pressure, is found to be reproduced by the calculations. The calculated transition pressure of the fcc → bcc phase transformation is 15 GPa, which compares rather well with the observed pressure of 19.5 GPa [174]. The calculated pressure for the bcc → sc transition is 33 GPa which also compares favorably with the observed transition pressure of 32 GPa [174]. The observed transition sequence of Ca was analyzed in detail in [4] and found to occur because of a pressure-induced transfer of electron states from the s-projected orbitals to d-projected orbitals, and that the filling of the d-projected states drives the transition to the sc phase [4].
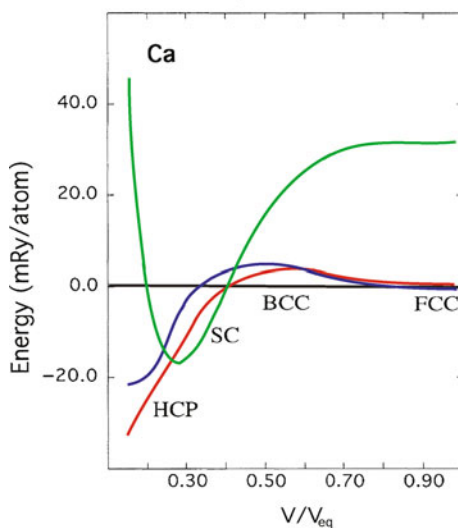
Fig. 11.9. Structural stability of Ca as a function of compression. The bcc structure is the reference energy and is set to zero energy. The energy of the hcp phase is marked as *red*, the fcc phase is marked as *blue*, and the sc phase is marked as *green*. Figure redrawn after [4]

Note from the figure that theory predicts a destabilization of the sc structure and that at sufficiently small volumes, the hcp structure should be stable. So far, this phase has not been verified, although the destabilization of the sc structure is an experimental fact. Recent experimental work on Ca reported two new high pressure phases at 113 GPa [265]. The structures of these phases have so far not been identified, but recent theory have proposed an incommensurate crystal structure of Ca at these pressures [17].

11.5.2 Transition Metals

The group IV elements, Ti, Zr, and Hf, have similar structural properties as a function of temperature or pressure. At room temperature and ambient pressure the hcp phase is stable, but with an applied pressure the so-called ω-phase is stabilized. A further applied pressure is known to stabilize the bcc structure, at least for Zr and Hf [6]. Hence the phase diagram of these elements is sufficiently complex to serve as a good test on the accuracy of a first principles theory. For this reason we have chosen to illustrate the accuracy of RSPt in reproducing the structural properties of transition metals for one of the group IV elements, Ti. The structural properties of Ti at very low temperature have not been reported, so it is in principle difficult to compare first principles theory with observations. However, an extrapolation of the known phase diagram to low temperatures and zero pressure suggests that the hcp and ω-phase are close to being degenerate in energy [266]. Hence the experimental data available suggest that the phase stability at zero temperature is expected to start at ambient pressure with the hcp and ω-phase being close to degenerate and that with increasing applied pressure a stabilization first of the ω-phase and second of the bcc structure. This trend is captured in its entity by RSPt, as shown in Fig. 11.10, where the crystallographic phase stability of this element is shown. Several studies of structural phase stabilities of transition metal elements and compounds have in the past been published with RSPt, especially
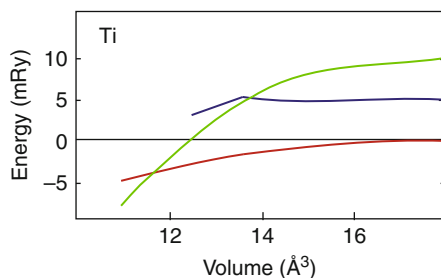
Fig. 11.10. Calculated structural stability of Ti, as a function of volume, with the hcp structure being the reference level, which is set to zero energy. The experimental equilibrium volume is 17.6 Å^3. The energy of the ω-phase is given by the *red line*, the energy of the fcc phase is given by the *blue line*, and the energy of the bcc phase is given by the *green line*

concerning pressure-induced structural phase transitions [216, 217], often with excellent agreement between calculations and experimental observations.

11.5.3 Systems with f-Electrons

Concerning the electronic structure, plutonium is one of the most complex elements known, as discussed above. This is reflected also in the structural properties of this element, where as a function of increasing temperature a sequence of phase transitions are known experimentally [215]. Starting from the low-temperature monoclinic α-phase, which has 16 atoms per unit cell, a transition to the β, γ, δ, δ', and ϵ phases has been identified as a function of increasing temperature. The stability of the low-temperature α-phase is an excellent test for first principles theory, since this puts very high demands on the accuracy of the electronic structure method used. As an example of how RSPt performs for this task, we show in Fig. 11.11 a comparison between the calculated total energy of eight different crystal structures, as a function of volume [228]. The structures considered are typically found experimentally among the transition metals and the actinides. Note from the figure that of all the structures considered, the experimentally observed α-phase has the lowest total energy at the experimental equilibrium volume, clearly a gratifying result given the complexity of the electronic structure of this material. Further, a sequence of phase transitions is suggested by the data in Fig. 11.11, and
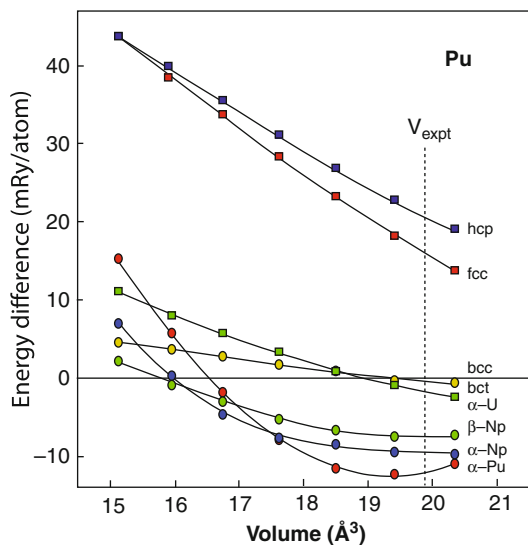
Fig. 11.11. Structural stability of Pu, as a function of volume. The different crystal structures are compared to the bcc structure. Therefore the total energy of the bcc phase represents the zero energy line. The experimental equilibrium volume is $\approx 20.3\,\text{Å}^3$

Pu is predicted to become bcc at sufficiently low volumes. A full account of the physics behind the complex crystallographic phases of Pu and the light actinides can be found in [218, 219, 259].

11.6 Valence Configuration of f-Elements

The stability of a particular electronic configuration, $f^n[spd]^3$ or $f^{n+1}[spd]^2$, is referred to as the valence stability. It has been shown that the energy difference between two or several such valence configurations, Δ_0, can be calculated using first principles theory. This involves calculating the contribution to the energy difference between the two configurations which comes from the itinerant [spd]-states, i.e., the generalized cohesive energy, and the contribution from the localized 4f states [127]. An example of such a calculation using RSPt is shown for the rare-earth elements in Fig. 11.12 and it may be noted that theory and experiment do not differ by more than ≈ 0.1 eV. This calculation thus reproduces the observed trivalent state of all the rare-earths except for Eu and Yb, where correctly the divalent configuration is reproduced. In addition it is known to reproduce the valence stability of rare-earth-based compounds as well [66].

It is in addition possible to calculate accurately the transition from one valence configuration to another as a function of pressure. This is illustrated in
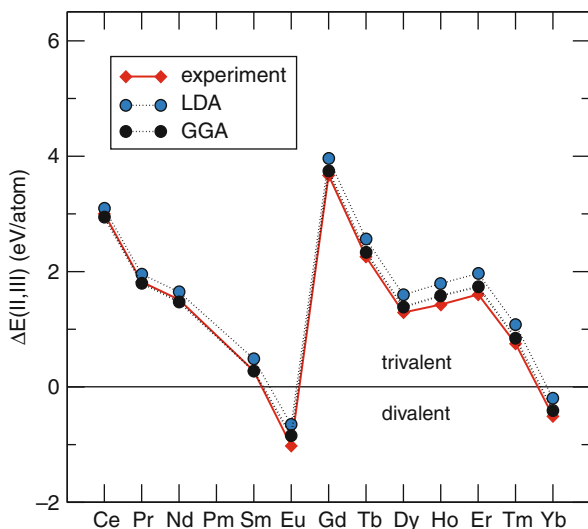
Fig. 11.12. Energy difference between divalent and trivalent phases of the 4f elements. The divalent phase is stable for negative values (Eu and Yb). Experimental values are given as *red diamonds* and theoretical values as *blue circles* (LDA) and *filled circles* (GGA)

Fig. 11.13 for elemental Yb, which is divalent at ambient pressure. In the high-pressure experiments of [53] it was concluded that Yb undergoes a pressure-induced transition to an intermediate valence state, i.e., a state where the valence configuration is not simply an integer, like divalent or trivalent, but a non-integer valence configuration. At 100 GPa it was estimated that Yb has transformed completely to a trivalent state.

The consideration of the electronic structure of an intermediate valence material requires a combination of data from density functional theory and the so-called Kimbal–Falicov model [101, 190]. One may start by considering a divalent rare-earth element, which corresponds to an f^{n+1} configuration. For a given volume, one can calculate the total energy difference, Δ_0, between the trivalent (f^n configuration) and the divalent states, as shown in Fig. 11.12. A straightforward calculation of Δ_0 cannot reproduce the energetics of an intermediate valence state, since it simply concludes that if $\Delta_0 > 0$, the divalent state is stable and if $\Delta_0 < 0$ the trivalent state is stable. As a first step, one considers the valence configuration $z = 2 + x$, which is determined by the energy balance between the difference of the f^{n+1} and f^n configurations and the variation of the band energy when promoting x electrons:

$$x = \int_{E_{\mathrm{F}}}^{E_{\mathrm{F}}+|\Delta(x)|} \mathrm{d}E N\left(E\right) , \tag{11.13}$$
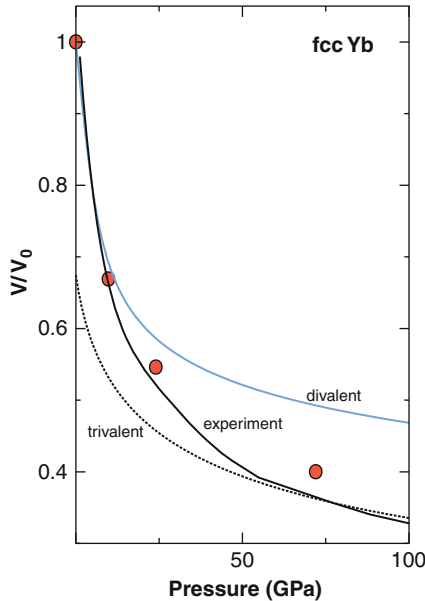
Fig. 11.13. Calculated equation of state for fcc Yb (*red circles*) compared to experiment (*full line*). The two *broken lines* are isothermal equation of states for divalent (*upper blue line*) and trivalent (*lower dotted line*) fcc Yb. Data taken from [56]

where E_{F} is the Fermi energy for the divalent state, $N(E)$ is the density of states of itinerant valence electrons (for Yb metal it is dominated by the $5d$ states), and $\Delta(x)$ is a renormalized promotion energy [101, 190].

In [121–123], a BCS-like theory of intermediate valence systems, with a $d-f$ excitonic pairing, was suggested. In that model, the main correlation effect on the valence stability is the Hartree–Fock renormalization of Δ_0, i.e.,

$$\Delta\left(x\right) = \Delta_0 + Gx\,, \tag{11.14}$$

where G is the Falicov interaction parameter. G can be determined as the derivative of the center of the $5d$ band with respect to the number of $4f$ electrons, and one obtains the valence, i.e., the correct self-consistent value of x, by solving (11.13) and (11.14) iteratively.

We plot in Fig. 11.13 the calculated EOS (open circles) together with the experimental data (full curve) of [53]. For comparison, the equation of state for divalent and trivalent Yb is also shown in the figure. The agreement between experiment and the theory based on the Kimbal–Falicov model is good, whereas the trivalent and divalent EOS curves do not capture the overall behavior of the experimental data.

11.7 Elastic Constants

The elastic response of a material gives information on how the material deforms and becomes strained when subjected to a given stress. This information is contained in the materials' elastic constants. The strain of the system is normally expressed in a matrix form as

$$\mathbf{e} = \begin{pmatrix} 1 + \alpha_{xx} & \alpha_{xy} & \alpha_{xz} \\ \alpha_{yx} & 1 + \alpha_{yy} & \alpha_{yz} \\ \alpha_{zx} & \alpha_{zy} & 1 + \alpha_{zz} \end{pmatrix}\,, \tag{11.15}$$

where the elements α_{ab} in the matrix $\mathbf{e}$ represent how the Bravais lattice vectors of the system become distorted (a thorough account for the theory of elasticity is given by Wallace [251]). First principles calculations of elastic constants are obtained first by making a Taylor expansion of the systems total energy in the strained state using the following expression:

$$E(V,\mathbf{e}) = E(V_0,\mathbf{1}) + V_0 \left(\sum_{a,b} \tau_{ab}\alpha_{ab} + \frac{1}{2} \sum_{ab,cd} C_{ab,cd}\alpha_{ab}\alpha_{cd} + \cdots \right)\,, \tag{11.16}$$

where $E(V,\mathbf{e})$ is the total energy of the strained system, $E(V_0,\mathbf{1})$ the total energy of the unstrained system, $\mathbf{1}$ is the matrix $\mathbf{e}$ with all values of α_{ab} equal to zero, τ_{ab} is an element in the stress tensor, and $C_{ab,cd}$ is the adiabatic elastic constant. Normally one adopts the Voigt notation that replaces the

index xx with 1, yy with 2, zz with 3, etc., and in this notation the elastic constant is written as C_{ij} where i and j are integers ranging from 1 to 6. The calculation of C_{ij} now proceeds by a suitable choice of α_i in (11.15) that gives rise to a strain corresponding to a specific elastic constant or a particular combination of elastic constants. For instance, the choice of all α_i equal to zero except α_3 results in the following total energy expression, $E(V, \alpha_3) = E(V_0, \mathbf{1}) + V_0(\tau_3\alpha_3 + \frac{1}{2}C_{33}\alpha_3\alpha_3)$. By first calculating the total energy of the system, e.g., using density functional theory, for different values of α_3 (typical values range between 0.01 and 0.1) and then fitting the resulting energy curve to the expression for $E(V, \alpha_3)$ quoted above one can extract a theoretical value of C_{33}. One must bear in mind that a precise calculation of elastic constants requires a very high accuracy in determining energy differences of different strain states, roughly on the order of µRy/atom. A significantly denser $\mathbf{k}$-point mesh is therefore needed to achieve accurate elastic constants, so that the number of $\mathbf{k}$-points has to reach of the order 10,000–20,000 points in the full Brillouin zone for an element with one atom per unit cell.

In Fig. 11.14 experimental and theoretical data using RSPt and LDA [261] of $\frac{1}{2}(C_{11} - C_{12})$ (this is a particular combination of elastic constants for cubic materials that is called C') and C_{44} are shown for a selection of the cubic transition elements (C_{11}, C_{12}, and C_{44} are the only independent elastic constants for a cubic material). The elements have been ordered in the way of increasing values of C'. Note that the experimental values of C' and C_{44} range from 0.02 to 3 Mbar and that despite this large span, the theory reproduces the experimental data within some $\approx$10%. First principles calculations of spin-polarized bcc Fe, fcc Co, and fcc Ni reproduce experiments with approximately the same accuracy [217]. For a hexagonal material the symmetry aspects result in five
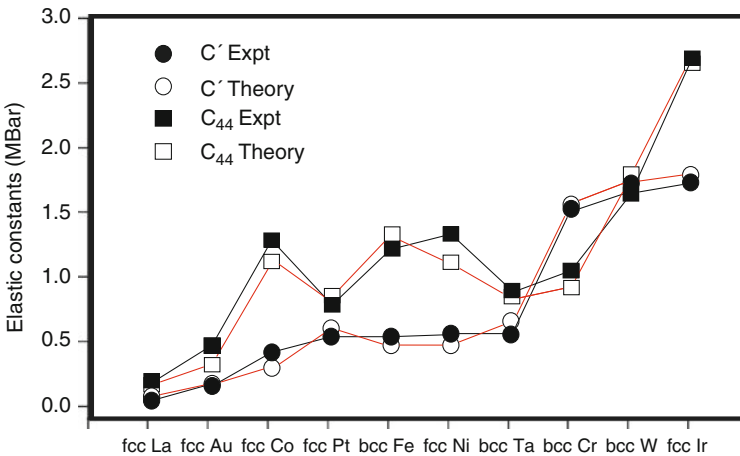
Fig. 11.14. Calculated (LDA) and experimental elastic constants of selected cubic transition metals

independent elastic constants, C_{11}, C_{33}, C_{55}, C_{12}, and C_{13} [251]. Among the transition metals there exist experimental data for several elements, and RSPt in the LDA approximation reproduces these data with an error not exceeding $\approx 15\%$ (see Fig. 11.15) [92].

The experimental elastic constants are typically reproduced with somewhat better accuracy using GGA compared to LDA, and the general deviation between experiment and theory, as shown in Figs. 11.14 and 11.15, is expected to be even smaller for GGA calculations. This is exemplified in Fig. 11.16 where the calculated values of C_{11}, C_{12}, and C_{44} are shown both from LDA and GGA calculations together with experimental values, for TiC, TiN, and TiO [5]. In Fig. 11.16 it may be seen that the GGA theory reproduces the experimental values somewhat better than the LDA calculations, but the general trend is not influenced by the choice of GGA or LDA.

Overall, GGA is known to reproduce the chemical binding better than LDA, so that quantitatively it results in a better agreement between experiment and theory. If one is interested in general trends, for instance, if a specific elastic constant is bigger in one element compared to another, or the trend
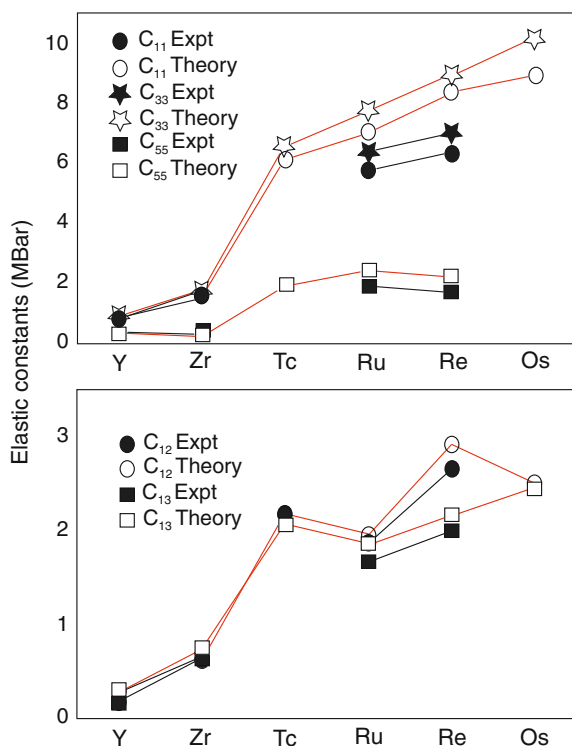
Fig. 11.15. Calculated (LDA) and experimental elastic constants of selected hexagonal transition metals
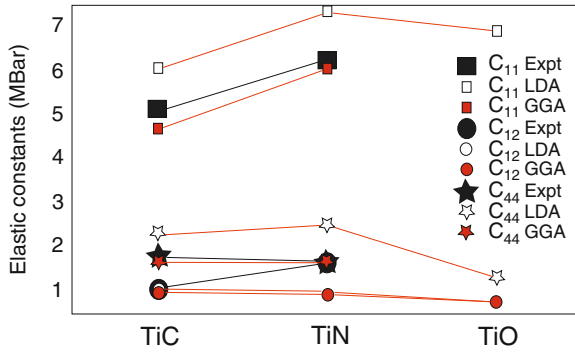
Fig. 11.16. Elastic constants for TiC, TiN, and TiO (NaCl structure) using LDA and GGA, compared to experimental data

of the equilibrium volume or the changes in structural properties across a transition metal series, LDA is as good as GGA. As concerns the magnetic properties, it is less clear if one can identify a general trend where GGA can be said to be better than LDA, as we will discuss in some detail in the next chapter.

12

Magnetism

Abstract Chapter 12 describes the theory of magnetism, with focus on spin and orbital moments, and the magnetic anisotropy. Numerical examples are presented, both for bulk and surfaces, and the particular symmetry aspects of relativistic one-electron theory and magnetism are described. The different contributions to the magnetic anisotropy are analyzed, as are the often cumbersome aspects of a slow convergence of the calculation of the magnetic anisotropy with respect to the number of k-points.

There are several properties of a magnetic material which determine functionality in a variety of applications, and for this reason have caught attention for scientific studies. Among the key magnetic properties, we note the saturation magnetization, the ordering temperature, the type of magnetic ordering, as well as the magnetic anisotropy. The saturation magnetization is obtained when all atoms of, e.g., a ferromagnetic material have atomic spins aligned, and the material is in a mono-domain state. A measurement of the saturation magnetization can hence give information about the size of the atomic moment, which in general is composed of a spin and an orbital part. A schematic picture of this is shown to the left in Fig. 12.1. Both these moments can be calculated from first principles theory, and we will give examples of such calculations in this chapter. Another property which is available for theoretical studies is the nature of the magnetic ordering, such as ferromagnetism, ferrimagnetism, and antiferromagnetism. By simply comparing total energies in DFT calculations, for different magnetic configurations, gives evidence for which magnetic structure should be observed experimentally. The final example we want to mention of a magnetic property which is available from first principles theory is the magnetic anisotropy. All materials have a tendency to have the magnetic moments aligned along crystallographic axis, the so-called easy axis. As an example we note that fcc Ni has the $\langle 111 \rangle$ axis as the easy axis and for bcc Fe it is the $\langle 001 \rangle$ axis. Only by applying an external field can the magnetization be made to rotate away from the easy axis, toward a hard axis (an example is shown in the right-hand side of Fig. 12.1).
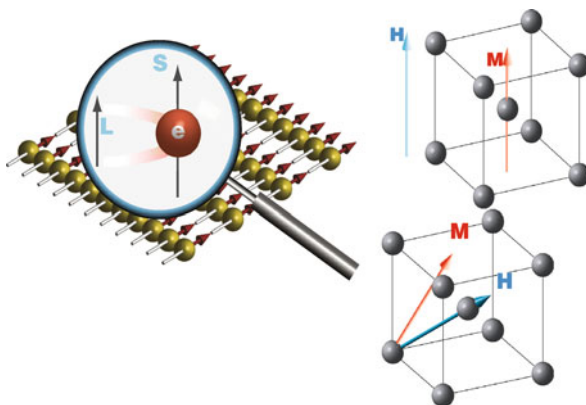
Fig. 12.1. Illustration of the contribution of spin (S) and orbital (L) angular momentum to the atomic magnetic moment (*left*). Picture of the rotation of the magnetic moment away from the easy axis by an external field (*right*) (picture kindly provided by O. Karis)

12.1 Spin and Orbital Moments of Itinerant Electron Systems

The calculation of spin moments can in the simplest procedure be done from a spin-polarized calculation, where one finds a solution to the Kohn–Sham equation, (2.18), for spin-up and spin-down states separately, in which an effective potential is constructed separately for each spin projection and the spin–orbit coupling is neglected. For some materials an asymmetric population of spin-up and spin-down states then appear; the material becomes spin polarized. Other materials do not become spin polarized when separate solutions to the Kohn–Sham equation are allowed for, which simply means that the used energy functional favors a spin-degenerate solution. When a comparison is made between spin-polarized calculations of the Kohn–Sham equation, and experimental observations, the agreement is near perfect. Theory reproduces the experimental observation of a spin-polarized or a spin-degenerate state for most materials. As a matter of fact, among the elements of the periodic table, it is only Cr, Mn, Fe, Co, Ni, the lanthanides, and a few of the heavy actinides (Am an onwards) which are experimentally known to have a lifted degeneracy between the two spin channels. Density functional theory in most implementations, and the RSPt code is no exception here, reproduces this fact perfectly.

In these calculations the spin moment is calculated from

$$m_{\mathrm{s}} = g_{\mathrm{s}} \Sigma_i \langle \psi_i \, | s_z | \, \psi_i \rangle \ , \tag{12.1}$$

where the sum is over all occupied states, and for a solid it is meant to the Brillouin zone. Furthermore, g_{s} is the *g*-factor of the electron spin (which

in practice is put equal to 2), and ψ_i is the solution to (2.18). For a spin-polarized calculation of a collinear configuration, in which spin–orbit coupling is neglected, all the solutions to (2.18) have pure spin projection, i.e., no mixing between spin states appears. This yields a contribution to the expectation value equal to $+m_s$ for spin-up states and $-m_s$ for spin-down states, and the sum in (12.1) can be made straightforwardly. An alternative to using (12.1) is to evaluate the density of states of the spin-up and the spin-down states, according to the procedures described in Chap. 3 and then integrate the density of states of each spin channel to the Fermi level. An example of such a calculation is shown in Fig. 12.2, where a spin-polarized calculation of bcc Fe is shown. From this figure it is clear that the occupation of spin-up states is larger than the occupation of the spin-down states. The calculated spin moment is the difference in occupation of the two spin channels, multiplied by g_s.

The calculation of an orbital moment is analogous to that of the spin moment and may be done in practice from the equation

$$m_l = \Sigma_i \langle \psi_i \,|l_z|\, \psi_i \rangle \ . \tag{12.2}$$

Note that the g-factor for the orbital moment is 1, but that otherwise the expressions in (12.1) and (12.2) are similar. It should be noted that in order for an orbital moment to appear, both spin polarization and spin–orbit coupling must be present in the calculation [39].
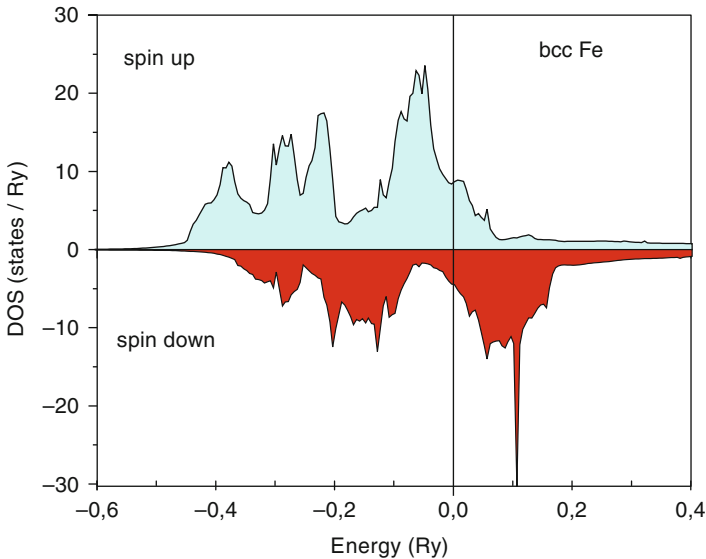
Fig. 12.2. Illustration of a spin-polarized electronic structure calculation, using RSPt. The Fermi level is at zero energy

12.1.1 Symmetry Aspects of Relativistic Spin-Polarized Calculations

The symmetry properties of a spin-polarized calculation which includes spin–orbit coupling requires some discussion, since in this case there is a coupling between spin degrees of freedom and real space. This can be seen easiest by noting that in the simplest form, spin–orbit coupling enters as $\xi l \cdot s$ to the Hamiltonian, where s is an operator of spin space and l an operator of real space. The consequences of this, as regards symmetries, maybe best discussed using the example of symmetries of a cubic crystal, described in Chap. 3. Here we discussed the 48 point group operations which are allowed if magnetism is neglected. If we consider a material where the magnetization ($\mathbf{M}$) is pointing along the 001 axis (bcc Fe is an example of this, since the 001 axis is the easy magnetization axis of this element), a $180°$ rotation around the x- or y-axis is no longer allowed, since this rotates the magnetization direction with $180°$, and hence $\mathbf{M} \rightarrow -\mathbf{M}$. In a similar fashion a $120°$ rotation around the 111 axis rotates the magnetization from the 001 direction to the 010 direction, and again the original magnetic structure is not found. Further examples of operations which are allowed in a non-magnetic crystal, but are not allowed in a magnetic calculation, where the spin–orbit coupling is included in the Hamiltonian, are the $90°$ rotations around the x- or y-axis. For both these operations the magnetization is rotated away from the 001 direction. As a matter of fact, the only operations which are allowed are the identity and three $90°$ rotations around the 001 axis. Also, a $180°$ rotation around the x-axis results in that $\mathbf{M} \rightarrow -\mathbf{M}$, and if this operation is followed by the time reversal operator (which changes the sign of the magnetization) we end up with the magnetization pointing along 001, and we have an allowed symmetry operation. The inclusion of additional symmetry operations for magnetic materials, i.e., the time reversal operator, defines the so-called double group, which has been discussed by Bradley [54]. In a similar fashion, a $180°$ rotation around y followed by the time reversal operator is an allowed symmetry operation, as is a $180°$ rotation around the vectors [111] and [111], followed by time reversal. This results in a total of eight allowed symmetry operations. Any of these eight operations can also be multiplied by the inversion operation, producing eight more allowed symmetry operations (since the spin is a pseudo-vector, it is not modified by the inversion). As a result we obtain a total of 16 symmetry operations for a bcc structure with the magnetization aligned along a $\langle 001 \rangle$ direction. If, e.g., the magnetization is chosen to point along a $\langle 111 \rangle$ direction, only 12 symmetry operations are allowed.

12.1.2 Elements and Compounds

In Table 12.1 we show as an example, a comparison between measured spin and orbital moments and the corresponding RSPt calculations of bcc Fe, hcp Co, and fcc Ni. It can be seen that the agreement between theory and experiment

Table 12.1. Calculated spin and orbital moments for bcc Fe, hcp Co, and fcc Ni, compared to experimental values [226]. Note that values are obtained with the quantization axis pointing along different crystallographic directions

Element	Direction	μ_s (SO)	μ_l (SO)	μ_s (OP)	μ_l (OP)	μ_s (expt)	μ_l (expt)
bcc Fe	001	2.193	0.049	2.193	0.078	2.13	0.08
bcc Fe	111	2.193	0.049	2.193	0.078		
hcp Co	0001	1.590	0.076	1.590	0.123	1.52	0.14
hcp Co	$10\bar{1}0$	1.590	0.076	1.590	0.118		
fcc Ni	001	0.608	0.048	0.611	0.066		
fcc Ni	111	0.608	0.048	0.611	0.065	0.57	0.05

is very good concerning the spin moment, a level of agreement that is rather typical for magnetic materials. As concerns the orbital moment there are two levels of approximations used, one is a regular calculation in which spin–orbit coupling has been introduced (data labeled SO) and the other is a calculation in which the so-called orbital polarization [86] was used. It may be seen that theory reproduces the observed orbital moment best from the OP calculation. We mention here that recent calculations based on DMFT, by Chadov et al. [55], also give very good orbital moments for these elements, highlighting the importance of electron correlations to obtain an accurate orbital moment. Note from Table 12.1 that the calculated spin and orbital moments are almost independent of which quantization axis is chosen. This is a general effect for magnetic 3d transition elements, where the spin–orbit interaction is weak, but for materials composed of heavier elements there is a stronger dependence. If anything should be distinguished in the table, it is that for hcp Co, the orbital moment is larger (for the OP calculation) when the moments are pointing along the 0001 direction (the easy axis). This is referred to as an orbital moment anisotropy (OMA). The results for hcp Co is a general behavior, and it can as a matter of fact be derived from perturbation theory that there is a proportionality between the magnetic anisotropy energy (MAE) and the OMA [42]. This derivation is made under the assumption that cross-terms in the spin–orbit interaction (i.e., $\xi(l_+s_- + l_-s_+)$) are neglected compared to diagonal terms (i.e., $\xi l_z s_z$). For the materials listed in Table 12.1 this relationship holds well.

The spin moments listed in Table 12.1 represent the magnetization density integrated over the whole unit cell. In RSPt, as well as in other methods which define space in a muffin-tin geometry, one can extract this information inside the muffin-tin spheres and in the interstitial region. One finds from such a division of space that the magnetic moment is always dominated by the muffin-tin contribution (typically over 95% of the moment comes from the muffin-tin region), which simply means that the magnetization density is located close to the atomic nucleus, with only a small part extending into the interstitial region. The orbital moment is typically even more localized around

Table 12.2. Calculated spin and orbital moments for the V atom in VAu_4. Note that in addition to a normal RSPt calculation we list spin and orbital moments of the V atom for a calculation with the spin–orbit coupling switched of on the Au site (second row in the table)

atom	μ_s	μ_l
V (with spin–orbit on Au site)	1.67	0.16
V (no spin–orbit on Au site)	1.71	−0.10

the atomic nucleus, and hence its contribution is expected to be almost entirely localized inside the muffin-tin sphere. As a matter of fact, the orbital moments listed in Table 12.1 are extracted only from the muffin-tin region. There is a practical reason behind this, since (12.2) is easiest evaluated over this region. By performing calculations with different values of the muffin-tin radii one obtains very minor changes in the orbital moment (of order of a few percent), which demonstrates that the orbital moment of the interstitial region can be neglected.

In Table 12.2 we show the calculated spin and orbital moments of VAu_4 [124], a magnetic material which has the peculiarity of being composed of atomic species which in the elemental form are not magnetically ordered. The moments shown in the table are the spin and orbital moment of the V atom, the Au atoms have only tiny-induced moments which we do not show. Table 12.2 shows a peculiar fact, in that the spin and orbital moments are parallel for V. Hund's third rule dictates that the spin and orbital moments should be parallel for electron shells which are more than half filled (e.g., for Fe, Co, and Ni, where the spin and orbital moments indeed are parallel – see Table 12.1) and antiparallel for materials with electron shells which are less than half filled. Vanadium is an example of the latter, but the coupling in VAu_4 is nevertheless parallel. For a calculation when the spin–orbit coupling is switched of on the Au site (see second row in Table 12.2) the coupling is the expected antiparallel one. This demonstrates that for the full calculation the spin–orbit coupling of the Au atom also influences the orbital moment of the V atom, rotating it with 180° to become parallel to the V spin moment. As a matter of fact it can be shown from perturbation theory that the spin–orbit interaction of a ligand atom, like Au in VAu_4, can influence the orbital moment and anisotropy of a magnetic atom, like V in VAu_4 [124].

12.1.3 Surfaces

We show in Fig. 12.3 the calculated orbital moments for a system with reduced symmetry, a thin film of Co on a Cu (001) surface. In the experiments, which were based on X-ray magnetic circular dichroism (XMCD – to be discussed in detail in Chap. 13), the ratio between orbital and spin moment is extracted most accurately, and it is for this reason this ratio is shown in Fig. 12.3, also
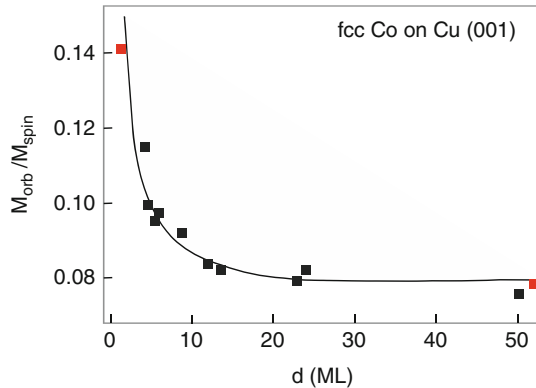
Fig. 12.3. Calculated (*red squares*) and measured (*black squares*) ratios between the orbital and spin moment. The measurements were done with X-ray magnetic circular dichroism (XMCD). Both experiment and theory are obtained as a function of Co thickness (d). Data redrawn after [238]

for the theoretical calculations. It may be noted from the figure that the ratio between orbital and spin moment increases as the Co thickness decreases, since the surface layer represents a low symmetry structure where spin–orbit effects are enhanced. As a matter of fact it can be shown from perturbation theory that for a cubic systems the spin–orbit effect enters the OMA and MAE effectively as $(\frac{\xi}{W})^4$, where ξ is the strength of the spin–orbit coupling and W the bandwidth. For a tetragonal symmetry, e.g., a mono-layer of Co on Cu (001), the spin–orbit effect enters as $(\frac{\xi}{W})^2$. Since for 3d transition metals the value of ξ is of the order of 50–70 meV/atom and W is of the order of 5 eV, it is clear that materials with reduced symmetry have much larger spin–orbit effects. A final note from this section is that both theoretical and experimental values can be fitted with a common function (solid line in the figure), a sign of good agreement between theory and experiment.

12.2 Magnetic Anisotropy Energy

Van Vleck [244] was first in pointing out that the magnetic anisotropy energy, the MAE, comes from the spin–orbit interaction. Typically the MAE is tiny compared to most other energies of a solid. The cohesive energy is as an example of the order of 1–10 eV/atom, whereas the energies involved for structural stabilities are typically not larger than 0.5 eV. Magnetic excitations, such as magnon curves, also involve energies typically less than 0.5 eV/atom [35, 197]. Compared to these energies, the MAE is for many materials tiny, with values of a few μeV/atom for elements like Fe and Ni, and a few tens of μeV/atom for hcp Co. Hence an extremely high accuracy is needed in order to reproduce measured MAE values. We discuss in this section how RSPt performs in this

task. Before entering this discussion we note that when it comes to theoretical work on the MAE, based on electronic structure calculations, several seminal works have been published in the past [58, 78, 141].

12.2.1 k-Space Convergence

The most important technical aspect of calculations of the MAE is the integration of **k**-space. As discussed in Sect. 4.4 there are several ways of how to do this, and it seems that the method which in most cases gives the most reliable result is the modified tetrahedron method (MTM). In some cases the Gaussian broadening method (GBM) also gives good results, whereas the tetrahedron method in general gives less accurate results and should be avoided. We show in Fig. 12.4, as an example of how the **k**-space integration converges, the MAE of fct Co (with a c/a ratio of 1.1). This result was published in [43]. It should be noted that an fct structure of Co could only be stabilized if thin films of Co were grown on a substrate; in bulk form Co crystallizes in the hcp structure. Note from the figure that for the tetragonal fct geometry, the 001 axis is the easy axis with a rather large value of the MAE, which reaches values of the order of $1 \mu eV/atom$. Calculations in a hypothetical cubic fcc structure give values of the order of $1–2 \mu eV/atom$. The reason for the enhanced MAE of the fct phase, compared to the fcc phase, is as discussed above, due to how the spin–orbit coupling enters the calculation to a lower (more important) order for low symmetry structures. As for the actual value of the MAE we note that within a 20% deviation all calculations give similar results. It further seems that the GBM data are in better agreement with the MTM data if smaller values of the Gaussian width is used. This is a general behavior.
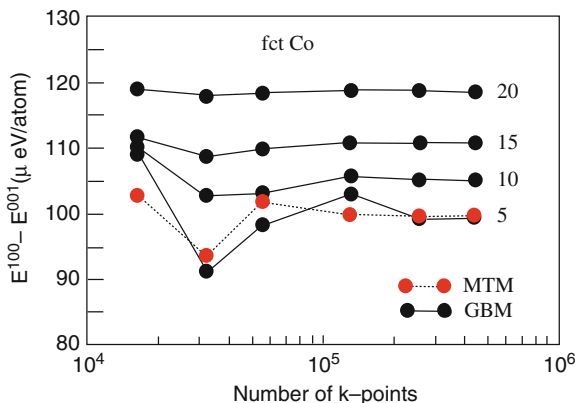
Fig. 12.4. Calculated MAE of fct Co using the GBM and the MTM. For the GBM the width of the Gaussian used in the calculations is given for the different calculations (in mRy). Note the logarithmic scale on the x-axis, which shows the number of **k**-points used in the full Brillouin zone

The MTM data must be considered as the most precise one, since when the sampling density approaches infinity this **k**-space integration should be exact, a statement which cannot be made by the GBM. However, if not too large values of the Gaussian is used (i.e., $\leq 10\,\mathrm{mRy}$) this technique is also reliable, and in some cases it converges faster than the MTM. A final note in this section is that of order of 100,000 **k**-points of the full Brillouin zone is needed to achieve a converged result. For magnetic materials based on 3d elements, with low symmetry, this is a typical number which is needed. For cubic materials a higher number of **k**-points is needed, sometimes approaching 10^6. This is, however, not a huge problem in the RSPt implementation, which can handle this on a single-processor calculation. Calculations done in a parallel mode are of course preferred, since **k**-space parallelization is extremely efficient in RSPt and most other solid state softwares.

12.2.2 MAE of hcp Gd

We now describe the calculated MAE of an example which illustrates some of the complexities of these calculations. In Fig. 12.5 we show the MAE of hcp Gd. In this calculation the 4f states were treated as localized, core electrons. Hence they were not allowed to hybridize with the dispersive valence electron states. The division of electrons as valence or core states is extremely easy in RSPt and other all-electron methods with numerical basis functions (e.g., the LAPW method). The reason for treating the 4f electrons as core states in hcp Gd is simply that it is a well-known experimental fact that for the rare-earth elements (except the α-phase of Ce) these states do not hybridize with other electron states. Instead they are atomic states with a many-electron wave function which should be calculated from angular momentum vector coupling algebra. The calculated data [56] in Fig. 12.5 are also compared to measurements, and it can be seen that experiment give an easy axis which is at an angle of some $30°$ away from the c-axis. The first principles calculations (right side of the figure) also give an easy axis which is tilted away from the c-axis, with an energy minimum at $30°$ from the c-axis and with an energy gain of $\approx 2\,\mu\mathrm{eV}$/atom, compared to when the moment is parallel to the c-axis. When the classical dipole contribution is added to the MAE calculation, the easy axis is at an angle of $20°$ from the c-axis [56]. Hence theory reproduces the peculiar feature of an easy axis of Gd which is not aligned along a crystallographic direction, but is pointing away from the c-axis. However, the angle is somewhat underestimated in the calculations and illustrates that it is difficult to achieve an accuracy of $\mu\mathrm{eV}$/atom level.

In the left part of Fig. 12.5 the contribution to the MAE is broken up into different contributions, e.g., from states that are close to the Fermi level, and for states with energies lower in energy, for different regions in **k**-space. It may be seen in the figure that the majority of the contribution to the MAE comes from states close to the Fermi level. This is a general phenomenon, since the MAE can be shown to be the result of occupied states which are
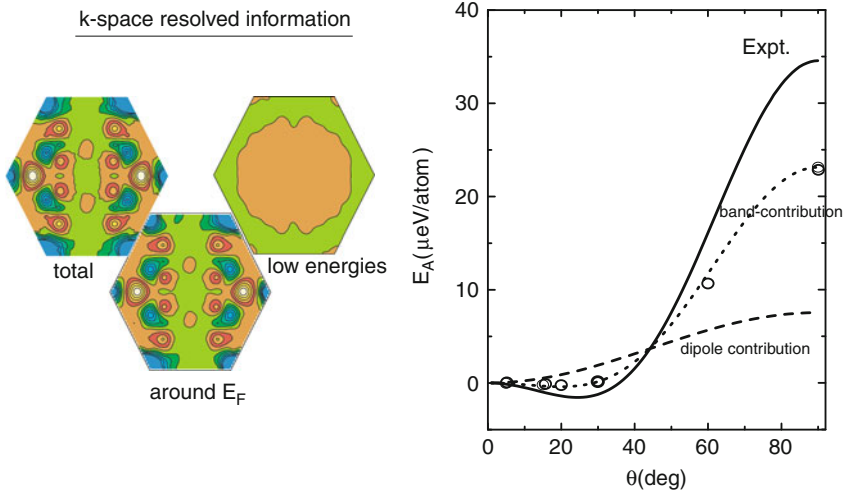
Fig. 12.5. (*Right part*) Calculated and measured contribution to the MAE of hcp Gd. The experimental data is given as a *full line*, the band contribution (MAE) is given as a *dotted line* and the dipole term as a *dashed line*. (*Left part*) Different contributions to the MAE over the Brillouin zone (at $k_z = 0$). The inclusion of all states is labeled "total", whereas the states close to the Fermi level are labeled "around E_F", and contributions from deeper lying states is labeled "lower energies". Data from [56]

spin–orbit coupled to unoccupied states. In second-order perturbation theory (which is appropriate for hcp Gd with a non-cubic symmetry), the MAE can be approximated as

$$E_{\mathrm{MAE}} \approx \Sigma_{\mathrm{o,u}} \frac{|\langle o\,|\xi\,\mathbf{l}\cdot\mathbf{s}|\,u\rangle|^2}{\epsilon_{\mathrm{o}} - \epsilon_{\mathrm{u}}}, \tag{12.3}$$

where ξ is the strength of the spin–orbit coupling, whereas $|o\rangle$ and $|u\rangle$ are the eigenstates of occupied and unoccupied levels, respectively. Since this contribution clearly becomes more important when the difference between ϵ_{o} and ϵ_{u} is small, it is states close to the Fermi level which are the most important ones for the MAE. Hence, in a sense the calculation of the MAE of a material is to a large extent a matter of very accurately resolving the Fermi surface of that material.

12.3 Magnetism of Nano-objects

We have seen earlier in this chapter that for the case of fcc Co, the ratio between the orbital and spin moments increases dramatically as the thickness of the surface layer is reduced. In general, the dimensionality of a system has

profound consequences for its magnetic properties. This means that clusters, nanowires, and surfaces may have very different magnetic properties compared to the corresponding bulk material.

RSPt has been used to analyze the magnetic properties of transition metals in the form of ultra-thin nanowires, i.e., wires that are only one atom thick [69, 70, 214]. When interpreting the calculations, it is important to realize that the magnetic phase we attempt to describe in this way is a superparamagnetic one rather than a static one since thermal fluctuations tend to be large in nanosystems.

In transition metal nanowires, the d-bandwidth is considerably smaller than in the bulk. For metals such as Pd or Pt, which have a relatively high magnetic susceptibility already as bulk, the decreased d-bandwidth makes it favorable to spin-polarize. Pd is an especially illustrative case since the isolated atom is a singlet with a full 4d shell and an empty 5s shell. The two levels are almost degenerate, with the 5s level just slightly above the 4d level. In the bulk, the Pd 4d band is partially filled but too wide to produce a spin-polarized ground state. The nanowire forms an intermediate between the atomic and bulk situations. Both the 4d and 5s atomic levels broaden into bands, but since the 5s band becomes much broader than the 4d band, it is favorable for the system to partially empty the 4d band into the 5s band. At the same time, the one-dimensional 4d density of states is large enough at the Fermi level to fulfill the Stoner criterion, and thus a magnetic ground state results.

In Pt nanowires, the large spin–orbit coupling gives rise to a very interesting phenomenon. The ground state is magnetic, with the moments pointing in the wire direction. However, it turns out that the magnetic moment decreases as it is rotated away from the wire direction. At an angle of 45° from the direction of the wire, the moment disappears completely. This phenomenon is called colossal magnetic anisotropy (CMA) and is predicted to give rise to anomalous tunneling behavior in Pt nanowires [214].

13

Excited State Properties

Abstract The phenomenological theory of optical properties of materials is presented. The general theory of calculations of optical properties from first principles theory is given, with special emphasis on the implementation in the FP-LMTO method. Numerical examples of semi-conductors as well as metals are presented. Interband and intraband transitions are discussed, as are maneto-optical effects. The chapter ends with a description of the theory of x-ray magnetic circular dichroism, and how its calculation is made possible in the FP-LMTO method.

With RSPt, it is possible to calculate optical and magneto-optical spectra as well as X-ray absorption (XAS) and X-ray magnetic circular dichroism XMCD. The implementation is based on the dipole approximation. Furthermore, the usual DFT underestimation of the energy band gap is dealt with using the scissors operator. This very simple model makes the calculations fast. More elaborate, alternative ways of computing excited states within DFT involve the GW approximation, the two-particle Dyson equation, or time-dependent DFT. In this chapter, we give details on our implementation and its limitations and strengths and we discuss the physical reasons as to why the simple dipole approximation combined with the scissors operator give such good results. We also present some general background theory for these types of excitation spectra and give examples of calculated spectra.

13.1 Phenomenology

Let us introduce the subject of calculating excitation spectra by briefly reviewing the macroscopic theory of optical and magneto-optical properties. The interaction of electromagnetic radiation with a magnetic medium is described classically by Maxwell's equations [125]. For linear materials the electric displacement **D** is related to the total electric field **E** and the polarization **P** as

$$\mathbf{D} = \epsilon_0 \mathbf{E} + \mathbf{P} = (1 + \chi_e)\epsilon_0 \mathbf{E} = \boldsymbol{\epsilon} \mathbf{E} \,. \tag{13.1}$$

Similarly, the magnetic field $\mathbf{B}$ is related to $\mathbf{H}$ and the magnetization $\mathbf{M}$ according to

$$\mathbf{B} = \mu_0(\mathbf{H} + \mathbf{M}) = (1 + \chi_m)\mu_0 \mathbf{H} = \boldsymbol{\mu} \mathbf{H} \,. \tag{13.2}$$

Here, ϵ_0, μ_0, χ_e, and χ_m are the vacuum permittivity, the vacuum permeability, the electric susceptibility, and the magnetic susceptibility, respectively. $\boldsymbol{\epsilon}$ is the dielectric function and $\boldsymbol{\mu}$ the magnetic permeability. A third fundamental equation is Ohm's law, which connects the macroscopic current density $\mathbf{J}$ with the electric field $\mathbf{E}$ according to

$$\mathbf{J} = \boldsymbol{\sigma}.\mathbf{E} \,, \tag{13.3}$$

where $\boldsymbol{\sigma}$ is the conductivity. Equations (13.1), (13.2), and (13.3) are known as the material equations. They characterize the *response functions of the medium to external excitations.* In general the dielectric function is a function of both spatial and time variables that relate the displacement field $\mathbf{D}(\boldsymbol{r}, t)$ to the total electric field $\mathbf{E}(\boldsymbol{r}', t')$ according to

$$\mathbf{D}(\mathbf{r}, t) = \int \int_{-\infty}^{t} \boldsymbol{\epsilon}(\mathbf{r}, \mathbf{r}', t')\mathbf{E}(\mathbf{r}', t')\mathrm{d}t'\mathrm{d}r' \,. \tag{13.4}$$

In the following we neglect the spatial dependence of the dielectric function and consider only its frequency dependence $\boldsymbol{\epsilon}(\omega)$. Usually, the effect of the magnetic permeability $\boldsymbol{\mu}(\omega)$ on optical phenomena is small and we therefore assume from now on that $\boldsymbol{\mu}(\omega) = \mu_0 \boldsymbol{I}$ where $\boldsymbol{I}$ is a unit tensor. It should be stressed also that $\boldsymbol{\epsilon}$ and $\boldsymbol{\mu}$ may depend on the field strength. In such cases higher order terms in a Taylor expansion of the material parameters lead to the appearance of non-linear effects [34]. Using the material equations and Maxwell's equations it can be shown that the dielectric function and the conductivity are connected according to

$$\boldsymbol{\epsilon} = \frac{1}{\epsilon_0}\left(1 + \mathrm{i}\frac{\boldsymbol{\sigma}}{\omega}\right) \,. \tag{13.5}$$

The real part of the dielectric function $\boldsymbol{\epsilon}$ is often denoted $\boldsymbol{\epsilon}^{(1)}$ or $\boldsymbol{\epsilon}_1$ and the imaginary part is denoted $\boldsymbol{\epsilon}^{(2)}$ or $\boldsymbol{\epsilon}_2$. Similar notation for the conductivity $\boldsymbol{\sigma}$ is also in use.

For non-magnetic materials with cubic structure, the form of the dielectric tensor becomes particularly simple. The three diagonal components of the dielectric tensor are then equal, the off-diagonal components are zero, and thus we can write

$$\boldsymbol{\epsilon}(\omega) = \epsilon(\omega)\boldsymbol{I} \,. \tag{13.6}$$

With a macroscopic magnetization $\mathbf{M}$ directed along the z-axis, the symmetry is lowered and $\boldsymbol{\epsilon}(\omega)$ becomes [135]

$$\epsilon(\mathbf{M}, \omega) = \begin{pmatrix} \epsilon_{xx} & \epsilon_{xy} & 0 \\ -\epsilon_{xy} & \epsilon_{xx} & 0 \\ 0 & 0 & \epsilon_{zz} \end{pmatrix}. \tag{13.7}$$

The components of the dielectric tensor depend on the magnetization and satisfy the Onsager relations

$$\epsilon_{ij}(-\mathbf{M}, \omega) = \epsilon_{ji}(\mathbf{M}, \omega), \tag{13.8}$$

where $i, j = x, y,$ or z. The diagonal components of the dielectric tensor are therefore even functions of $\mathbf{M}$ and the non-diagonal ones are odd functions of $\mathbf{M}$. In the lowest order in $\mathbf{M}$

$$\epsilon_{xy} \sim M, \ \epsilon_{zz} - \epsilon_{xx} \sim M^2. \tag{13.9}$$

In the absence of an external current ($\mathbf{J} = 0$) and free charges ($\rho = 0$) Maxwell's equations reduce to

$$\nabla \times \mathbf{E} = -\mu_0 \frac{\partial \mathbf{H}}{\partial t}, \tag{13.10}$$

$$\nabla \times \mathbf{H} = \epsilon \frac{\partial \mathbf{E}}{\partial t}. \tag{13.11}$$

After substitution of $\mathbf{E}$ and $\mathbf{H}$ in the form of plane waves

$$\mathbf{E} = \mathbf{E}_0 e^{[i(\mathbf{q} \cdot \mathbf{r} - \omega t)]}, \tag{13.12}$$
$$\mathbf{H} = \mathbf{H}_0 e^{[i(\mathbf{q} \cdot \mathbf{r} - \omega t)]},$$

we obtain (for the cubic example with $\mathbf{M}$ along the z-axis) the secular equation

$$\begin{pmatrix} N^2 - \epsilon_{xx} & -\epsilon_{xy} & 0 \\ \epsilon_{xy} & N^2 - \epsilon_{xx} & 0 \\ 0 & 0 & N^2 - \epsilon_{zz} \end{pmatrix} \begin{pmatrix} E_x \\ E_y \\ E_z \end{pmatrix} = 0, \tag{13.13}$$

where ω is the frequency of the radiation and $\mathbf{q}$ the wave vector of light. When the light propagates along the z-direction, $E_z = 0$, and one finds the eigenvalues

$$N_\pm^2 = \epsilon_{xx} \pm i\epsilon_{xy}. \tag{13.14}$$

This means that the normal modes accounting for the response (the displacement field $\mathbf{D}$) to the plane-wave field $\mathbf{E}$ are

$$\mathbf{D}_\pm = N_\mp^2 (\mathbf{E}_x \pm i\mathbf{E}_y), \tag{13.15}$$

i.e., a left and right polarized light wave with complex refractive indices of N_- and N_+, respectively. The eigenmodes or eigenfunctions (13.15) correspond to photons with helicity of $+1$ (spin and momentum parallel) and -1 (spin and momentum antiparallel). The eigenvalues $N_\pm$ determine the response of the system to the circular waves. We see that the response to D_- will be different

from the response to D_+ if and only if the off-diagonal components of the conductivity tensor are non-zero. Since this occurs when a magnetic field is present (assuming that the spin–orbit interaction is present), the difference in response to the circular waves caused by the magnetic field is named magneto-optical effects. Time reversal of D_- gives D_+ and vice versa, and thus the magneto-optical effects can also be viewed as originating from broken time reversal symmetry. From the form of the eigenvalues we see that the absorptive part of the off-diagonal optical conductivity is proportional to the difference in absorption of left and right circularly polarized light, and its sign is directly related to the spin polarization of the states responsible for the transitions.

Experimental optical results often come in the form of reflectivity spectra, energy loss, absorption, refractive indices, and changes in the direction of polarization upon reflection or transmittance. Below, we summarize some of the most common formulas connecting the dielectric function and optical conductivity with measured quantities. In the following formulas, the Cartesian coordinate subscripts and the functional dependence on ω have been suppressed.

13.1.1 Index of Refraction and Attenuation Coefficient

The complex index of refraction N is often written as $N = n + \mathrm{i}k$, where n is referred to as the (real) index of refraction and k the extinction coefficient. The physical interpretation of these quantities is that when a plane wave of light is propagating through a material, the velocity of propagation is c/n, i.e., lower compared to the velocity of light of vacuum, c. The amplitude is also attenuated with a factor e^{-kr}, where r is the distance traveled in the material.

13.1.2 Reflectivity

The reflectivity is the ratio between the incident and reflected light intensities. Since the intensity is proportional to the square of the wave amplitude, this can be written as

$$R = r^*r\,, \tag{13.16}$$

where r is called the reflection coefficient. It is the (complex) ratio between the incident and the reflected electric field of the plane wave. For normal incidence, the reflection coefficient is given by [37]

$$r = \frac{N-1}{N+1} \tag{13.17}$$

and the reflectivity becomes

$$R = \left|\frac{N-1}{N+1}\right|^2\,. \tag{13.18}$$

13.1.3 Absorption Coefficient

The absorption coefficient α is defined as

$$\alpha = -\frac{1}{I}\frac{dI}{dr}\,, \qquad (13.19)$$

where I is the intensity of the plane wave a distance r into the material. By differentiation of I expressed using the plane wave (13.12), one finds that α is proportional to the imaginary part of the refractive index times the frequency:

$$\alpha = \frac{2\omega k}{c}\,. \qquad (13.20)$$

13.1.4 Energy Loss

When a beam of monoenergetic electrons impinges on a solid, excitations in the solid, e.g., plasmon excitations or interband transitions, result in energy losses in the electron beam. In this case, the electric field causing the response is in the direction of propagation of the beam, and not perpendicular to it, as is the case for photons. From dielectric theory one can show that the energy loss of the electron beam is proportional to the energy loss function L, which is defined as

$$L = -\mathrm{Im}\,\frac{1}{\epsilon}\,. \qquad (13.21)$$

13.1.5 Faraday Effect

In 1845, Faraday discovered [91] that the polarization vector of linearly polarized light is rotated upon transmission through a sample of thickness d that is exposed to a magnetic field parallel to the propagation direction of light. Indeed, in a ferromagnet, the left-hand and right-hand circularly polarized light waves propagate with different refractive indices or different velocities c/n_- and c/n_+, i.e., there is magnetic circular birefringence. When the two transmitted light waves are combined at the exit surface of the sample, they yield again linearly polarized light, but its plane of polarization is rotated by the so-called Faraday angle θ_F. Further, if two circularly polarized waves attenuate at different rates, then after traveling through the sample, their relative amplitude changes. The transmitted light becomes elliptically polarized, with an ellipticity η_F corresponding to the ratio of the minor to the major axes of the polarization ellipsoid.

The Faraday rotation and ellipticity are related to the complex refractive index N through

$$\theta_\mathrm{F} + \mathrm{i}\eta_\mathrm{F} = \frac{\omega d}{2c}\,(N_+ - N_-)\,, \qquad (13.22)$$

where c is the velocity of light in vacuum and d is the thickness of the film.

The Faraday ellipticity is closely related to the magnetic circular dichroism, which is defined as the difference of the absorption coefficient μ between right and left circularly polarized light

$$\Delta\mu = (\mu_+ - \mu_-) = -\frac{4\eta_F}{d} . \tag{13.23}$$

13.1.6 Magneto-optical Kerr Effect

About 30 years after Faraday's work, Kerr [132] observed that when linearly polarized light is reflected from a magnetic material, its polarization plane (the major axis of the ellipse) rotates over a small angle with respect to that of the incident light.

The relative orientation of the magnetization vector with respect to the reflective surface and the plane of incidence of the light beam determines the three types of the magneto-optical effects in reflection: the polar, the longitudinal, and the transversal or equatorial Kerr effects; see Fig. 13.1. For linearly polarized incident light the reflected light will be elliptically polarized in the polar Kerr geometry. For most materials the Kerr rotation and ellipticity are of the order of 1°. Some original papers on the basic theory and review articles on the subject are listed in [19, 29, 184]. In the polar geometry, which is the only one discussed here, the magnetic moment is perpendicular to the surface and parallel to the z-axis and the light beam. In a magnetic material, the normal modes, or eigenfunctions, of the conductivity tensor are circular waves or helicity eigenfunctions. Normal modes are reflected separately, since the response of one normal mode by definition never contain components from any other normal mode. In analogy with reflection of a plane wave discussed above, the reflection coefficients $r_\pm$ for the two circular waves are

$$r_\pm = \frac{N_\pm - 1}{N_\pm + 1} , \tag{13.24}$$

where $N_\pm$ are the refractive indices (13.14). In order to define the Kerr rotation and ellipticity, we rewrite the reflection coefficients for the circular waves as

$$r_\pm = |r_\pm| e^{i\Delta_\pm} . \tag{13.25}$$
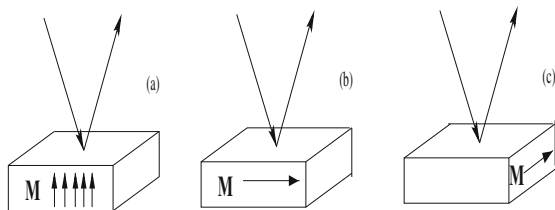
Fig. 13.1. The different geometries for the MO Kerr effect: (**a**) the polar, (**b**) the longitudinal, and (**c**) the transversal Kerr effects

Here, $\Delta_\pm$ are the phase shifts experienced by the circularly polarized waves upon reflection. The *polar Kerr rotation* θ_K is half the relative phase shift in the reflected amplitude of the two circular polarizations, i.e.,

$$\theta_K = -\frac{1}{2}\left(\Delta_+ - \Delta_-\right). \tag{13.26}$$

If the two circular waves experience the same phase shift, the reflected wave will have the same polarization direction as the incident wave, and θ_K is zero. A finite phase change difference will result in that the plane of polarization of the light is rotated. The maximum possible (meaningful) phase shift difference between two waves is $90°$, and so the extreme values of θ_K are $\pm 90°$. The *polar Kerr ellipticity* η_K is a measure of how the shape of the wave has changed upon reflection and depends only on the absolute magnitudes of the reflection coefficients according to

$$\tan\eta_K = -\frac{|r_+| - |r_-|}{|r_+| + |r_-|}. \tag{13.27}$$

As an explicit example, consider the case when the incident wave is a plane wave. Then, if the outgoing wave is also a plane wave, $|r_+| = |r_-|$ and η_K is zero. In the other extreme only one of the circular waves is reflected at all and either $|r_+|$ or $|r_-|$ is zero. Then η_K reaches its extremum value of $\pm 45°$. The formulas (13.24), (13.25), (13.26), and (13.27) above can be summarized in a compact form as the quotient between the two reflection coefficients:

$$\frac{r_-}{r_+} = \frac{1 + \tan\eta_K}{1 - \tan\eta_K}e^{2i\theta_K} = \frac{(N_- - 1)(N_+ + 1)}{(N_- + 1)(N_+ - 1)}. \tag{13.28}$$

For small Kerr signals, the complex Kerr angle is approximately given by [129]

$$\theta_K + i\eta_K = \frac{-\sigma_{xy}}{\sigma_{xx}\sqrt{1 + \frac{4\pi i}{\omega}\sigma_{xx}}}. \tag{13.29}$$

This last expression is the one normally used in the calculations of the magneto-optical Kerr effect.

13.2 Excited States with DFT: A Contradiction in Terms?

The density functional theory (DFT) of Hohenberg, Kohn, and Sham is the method of choice for describing the ground state properties of materials [116, 140]. However, in the initial derivation of the DFT, the eigenvalues are Lagrange multipliers introduced to minimize the energy functional with a constraint on the number of particles, which also leads to an orthogonalization of the eigenstates, which in turn are used to compute the total energy and the

charge density. In this formulation the eigenvalues therefore have no physical meaning and should not be considered as excited states. Nevertheless, the DFT in the local density approximation (LDA) or in its spin-resolved local density formulation (LSDA) has been used successfully to compute the excited states, namely, optical and magneto-optical properties, X-ray absorption, and magnetic dichroism spectra.

The LDA or LSDA were indeed intended to compute the ground state properties of materials, and their use during the last two decades has produced an excellent track record in the computation of these properties for a wide variety of materials, ranging from simple metals to complex semiconductor superlattices. However, it is now believed that the DFT can do more than just compute the ground state properties. This is because the Kohn–Sham equations may be viewed as deriving from a simplified quasiparticle (QP) theory where the self-energy is local and time averaged, i.e., $\Sigma(\boldsymbol{r}, \boldsymbol{r}', t) \approx V_{xc}(\boldsymbol{r})\delta(\boldsymbol{r} - \boldsymbol{r}')\delta(t)$, here $V_{xc}(\boldsymbol{r})$ is the local exchange and correlation potential as, for example, parameterized by Von Barth and Hedin [250]. Viewed in this way, the KS eigenvalues are then approximate QP energies and may be compared to experimental data. This argument is supported by quasiparticle calculations within the so-called GW approximation of Hedin [114] showing that the valence QP energies of semiconductors are in good agreement with these obtained using LDA, and the conduction QP energies differ by, approximately, a rigid energy shift [100, 118]. In the literature this shift is often called "scissors-operator" shift [155, 156].

Spectroscopy has become a standard tool for measuring excited states of materials. It owes its impressive advances mainly to the availability of synchrotron-tunable highly polarized radiation. In particular, the measurement of optical, magneto-optical properties as well as magnetic X-ray dichroism are now becoming routine tasks for probing the structural and magnetic properties of materials. Considerable attention has been focused on transition metal surfaces and thin films due to their novel physical properties different from that of bulk materials, as well as due to potential industrial applications such as magneto-optical recording, sensors, or technology based on giant magneto-resistance. In this respect, theory is falling far behind experiment and it is becoming hard to give a basic interpretation of experimental data.

13.3 Quasiparticle Theory Versus the Local Density Approximation

The quasiparticle (QP) electronic structure of an interacting many-body system is described by the single-particle eigenstates resulting from the interaction of this single particle with the many-body electron gas of the system. The single-particle eigenstate energies are the results of solving a Schrödinger-like equation containing the non-local and energy-dependent self-energy instead of the exchange-correlation potential appearing in Kohn–Sham-like equations:

$$(T + V_H + V_{\text{ext}})\Psi(\mathbf{r}) + \int \mathrm{d}^3 r' \Sigma(\mathbf{r}, \mathbf{r}', E)\Psi(\mathbf{r}') = E\Psi(\mathbf{r}). \qquad (13.30)$$

Note that in this equation we have used E to symbolize an eigenvalue, unlike ϵ used in all other chapters of this book. The reason for this change of nomenclature is that historically ϵ is used in the definition of the dielectric function, (13.1). In (13.30), the self-energy Σ contains all many-body effects. Almost all ab initio QP studies were performed within the so-called GW approximation, where the self-energy Σ is calculated within Hedin's GW approximation. This method consists of approximating the self-energy as the convolution of the LDA self-consistent Green function G and the screened Coulomb interaction W within the random-phase approximation. The QP eigenvalues are often obtained using first-order perturbation theory starting from LDA eigenvalues and eigenvectors [98, 118, 119], although there are early calculations starting from Hartree–Fock [231] or tight-binding [228] methods. Nevertheless, the best results are based on a DFT starting point [18, 25, 98, 99, 118, 119, 195].

Thus the GW-predicted optical excitation energies of semiconductors are within 0.1 eV from the experimental results and the surprising fact is that the QP wave functions are almost identical to those produced within the LDA [118] (the wave function overlap is more than 99%). For a general review of GW calculations, see the review by Araysetianwan and Gunnarsson [18] or by Aulbur et al. [25].

It is clear that the quasiparticle Schrödinger equation resembles the Kohn–Sham equation. Both equations describe a fictitious electron moving in an effective potential. The difference is that the self-energy is non-local and energy dependent, whereas the LDA potential is local and averaged over time. This resemblance can be further pushed by noticing that DFT can be used to obtain excitation energies. For example, the ionization energy, I, and the electron affinity, A, are both defined as differences between ground state energies:

$$I = E(N - 1) - E(N) \quad \text{and} \quad A = E(N) - E(N + 1), \qquad (13.31)$$

where N is the number of electrons of the system. Since the DFT gives the correct ground state energies it should produce, in principle, the correct ionization and electron affinity energies. For metals, the addition or removal of an electron from the system costs the same energy, and hence the ionization energy is equal to the electron affinity. For insulators, the energy gap makes all the difference and hence breaks this symmetry. Thus the energy band gap is given by $E_{\mathrm{g}} = I - A = E(N + 1) + E(N - 1) - 2E(N)$. In practice, however, the calculation is often obtained within the LDA and the energy band gap is calculated as the difference between the lowest conduction band and the highest valence band. It was shown by Sham and Schlüter [204, 205] and Perdew and Levy [181] that the calculated energy gap differs from the true band gap by an amount Δ even when the DFT is used without the LDA. For silicon, the calculated LDA energy gap is about half of the true band gap. In germanium the situation is even worse – the calculated

LDA energy gap is zero. For most of the semiconductors, the *GW* calculations show that the LDA eigenvalues differ from the *GW* quasiparticle energy by a constant Δ which is almost independent of the $\boldsymbol{k}$-point. This finding is important and shows that the LDA eigenvalues have some meaning and could be used to calculate excited states. So as stated in the introduction, the Kohn–Sham equations could be viewed as deriving from a simplified quasiparticle (QP) theory where the self-energy is made local and time averaged, i.e., $\Sigma(\mathbf{r}, \mathbf{r}', t) \approx V_{\mathrm{xc}}(\mathbf{r})\delta(\mathbf{r} - \mathbf{r}')\delta(t)$. This approximation is certainly good for metals where we have a good database for excited state calculated within the LDA [3, 8, 10, 62, 110, 111, 144, 151, 175, 192, 239, 252, 256] and where the agreement with experiment is good. For semiconductors, this approximation is not bad either, provided we know the value of the discontinuity of the exchange and correlation. Usually, this value is provided by *GW* calculations or by experiment.

13.4 Calculation of the Dielectric Function

We now turn our focus to the quantum-mechanical description of the dielectric function and how it can be approximately calculated using the momentum matrix elements. We also provide technical details regarding the implementation in RSPt.

13.4.1 Dynamical Dielectric Function

An electromagnetic field of frequency ω and a wave vector $\mathbf{q} + G$ interacting with atoms in a crystal produces a response of frequency ω and a wave vector $\mathbf{q} + G'$ ($\mathbf{G}$ and $\mathbf{G}'$ being reciprocal lattice vectors). The microscopic field of wave vector $\mathbf{q} + G'$ is produced by the Umklapp processes as a result of the applied field $E_0(\mathbf{q} + G, \omega)$

$$E_0(\mathbf{q} + \mathbf{G}, \omega) = \sum_{\mathbf{G}'} \epsilon_{\mathbf{G},\mathbf{G}'}(\mathbf{q}, \omega) E(\mathbf{q} + \mathbf{G}', \omega), \qquad (13.32)$$

where $E(\mathbf{q} + G, \omega)$ is the total field producing the non-diagonal elements in the microscopic dielectric function $\epsilon_{\mathbf{G},G'}(\mathbf{q}, \omega)$. The microscopic dielectric function in the random-phase approximation is given by [2, 262]

$$\epsilon_{\mathbf{G},\mathbf{G}'}(\mathbf{q}, \omega) = \delta_{\mathbf{G},\mathbf{G}'} - \frac{8\pi e^2}{\Omega|\mathbf{q} + \mathbf{G}||\mathbf{q} + \mathbf{G}'|} \qquad (13.33)$$

$$\times \sum_{\mathbf{k},n,n'} \frac{f_{n',\mathbf{k}+\mathbf{q}} - f_{n,\mathbf{k}}}{\epsilon_{n',\mathbf{k}+\mathbf{q}} - \epsilon_{n,\mathbf{k}} - \hbar\omega + \mathrm{i}\delta}$$

$$\langle n', \mathbf{k} + \mathbf{q}|\mathrm{e}^{\mathrm{i}(\mathbf{q}+\mathbf{G})\mathbf{r}}|n, \mathbf{k}\rangle\langle n, \mathbf{k}|\mathrm{e}^{-\mathrm{i}(\mathbf{q}+\mathbf{G}')\mathbf{r}}|n', \mathbf{k} + \mathbf{q}\rangle.$$

Here n and n' are the band indexes, $f_{n,\mathbf{k}}$ is the zero temperature Fermi distribution, and Ω is the cell volume. The energies $\epsilon_{n,\mathbf{k}}$ and the crystal wave function $|n,\mathbf{k}\rangle$ are produced for each band index n and for each wave vector $\mathbf{k}$ in the Brillouin zone.

The macroscopic dielectric function in the infinite wavelength limit ($\mathbf{q} \to 0$) is given by the inversion of the microscopic dielectric function

$$\epsilon(\omega) = \lim_{\mathbf{q}\to\mathbf{0}} \frac{1}{[\epsilon^{-1}_{\mathbf{G},\mathbf{G}'}(\mathbf{q},\omega)]_{\mathbf{0},\mathbf{0}}} \tag{13.34}$$

$$= \epsilon_{0,0}(\omega) - \lim_{\mathbf{q}\to\mathbf{0}} \sum_{\mathbf{G},\mathbf{G}'\neq\mathbf{0}} \epsilon_{0,\mathbf{G}}(\mathbf{q},\omega)T^{-1}_{\mathbf{G},\mathbf{G}'}(\mathbf{q},\omega)\epsilon_{\mathbf{G}',0}(\mathbf{q},\omega)\,,$$

where $T^{-1}_{\mathbf{G},\mathbf{G}'}$ is the inverse matrix of $T_{\mathbf{G},G'}$ containing the elements $\epsilon_{\mathbf{G},G'}$ with $\mathbf{G}$ and $\mathbf{G}' \neq \mathbf{0}$, and $\epsilon_{0,0}$ is the macroscopic dielectric function without local field effects. The first term of this equation is the interband contribution to the macroscopic dielectric function and the second term represents the local-field correction to ϵ. The most recent ab initio pseudo-potential calculation found that the local-field effect reduces the static dielectric function by at most 5% [155]. Previous calculations with the same method have also found a decrease of ϵ_∞ by about the same percentage [28, 118]. For insulators the dipole approximation of the imaginary part of the first term $\epsilon_{0,0}$ of (13.34) is given by [83]

$$\epsilon^{(2)}(\omega) = \frac{e^2}{3\omega^2\pi} \sum_{n,n'} \int \mathrm{d}\mathbf{k}|\langle n,\mathbf{k}|\mathbf{v}|n',\mathbf{k}\rangle|^2 f_{n,\mathbf{k}}(1 - f_{n',\mathbf{k}})\delta(e_{\mathbf{k},n',n} - \hbar\omega)\,. \tag{13.35}$$

Here, $\mathbf{v}$ is the velocity operator and in the LDA $\mathbf{v} = \mathbf{p}/m$ ($\mathbf{p}$ being the momentum operator), and where $e_{\mathbf{k},n,n'} = \epsilon_{n',\mathbf{k}} - \epsilon_{n,\mathbf{k}}$. Since $\epsilon^{(2)}(\omega)$ is directly proportional to the absorption matrix elements, it is called the absorptive part of the dielectric function. In contrast, $\epsilon^{(1)}(\omega)$ is called the dispersive part and can be calculated from $\epsilon^{(2)}(\omega)$ using the Kramers–Kronig relations [31]. The real and imaginary parts of the dielectric function will also be called ϵ_1 and ϵ_2.

As an alternative to the above approach based on the dielectric function, one can derive a microscopic model the optical conductivity tensor (in atomic units $e^2 = 1$ and $m = 1/2$) using Kubo formalism. Within linear response theory and using band structure methods Callaway and Wang [151, 252] found that the optical conductivity is given by

$$\sigma^{(1)}_{\alpha\beta}(\omega) = \frac{4\pi}{\omega} \sum_{\mathbf{k}} \sum_{\nu\nu'} \frac{(f(\epsilon_{\nu\mathbf{k}}) - f(\epsilon_{\nu'\mathbf{k}}))}{(\omega - \omega_{\nu\nu'}(\mathbf{k})+i\gamma)} \frac{M^\alpha_{\nu'\nu}(\mathbf{k})M^\beta_{\nu\nu'}(\mathbf{k})}{\omega_{\nu\nu'}(\mathbf{k})}\,, \tag{13.36}$$

where $M^\alpha_{\nu'\nu}(\mathbf{k})$ are transition matrix elements. The two descriptions are of course equivalent. The matrix elements $\langle n,\mathbf{k}|\mathbf{p}|n',\mathbf{k}\rangle$ are calculated for each

projection p_j, $j = x$, y, z, with the wave function $|n, \mathbf{k}\rangle$ expressed in terms of the full-potential LMTO crystal wave function. The $\mathbf{k}$-space integration is performed using the tetrahedron method [126, 153] with a large number of irreducible $\mathbf{k}$-points the Brillouin zone. The irreducible $\mathbf{k}$-points are obtained from a shifted $\mathbf{k}$-space grid with respect to the high symmetry planes and Γ point. The shift should be a half step in each of the k_x, k_y, and k_z directions. This scheme produces highly accurate integration in the Brillouin zone by avoiding high symmetry points. In this way, the problem of connecting degenerate energies to non-degenerate energies is avoided. To take into account the fractional occupancy at the Fermi level, the BZ integration is performed using the algorithm of Rath and Freeman [191].

13.4.2 Momentum Matrix Elements

To calculate the momentum matrix elements, we first define a tensor operator of order 1 from the momentum operator $\nabla_0 = \nabla_z = \partial/\partial z$ and $\nabla_{\pm 1} = \mp 1/\sqrt{2}(\partial/\partial x \pm i\partial/\partial y)$. The muffin-tin part of the momentum matrix elements is calculated using the commutator $[\nabla^2, x_\mu] = 2\nabla_\mu$ so that

$$\int_{S_\tau} \mathrm{d}\mathbf{r}\phi_{\tau\ell'}(r)\, Y_{\ell'm'}(\widehat{\mathbf{r} - \tau})\nabla_\mu\phi_{\tau\ell}(r)Y_{\ell m}(\widehat{\mathbf{r} - \tau}) = -\tfrac{i}{2}G^{1\mu}_{\ell m, \ell', m'}$$

$$\int_0^{S_\tau} r^2\mathrm{d}r\phi_{\tau\ell'}\big(\tfrac{2}{r}\tfrac{\mathrm{d}}{\mathrm{d}r}r + \tfrac{\ell(\ell+1)-\ell'(\ell'+1)}{r}\big)\phi_{\tau\ell}(r)\,, \quad (13.37)$$

where $G^{1\mu}_{\ell m, \ell', m'}$ are the Gaunt coefficients and S_τ is the radius of the muffin-tin sphere of atom τ. In the interstitial region the plane-wave representation of the wave function makes the calculation straightforward. However, special care has to be taken regarding the removal of the extra contribution in the muffin-tin spheres. We find it much easier and faster to transform the interstitial matrix elements to an integral over the surface of the muffin-tin spheres, using the commutation relation of the momentum operator and the Hamiltonian in the interstitial region. The calculation of the interstitial momentum matrix elements is then similar to the calculation of the interstitial overlap matrix elements (see Chap. 6). The $\kappa = 0$ case has been already derived by Chen using the Korringa, Kohn, and Rostoker Green function method [49]. We have tested that the plane-wave summation and the surface integration provide the same results.

The momentum operator commutes with the Laplacian; therefore, the matrix elements of the momentum operator over the interstitial region can be calculated as an integral over the surface of the muffin-tin spheres. We use the fact that

$$-\nabla^2\, \mathbf{p}\psi = \kappa^2\mathbf{p}\psi\,.$$

A Hankel function can be integrated over a volume by knowing its integral over the bounding surface, i.e.,

$$\int_{\mathcal{I}} d^3r \nabla \left(\psi_1^* \nabla p_i \psi_2 - (\nabla \psi_1^*) \, p_i \psi_2 \right) = \left(\kappa_1^2 - \kappa_2^2 \right) \int_{\mathcal{I}} d^3r \psi_1^* p_i \psi_2 \,. \tag{13.38}$$

The surface of the interstitial consists of the exterior of the muffin-tin spheres and the unit cell boundary.

Over the surface of the muffin tins, the surface area is $S^2 d\Omega$ and the normal to the sphere points inward:

$$\left(\kappa_1^2 - \kappa_2^2 \right) \int_{\mathcal{I}} d^3r \; \psi_1^* p_i \psi_2$$
$$= - \sum_\tau S_\tau^2 \int dS \; \left(\psi_1^* \frac{\partial}{\partial r} p_i \psi_2 - \left(\frac{\partial}{\partial r} \psi_1^* \right) p_i \psi_2 \right) . \tag{13.39}$$

At a muffin-tin sphere boundary S_τ the Bloch wave function is given by (6.15). We let W denote the Wronskian $W(f,g) = fg' - f'g$. We further define

$$S^2 W_0 = S^2 W(K_\ell^T(\kappa), K_\ell(\kappa)) = \begin{pmatrix} 0 & 1 \\ -1 & 0 \end{pmatrix}$$

and

$$w_{\tau \ell} \kappa_1, \kappa_2 = S_\tau \frac{W(K_\ell^T(\kappa)), K_\ell(\kappa) - W_0}{\kappa_1^2 - \kappa_2^2},$$

$$\mathbf{p}\psi_i|_\tau = \sum_\mu \hat{\mathbf{e}}_\mu \sum_{\ell m} \left[K_{\ell-1m-\mu} \begin{pmatrix} \kappa_i^2 & 0 \\ 0 & 1 \end{pmatrix} \mathcal{G}(\ell-1, \, m-\mu; \, \ell, \, m; \, 1, \, \mu) \right.$$
$$\times - K_{\ell+1m-\mu} \begin{pmatrix} 1 & 0 \\ 0 & \kappa_i^2 \end{pmatrix} \mathcal{G}(\ell+1, \, m-\mu; \, \ell, \, m; \, 1, \, \mu) \Big]$$
$$\times B_{\ell m, \ell_i m_i}(\tau - \tau_i, \kappa_i, \mathbf{k}) \tag{13.40}$$

then

$$\langle \psi_f \mathbf{p}\psi_i \rangle_\tau = \sum_\tau \sum_\mu \hat{\mathbf{e}}_\mu \sum_{\ell m} \left[B_{\ell-1m-\mu, \ell_f m_f}(\tau - \tau_f, \kappa_f, \mathbf{k}) \mathbf{w}_{\tau \ell-1}(\kappa_\mathbf{f}, \kappa_\mathbf{i}) \right.$$
$$\times \begin{pmatrix} \kappa_i^2 & 0 \\ 0 & 1 \end{pmatrix} \mathcal{G}(\ell-1, \, m-\mu; \, \ell, \, m; \, 1, \, \mu)$$
$$\times - B_{\ell+1m-\mu, \ell_f m_f}(\tau - \tau_f, \kappa_f, \mathbf{k}) \mathbf{w}_{\tau \ell+1}(\kappa_\mathbf{f}, \kappa_\mathbf{i})$$
$$\times \begin{pmatrix} 1 & 0 \\ 0 & \kappa_i^2 \end{pmatrix} \mathcal{G}(\ell+1, \, m-\mu; \, \ell, \, m; \, 1, \, \mu) \Big]$$
$$\times B_{\ell m, \ell_i m_i}(\tau - \tau_i, \kappa_i, \mathbf{k}) \bigg) + \boldsymbol{\Delta}(\mathbf{f}, \mathbf{i}, \kappa_\mathbf{i}) , \tag{13.41}$$

where

$$(\kappa_f^2 - \kappa_i^2)\boldsymbol{\Delta}(\mathbf{f}, \mathbf{i}, \kappa_i) = \sum_\mu \hat{\mathbf{e}}_\mu(\tau_i) \Bigg[\tag{13.42}$$

$$+ B^\star_{\ell_i+1 m_i-\mu, \ell_f m_f}(\tau_i - \tau_f, \kappa_f, \mathbf{k})$$

$$\times \mathcal{G}\big(\ell_i + 1, m_i - \mu; \ell_i, m_i; 1, \mu\big)\kappa^2$$

$$- B^\star_{\ell_i-1 m_i-\mu, \ell_f m_f}(\tau_i - \tau_f, \kappa_f, \mathbf{k})$$

$$\times \mathcal{G}\big(\ell_i - 1, m_i - \mu; \ell_i, m_i; 1, \mu\big)\kappa^2 \Bigg]$$

$$+ \sum_\mu \hat{\mathbf{e}}_\mu(\tau_f) \Bigg[\tag{13.43}$$

$$+ B_{\ell_f+1 m_i+\mu, \ell_f m_f}(\tau_f - \tau_i, \kappa_i, \mathbf{k})$$

$$\times \mathcal{G}\big(\ell_f, m_i; \ell_f + 1, m_f + \mu; 1, \mu\big)$$

$$- B_{\ell_f-1 m_f-\mu, \ell_i m_i}(\tau_f - \tau_i, \kappa_i, \mathbf{k})$$

$$\times \mathcal{G}\big(\ell_f, m_f; \ell_f - 1, m_f + \mu; 1, \mu\big)\kappa^2 \Bigg].$$

The implementation used in the current version of RSPt makes use of the above equations.

13.4.3 Velocity Operator and Sum Rules

Equation (13.35) cannot be used directly to determine the optical properties of semiconductors, when the GW approximation or the scissors operator is used to determine the electronic structure. The velocity operator should be obtained from the effective momentum operator $\mathbf{p}^{\text{eff}}$ which is calculated using the self-energy operator, $\Sigma(\mathbf{r}, \mathbf{p})$, of the system [61]

$$\mathbf{v} = \frac{\mathbf{p}^{\text{eff}}}{m} = \frac{\mathbf{p}}{m} + \frac{\partial \Sigma(\mathbf{r}, \mathbf{p})}{\partial \mathbf{p}}. \tag{13.44}$$

As already mentioned, GW calculations show that the quasiparticle wave function almost equals the LDA wave function [100, 118]. Based on this assumption, it can be shown [61] that in the case of the scissors operator, where all the empty states are shifted rigidly by a constant energy Δ, the imaginary part of the dielectric function is a simple energy shift of the LDA dielectric function toward the high energies by an amount Δ, i.e., $\epsilon_2^{\text{QP}}(\omega) = \epsilon_2^{\text{LDA}}(\omega - \Delta/\hbar)$. The real part of the dielectric function is then obtained from the shifted ϵ_2 using Kramers–Kronig relations. The expression for the static dielectric function $\epsilon_1(0) = \epsilon_\infty^{QP}$ (the phonon contribution is neglected) is given by

$$\epsilon_\infty^{\text{QP}} = 1 + \frac{2e^2}{3\omega^2\pi^2} \sum_{n,n'} \int d\mathbf{k} f_{n,\mathbf{k}}(1 - f_{n',\mathbf{k}}) \frac{|\langle n, \mathbf{k}|\mathbf{p}|n', \mathbf{k}\rangle|^2}{(e_{\mathbf{k},n',n} + \Delta)e_{\mathbf{k},n',n}^2}, \tag{13.45}$$

$\epsilon_\infty^{\text{QP}}$ is very similar to $\epsilon_\infty^{\text{LDA}}$ except that the interband gap $e_{\mathbf{k},n',n}$ is substituted by the QP interband gap $e_{\mathbf{k},n',n} + \Delta$.

It is useful to check whether the LDA calculations fulfill the f-sum rule :

$$\frac{2}{3mn_{\text{v}}} \sum_{\mathbf{k}} \sum_{n,n'} f_{n,\mathbf{k}}(1 - f_{n',\mathbf{k}}) \frac{|\langle n, \mathbf{k}|\mathbf{p}|n', \mathbf{k}\rangle|^2}{e_{\mathbf{k},n',n}} = 1 \,, \tag{13.46}$$

where n_{v} is the number of valence bands, should be always checked to ensure the accuracy of the calculations.

It is seen that the dielectric function ϵ_2^{QP} calculated using the scissors-operator shift does not satisfy the sum rule (ω_{P} is the free electron plasmon frequency):

$$\int_0^\infty \omega \epsilon_2(\omega) \text{d}\omega = \frac{\pi}{2} \omega_{\text{P}}^2 \,, \tag{13.47}$$

because (i) ϵ_2^{LDA} satisfies this rule and (ii) ϵ_2^{QP} is obtained by a simple shift of ϵ_2^{LDA} by the scissors-operator Δ toward higher energies. The impossibility to satisfy both the f-sum rule and the integral sum rule within the scissors approximation shows the limitation of this approximation. While the scissors-operator approximation describes nicely the low-lying excited states, which is demonstrated by the good determination of the static dielectric function and the low energy structures, i.e., E_1 and E_2, in the imaginary part of the dielectric function, it seems to fail in describing the higher excited states. This is not surprising because the higher excited states, which are free electron like, are most probably well described within LDA and need no scissors-operator shift. This is supported by the fact that the energy loss function, $-\text{Im}\epsilon^{-1}$, within the LDA has its maximum roughly at the free electron plasmon frequency whereas within the scissors approximation the maximum is artificially shifted to higher energies. For our purpose, the scissors-operator shift remains a good approximation for the description of the low-lying excited states of semiconductors and their optical properties.

13.5 Optical Properties of Semiconductors

We have used RSPt, with the formalism outlined above, to calculate the optical properties of several materials [3, 9, 62, 185, 192]. In general the results are in good agreement with the experimental results. For semiconductors, however, good agreement with experiment is only achieved when the so-called scissors-operator shift is used. Figure 13.2 presents a relativistic calculation of the imaginary part of the dielectric function of GaAs compared to the experimental results of [23].

The LDA relativistic results underestimate the band gap by about $1.3\,\text{eV}$. When the imaginary part of the dielectric function is shifted to higher energies by $1.3\,\text{eV}$, we find that the E_1 and E_2 peaks are located at too high energy in the calculation. One needs to shift the spectrum by less than the band gap as
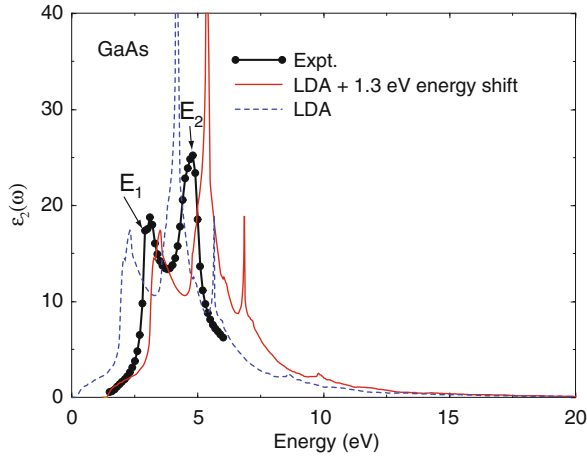
Fig. 13.2. Calculated imaginary part of the dielectric function of GaAs at the experimental equilibrium volume both within LDA and shifted by 1.3 eV, compared with the experimental results of [23]. The experimental E_1 is only slightly underestimated while E_2 is overestimated. Notice that the dielectric function shifted by 1.3 eV, which produces the correct band gap, overestimates the peak positions by about 0.3 eV. Excitonic effect should shift these peaks to lower values in agreement with experiment

done in [9] to produce good agreement with experiment. It seems then that the optical band gap is less than the band energy gap (1.5 eV). The optical band gap is produced by interband transitions to the low-lying conduction states. Excitonic effects are therefore important and are responsible for the reduction of the energy gap of semiconductors. It is interesting to notice though that the static dielectric function is in good agreement with experiment for GaAs, Si, and Ge when the shift correspond to the energy band gap obtained from photoluminescence [9, 155, 156].

More interesting are the wide band gap materials where the LDA calculated static dielectric function is in good agreement with experiment despite that the band gap is still underestimated by LDA. Correcting the band gap using the scissors operator makes the static dielectric much smaller than the measured value. As an example of wide gap material, we present in Fig. 13.3 the imaginary part of the dielectric function of GaN for the cubic (3) and wurtzite structures (B4).

Table 13.1 shows that the LDA dielectric constant calculations are in agreement with available experimental results and the pseudo-potential (PP) results [52] including local-field effects (an error concerning our calculation is reported in [52]; our value for $\epsilon_\infty^\parallel$ is not 4.48 but 5.48 and the PP value should then be 5.54). It is interesting to notice that the static dielectric function is in good agreement for all the nitrides [52] while the band gap is underestimated. The scissors-operator shift fails to explain the static dielectric function
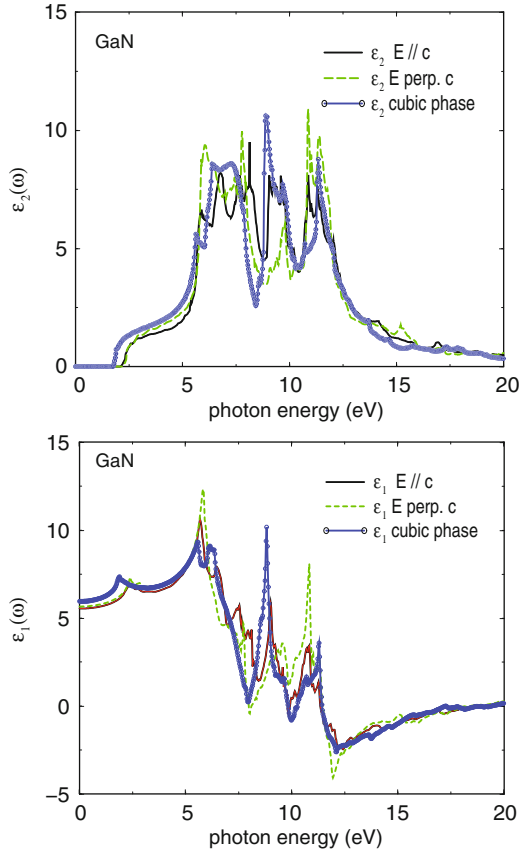
Fig. 13.3. Calculated imaginary and real parts of the dielectric function of GaN in its cubic and wurtzite forms. The LDA band gap for the cubic phase is 1.8 eV and for the wurtzite phase 2.2 eV

Table 13.1. Calculated static dielectric function ϵ_∞ for GaN compared to pseudo-potential (PP) results and experiment. For the wurtzite structure we have calculated the dielectric function for two polarization directions $-\epsilon_\infty^\parallel$ for a polarization parallel to the xy-plane and $\epsilon_\infty^\perp$ which is perpendicular to the xy-plane

	Zinc blende	Wurtzite	
	ϵ_∞	$\epsilon_\infty^\parallel$	$\epsilon_\infty^\perp$
PP	5.74	5.54	5.60
Present work	5.96	5.48	5.65
Expt.		5.35	5.35 ± 0.2

of large gap semiconductors. Recently, both local-field effects and electron–
hole interaction were included on an ab initio computation of the dielectric
function of few semiconductors [7, 29, 30] by extending the semi-empirical
approach by Hanke and coworkers [60, 165, 167, 230, 231] which is based
on the solution of the Bethe–Salpeter equation [60, 165, 167, 230]. The ex-
citonic effects seem to improve significantly the agreement between theory
and experiment. However, for large band gap semiconductors, such as dia-
mond, the inclusion of the excitonic effects seems to underestimate the optical
band gap by as much as 1 eV [29, 30]. It is not clear from these calculations
whether the static dielectric function for wide-band gap semiconductors is
improved when excitonic effects are included. More theoretical work along
these lines is needed to fully understand the dielectric function of wide-gap
semiconductors.

13.6 Optical Properties of Metals

In the case of metals, the problem associated with the self-energy and the dis-
continuity of the exchange-correlation derivate disappears due to screening.
On the other hand, at low photon energies, a large contribution to the optical
response will come from the metallic electrons. For materials with a band gap,
intraband transitions cannot take place since no bands are partially occupied.
The opposite is true for metals. Here, low-energy intraband transitions con-
stitute an important part of the total response for the diagonal components
of the conductivity tensor. They are usually modeled with the Drude formula,
which is based on the free electron model. The Drude formula is

$$\sigma_{\mathrm{D}}(\omega) = \frac{\omega_{\mathrm{P}}^2}{4\pi(\gamma_{\mathrm{D}} - \mathrm{i}\omega)} \,, \tag{13.48}$$

where γ_{D} is the inverse relaxation time and ω_{P} is the (unscreened) plasma
frequency. This contribution is also called the intraband contribution to the
optical spectra, to distinguish them from the interband contribution calculated
from (13.35). The plasma frequency can be calculated by integrating over the
Fermi surface and can thus be predicted from band structure calculations. In
the free electron model, the relation between the plasma frequency and the
number of electrons per unit volume N is given by

$$\omega_{\mathrm{P}}^2 = \frac{4\pi N e^2}{m} \,, \tag{13.49}$$

which can be used as a definition of the effective number of electrons N_{eff} per
unit volume. The other Drude parameter, γ_{D}, is proportional to the inverse of
the mean free time between scattering events. This parameter changes from
sample to sample of the same material, since it depends on, e.g., the amount
of impurities and dislocations.

Experimentally, the Drude parameters are calculated by fitting the Drude formula to a region of the optical spectrum where the interband transitions can be neglected. It is not always the case that such a region exists. One example of this is Fe, and the Drude parameters for Fe extracted from experimental data should therefore be interpreted with care. In magnetic metals, there is an intraband contribution also to the off-diagonal components of the conductivity tensor [88, 193].

The calculated optical properties of the group 4B transition metal carbides, nitrides, and oxides have been reported in [64]. These materials, also called refractory metal compounds, are hard and chemically stable, making them suitable as coatings of various kinds. The spectra of all compounds are related, and the differences can be qualitatively understood in terms of band filling, nuclear charge, and bandwidth. Since these materials are wideband systems, the achieved good agreement with experimental spectra, see Fig. 13.4, is not unexpected. An important aspect governing the optical properties is the onset of interband transitions. This occurs quite early in the carbides, whereas it is postponed in the nitrides. In fact, ZrN and HfN have virtually no interband transitions below 4 eV.

In the energy region lacking interband transitions, the reflectivity will be high, and as the interband transitions begin, the material will start to absorb light. The reflectivity then decreases, with the result that a thin film of the material will appear transparent. This spectral selectivity can be used in, e.g., energy saving window coatings, radiative coolers, and solar collectors. In general one wishes to have complete transmittance in the visible wavelength range 0.38–0.78 µm, whereas thermal radiation (approx. 2 µm and longer wavelengths) should be reflected. The optimal ranges of absorption and reflection differ slightly depending on the application. TiN rather closely meets the criteria for an energy-efficient window coating [245].
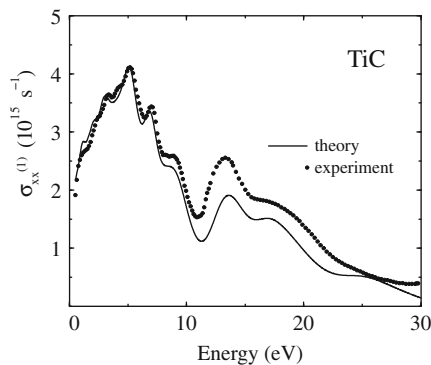
Fig. 13.4. Calculated optical conductivity of TiC compared with experiment. The experimental optical conductivity is for $TiC_{0.90}$ and is calculated from reflectivity data [161]
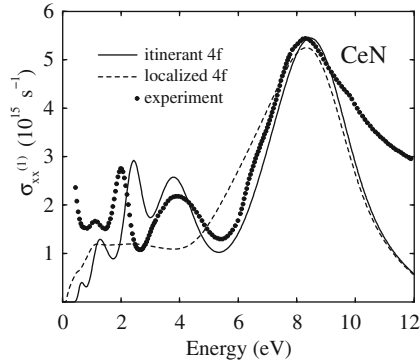
Fig. 13.5. Calculated real part of the optical conductivity, $\sigma_{xx}^{(1)}$, of CeN compared with experimental data [200]

More surprisingly, the optical properties of CeN are also well described using RSPt [68]. It is expected that electron–electron correlation effects be important in this material due to the presence of Ce $4f$ electrons. Despite this, an itinerant description of the $4f$ electrons produces an optical spectrum in close agreement with the experimental results [200, 201] (see Fig. 13.5). In contrast, the localized description of the $4f$ electrons does not reproduce any of the low-energy features in the spectrum. The itinerant picture also reproduces the experimental lattice parameter and provides good agreement with experimental data for the magnetic susceptibility and the electronic specific heat.

13.7 Magneto-optical Properties

Magnetism affects the polarization of light, both reflected and transmitted. Thus, measuring these polarization changes has become an important experimental tool for characterizing materials and calculating the magneto-optical spectra with electronic structure methods is a very sensitive test on how well the methods manage to describe the electron states in the material. In RSPt, the magneto-optical Faraday and Kerr effects can be calculated on the level of the dipole approximation. As an example of such a calculation, we show here Kerr rotation spectra for Fe, Co, and Ni; see Fig. 13.6. We find generally good agreement between our calculations, earlier calculations, and experiment for the absorptive conductivities and the Kerr rotation. For the off-diagonal dispersive conductivity and the ellipticity of Fe and Co, our calculations have larger amplitudes at higher energies. A general feature of all standard density functional calculations on these materials is that the bandwidths are overestimated, which causes structures in the calculated spectra be shifted to
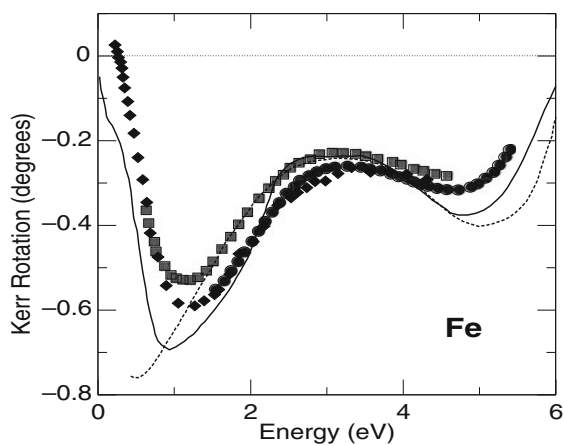
Fig. 13.6. Calculated and measured polar MOKE rotation for bcc Fe. *Solid line*: calculation with FP-LMTO [63]. *Dashed line*: calculation with ASW [175]. The experimental data shown are as follows: *filled circles* (Visnovsky et al., unpublished), *gray squares* [243], and *filled diamonds* [145, 146]
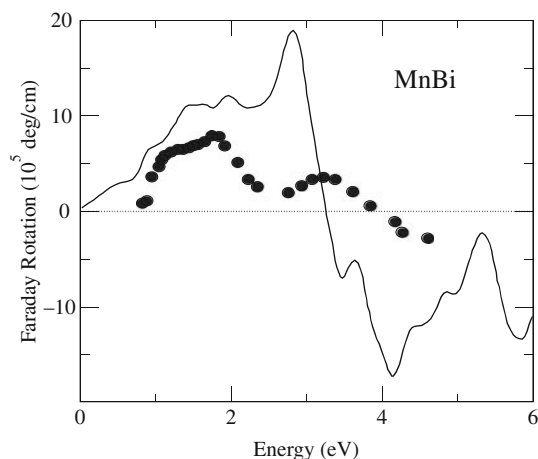
Fig. 13.7. Calculated and measured Faraday rotation for MnBi. The *solid line* refers to a calculation with FP-LMTO [192] and the *circles* refer to data measured by Di and Uchiyama [71]

higher energies compared to experiment. It is reasonable to believe that this is due to underestimation of correlation effects.

In Fig. 13.7, we show calculated Faraday rotation spectra for the manganese pnictides MnAs, MnSb, and MnBi [192]. For MnBi, experimental data exist and we see that our calculation reproduces the trend in those data.

13.8 X-Ray Absorption and X-Ray Magnetic Circular Dichroism

In recent years the study of magneto-optical effects in the X-ray range has gained a great importance as a tool for the investigation of magnetic materials [10, 80]. X-ray absorption spectroscopy (XAS) probes selectively each core orbital of each atomic species in a material. Two decades ago the theoretical work of Erskine and Stern showed that the X-ray absorption could be used to determine the X-ray magnetic circular dichroism (XMCD) in transition metals when left and right circularly polarized X-ray beams are used [89]. More recently, these ideas were implemented experimentally and XAS was used to determine the local magnetic properties of each magnetic atomic orbital in a magnetic compound [202, 242]. Thus the circular magnetic X-ray dichroism is an important tool for the investigation of magnetic materials [16, 40, 45, 46, 50, 80, 81, 109, 202, 213, 229, 235, 242, 263, 264], especially through the use of sum rules for the direct determination of the local orbital and spin contributions to the total magnetic moment [47, 235].

The first theoretical investigations of XMCD are those of Thole et al. [47, 235] who implemented an atomic multiplet approach [57]. This approach is based on an empirical atomic calculation. In addition to the absence of hybridization effects, this method – as all other empirical methods – relies on data from experimental spectra. Results from calculations applying this method to the $3d^9 4f^{n+1}$ multiplets of the $M_{4,5}$ edges of lanthanides are summarized in the paper of Thole et al. [47, 235].

Some years later Chen et al. [50] made use of the Erskine and Stern model[1] [88] for their experimental $L_{2,3}$-edge spectra of nickel. The disagreement between the measured branching ratio and that predicted by the model has been ascribed to the change of spin-dependent unoccupied density of states near the Fermi level caused by the spin–orbit coupling effect. A year later the same group [51] published results of a tight-binding analysis in which they presented an attempt to include the spin–orbit coupling for d valence states. The valence spin–orbit ξ and exchange splitting Δ_{ex} parameters extracted from numerical experiments are found to be, respectively, larger and smaller than those of the ground state to achieve an optimal agreement between the simulated and experimental spectra. Later Smith et al. [213] included properly the spin–orbit coupling within a tight binding scheme. The results for nickel are not too different from those of the previous calculation [51] but the parameters $(\xi, \Delta_{\text{ex}})$ found for iron revealed the sensitivity of the XMCD spectra on the unfilled d bandwidth. The discrepancies between the calculated and the experimental parameters were imputed to many-body effects, e.g., since the core hole is created, the $3d$ valence electrons will see a stronger attractive core

---

[1] According to this model the large spin–orbit coupling of the core states and its small value for valence states should allow us to treat these valence states without spin–orbit coupling.

potential and the spatial extent of their orbitals will contract. Consequently, relativistic effects such as the spin–orbit coupling will be stronger, and the exchange interaction among the first neighbors will be weaker.

The development of X-ray spectroscopy experiments probing the magnetic properties of a large variety of magnetic rare-earth materials and the growing interest in the scientific community toward their applications in media storage, strong magnets, and the emerging field of spintronics have stimulated our XMCD calculations for these materials. The discovery of XMCD sum rules may be a powerful tool for understanding and characterizing magnetic properties.

13.8.1 The XMCD Formalism

The attenuation of the X-ray intensity when passing through a sample of thickness d is given by Beer's law:

$$I(d) = I_0 e^{-\mu_{\mathbf{q}\lambda}(\omega)d}, \tag{13.50}$$

where $\mu_{\boldsymbol{q}\lambda}(\omega)$ is the absorption coefficient which in general depends on the wave vector $\mathbf{q}$, the energy $\hbar\omega$, and the polarization λ of the radiation. In the X-ray regime the absorption coefficient $\mu_{\mathbf{q}\lambda}$ is related to the absorptive part of the dielectric function $\epsilon_{\mathbf{q}\lambda}$ or the optical conductivity $\sigma_{\mathbf{q}\lambda}$ via [81]

$$\mu_{\mathbf{q}\lambda}(\omega) = \frac{\omega}{c}\epsilon^{(2)}_{\mathbf{q}\lambda}(\omega) = \frac{4\pi}{c}\sigma^{(1)}_{\mathbf{q}\lambda}(\omega). \tag{13.51}$$

This means that $\mu_{\boldsymbol{q}\lambda}(\omega)$ can be evaluated[2] from

$$\mu_{\mathbf{q}\lambda}(\omega) = \frac{\pi c^2}{\hbar\omega m V}\sum_{i}^{\text{occ}}\sum_{f}^{\text{unocc}}|M_{if}^{\mathbf{q}\lambda}|^2\delta(\hbar\omega - E_f + E_i). \tag{13.52}$$

In contrast to the optical and magneto-optical calculations described earlier in this chapter, in which the matrix elements of the electron–photon interaction are evaluated between two Bloch states, the matrix elements $M_{if}^{\mathbf{q}\lambda}$ are calculated between a well-localized initial core state i and an extended final state f. The sum over initial states i is usually restricted to one core shell which could be achieved by an experimental fine-tuning of a particular absorption edge. This important property makes X-ray absorption an element-specific probe.

---

[2] Equation (13.52) can be considered as the limit of the real part of the matrix elements (13.36) when the frequency (ω) becomes too high (X-ray regime). In this case the frequency ω can be rewritten as $\omega = \omega_0 + \delta\omega$ because of the sharp energy of the involved core levels, and therefore

$$\frac{1}{\omega} = \frac{1}{\omega_0 + \delta\omega} \sim \frac{1}{\omega_0}.$$

This is why the factor $\frac{1}{\omega}$ is again present in (13.52).

The $M_{if}^{\mathbf{q}\lambda}$ matrix transitions account for the electron–photon interaction operator

$$\hat{H}_{\mathrm{el-ph}} = -\frac{1}{c}\mathbf{J}\mathbf{A}_{\mathbf{q}\lambda}(\mathbf{r}) = -\frac{1}{c}\mathbf{J}\mathbf{e}_\lambda A \mathrm{e}^{\mathrm{i}\mathbf{q}\mathbf{r}}\,, \tag{13.53}$$

where $\mathbf{A}_{\mathbf{q}\lambda}(\mathbf{r})$ is the vector potential with the wave vector $\mathbf{q}$ and polarization λ, $\mathbf{J}$ is the electronic current density operator

$$\mathbf{J} = -\mathbf{ec}\boldsymbol{\alpha}\,, \tag{13.54}$$

and $\boldsymbol{\alpha}$ accounts for the electronic momentum operator[3] $(\hbar/\mathrm{i})\boldsymbol{\nabla}$. The components of the polarization vector for linearly polarized light are given by

$$\mathbf{e}_x = \begin{pmatrix} 1 \\ 0 \\ 0 \end{pmatrix}, \quad \mathbf{e}_y = \begin{pmatrix} 0 \\ 1 \\ 0 \end{pmatrix}, \quad \mathbf{e}_z = \begin{pmatrix} 0 \\ 0 \\ 1 \end{pmatrix}. \tag{13.56}$$

For $\mathbf{q}$ pointing along the z-axis, left $(+)$ and right $(-)$ circularly polarized lights are presented by the polarization vector

$$\mathbf{e}_\pm = \frac{1}{\sqrt{2}} \begin{pmatrix} 1 \\ \pm\mathrm{i} \\ 0 \end{pmatrix}. \tag{13.57}$$

In order to get insight into the corresponding absorption phenomena one needs to calculate matrix elements of the form

$$M_{if}^{\mathbf{q}\lambda} = \langle\psi_i|\hat{H}_{\mathrm{el-ph}}|\psi_f\rangle\,. \tag{13.58}$$

It is generally argued that in the frequency range of conventional optics the amplitude of the vector potential varies only on a microscopic scale. This implies that it is sufficient to expand the exponential factor in (13.53)

$$\mathrm{e}^{\mathrm{i}\mathbf{q}\mathbf{r}} = 1 + \mathrm{i}\mathbf{q}\mathbf{r} - \frac{1}{2}(\mathbf{q}\mathbf{r})^2 \ldots \tag{13.59}$$

and retain just the first constant term, in which case only the electric dipole interaction is accounted for. For X-ray regime (XMCD) the next term in the expansion that represents the quadrupolar interaction may also be important. However, Arola et al. [21] showed that the contribution from the quadrupolar interaction to the K edge cross sections of iron is two orders of magnitude smaller than that of the electric dipole contribution. Within the dipolar approximation the absorption coefficient reduces to

---

[3] Within a relativistic formalism the total momentum operator is expressed as

$$\alpha = \mathbf{p} + \frac{\hbar}{4mc^2}\boldsymbol{\sigma} \times \boldsymbol{\nabla}V = \frac{\hbar}{i}\boldsymbol{\nabla} + \frac{\hbar}{4mc^2}\boldsymbol{\sigma} \times \boldsymbol{\nabla}V\,, \tag{13.55}$$

while in the non-relativistic case $(c \to \infty)$ this operator reduces to the electronic momentum operator.

$$M_{if}^{\mathbf{q}\lambda} = \langle \psi_i | \boldsymbol{\alpha} \mathbf{e}_\lambda | \psi_f \rangle . \tag{13.60}$$

The ec constant is deliberately omitted. It is worth mentioning that the symmetry reduction due to the presence of spontaneous magnetization, that leads to the appearance of non-zero off-diagonal components of the dielectric tensor, e.g., ϵ_{xy} in (13.7), occurs only if both the spin polarization and the spin–orbit coupling are simultaneously taken into account in the calculations. The XMCD calculations are performed in two steps. First, a good convergence is achieved (in terms of total energy and charge density) within a relativistic calculation where the Spin-orbit coupling is included in the variational step, after that one iteration is carried out in order to calculate the absorption coefficients using the electronic wave functions accounting for the supposed ground state. The initial core wave functions ψ_i are given by

$$
\begin{aligned}
\psi_i = \psi_{j\mu} &= \sum_{m_{\rm sc}} C^{j\mu}_{l_{\rm c}\mu-m_{\rm sc}, \frac{1}{2}m_{\rm sc}} \phi_{l_{\rm c}}(r) Y_{l_{\rm c}\mu-m_{\rm sc}}(\hat{\mathbf{r}}) \chi_{m_{\rm sc}} \\
&= \sum_{m_{\rm sc}} C^{j\mu}_{l_{\rm c}m_{\rm c}, \frac{1}{2}m_{\rm sc}} \phi_{l_{\rm c}}(r) Y_{l_{\rm c}m_{\rm c}}(\hat{\mathbf{r}}) \chi_{m_{\rm sc}} ,
\end{aligned}
\tag{13.61}
$$

and the final wave functions ψ_f are the dispersive ($\mathbf{k}$-dependent) FP-LMTO valence wave functions, (6.27), which we here recast in a slightly different form,

$$\psi_f = \psi_\nu^\sigma(\mathbf{k}, r) = \sum_{lm}(A_{lm}(\mathbf{k})\phi_l(r)Y_{lm}(\hat{\mathbf{r}}) + B_{lm}(\mathbf{k})\dot{\phi}_l Y_{lm}(\hat{\mathbf{r}}))\chi_{ms} , \tag{13.62}$$

where $\chi_{\rm sc}$, $\chi_{\rm s}$, $m_{\rm sc}$, and $m_{\rm s}$ are the core spin functions, the valence spin functions, the corresponding magnetic quantum numbers, respectively. $C^{j\mu}_{l_{\rm c}\mu-m_{\rm s}, \frac{1}{2}\mu}$ are the Clebsh–Gordan coefficients, j is the total momentum of the electron, $l_{\rm c}$ and l are the core and valence angular momentum quantum numbers, μ (or m_j) and m are the corresponding magnetic quantum numbers. The core and valence states are calculated separately and in a different way, that is to say that the core wave functions corresponding to deep energy levels are determined within a fully relativistic calculation while valence eigenfunctions are evaluated within a scalar relativistic calculation including the SOC at the variational step. Let us consider one edge transitions involving the initial i states and the final f states. The $M_{if}^{q\lambda}$ matrix can be rewritten as

$$
\begin{aligned}
M_{if}^{\mathbf{q}\lambda} = \sum_{m,m_{\rm sc}} C^{j\mu}_{l_{\rm c}m_{\rm c}, \frac{1}{2}m_{\rm sc}} \langle \phi_{l_{\rm c}}(r)Y_{l_{\rm c}m_{\rm c}}(\hat{\mathbf{r}}) | \boldsymbol{\alpha}\mathbf{e}_\lambda | (A_{lm}(\mathbf{k})\phi_l(r)Y_{lm}(\hat{\mathbf{r}}) \\
+ B_{lm}(\mathbf{k})\dot{\phi}_l Y_{lm}(\hat{\mathbf{r}})) \rangle \delta_{m_{\rm sc}m_{\rm s}} .
\end{aligned}
\tag{13.63}
$$

Using the relation

$$\boldsymbol{\alpha}\mathbf{e}_\lambda = \frac{\mathbf{e}_r.\mathbf{e}_\lambda}{\mathrm{i}} \frac{\partial}{\partial r} - \frac{1}{r}(\mathbf{e}_r \times \mathbf{L}).\mathbf{e}_\lambda, \tag{13.64}$$

where $\mathbf{L}$ is the orbital angular momentum operator, (13.63) becomes

$$M_{if}^{\mathbf{q}\lambda}(\mathbf{k}) = \sum_{m,m_s} C_{l_c m_c, \frac{1}{2} m_s}^{j\mu}$$

$$\left(\left\langle \phi_{l_c} Y_{l_c m_c} \left| \frac{\mathbf{e}_r.\mathbf{e}_\lambda}{\mathrm{i}} \frac{\partial}{\partial r} \right| (A_{lm}(\mathbf{k})\phi_l Y_{lm} + B_{lm}(\mathbf{k})\dot\phi_l Y_{lm} \right\rangle \right. \qquad (13.65)$$

$$\left. - \left\langle \phi_{l_c} Y_{l_c m_c} \left| \frac{1}{r}(\mathbf{e}_r \times \mathbf{L}).\mathbf{e}_\lambda \right| (A_{lm}(\mathbf{k})\phi_l Y_{lm} + B_{lm}(\mathbf{k})\dot\phi_l Y_{lm} \right\rangle \right).$$

Both of the terms inside the parenthesis can be separated into radial and angular part and integrated. We can therefore perform the $\mathbf{k}$ integration using the tetrahedron method; we can calculate the corresponding absorption coefficients $\mu^{\mathbf{q}+}(\omega)$, $\mu^{\mathbf{q}-}(\omega)$, and $\mu^{\mathbf{q}0}(\omega)$ for left, right, and z polarized light, and therefore calculate the *key* physical quantity:

$$\Delta\mu(\omega) = \mu^{\mathbf{q}+}(\omega) - \mu^{\mathbf{q}-}(\omega) \neq 0. \qquad (13.66)$$

If X-rays are absorbed by a magnetic solid the absorption coefficients for left and right circularly polarized photons are in general different so that $\Delta\mu \neq 0$. This quantity can be measured experimentally [202] and is called X-ray magnetic circular dichroism (XMCD).

The corresponding matrix transitions elements $M_{if}^{\mathbf{q}\lambda}(\mathbf{k})$ are non-zero only if

$$\begin{cases} \Delta l &= l - l_c &= \pm 1 \\ \Delta m &= m - m_c &= \lambda \\ \Delta m_s &= m_s - m_{sc} &= 0 \end{cases} \qquad (13.67)$$

These conditions are used to select the allowed transitions within the dipolar approximation and they are known as the dipole selection rules.

13.8.2 The XMCD Sum Rules

Magnetic compounds and alloys characterization represents one of the outstanding problems in condensed matter physics. Recently, a considerable evolution of the spectroscopic techniques has been achieved and was helped by theoretical efforts. With the derivation of the sum rules by Thole and coworkers [45, 46, 235] XMCD spectroscopy became the most used technique for studying magnetic materials. These sum rules supply a firm basis to estimate directly from XMCD spectra the orbital moment $(M_L = -\frac{\mu_B}{\hbar}\langle L_z\rangle)$ and the magnetic moment $(M_S = -2\frac{\mu_B}{\hbar}\langle S_z\rangle)$ contributions to the total magnetic moment associated with a specific state of given symmetry. Thus the magnetic spin and orbital moments of the absorber atom are related to the integrated absorption spectra for a specific core shell and polarization of the radiation as

$$\int_{j_+} \Delta\mu \mathrm{d}E - \left[\frac{l_{\mathrm{c}}+1}{l_{\mathrm{c}}}\right] \int_{j_-} \Delta\mu \mathrm{d}E$$

$$= \frac{N}{n_h} \left[\frac{l(l+1) - 2 - l_{\mathrm{c}}(l_{\mathrm{c}}+1)}{3l_{\mathrm{c}}} \langle S_z \rangle \right. \tag{13.68}$$

$$\left. + \frac{l(l+1)\left[l(l+1) + 2l_{\mathrm{c}}(l_{\mathrm{c}}+1) + 4\right] - 3(l_{\mathrm{c}}-1)^2(l_{\mathrm{c}}+2)^2}{6ll_{\mathrm{c}}(l+1)} \langle T_z \rangle \right]$$

and

$$\int_{j_++j_-} \Delta\mu \mathrm{d}E = \frac{N}{2n_{\mathrm{h}}} \left[\frac{l(l+1) + 2 - l_{\mathrm{c}}(l_{\mathrm{c}}+1)}{l(l+1)} \right] \langle L_z \rangle , \tag{13.69}$$

where N is the total integrated spectrum corresponding to the unpolarized radiation (known also as the isotropic absorption contribution)

$$N = \int_{j_++j_-} \left(\sum_{\lambda=+,-,0} \mu^\lambda \right) \mathrm{d}E , \quad \Delta\mu = \mu^+ - \mu^- , \tag{13.70}$$

and T_z is the magnetic dipole operator

$$T_z = \frac{1}{2} \left[\boldsymbol{\sigma} - 3\hat{\mathbf{r}}(\hat{\mathbf{r}}.\boldsymbol{\sigma}) \right]_z . \tag{13.71}$$

$\int_{j_++j_-}$ means that the integral is performed over both of the $j_+ = l+1/2$ and $j_- = l-1/2$ edge spectra, e.g., $j_+ = 3/2$ and $j_- = 1/2$ for the $L_{2,3}$ edges of transition metals, $\hat{\mathbf{r}}$ is the unit vector, n_{h} denotes the number of holes or the number of unoccupied final states, and $\langle S_z \rangle$, $\langle L_z \rangle$, and $\langle T_z \rangle$ are, respectively, the expectation values of the magnetic moment, the orbital moment, and the magnetic dipole operator.

The expectation value of the magnetic dipole operator accounts for the asphericity of the spin magnetization. This asphericity can be considered as a magnetic anisotropy resulting from the spin–orbit coupling or crystal-field effects.

The application of these sum rules provides us with the magnetic spin and orbital moments since the expectation value of the T_z operator is determined. In order to extract these moments from the absorption spectra we have used the sum rules for the different edges:

K edge

$$\int_{E_{\mathrm{F}}}^{E_{\mathrm{cut}}} \Delta\mu \mathrm{d}E = \frac{N}{n_{\mathrm{h}}} \langle L_z \rangle , \tag{13.72}$$

where

$$N = \sum_{\lambda=+,-,0} \int_{E_{\mathrm{F}}}^{E_{\mathrm{cut}}} \Delta\mu^\lambda , \tag{13.73}$$

$L_{2,3}$ edges

$$\int_{E_{\mathrm{F}}}^{E_{\mathrm{cut}}} \left[(\mu_{L_3}^+ - \mu_{L_3}^-) - 2(\mu_{L_2}^+ - \mu_{L_2}^-)\right] \mathrm{d}E = \frac{N}{3n_{\mathrm{h}}} \left[\langle S_z\rangle + 7 \langle T_z\rangle\right], \quad (13.74)$$

$$\int_{E_{\mathrm{F}}}^{E_{\mathrm{cut}}} \left[(\mu_{L_3}^+ - \mu_{L_3}^-) + (\mu_{L_2}^+ - \mu_{L_2}^-)\right] \mathrm{d}E = \frac{N}{2n_h} \langle L_z\rangle, \quad (13.75)$$

where

$$N = \sum_{\lambda=+,-,0} \int_{E_{\mathrm{F}}}^{E_{\mathrm{cut}}} (\Delta\mu_{L_3}^\lambda + \Delta\mu_{L_2}^\lambda), \quad (13.76)$$

$M_{4,5}$ edges

$$\int_{E_{\mathrm{F}}}^{E_{\mathrm{cut}}} \left[(\mu_{M_5}^+ - \mu_{M_5}^-) - \frac{3}{2}(\mu_{M_4}^+ - \mu_{M_4}^-)\right] \mathrm{d}E = \frac{N}{3n_{\mathrm{h}}} \left[\langle S_z\rangle + 6 \langle T_z\rangle\right], \quad (13.77)$$

$$\int_{E_{\mathrm{F}}}^{E_{\mathrm{cut}}} \left[(\mu_{M_5}^+ - \mu_{M_5}^-) + (\mu_{M_4}^+ - \mu_{M_4}^-)\right] \mathrm{d}E = \frac{N}{3n_{\mathrm{h}}} \langle L_z\rangle, \quad (13.78)$$

where

$$N = \sum_{\lambda=+,-,0} \int_{E_{\mathrm{F}}}^{E_{\mathrm{cut}}} (\Delta\mu_{M_5}^\lambda + \Delta\mu_{M_4}^\lambda). \quad (13.79)$$

The integrations are carried out from the Fermi energy E_{F} up to an energy cutoff E_{cut}. This energy represents the energy of the top of the final magnetic states. The number of holes n_{h} is also calculated from the density of states, and it is determined from the integration of the unoccupied part of the partial density of final states.

In order to make useful and relevant application of these sum rules one should know their limitations due to the assumptions made in order to derive them. In fact, to derive the XMCD sum rules, Thole and coworkers adopted a single ion model combined with a scalar relativistic approach. The main assumption of the derivation is that of the two-step model [202]. Depending on the photon polarization, the XMCD transitions occur in two steps. Because of the conservation of the angular momentum during the absorption process the angular momentum carried out by the photon is completely or partially transferred to the photo-electron, in a second step the exchange spin splitting of the final state is different whether the spin of the incoming electron is up or down. This could simulate the eventual change of the exchange splitting resulting from the spin dependence of the incoming photo-electron. The other assumptions of the underlying physics of the XMCD sum rules are to ignore the following [79]:

1. The exchange splitting of the core states
2. The asphericity of the core states

3. The difference between the radial relativistic part of the final wave functions, i.e., the radial parts $\phi_l(r)$ of $p_{1/2}$ and $p_{3/2}$ or $d_{3/2}$ and $d_{5/2}$ are the same
4. The energy dependence of the wave function

Despite such limiting approximations, the validity of the sum rules appears to be now rather well established, at least in the cases of the $L_{2,3}$ absorption edges of $3d$ [50, 93, 264], $4d$ [250], and $5d$ [104] transition metals. However, one should keep in mind that there are some problems when applying the sum rules to XMCD spectra. The most severe one is the separation of the L_2- and L_3-spectra, e.g., because of the strong hybridization between the $2p$ N orbitals.

Thole and coworkers show that the circular magnetic X-ray dichroism is related to the magnetic moment of the photo-excited atom when the core electron is excited to the conduction states that are responsible of the magnetic properties of the material. On the theoretical side, Ebert and his coworkers [81, 109] have developed a fully relativistic local spin density approximation approach that was used with success to calculate the XMCD at the K-edge of Fe, the L_3-edge of gadolinium, and Fe and Co multilayers. Wu et al. used slab linear-augmented plane-wave method to study the $L_{2,3}$ XMCD of Fe [264]. Brouder and coworkers use multiple scattering theory to solve the Schrödinger equation using spherical potentials and spin–orbit coupling as a perturbation in the final state [40]. Recently, Ankudinov and Rehr used a method based on a non-relativistic treatment of propagation based on high order multiple scattering theory and spinor-relativistic Dirac–Fock treatment of the dipole matrix elements to calculate the Fe–K edge and Gd–L_3 edge XMCD [16].

Figure 13.8 represents the K-edge X-ray absorption of Fe, for left and right circularly polarized light, compared to the experimental results. The agreement at low energy with experiment is good and starts degrading at higher energies above the mean absorption peak. It is of interest to point out that the magnetic X-ray dichroism at the K-edge which is due to the spin polarization and the spin–orbit in the final state is very small in the case of Fe. The difference between the right and left circular polarization of the light is not even visible on the graph. However, the X-ray magnetic circular dichroism can be measured and Fig. 13.9 shows a good agreement between the calculated dichroic signal and the experimental results of Shütz [202].

At the $L_{2,3}$ edge of $3d$ transition metals the X-ray magnetic dichroism is much important because it is meanly due to the presence of the strong spin–orbit coupling in the initial $2p$ states (in the case of Fe the spin–orbit splitting between the $2p_{3/2}$ and $2p_{1/2}$ is about 13 eV). In Fig. 13.10 we show the calculated X-ray absorption and XMCD at the Co in PtCo-ordered alloy [103].

To compare the results with experiment we have to take into account the effect of the core hole and the experimental resolution. This is done by convoluting the calculated spectra by a Lorentzian of widths of 0.9 and 1.4 eV for the L_2 and L_3 edges, respectively; in addition, a Gaussian broadening of
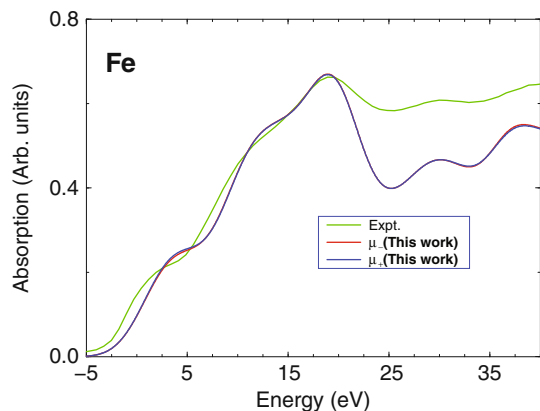
Fig. 13.8. Calculated X-ray absorption at the K-edge of Fe for left and right circularly polarized light compared to the experimental spectrum. The difference between the two spectra (barely visible on the graph) represents the X-ray magnetic circular dichroism
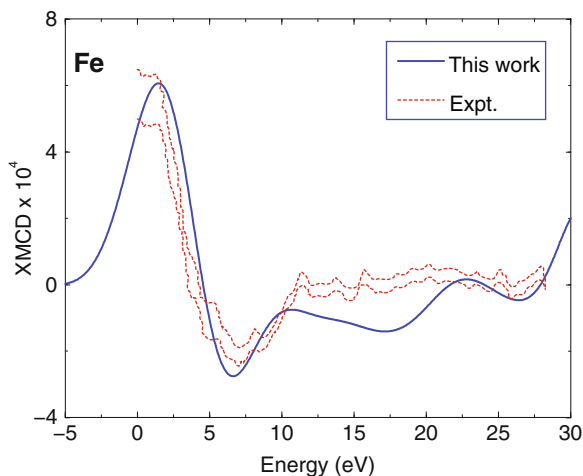
Fig. 13.9. Calculated X-ray magnetic dichroism at the K-edge of Fe compared to the experimental spectrum of Shütz [202]

0.4 eV is added to take into account the experimental resolution. The calculation of the X-ray magnetic circular dichroic signal ignoring the electron–hole recombination effect provides a semi-quantitative agreement with the experimental spectra. Hence, we believe that the core hole effect represented here by a Lorentzian broadening plays a significant role in determining the correct L_3/L_2 branching ratio for $3d$ transition metals. The underestimation of the $L_{2,3}$ branching ratio remains a challenge for theorists, and further theoretical
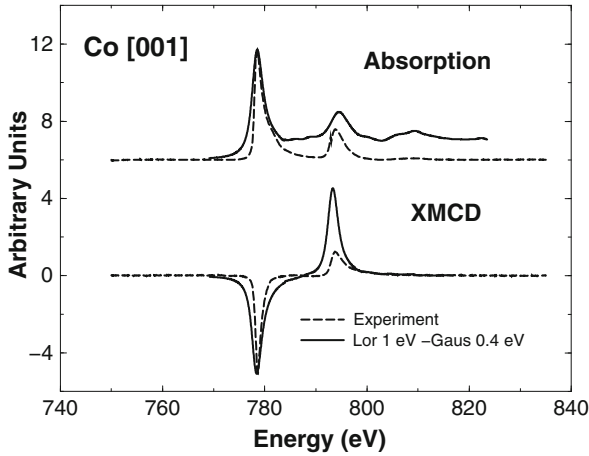
Fig. 13.10. Calculated X-ray absorption and magnetic X-ray dichroism at the $L_{2,3}$-edge of Fe compared to the experimental spectrum of Grange et al. [103]

development along the line proposed by Schwitalla and Ebert [203] is needed to bring the theory at the level of the experiment.

For the $4d$-transition metals, the core hole is deeper, and the agreement with the experimental result is satisfactory. Figure 13.11 shows the calculated XMCD at the site of Pt of the CoPt-ordered alloy. In contrast to what is
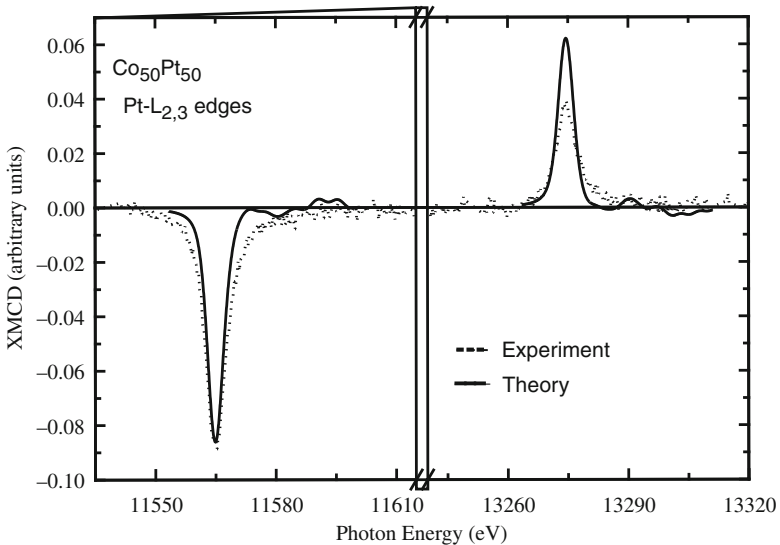
Fig. 13.11. Calculated X-ray magnetic dichroism at the $L_{2,3}$-edge of Pt compared to the experimental spectrum of Grange et al. [103]

obtained for Co, the results for the Pt site show a much better agreement with experiment, due to the fact that the core hole effect is less intense (core hole much deeper than that of Co). For the Pt atom we used both a Lorentzian (1 eV) and a Gaussian (1 eV) to represent the core hole effect and a Gaussian of 1 eV width for the experimental resolution. The experimental and theoretical L_2 and L_3 edges are separated by a spin–orbit splitting of the $2p$ core states of 1,709 and 1,727 eV, respectively. The widths of both L_2 and L_3 edges are comparable to experiment, but the calculated L_2 intensity is much larger. This produces a calculated integrated branching ratio of 1.49 which is much smaller than the experimental ratio of 2.66. Here again the theory is underestimating the branching ratio.

We have also applied our method of calculating XAS and XMCD on two magnetic double perovskites – Sr_2FeMoO_6 (SFMO) and Sr_2CrReO_6 (SCRO). These systems are of technological interest in the field of spintronics, and especially SFMO has received great attention due to its alleged perfect half-metallicity [136]. Perfectly half metallic materials could in principle produce a completely spin-polarized current which would be highly useful for spin-injection applications. In practice, the half-metallicity will be destroyed by, e.g., surface effects, lattice imperfections, grain boundaries, and finite temperature. Furthermore, there is actually no need for perfect half-metallicity in order to obtain a low-field magneto-resistive effect based on intergrain tunneling. Thus, it is envisaged that many of the systems belonging to the family of magnetic double perovskites may be highly relevant for applications in spintronics. In addition, these complex magnetic oxides are very interesting systems in themselves to study. They can be viewed as magnetic semiconductor
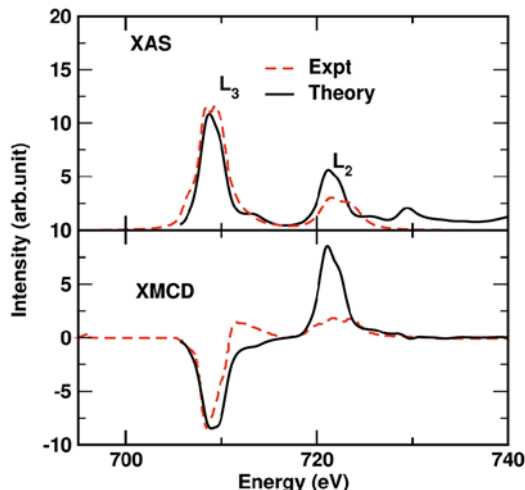
Fig. 13.12. Calculated XAS and XMCD for the Fe $L_{2,3}$-edges in SFMO, compared to experimental data

materials, and analyzing the XMCD spectra may aid in elucidating the nature of the magnetic state in these systems, especially the size and direction of the moments on the Mo and Re sites.

Figure 13.12 shows the L-edge Fe XAS and XMCD signal in SFMO [135]. The calculations are seen to reproduce most of the experimental features, but the calculated branching ratios are not well reproduced, probably due to our neglect of the core–hole interactions. Another possible explanation for the discrepancies is the anti-site disorder always present in these complex magnetic oxides. The L-edge spectra from Mo are shown in Fig. 13.13. In SFMO, the Mo moments are very small but despite this added complication, the calculations reproduce the experimental spectra rather well. The Mo states are rather delocalized, so in this case, core–hole interactions might be less important.
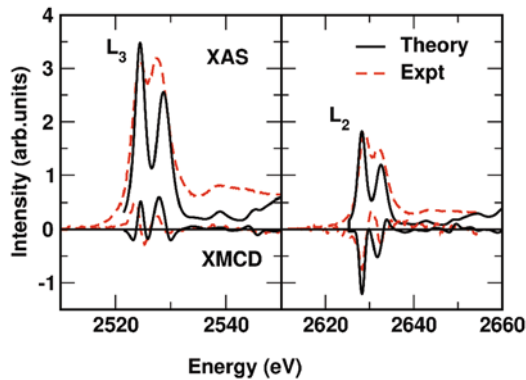
Fig. 13.13. Calculated XAS and XMCD for the Mo $L_{2,3}$-edges in SFMO, compared to experimental data
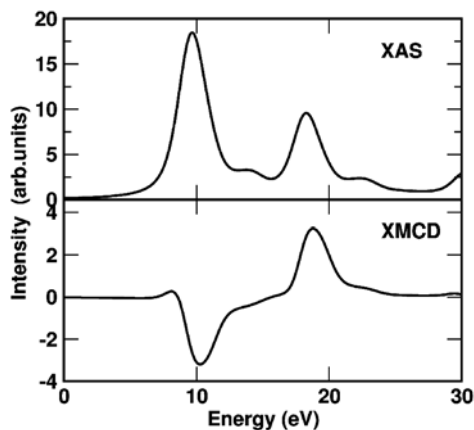
Fig. 13.14. Calculated XAS and XMCD for the Cr $L_{2,3}$-edges in SCRO
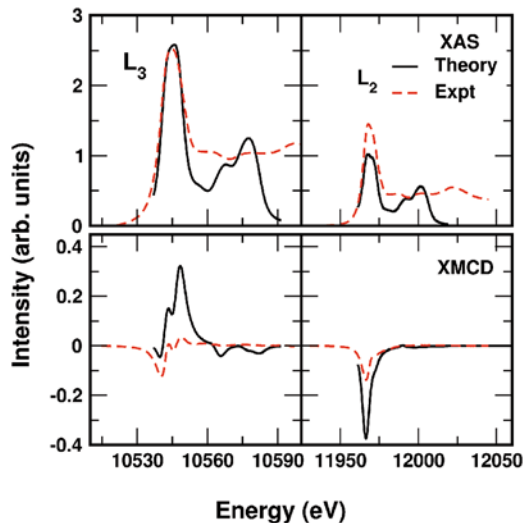
Fig. 13.15. Calculated XAS and XMCD for the Re $L_{2,3}$-edges in SCRO, compared to experimental data

In the next two figures, we show XAS and XMCD results for SCRO, a pseudo-half-metallic double perovskite [240, 241] with a relatively high Curie temperature (635 K). Figure 13.14 shows calculated spectra for the Cr L-edges (no experimental comparison available) and Fig. 13.15 shows spectra for the Re L-edges. The calculated Cr XMCD spectra exhibit a clear XMCD signal with a simple structure – a negative peak at the L_2 edge followed by a positive peak at the L_3 edge. In contrast, the Re spectra have much more structure. Our calculation reproduces the main features of the experimentally measured signal. We also note that the calculated XMCD-integrated peak areas are significantly larger than the measured ones.

The calculated spectra can be combined with the XMCD sum rules for calculating the spin and orbital moments. Thus in this way recalculated moments are then compared with the moments calculated directly in the ground state calculation. This procedure gives interesting insights into the precision of the sum rules and overall self-consistency of the XMCD calculations. For example, the SFMO directly calculated and sum-rule-derived Mo spin moments are identical ($-0.29\,\mu_{B}$), whereas the orbital moments are 0.02 and 0.056 μ_{B}, respectively. A longer discussion of this issue for both SFMO and SCRO can be found in [131, 240].

14

A Database of Electronic Structures

Abstract In this short chapter, an data-base of electronic structures are described and a method in data-mining technology is presented, for how such a data-base might be used to search for new functional materials.

It is now possible to extract electronic structures and ground state properties from RSPt at the web site http://gurka.fysik.uu.se/ESP/ (we will henceforth refer to this database as the electronic structure database, ESD). The method with which this was done is described in [176] and is due to the efforts of Dr. M. Klintenberg. The purpose of this database is partly to provide a benchmark for beginners in the field of electronic structure theory, who can compare their calculations of electronic structures to already existing data. It is advised that when being in a learning stage of using RSPt, to perform a few calculations on materials with varying complexity, which are found in the ESD. This could involve transition metal elements and compounds, e.g., YNi_2, as well as semiconducting materials, like Si or ZnO. So far only non-spinpolarized calculations have been listed, but the electronic structure and magnetism of magnetic systems are currently being developed. However, the database generated in ESD also offers an entirely new way to perform theoretical materials research, since when combined with data-mining algorithms it can significantly accelerate the search for new compounds with specified properties. We will below exemplify this possibility with one example, which has been published in full detail in [176].

14.1 Database Generation

The first step toward generating a useful database for electronic structures and ground state properties using RSPt has, as mentioned, now been published [176]. In this work it is described how the majority of materials synthesized and characterized structurally to this date have had their electronic structures

calculated by means of RSPt. Of the over 140,000 compounds currently listed in the *international crystal structure database* (ICSD), almost all have had the electronic structure investigated and published on the ESD. These calculations are done for the experimentally observed crystal structure and density, in a fully automatic mode where scripts generate input files automatically and without manual inspection [176]. Since setting up input datafiles is still an obstacle in electronic structure calculations in general, the automatization drastically improves on the speed with which electronic structure calculations are done, and this is a key reason for why over a relatively short time, a large number of calculations have been published. However, since the quality of each individual calculation is not monitored manually, the approach is in need of a robust and accurate electronic structure method, like RSPt. In addition, quality control is important, and the best way to do this is by inspection of the results. The reader is encouraged to consult the ESD web site, perform a search for a few known electronic structures, and test if the result is the expected one.

14.2 Data-Mining: An Example from Scintillating Materials

Once a huge number of (hopefully) accurate electronic structures and ground state properties have been generated, the question naturally arises what one should do with all these results. A possible answer is to find suitable algorithms for searching among all these data and to extract information, e.g., about a specific material property which is of interest. This could involve large magnetic anisotropies, stiff materials with a large bulk modulus, or materials with suitable band gaps for optical properties. We give here as an example of the fruitfulness of this approach, some of the details of a data-mining study for the identification of novel materials for scintillating materials, a work which is published in [176].

One sub-group of scintillator materials is the so-called activated semiconductors, like Ga-doped ZnO [154]. Among the already known semiconducting scintillators certain material characteristics stand out, and it is information of this kind which can be used when searching for new materials in a large database. Experience shows that efficient scintillator materials should have an electronic band gap in the range 0.4–4 eV and they should have effective masses of the valence band and conduction band which are above a threshold value [176]. In addition there is a requirement that the density of the material should be high and that high-energy photons which enter the material are absorbed primarily by the photo-electric effect and not by Compton scattering. One may now search among all the materials listed in the ESD, if new compounds can be predicted which also obey the necessary criteria for activated semiconductors for scintillating properties. As was shown in [176], a data mining with these criteria of all compounds in ESD resulted in 66 predicted

compounds which should be suitable for scintillating applications. Among the 66 identified compounds, all of the already known activated semiconductors were found, and this serves as a test of the accuracy of the data-mining algorithms. However, in addition to the known materials, the data-mining procedure of [176] resulted in several new materials which await testing for their performance as scintillators.

The example above serves as an example for how large databases might be used for predicting new materials. The challenge with this approach of theoretical materials science is to identify suitable material properties to use in the data-mining algorithms. Here physical and chemical insight and experience of a specific class of functional materials become important. However, in the field of theoretical bio-chemistry this has been an important mode of operation for quite some time, with several important findings, and it is time the materials science community also adopt this approach.

15

Future Developments and Outlook

Abstract In this final chapter a short summary and outlook is presented. In addition, future, anticipated developments of the FP-LMTO method are listed.

This book has given an introduction to current research into the electronic structure-related properties of materials, in particular using the software RSPt. In this final chapter, we speculate about future developments in RSPt that will incorporate current and evolving developments in electronic structure theory and modeling. RSPt, a volunteer effort, develops when some interested individual takes the initiative to implement a needed capability, so development depends on the interests of users. However, some areas have been consistently represented in the development of RSPt, such as structural stability and phase transitions under pressure, mechanical properties and equation of state, magnetic structure and magneto-crystalline anisotropy, and the structural, electronic, and magnetic properties of f-electron materials. If nothing else, RSPt is likely to grow in capabilities applicable to these areas.

Electronic structure, density functional, and dynamical mean field theories, and the methods for solving the equations encapsulating these theories have been presented in Part I. Developments in density functional theory and the realization of non-DFT theories are providing increased flexibility and predictability to electronic structure calculations and in coming years will no doubt become part of a new and richer suite of tools. Explicit, nearly local exchange-correlation density functionals fit naturally in the RSPt framework and so are relatively straightforward to implement. As an example, RSPt was one of the first electronic structure codes to incorporate the recently developed functional AM05 [20].

A rigorous functional formalism and form for relativistic calculations is of interest and would fit well with the structure and applications of RSPt. It seems unlikely, however, that a nearly local density functional will ever give a good description of materials with strong electron correlation, an area that

has been a driving theme of many developments in RSPt. Dynamical mean field theory – DMFT – is the most recent capability to be added to the code and is still in intense development. Important improvements in this capability include the development of a fast single impurity solver accurate for all values of the correlation parameter and a consistent connection in energy to the density functional host. The application of DMFT would benefit from efficient distributed inversion in the transition between DFT and DMFT. Other non-DFT methodologies, such as the Gutzwiller variational approach, are also of interest and under consideration.

Part II of this book has described the application of the theories and methodologies of Part I to problems in materials and condensed matter physics. Chapters on total energy and forces, chemical bonding, and magnetism highlight applications at which RSPt excels. As examples, RSPts ability to transition seamlessly through core-valence transitions is especially useful in equation of state calculations, while its handling of full-potential components and ability to resolve fine energy differences enable the direct calculation of magneto-crystalline anisotropy and structural phase transitions. Magneto-crystalline anisotropy energies depend on fine details of the Fermi surface and hence require a very large sampling of the Brillouin zone to converge. This application is ideally suited to parallel sampling. Similarly, structural stability, in particular the search for stable or metastable structures in complex materials, is suited for sampling configurations in parallel.

RSPt has both capabilities nicely implemented. However, RSPt has always been written to minimize operations, rather than memory, and uses somewhat complex logical structures to both minimize operations and improve accuracy. Both of these design aspects are detrimental to the implementation of RSPt on developing architectures, homo- or heterogenous, where memory per node is drastically decreasing. Re-designing the code to take advantage of new architectures would range in difficulty from using appropriate library calls to reworking the relationship between program components. As currently implemented, RSPt is never "short range." Basis functions and densities are expressed partially in real space and partly in reciprocal space, in order to allow convergence of expansions with minimum calculation. A representation entirely in real space, for example, either with or without a Brillouin representation, might ultimately simplify implementation and thus prove preferable for new supercomputing architectures.

The final chapter of Part II describes the electronic structure database which contains the results of a large number of electronic structure calculations, done with RSPt, categorized by calculated physical properties. The chapter gives an example of data mining to search for new scintillators. Other disciplines, such as astrophysics, are finding that data-mining large experimental databases is becoming a new mode of discovery. As with these experimental databases, the ESD can implement a new mode of materials discovery. With increased capacity, or increased participation, the ESD could be expanded to

include, for example, theoretically stable complex materials correlating material properties with structure.

RSPt has reached its present state through the efforts of motivated researchers who modify it to suit their own interests. Similarly, its future developments will depend on the interests of current and future users. In Part I, Chap. 9 described the rspt.org web site and gave instructions for obtaining RSPt source and a manual. rspt.org also has support pages and information on current development. We hope that this site will serve as a focal point for introducing RSPt to new users and lure them into the web of developers.

References

1. I.A. Abrikosov, H. Skriver, Phys. Rev. B **47**, 16532 (1993)
2. S.L. Adler, Phys. Rev. **126**, 413 (1962)
3. R. Ahuja, S. Auluck, J.M. Wills, M. Alouani, B. Johansson, O. Eriksson, Phys. Rev. B **55**, 4999 (1997)
4. R. Ahuja, O. Eriksson, J.M. Wills, B. Johansson, Phys. Rev. Lett. **75**, 3473 (1995)
5. R. Ahuja, O. Eriksson, J.M. Wills, B. Johansson, Phys. Rev. B **53**, 3072 (1996)
6. R. Ahuja, J.M. Wills, B. Johansson, O. Eriksson, Phys. Rev. B **48**, 16269 (1993)
7. S. Albrecht, L. Reining, R. Del Sole, G. Onida, Phys. Rev. Lett. **80**, 4510 (1998)
8. M. Alouani, J.M. Koch, M.A. Khan, J. Phys. F **16**, 473 (1986)
9. M. Alouani, J.M. Wills, Phys. Rev. B **54**, 2480 (1996)
10. M. Amiotti, G. Guizzetti, F. Marabelli, A. Piaggi, V.N. Antonov, V.N. Antonov, O. Jepsen, O.K. Andersen, A. Borghesi, F. Nava, V.V. Nemoshkalenko, R. Madar, A. Rouault, Phys. Rev. B **45**, 13285 (1992)
11. O.K. Andersen, Phys. Rev. B **12**, 3060 (1975)
12. O.K. Andersen, O. Jepsen, Phys. Rev. Lett. **53**, 2571 (1984)
13. O.K. Andersen, O. Jepsen, G. Krier, *Lectures on Methods of Electronic Structure Calculations* (World Scientific Publishing, Singapore, 1994), pp. 63–124
14. V.I. Anisimov et al., Phys. Rev. B **48**, 16929 (1993)
15. V.I. Anisimov, A.I. Poteryaev, M.A. Korotin, A.O. Anokhin, G. Kotliar, J. Phys. Cond. Matt. **9**, 7359 (1997)
16. A. Ankudinov, J.J. Rehr, Phys. Rev. B **56**, 1712 (1997)
17. S. Arapan, H.-K. Mao, R. Ahuja, PNAS **105**, 20627 (2008)
18. F. Araysetianwan, O. Gunnarsson, Rep. Prog. Phys. **61**, 237 (1998)
19. P.N. Argyres, Phys. Rev. **97**, 334 (1955)
20. R. Armiento, A.E. Mattsson, Phys. Rev. B **72**, 85108 (2005)
21. E. Arola, P. Strange, and B. Gyorffy, Phys. Rev. B **55**, 472 (1997)
22. N.W. Ashcroft, D. Mermin, *Solid-State Physics*, 1st edn. (Saunders College, Philadelphia, PA, 1976)
23. D.E. Aspnes, A.A. Studna, Phys. Rev. B **27**, 985 (1983)

24. P.W. Atkins, R. Friedman, *Molecular Quantum Mechanics*, 4th edn. (Oxford University Press, New York, NY, 2005)
25. W.G. Aulbur, L. Jönsson, J.W. Wilkins, Quasiparticle calculations in solids. Solid State Phys. **54**, 1–218 (2000)
26. A. Baldereschi, R. Resta, *Ab Initio Calculations of Phonon Spectra* (Plenum, New York, NY, 1981)
27. S. Baroni, P. Gianozzi, A. Testa, Phys. Rev. B **58**, 1861 (1987)
28. S. Baroni, R. Resta, Phys. Rev. B **33**, 7017 (1986)
29. L.X. Benedict, E.L. Shirley, R.B. Bohn, Phys. Rev. B **57**, R9358 (1998)
30. L.X. Benedict, E.L. Shirley, R.B. Bohn, Phys. Rev. Lett. **80**, 4514 (1998)
31. H.S. Bennett, E.A. Stern, Phys. Rev. **137**, A448 (1965)
32. T. Björkman. *Magnetic and Structural Properties of f-electron Systems from First Principles Theory*. Ph.D. thesis, Uppsala University, Materials Theory, 2009
33. P. Blochl, O. Jepsen, O.K. Andersen, Phys. Rev. B **49**, 16223 (1994)
34. N. Bloembergen, *Nonlinear Optics* (Benjamin, New York, NY, 1965)
35. S. Blugel, M. Weinert, P.H. Dederichs, Phys. Rev. Lett. **60**, 1077 (1988)
36. A.M. Boring, R.C. Albers, O. Eriksson, D.D. Koelling, Phys. Rev. Lett. **68**, 2652 (1992)
37. M. Born, *Principles of Optics* (Springer, London, 1964)
38. M.S.S. Brooks, D. Glotzel, J. Magn. Magn. Mater. **873**, 15–18 (1980)
39. M.S.S. Brooks, P. Kelly, Phys. Rev. Lett. **51**, 1708 (1983)
40. Ch. Brouder, M. Alouani, K.H. Bennamann, Phys. Rev. B **54**, 7334 (1996)
41. C.G. Broyden, Math. Program. **87**, 209 (2000)
42. P. Bruno, Phys. Rev. B **39**, 865 (1989)
43. T. Burkert, *Materials for Magnetic Recording Applications*. Ph.D. thesis, Uppsala University, Uppsala, 2005
44. J.F. Capitani, R.F. Nalewajski, R.G. Parr, J. Chem. Phys. **76**, 568 (1982)
45. P. Carra, M. Alterelli, Phys. Rev. Lett. **64**, 1286 (1990)
46. P. Carra, B.N. Harmon, B.T. Thole, M. Altarelli, G.A. Sawatzky. Phys. Rev. Lett. **66**, 2595 (1991)
47. P. Carra, B.T. Thole, M. Altarelli, X. Wang, Phys. Rev. Lett. **70**, 694 (1993)
48. D.M. Ceperley, B.J. Alder, Phys. Rev. Lett. **45**, 566 (1980)
49. A.B. Chen, Phys. Rev. B **14**, 2384 (1976)
50. C.T. Chen, Y.U. Idzerda, H.J. Lin, N.V. Smith, G. Meigs, E. Chaban, G. H. Ho, E. Pellegrin, F. Sette, Phys. Rev. Lett. **75**, 152 (1995)
51. C.T. Chen, N.V. Smith, F. Sette, Phys. Rev. B **43**, 6785 (1991)
52. J. Chen, Z.H. Levine, J.W. Wilkins, Appl. Phys. Lett. **66**, 1129 (1995)
53. G.N. Chestnut, Y.K. Vohra, Phys. Rev. Lett. **82**, 1712 (1999)
54. C.J. Bradley, A.P. Cracknel, Prog. Theor. Phys. **36**, 648 (1966)
55. S. Chadov et al., Eur. Phys. Lett. **82**, 37001 (2008)
56. M. Colarieti-Tosti, M.I. Katsnelson, S. Simak, R. Ahuja, B. Johansson, O. Eriksson, Phys. Rev. Lett. 93, 96403 (2004)
57. R.D. Cowan, J. Opt. Soc. Am. **58**, 808 (1968)
58. G.H.O. Daalderop, P.J. Kelly, M.F.H. Schuurmans, Phys. Rev. B **41**, 11919 (1990)
59. C. Dallera, M. Grioni, A. Shukla, G. Vanko, J.L. Sarrao, J.P. Rueff, D.L. Cox, Phys. Rev. Lett. **88**, 196403 (2002)
60. M. del Castello-Mussot, L.J. Sham, Phys. Rev. B **31**, 2092 (1985)

61. R. Del Sole, R. Girlanda, Phys. Rev. B **48**, 11789 (1993)
62. A. Delin, *Density Functional Calculations of Optical Spectra and Narrow Band Systems.* Ph.D. thesis, Uppsala University, Uppsala, 1998
63. A. Delin, S. Auluck, O. Eriksson, B. Johansson, J.M. Wills, Phys. Rev. B **60**, 14105 (1999)
64. A. Delin, O. Eriksson, R. Ahuja, B. Johansson, M.S.S. Brooks, T. Gasche, S. Auluck, J.M. Wills, Phys. Rev. B **54**, 1673 (1996)
65. A. Delin, L. Fast, O. Eriksson, B. Johansson, J. Alloys Compd. **275–277**, 472 (1998)
66. A. Delin, L. Fast, B. Johansson, O. Eriksson, J.M. Wills, Phys. Rev. Lett. **79**, 4637 (1997)
67. A. Delin, L. Fast, B. Johansson, O. Eriksson, J.M. Wills, Phys. Rev. B **58**, 4345 (1998)
68. A. Delin, P.M. Oppeneer, M.S.S. Brooks, T. Kraft, J.M. Wills, B. Johansson, O. Eriksson, Phys. Rev. B **55**, 10173 (1997)
69. A. Delin, E. Tosatti, Phys. Rev. B **68**, 144434 (2003)
70. A. Delin, E. Tosatti, R. Weht, Phys. Rev. Lett. **92**, 057201 (2004)
71. G.Q. Di, S. Uchiyama, Phys. Rev. B **53**, 3327 (1996)
72. I. Di Marco, *Correlation Effects in the Electronic Structure of Transition Metals and Their Compounds.* Ph.D. thesis, Radboud University, Nijmegen, 2009
73. I. Di Marco, J. Minar, S. Chadov, M.I. Katsnelson, H. Ebert, A.I. Lichtenstein, Phys. Rev. B **79**, 115111 (2009)
74. P.A.M. Dirac, Proc. Cambridge Phil. Roy. Soc. **26**, 376 (1930)
75. R.M. Dreizler, E.K.U. Gross, *Density Functional Theory, An Approach to the Many-Body Problem* (Springer, Berlin, 1990)
76. B. Dritter, M. Weinert, R. Zeller, P.H. Dederichs, Solid State Commun. **79**, 31 (1991)
77. R. Dronsowski, P. Blöchl, J. Phys. Chem. **97**, 8617 (1993)
78. R. Wu, D.S. Wang, A.J. Freeman, Phys. Rev. B **47**, 14932 (1993)
79. H. Ebert, *Circular Magnetic X-ray Dichroism in Transition Metals Systems in Spin-Orbit-Influenced Spectroscopies of Magnetic Solids* (Springer, Herrsching, 1995), Chap. 9, p. 159
80. H. Ebert, Rep. Prog. Phys. **59**, 1665 (1996)
81. H. Ebert, P. Strange, and B.L. Gyorffy, J. Appl. Phys. **63**, 3055 (1988)
82. A.R. Edmonds, *Angular Momentum in Quantum Mechanics* (Princeton University Press, Princeton, NJ, 1974)
83. H. Ehrenreich, M.L. Cohen, Phys. Rev. **115**, 786 (1959)
84. H. Englisch, R. Englisch, Phys. Stat. Sol. (b) **123**, 711 (1984)
85. O. Eriksson, D.J. Becker, J.M. Wills, S. Balatsky, J. Alloys Compd. **287**, 1 (1999)
86. O. Eriksson, M.S.S. Brooks, B. Johansson, Phys. Rev. B **41**, 7311 (1990)
87. O. Eriksson, J.M. Wills, P. Söderlind, Phys. Rev. B **45**, 12588 (1992)
88. J. Erskine, E. Stern, Phys. Rev. B **8**, 1239 (1973)
89. J.L. Erskine, E.A. Stern, Phys. Rev. B **12**, 5016 (1975)
90. V. Eyert, *The Augmented Spherical Wave Method: A Comprehensive Treatment.* Lecture Notes in Physics, vol. 719 (Springer, Heidelberg, 2007)
91. M. Faraday, Phil. Trans. R. Soc. **131**, 1 (1846)
92. L. Fast, J.M. Wills, B. Johansson, O. Eriksson, Phys. Rev. B **51**, 17431 (1995)

93. I. Galanakis, S. Ostanin, M. Alouani, H. Dreysse, J.M. Wills, Phys. Rev. B **61**, 599 (2000)
94. J.M. Garcia-Ruiz, R. Villasuso, C. Ayora, A. Canals, F. Otalora, Geology **35**, 327 (2007)
95. A. Georges, Strongly correlated electron materials: Dynamical mean-field theory and electronic structure. In *AIP Conference Proceedings*, 2004, pp. 3–74
96. A. Georges, G. Kotliar, W. Krauth, M.J. Rozenberg, Rev. Mod. Phys. **68**, 13 (1996)
97. G. Gilat, R.M. Nicklow, Phys. Rev. **143**, 487 (1966)
98. R.W. Godby, M. Schlüter, L.J. Sham, Phys. Rev. Lett. **56**, 2416 (1986)
99. R.W. Godby, M. Schlüter, L.J. Sham, Phys. Rev. B **35**, 4170 (1987)
100. R.W. Godby, M. Schlüter, L.J. Sham, Phys. Rev. B **37**, 10159 (1988)
101. C.E.T. Goncalves da Silva, L.M. Falicov, J. Phys. C **5**, 906 (1972)
102. A. Gorling, Phys. Rev. A **54**, 3912 (1996)
103. W. Grange, I. Galanakis, M. Alouani, M. Maret, J.P. Kappler, A. Rogalev, Phys. Rev. B **62**, 1157 (2000)
104. W. Grange, M. Maret, J.P. Kappler, J. Vogel, A. Fontaine, F. Petroff, G. Krill, A. Rogalev, J. Goulon, M. Finazzi, N. Brookes, Phys. Rev. B **58**, 6289 (1998)
105. A. Grechnev, R. Ahuja, O. Eriksson, J. Phys. Cond. Matt. **15**, 7751 (2003)
106. A. Grechnev, I. Di Marco, M.I. Katsnelson, A.I. Lichtenstein, J. Wills, O. Eriksson, Phys. Rev. B **76**, 35107 (2007)
107. O. Gunnarsson, M. Jonson, B.I. Lundqvist, Phys. Rev. B **20**, 3136 (1979)
108. O. Gunnarsson, B.I. Lundqvist, Phys. Rev. B **13**, 4274 (1976)
109. G.Y. Guo, H. Ebert, W.M. Temmerman, P.J. Durham, Phys. Rev. B **50**, 3861 (1994)
110. S.V. Halilov, J. Phys. Cond. Matt. **4**, 1299 (1992)
111. S.V. Halilov, Y.A. Uspenskii, J. Phys. Cond. Matt. **2**, 6137 (1990)
112. W.A. Harrison, *Electronic Structure and the Properties of Solids* (Freeman, San Francisco, CA, 1980)
113. D.R. Hartree, *Elektronentheorie der Metalle*, volume 24 of *Handbuch der Physik* (Springer, Berlin, 1933), pp. 333–622
114. L. Hedin, Phys. Rev. **139**, 796 (1965)
115. K. Held, Adv. Phys. **56**, 829 (2007)
116. P. Hohenberg, W. Kohn, Phys. Rev. **136**, 864 (1964)
117. T. Hughbanks, R. Hoffmann, J. Am. Chem. Soc. **105**, 3528 (1983)
118. M.S. Hybertsen, S.G. Louie, Phys. Rev. B **32**, 7005 (1985)
119. M.S. Hybertsen, S.G. Louie, Phys. Rev. B **34**, 5390 (1986)
120. I. Galanakis, P.M. Oppeneer, P. Ravindran, L. Nordstrom, P. James, M. Alouani, H. Dreysse, O. Eriksson, Phys. Rev. B **63**, 172405 (2001)
121. V.Yu. Irkhin, M.I. Katsnelson, J. Phys. C **17**, 699 (1984)
122. V.Yu. Irkhin, M.I. Katsnelson, Solid State Commun. **58**, 881 (1986)
123. V.Yu. Irkhin, M.I. Katsnelson, Sov. Phys. JETP **63**, 631 (1986)
124. J.D. Jackson, *Classical Electrodynamics*, 2nd edn. (Wiley, New York, NY, 1975)
125. J.D. Jackson, *Classical Electrodynamics*, 3rd edn. (Wiley, New York, NY, 1998)
126. O. Jepsen, O.K. Andersen, Solid State Commun. **9**, 1763 (1971)
127. B. Johansson, A. Rosengren, Phys. Rev. B **11**, 1367 (1975)
128. B. Judd, *Operator Techniques in Atomic Spectroscopy* (Princeton University Press, Princeton, NJ, 1998)
129. F.J. Kahn, P.S. Pershan, J.P. Remeika, Phys. Rev. **186**, 891 (1969)

130. R.K. Kalia, P. Vashishta, Phys. Rev. B **17**, 2655 (1978)
131. V. Kanchana, G. Vaitheeswaran, M. Alouani, A. Delin, Phys. Rev. B **75**, 220404 (2007)
132. J. Kerr, Philos. Mag. **3**, 321 (1877)
133. J.C. Kimball, Phys. Rev. A **7**, 1648 (1973)
134. C. Kittel, *Introduction to Solid State Physics*, 8th edn. (Wiley, New York, NY, 2004)
135. W.H. Kleiner, Phys. Rev. **142**, 318 (1966)
136. K.I. Kobayashi, T. Kimura, H. Sawada, K. Terakura, Y. Tokura, Nature **395**, 677 (1998)
137. D.D. Koelling, B.N. Harmon, J. Phys. C: Solid State Phys. **10**, 3107 (1977)
138. W. Kohn, *Highlights of Condensed Matter Theory* (North-Holland, New York, NY, 1985)
139. W. Kohn, N. Rostoker, Phys. Rev. **94**, 1111 (1954)
140. W. Kohn, L.J. Sham, Phys. Rev. **140**, 1133 (1965)
141. E.I. Kondorski, E. Straub, Zh. Eksp. Teor. Fiz. **63**, 356 (1972)
142. J. Korringa, Physica **13**, 392 (1947)
143. G. Kotliar, S. Savrasov, K. Haule, V. Oudovenko, O. Parcollet, C. Marianetti, Rev. Mod. Phys. **78**, 856 (2006)
144. T. Kraft, P.M. Oppeneer, V.N. Antonov, H. Eschrig, Phys. Rev. B **52**, 3561 (1995)
145. G.S. Krinchik, V.A. Artemjev, Zh. Eksp. Teor. Fiz. **53**, 1901 (1967)
146. G.S. Krinchik, V.A. Artemjev, Sov. Phys. JETP **26**, 1080 (1968)
147. G.H. Kwei, A.C. Lawson, S.J.L. Billinge, S.W. Cheong. J. Phys. Chem. **97**, 2368 (1993)
148. B. Johansson, L. Vitos, J. Kollar, H.L. Skriver, Phys. Rev. B **62**, 10046 (2000)
149. C. Lanczos, *Applied Analysis* (Dover Publications Inc., New York, NY, 1988)
150. L.D. Landau, Sov. Phys. JETP. **3**, 920 (1957)
151. D.G. Laurent, J. Callaway, C.S. Wang, Phys. Rev. B **19**, 5019 (1979)
152. S. Lebegue, G. Santi, A. Svane, O. Bengone, M.I. Katsnelson, A.I. Lichtenstein, O. Eriksson, Phys. Rev. B **72**, 245102 (2005)
153. G. Lehmann, M. Taut, Phys. Stat. Sol. **54**, 469 (1972)
154. W. Lehmann, Solid-State Electron. **9**, 1107–1110 (1966)
155. Z.H. Levine, D. Allan, Phys. Rev. B **43**, 4187 (1991)
156. Z.H. Levine, D. Allan, Phys. Rev. Lett. **66**, 41 (1991)
157. A.I. Lichtenstein, M.I. Katsnelson, Phys. Rev. B **57**, 6884 (1998)
158. E.H. Lieb, *Density Functional Methods in Physics*. NATO ASI Series B123. (Plenum, New York, NY, 1985)
159. F. Lopez-Aguilar, J. Costa-Quintana, Phys. Stat. Sol. b **123**, 219 (1984)
160. T.L. Loucks, *Augmented Plane Wave Method* (W.A. Benjamin, New York, NY, 1967)
161. D.W. Lynch, C.G. Olson, D.J. Peterman, J.H. Weaver, Phys. Rev. B **22**, 3991 (1980)
162. A.H. MacDonald, S.H. Vosko, J. Phys. C **12**, 2977 (1979)
163. M.P. Marder, *Condensed Matter Physics* (Wiley, New York, NY, 2000)
164. R.M. Martin, *Electronic Structure, Basic Theory and Practical Methods* (Cambridge University Press, Cambridge 2004)
165. H.J. Mattausch, W.R. Hanke, G. Strinati, Phys. Rev. B **27**, 3735 (1983)
166. N.D. Mermin, Phys. Rev. A **137**, 1441 (1965)

167. N. Meskini, H.J. Mattausch, W. Hanke, Solid State Commun. **48**, 807 (1983)
168. M. Methfessel, Phys. Rev. B **38**, 1537 (1988)
169. M. Methfessel, A.T. Paxton, Phys. Rev. B **40**, 3616 (1989)
170. R.S. Mulliken, J. Chem. Phys. **23**, 1833 (1955)
171. J. Nagamatsu, N. Nakagawa, T. Muranaka, Y. Zenitani, Nature **410**, 63 (2001)
172. L. Nordström, J.M. Wills, P.H. Andersson, P. Söderlind, O. Eriksson, Phys. Rev. B **63**, 35103 (2000)
173. R. Nozawa, J. Math. Phys. **7**, 1841 (1966)
174. H. Olijnyk, W.B. Holzapfel, Phys. Lett. **100A**, 191 (1984)
175. P.M. Oppeneer, T. Maurer, J. Sticht, J. Kübler, Phys. Rev. B **45**, 10924 (1992)
176. C. Ortiz, O. Eriksson, M. Klintenberg, Comput. Mater. Sci. **44**, 1042 (2009)
177. J.P. Perdew, Phys. Rev. B **33**, 8822 (1986)
178. J.P. Perdew, *Electronic Structure of Solids 1991*, vol. 11 (Akademie Verlag, Berlin, 1991)
179. J.P. Perdew, K. Burke, M. Ernzerhof, Phys. Rev. Lett. **77**, 3865 (1996)
180. J.P. Perdew, K. Burke, Y. Wang, Phys. Rev. B **54**, 16533 (1996)
181. J.P. Perdew, M. Levy, Phys. Rev. Lett. **51**, 1884 (1983)
182. J.P. Perdew, M. Levy, Int. J. Quantum Chem. **31**, 6264 (1985)
183. J.P. Perdew, A. Zunger, Phys. Rev. B **23**, 5048 (1981)
184. P.S. Pershan, J. Appl. Phys. **38**, 1482 (1967)
185. J. Petalas, S. Logothetidis, S. Boultadakis, M. Alouani, J. M. Wills, Phys. Rev. B **52**, 8082 (1995)
186. S. Pisana et al., Nat. Mater. **6**, 198 (2007)
187. D.L. Price, B.R. Cooper, J.M. Wills, Phys. Rev. B **46**, 11368 (1992)
188. A.K. Rajagopal, J. Callaway, Phys, Rev. B **7**, 1912 (1973)
189. A.K. Rajagopal, J.C. Kimball, M. Banerjee, Phys, Rev. B **18**, 2339 (1978)
190. R. Ramirez, L.M. Falicov, J.C. Kimball, Phys. Rev. B **2**, 3383 (1970)
191. J. Rath, A.J. Freeman, Phys. Rev. B **11**, 2109 (1975)
192. P. Ravindran, A. Delin, P. James, B. Johansson, J.M. Wills, R. Ahuja, O. Eriksson, Phys. Rev. B **59**, 15680 (1999)
193. W. Reim, O. Hüsser, J. Schoenes, E. Kaldis, P. Wachter, K. Seller, J. Appl. Phys. **55**, 2155 (1984)
194. P.J. Rijnierse, Proc. R. Soc. Lond. A **292**, 288 (1966)
195. M. Rohlfing, P. Krüger, J. Pollmann, Phys. Rev. B **48**, 17791 (1993)
196. L.M. Sander, H.B. Shore, L.J. Sham, Phys. Rev. Lett. **31**, 533 (1973)
197. L. Sandratskii, Adv. Phys. **47**, 91 (1998)
198. S.Y. Savrasov, G. Kotliar, E. Abrahams, Nature **410**, 793 (2001)
199. S.Y. Savrasov, D.Y. Savrasov, Phys. Rev. B **54**, 16487 (1996)
200. J. Schoenes, *Handbook on the Physics and Chemistry of the Actinides*, vol. 1, Chap. 5 (North-Holland, Amsterdam, 1984)
201. J. Schoenes, *Proc. Nato School on Moment Formation in Solids* (Plenum, New York, NY, 1984), p. 237
202. G. Schütz, W. Wagner, W. Wilhelm, P. Kienle, R. Zeller, R. Frahm, G. Materlik, Phys. Rev. Lett. **58**, 737 (1987)
203. J. Schwitalla, H. Ebert, Phys. Rev. Lett. **80**, 4586 (1998)
204. L.J. Sham, M. Schlüter, Phys. Rev. Lett. **51**, 1888 (1983)
205. L.J. Sham, M. Schlüter, Phys. Rev. B **32**, 3883 (1985)
206. A.B. Shick, V. Drchal, L. Havela, Europhys. Lett. **69**, 588 (2005)
207. H.L. Skriver, Phys. Rev. B **14**, 5187 (1976)

208. H.L. Skriver, Phys. Rev. B **15**, 1894 (1977)
209. H.L. Skriver, *The LMTO Method: Muffin-Tin Orbitals and Electronic Structure* (Springer, Berlin, 1983)
210. H.L. Skriver, N.M. Rosengaard, Phys. Rev. B **43**, 9538 (1991)
211. J.C. Slater, Phys. Rev. **34**, 1293 (1929)
212. J.C. Slater, Phys. Rev. **51**, 846 (1937)
213. N.V. Smith, C.T. Chen, F. Sette, L.F. Mattheiss, Phys. Rev. B **46**, 1023 (1992)
214. A. Smogunov, A. Dal Corso, A. Delin, R. Weht, E. Tosatti, Nat. Nanotechnol. **3**, 22 (2008)
215. P. Söderlind, Adv. Phys. **47**, 959 (1998) For a review of the actinide elements.
216. P. Söderlind, R. Ahuja, O. Eriksson, B. Johansson, J.M. Wills, Phys. Rev. B **49**, 9365 (1994)
217. P. Söderlind, R. Ahuja, O. Eriksson, J.M. Wills, B. Johansson, Phys. Rev. B **50**, 5918 (1994)
218. P. Söderlind, O. Eriksson, B. Johansson, J.M. Wills, A.M. Boring, Nature **374**, 524 (1995)
219. P. Söderlind, J.M. Wills, B. Johansson, O. Eriksson, Phys. Rev. B **55**, 1997 (1997)
220. I.V. Solovyev, J. Phys: Cond. Matter **20**, 293201 (2008)
221. A. Sommerfeld, H. Bethe, The wave mechanics of an atom with non-coulombic central field: part i. Proc. Camb. Philol. Soc. **24**, 89 (1928)
222. A. Sommerfeld, H. Bethe, The wave mechanics of an atom with non-coulombic central field: part ii. Proc. Camb. Philol. Soc. **24**, 111 (1928)
223. A. Sommerfeld, H. Bethe, The wave mechanics of an atom with non-coulombic central field: part iii. Proc. Camb. Philol. Soc. **24**, 426 (1928)
224. P. Souvatzis et al., J. Phys. Cond. Matt. **16**, 5241 (2004)
225. M. Springborg, O.K. Andersen, J. Chem. Phys. **87**, 7125 (1986)
226. M.B. Stearns, *3d, 4d and 5d Elements, Alloys and Compounds* (Springer, Berlin, 1986)
227. P.J. Stephens, F.J. Devlin, C.F. Chabalowski, M.J. Frisch, J. Phys. Chem. **98**, 11623 (1994)
228. P.A. Sterne, J.C. Inkson, J. Phys. C **17**, 1497 (1984)
229. P. Strange, B.L. Gyorffy, Phys. Rev. B **52**, R13091 (1995)
230. G. Strinati, H.J. Mattausch, W. Hanke, Phys. Rev. Lett. **45**, 290 (1980)
231. G. Strinati, H.J. Mattausch, W. Hanke, Phys. Rev. B **25**, 2867 (1982)
232. A. Svane, Solid State Commun. **140**, 364 (2006)
233. P. Thalmeier, L. Falicov, Phys. Rev. B **20**, 4637 (1979)
234. A.K. Theophilou, N.I. Gidopoulos, Phys. Rev. B **56**, 333 (1995)
235. B.T. Thole, P. Carra, F. Sette, G. van der Laan, Phys. Rev. Lett. **68**, 1943 (1992)
236. L.H. Thomas, Proc. Camb. Philol. R. Soc. **23**, 542 (1927)
237. P. Thunström, I. Di Marco, A. Grechnev, S. Lebegue, M. I. Katsnelson, A. Svane, O. Eriksson, Phys. Rev. B **79**, 165104 (2009)
238. M. Tisher et al., Phys. Rev. Lett. **75**, 1602 (1995)
239. Yu.A. Uspenski, E.G. Maksimov, S.U. Rashkeev, I.I. Mazin, Z. Phys. B **53**, 263 (1983)
240. G. Vaitheeswaran, V. Kanchana, M. Alouani, A. Delin, Europhys. Lett. **84**, 47005 (2008)
241. G. Vaitheeswaran, V. Kanchana, A. Delin, Appl. Phys. Lett. **86**, 32513 (2005)

242. G. van der Laan, B.T. Thole, G.A. Sawatzky, J.B. Goedkoop, J.C. Fuggle, J.M. Esteva, R.C. Karnatak, J.P. Remeika, H.A. Dabkowska, Phys. Rev. B **34**, 6529 (1986)
243. P.G. van Engen, Ph.D. thesis, Technical University, Delft, 1983
244. J.H. van Vleck, Phys. Rev. B **52**, 1178 (1937)
245. M. Veszelei, *Preparation and Characterization of Sputtered Metal Oxides and Nitrides for Optical Applications*. Ph.D. thesis, Uppsala University, Uppsala, 1997
246. G. Vignale, M. Rasolt, Phys. Rev. B **37**, 10685 (1988)
247. L. Vitos, Phys. Rev. B **64**, 14107 (2001)
248. L. Vitos, J. Kollar, H.L. Skriver, Phys. Rev. B **49**, 16694 (1994)
249. J. Vogel, A. Fontaine, V. Cros, F. Petroff, J.P. Kappler, G. Krill, A. Rogalev, J. Goulon, Phys. Rev. B **55**, 3663 (1997)
250. U. Von Barth, L. Hedin, J. Phys. C **5**, 1629 (1972)
251. D.C. Wallace, *Thermodynamics of Crystals* (Wiley, New York, NY, 1972)
252. C.S. Wang, J. Callaway, Phys. Rev. B **9**, 4897 (1979)
253. M. Weinert, J. Math. Phys. **22**, 2433 (1980)
254. B. Wenzien, J. Kudrnovsky, V. Drchal et al., J. Phys. Cond. Matt. **1**, 9893 (1989)
255. K.H. Weyrich, Phys. Rev. B **37**, 10269 (1988)
256. K.W. Wierman, J.N. Hifiker, R.F. Sabiryanov, S.S. Jaswal, R.D. Kirby, J.A. Woollam, Phys. Rev. B **55**, 3093 (1997)
257. A.R. Williams, J. Kübler, C.D. Gelatt, Phys. Rev. B **19**, 6094 (1979)
258. J.M. Wills, B.R. Cooper, Phys. Rev. B **36**, 3809 (1987)
259. J.M. Wills, O. Eriksson, Phys. Rev. B **45**, 13879 (1992)
260. J.M. Wills, O. Eriksson, Ground state properties of the actinide elements: a theoretical overview, past, present and future. LA-Science **26**, 128 (2000). This fact has been analysed many times, and a recent reference can be found here.
261. J.M. Wills, O. Eriksson, P. Söderlind, A.M. Boring, Phys. Rev. Lett. **68**, 2802 (1992)
262. N. Wiser, Phys. Rev. **129**, 62 (1963)
263. R. Wu, A.J. Freeman, Phys. Rev. Lett. **73**, 1994 (1994)
264. R. Wu, D. Wang, A.J. Freeman, Phys. Rev. Lett. **71**, 3581 (1993)
265. T. Yabuuchi, Y. Nakamoto, K. Shimizu, T. Kikegawa, J. Phys. Soc. Jpn. **74**, 2391 (2005)
266. D.A. Young, *Phase Diagrams of the Elements* (University of California Press, Berkeley, CA, 1991)
267. R. Yu, D. Singh, H. Krakauer, Phys. Rev. B **43**, 6411 (1991)

Index